



UNIVERSITÀ
DEGLI STUDI
DI PADOVA

Sede Amministrativa: Università degli Studi di Padova

Dipartimento di Ingegneria Industriale

CORSO DI DOTTORATO IN: INGEGNERIA INDUSTRIALE
CURRICOLO: INGEGNERIA CHIMICA, DEI MATERIALI E MECCANICA
CICLO XXIX

**DEVELOPMENT OF AN INNOVATIVE PROCESS TECHNOLOGY FOR THE
MANUFACTURE OF STRUCTURAL HYBRID COMPONENTS, MADE BY
FORMING AND OVERMOLDING OF THERMOPLASTIC
MATRIX COMPOSITES**

Coordinatore del Corso di Dottorato: Ch.mo Prof. PAOLO COLOMBO

Coordinatore d'Indirizzo: Ch.mo Prof. GIOVANNI MENEGHETTI

Supervisore: Ch.mo Prof. GIOVANNI LUCCHETTA

Dottorando: Ing. RUGGERO GIUSTI

“Real progress happens only when advantages of a new technology become available to everybody”

Henry Ford

To those who have believed, believe and will believe in me.

A Giuseppe, Mariagrazia e Lorenzo. La mia famiglia.

Abstract

Hybrid composite materials are even more used in order to answer to the lightweight requirements of the automotive industry. Reducing vehicle weight to reduce energy consumption and local CO₂ emission is one of the most important goal required by the regional regulation of transport. On the contrary, the safety of the driver, of the passenger and of the pedestrian too is even more leading to increase the volumes of the vehicle. In order to improve the overall stiffness, strength and impact energy absorption of the body of a car, each part must absolve to different function and be designed with different mechanical properties. Another important topic related to the CO₂ emission and to the environmental safety is the end-of-life treatment that pushes on high percentage of recycling and re-uses. Thermoplastic composites are wide spread in automotive industry also thanks to their high processability and their easier recyclability in comparison to the thermosetting, furthermore they allow an increased design freedom. These characteristics made such materials a good candidate for metal replacement.

Thermoplastic materials can be reinforced with various kinds of fillers, whether they are continuous and discontinuous, short or long. The reinforcing fibers play an important role in the diversification of the properties of the material and therefore of the part that they constitute. For example, the impact properties are strongly related to the length of the reinforcement, while the tensile strength and the elastic modulus are less sensitive. When the properties offered by thermoplastic composite materials cannot be further increased, plastic composites, thanks to their high specific performances, are combined with other materials in the final part by means of junctures that are based on different adhesion mechanisms.

In the last decade, several technologies that incorporate the injection molding process were proposed for manufacturing of hybrid parts. The main advantages are the suitability for high volume production and for the implementation of the in mold assembly or joining. Polymer metal hybrids had been used to reduce the amount of bolt joint and welded connection. A sheet metal is used as mold insert where ribs are overmolded to increase the stiffness and other features are directly added for joining the part to the assembly. The adhesion between sheet metal and polymer is ensured by physical interlocking due to the roughness of the surface and undercuts. During the injection phase, the melted material fills the cavities and, after the cooling phase, it works as riveting system. However, treatments of the metal-side interface such as sandblasting, drilling, laser ablating and or plasma activation are required to improve the adhesion. Moreover, riveting joining could be added for secondary assembly operations. Otherwise, when thermosetting adhesives ensure the connection, the technology is called in mold bonding. The adhesive that can be one-part, such as cyanoacrylates, two-part, such as epoxy, or a hybrid mix of the two, is applied on the insert side before the over-injection. Its curing time must be consistent with the cycle time of the injection molding process in order to maintain the high productivity.

Very recently, in mold forming technology, also known as FiberForm, Organomelt and Organo Sheet Injection, was proposed for manufacturing of full thermoplastic hybrid composites. An outer thermoformed shell reinforced with continuous fibers is internally stiffened with an over-injected ribs-system. This technology allows to directly coupling thermoforming and injection molding processes of fiber-reinforced material. The adhesion between parts is ensured by an interdiffusion of the macromolecules across the interface. The welding is based on the reptation theory and is promoted by the high process temperature. For semi-crystalline polymer, the overall degree of adhesion is related to the residence time of the interface at temperatures higher than the crystallization temperature.

Furthermore, a good adhesion is due to the compatibility of the matrices. For processes that involve the injection-molding phase, the residence time is short and strongly non-isothermal. This means that the maximum adhesion strength could be lower than the theoretical maximum, reached at the weld line of short-glass reinforced part that is equal to the matrix strength. Moreover, even if a good welding takes place, the weaker zone moves to the laminate side at the interface between the matrix and the glass-woven reinforcement. The direct consequence is a weaker zone at the welding area that could be subjected to delamination failure. Delamination of composite interfaces is commonly simulated with the cohesive zone model proposed many years ago by Dugdale and deepened by Barrenblatt. The cohesive law, which is based on a stress-opening relationship, describes the damage phenomenon at the interface. Various kinds of fracture can be described with dedicated cohesive law that requires a calibration on the experimental data. Linear law, also known as triangular law, is used for brittle fracture; exponential law or trapezoidal law are more suitable for ductile fracture; bi-triangular law is used to describe the fracture in composite materials where the fiber pullout becomes significant after the damage initiation and made the opening slighter.

On the base of what was previously highlighted, a good design of the part is required to justify the financial investment on the processing chain. Especially in the processes that are based on the injection molding process and are strongly volume sensitive, creating pre-series is time and cost consuming. However, in very recent time, new technologies for individualized or tailored production are under development. For example, the “LightFlex” project, which is funded by the Federal Ministry for Education and Research in Germany, is aimed to replace use of injection-molded components with components produced via additive production. 3D-printing permits parts to be customized to meet virtually any requirements and to be provided with the capability to perform any specified function prior to being joined to a thermoplastic fiber composite material in order to achieve the required level of load capacity. The two half-molds are constituted by the 3-D printed part and from the silicon membrane of the pressure-chambre that is aimed to form the organosheet. The welding between parts can take place after local heating of the interdice up to the melting temperature. Although the good idea, the project is still ongoing and also in this case, the adhesion between parts play a challenging role.

The only alternative to define the performance of the part is to optimize the finite element simulation. For this reason, the definition of the boundary condition as well the definition of the interface strength became of fundamental importance. However, increasing the welding strength pushes toward a better global performance of the part.

Sommario

I materiali compositi ibridi sono sempre più impiegati per rispondere alle esigenze *lightweight* dell'industria automobilistica. Ridurre il peso del veicolo per la riduzione del consumo energetico e le emissioni locali di CO₂ è uno degli obiettivi più importanti che le normative regolanti la produzione dei veicoli di trasporto richiedono. Al contrario, la sicurezza del guidatore, del passeggero e dei pedoni tende all'incremento dei volumi e generalmente anche il peso del veicolo. Al fine di aumentare la rigidità, la resistenza e l'assorbimento di energia del corpo del veicolo, ogni parte deve assolvere specifiche funzioni e deve essere progettata con diverse proprietà meccaniche. Un ulteriore aspetto legato all'emissione di CO₂ e alla sicurezza ambientale è il trattamento del veicolo a fine vita, anch'esso regolamentato, che richiede elevate percentuali di recupero e riutilizzo dei materiali. I compositi termoplastici sono largamente utilizzati dall'industria automobilistica per la loro elevata processabilità e per la più facile riciclabilità se comparati con i compositi termoindurenti. Inoltre, garantiscono una libertà di design superiore. Queste caratteristiche rendono i materiali termoplastici degli ottimi candidati alla sostituzione di parti in metallo.

I materiali termoplastici possono essere rinforzati con cariche di diverso genere, siano esse continue o discontinue, corte o lunghe. Le fibre di rinforzo rivestono un ruolo fondamentale nella diversificazione delle proprietà del materiale e quindi della parte che costituiscono. Per esempio, le proprietà di resistenza all'impatto sono fortemente connesse alla lunghezza del rinforzo, mentre la resistenza a trazione e il modulo elastico ne sono meno sensibili. Quando variando le tipologie di matrice e di carica non vi è possibilità di incrementare ulteriormente le proprietà dei compositi termoplastici, essi vengono combinati con altri materiali mediante giunzioni, basate su diversi meccanismi di adesione, al fine di rispettare i target di progettazione del componente.

Nell'ultimo decennio sono state proposte diverse tecnologie basate sul processo di stampaggio ad iniezione per la produzione di parti ibride. Il processo è ampiamente utilizzato per la predisposizione ad elevati volumi produttivi, all'automazione e all'integrazione di varianti che consentono l'*in-mold forming* (formatura in stampo) e l'*in-mold joining* (incollaggio, rivettatura o assemblaggio in stampo). I materiali ibridi metallo-plastica sono stati utilizzati per ridurre il numero di giunzioni bullonate e saldature. Una lamiera in metallo che assolve le funzioni prettamente resistenziali è utilizzata come inserto stampo e le nervature di rinforzo vengono sovrastampate per incrementare la rigidità del componente. Nella medesima fase possono essere ricavati gli elementi per l'assemblaggio con le altre parti dell'assieme. L'adesione tra lamiera metallica e materiale polimerico viene garantita dal bloccaggio fisico dovuto alla rugosità della superficie metallica, che può essere trattata, e dall'impiego di sottosquadri. Durante la fase di iniezione, il materiale fuso riempie la cavità e, dopo il raffreddamento della parte, lavora come un sistema di rivetti. Tuttavia, trattamenti della superficie come sabbiatura, foratura, ablazione laser o attivazione con plasma, sono preferibili per la preparazione della superficie dell'inserto e sono necessari all'incremento dell'adesione. Diversamente, quando adesivi termoindurenti o bicomponenti vengono utilizzati per la giunzione primaria, il processo viene chiamato *in-mold bonding*. L'adesivo, che può essere mono-componente come i cianoacrilati, bi-componente come le colle epossidiche o un mix dei due, è applicato sull'inserto prima del sovrastampaggio. Il suo tempo di reticolazione deve essere sufficientemente rapido per non incidere sul tempo ciclo del processo di stampaggio e garantire l'elevata produttività.

Molto recentemente, la tecnologia *in-mold forming*, anche conosciuta come FiberForm, Organomelt o Organo Sheet Injection (Iniezione di fogli organici), è stata proposta per la fabbricazione di compositi ibridi termoplastici. In particolare, un guscio termoformato

rinforzato con fibre continue, viene irrigidito da un sistema di nervature sovrainiettate. La tecnologia permette di accoppiare direttamente i processi di termoformatura e di stampaggio ad iniezione. L'adesione tra le due parti avviene grazie all'interdiffusione delle macromolecole attraverso l'interfaccia. La saldatura è basata sulla teoria della reptazione ed è promossa dalle elevate temperature di processo al quale le matrici termoplastiche si trovano al momento del contatto. Per materiali semi-cristallini, il grado di adesione è correlato al tempo in cui l'interfaccia permane a temperature superiori alla temperatura di cristallizzazione e di fusione della matrice polimerica. Inoltre, una buona adesione è favorita dalla buona compatibilità chimica delle matrici. Per processi in cui è integrato lo stampaggio ad iniezione, il tempo di permanenza è breve e fortemente non-isotermico. Questo indica che la massima forza di adesione raggiungibile sull'area della saldatura potrebbe essere inferiore a quella delle linee di giunzione di un composito e può teoricamente corrispondere alla resistenza della matrice termoplastica in quanto non vi è interdiffusione del rinforzo. Generalmente, se nei compositi ibridi termoplastici viene ottenuta una buona saldatura, la zona più debole della giunzione si sposta all'interfaccia matrice-tessuto in fibra all'interno del laminato. Conseguenza diretta di questo fenomeno è la presenza di una zona debole in prossimità dell'interfaccia che può essere sede di rottura per delaminazione.

La delaminazione in materiali compositi è largamente simulata con modelli coesivi proposti da Dugdale e approfonditi da Berrenblatt. La legge coesiva, che si basa su relazioni di sforzo-spostamento, descrive il danneggiamento dell'interfaccia. Ogni tipo di frattura che implica delaminazione può essere simulato ricorrendo alla più appropriata legge coesiva che richiede una calibrazione sui dati sperimentali. La legge bi-lineare, conosciuta anche come triangolare, è utilizzata per materiali che presentano una rottura fragile, mentre leggi esponenziali e trapezoidali sono più appropriate per descrivere rotture duttili. Anche la legge bi-triangolare può essere utilizzata e in particolare viene impiegata per descrivere la frattura nei materiali compositi dove le fibre che si trovano sulla superficie dell'area costituiscono l'unico collegamento tra le due parti del componente (fiber-bridging). Questo fa sì che dopo l'inizio del danneggiamento e una certa propagazione all'interno del composito, siano le fibre a sopportare il carico così da avere un'ulteriore propagazione che risulta essere meno repentina.

Sulla base di quanto è stato esposto, è richiesta una buona progettazione della parte per poter giustificare gli investimenti finanziari per la catena produttiva. Specialmente nei processi che si basano sulla stampaggio ad iniezione e che sono di conseguenza sensibili ai volumi produttivi, la creazione di pre-serie richiede tempo e strumentazioni semi-definitive caratterizzate da costi di produzione non trascurabili. Proprio per questo motivo sono state presentate delle nuove tecnologie, che sono tutt'ora in via di sviluppo, per produzioni individualizzate o customizzate. Per esempio, il progetto LightFlex, finanziato dal ministero federale tedesco per l'educazione e la ricerca, è finalizzato a proporre un'alternativa alla fase di sovrastampaggio ad iniezione. In particolare la parte iniettata viene sostituita da una ottenuta mediante tecniche additive, con i vantaggi ad essa legati, che costituisce la metà stampo inferiore, mentre la metà stampo superiore viene sostituita da una membrana elastomerica che è parte integrante della camera a pressione. Lo stampaggio 3D permette la customizzazione del prodotto, consentendo idealmente di ottenere qualsiasi geometria per l'asservimento di ogni specifica funzione (collegamenti, appendici, ecc.), mentre la camera in pressione provvede alla formatura del laminato termoplastico che viene formato sulla parte sottostante previo riscaldamento localizzato fino a fusione dell'interfaccia. Il progetto è ancora in via di sviluppo e anche in questo caso l'adesione tra le due parti è basata sull'interdiffusione e costituisce uno degli aspetti critici del processo.

L'unica alternativa per poter definire le prestazioni della parte è l'ottimizzazione delle simulazioni agli elementi finiti. Per questa ragione, la definizione delle condizioni a contorno, così come la definizione della resistenza dell'interfaccia, diventano di fondamentale importanza. Tuttavia, l'incremento della resistenza della saldatura ottenuto mediante l'ottimizzazione dei parametri di processo consente il miglioramento globale delle prestazioni meccaniche della parte.

Preface

The Ph.D. dissertation presents the research work that was carried out at the Te.Si. Laboratory of the Department of Industrial Engineering of the University of Padova, between January 2014 and December 2016. Part of the work, which is closely connected to the main research topic, was held at the Institute of Polymer Processing (IKV) of the RWTH University from July until October 2016. This work is structured in three different parts. The first part of the work shows an industrial case of re-design of an automotive front-end where the replacement of three metal parts of different thickness and function are replaced by reinforced thermoplastic laminate. The general motivation about the metal replacement approach is discussed and the main challenges in modeling the part are highlighted. The second and the third parts of the work are discussed in a parallel way. The part 2 is focused on the evaluation of the welding strength in full thermoplastic hybrid T-joint specimens made by injection overmolding of composite laminates. The part 3 discusses the importance of the length of the reinforcement in injection molded parts and provides a complete method for measuring the fiber length. The work is supported by two case studies that use the procedure.

Part 1

The first part of the work introduces the lightweight design and the importance of the bonding strength in hybrid composite parts. A real industrial case-study of part re-design in full-thermoplastic hybrid composite is presented. The study is aimed to the redesign and to the preliminary validation of an automotive front-end under four static loading conditions. The metal sheet that constitutes the main transversal beam and the flanges for connecting the front-end to the chassis were replaced by organosheet laminate of different thickness. The geometry of the overinjected part that constitutes the reinforcing ribs was re-designed at the interface area and many configurations of the layering of the organosheet were evaluated. Both the design and the modeling guideline provided by the customer constituted a strong limitation and made the approach challenging. The redesign phases, the definition of the boundary conditions and the intermediate optimization changes are widely discussed. Finally, the results of the simulation are presented and the main challenge in modeling is highlighted.

Part 2

The work in the part 2 investigates how the process parameters are related to welding strength in a hybrid T-Joint made of thermoplastic composite materials. Furthermore, the aspects of the interface that are related to the resistance were deepened. The maximum theoretical welding resistance is assumed equal to the strength of the matrices. The first experiments are aimed to define how the process parameters affect the ideal welding by neglecting the eventuality of the delamination. T-joint specimens were manufactured by overinjection molding of a polypropylene stem on a rectangular cut out from polypropylene laminate. The degree of healing at the interface was analytically modeled by using two different approaches. The hybrid T-joint specimens were manufactured by coupling two composite materials. The basis of the specimen is a polypropylene laminate reinforced with 50 wt-% glass woven while the stem is a polypropylene reinforced with 30 wt-% long glass fiber. The effects of the melt temperature and of the packing pressure, combined to a variothermal mold control system, were investigated in accordance to the design of experiments approach. The resistance of the welding was determined through tensile tests and the ultimate tensile stress was assumed as the response variable. The effect of an annealing heating on distension of the stress induced by the process was also evaluated. Moreover, the best injection process parameters setting was applied in overmolding of the

composite laminate provided in four different conditions, according to the industrial practice: after thermoforming compaction and cooling down and after softening and clamping inside the injection mold. Furthermore, the effect of a local heating on morphological changes was investigated. The laminate was provided both after a local heating with subsequent cooling down at room temperature and after a local heating before the positioning in the cavity. The global performance was evaluated by means of tensile test. Double cantilever beam (DCB) specimens were manufactured with the organosheet used for the basis. The interlaminar fracture toughness of the composite sheet was evaluated by calibrating the cohesive model on the experimental data. Finally, the cohesive zone model parameters were calibrated on the experimental tensile test results of the T-joint specimen. A higher variability in the behavior was observed and even if the specimens were manufactured with the same process conditions, two different kind of breakage were observed. The different breakage can be modeled respectively with a bilinear and a trilinear cohesive load. The CZM was then applied as boundary condition for the definition of the cohesive material that regulates the behavior of the interface in the finite element analysis of the specimens.

The part 2 also includes the activities carried out at the IKV, where the development of a new process technology for the manufacturing of individualized full thermoplastic hybrid parts is ongoing. The effects of the main process parameters on the welding resistance of “individualized” T-joint specimens were evaluated. In this technology, the welding is based on the same principles. The welding conditions of the conventional technology, which is the in-mold forming technology, is assumed as reference target.

Part 3

The work in part 3 introduces the importance of the length of the fibers and their distribution in evaluating the overall performance of an injected molded part. A complete method, which is based on image analysis, is thoroughly explained. The experimental produce for obtain the fibers involves the pyrolysis of the matrix and the spreading of the fibers on desktop scanner. The fibers are spread on a glass and they are grouped in 35 defined regions by using a mask. Then the images are acquired with the software supplied by the producer of the scanner and are preliminary processed before the final analysis. The image analysis was performed with an open source software programmed and distribute by the Laboratory for Optical and Computational Instrumentation of the University of Wisconsin, which was developed for the evaluation of the collagen fibers in biomedical application. The software was completely recalibrated for the measure of the length of the reinforcing fibers. The effect of all the parameters that regulate the fiber recognition and measuring was evaluated. Then, the conversion of the length from pixels to millimeter was performed after a previously calibration a sample on a CMM. The same machine was used for evaluating the measure uncertainty. Manual and automatic measuring are compared and after the complete validation of the procedure, two case studies were investigated. The first case study is aimed to evaluate the effect of the plasticating screw on the fiber breakage. First, the preliminary results were obtained when the development of the procedure was in an advanced step. Two screws with different geometry were used at two different process conditions for the plasticating of a LGF reinforced polymer. Then, after the optimization of the procedure, the fibers from one of the previous configurations were reprocessed. Finally, the measuring system was used for evaluating the effect of the nozzle of a hot runner system on the fibers breakage. The degree of openness of the nozzle was changed and the fiber length was calculated.

Acknowledgements

My sincere gratitude goes to Professor Giovanni Lucchetta for the opportunity he gave me in joint his research group and for his guidance during these years. I would like to thank him especially for the teaching in assigning the priority of the life whether private or public, and for make me gather the real sense of the research. His encouragement and support throughout this work were fundamental in finalize this dissertation and to be able to publish it.

I cannot fail to mention the closest colleagues, graduate students and not, with which were shared joys and sorrows during these three years and more. I am lucky to have had their fraternal presence. In particular, I say thank you for this to Marco, Luca, Federico, Francesco, Rachele, Davide, Riccardo, Filippo and Valentina.

Heartfelt thanks to Professor Hopmann for giving me the opportunity to undertake part of the doctorate at his institute and to Arne and Markus for having integrated me into their research team and for having guided me in the work.

I would like, at this point, to express my sincere gratitude to my family, to my parents Giuseppe and Mariagrazia for their encouragements, teaching, and their life examples and, along with my brother Lorenzo, for the love that, in their own way, they make me feel.

Contents	
Abstract.....	i
Sommario	iii
Preface	vii
Acknowledgements.....	ix
Contents.....	xi
List of figures.....	xv
List of tables.....	xxiii
Part 1.....	1
1. Lightweight design of a modular front-end.....	1
1.1. European Regulations	3
1.2. Lightweight design with polymer and polymer composites.....	5
The pioneering industrial case of an automotive metal/polymer composite.....	9
1.3 Lightweight design of modular automotive front-end.....	11
1.4 In Mold Forming technology	17
The Organosheet Injection Overmolding	19
Individualized and functionalized production	21
1.5 The case study of an automotive front-end (collaboration with Sole S.p.A.).....	25
1.5.1 Approach to the redesign of the Front-End	27
1.5.2 Structural target performances.....	30
1.5.3 Modeling of the Front-End.....	34
1.5.4 Results, optimization and validation	41
1.6 General remarks: introduction to the following parts.....	47
Part 2.....	49
2 Welding resistance in full-thermoplastic hybrid composites	49
2.1 Joining of polymers	51
2.1.1 Process-induced welding	52
2.1.2 Analytical healing model.....	54
The Reptation theory	54
Molecular interdiffusion.....	56
Non-isothermal healing model	58
Consideration about the model.....	59
Correlation between the quadratic distance of diffusion and the healing model.....	59
2.2 Finite Elements Analysis	61
Autodesk Moldflow environment.....	61

Autodesk Simulation Mechanical environment	63
2.2.1 Structural simulation	63
Cohesive Zone Modeling (CZM)	63
Bilinear and Trilinear traction separation law	64
Trilinear law	66
2.3 Materials and their characterization.....	69
2.3.1 Materials and their characterization	69
Rheological characterization: rotational rheometer.....	69
Rheological characterization: capillary rheometer	70
Rheological characterization: the Cross-WLF model	72
Thermal characterization: DSC	73
Molecular weight and MFI: bibliography research	73
2.3.2 Lukoil Buplen 6331	74
2.3.3 Commercial laminate in homopolymer polypropylene.....	77
2.3.4 Mechanical characterization of the organosheet	79
Tensile testing in the 0°, 90°, and 45° direction.....	79
Manufacturing and testing of DCB specimens.....	80
Testing of the DCB specimens	82
2.3.5 Materials used for Individualized production.....	83
2.4 Experimental apparatus.....	85
2.4.1 T-joint specimens	85
2.4.2 Injection over molding of the T-joint specimens	85
2.4.3 Annealing treatment on hybrid T-joint.....	87
2.4.4 Individualized manufacturing process (Lightflex Project).....	88
2.4.5 Morphological characterization of the interface.....	91
2.4.6 Mechanical testing of T-joint	92
2.5 Scheduling of the experiments.....	93
2.5.1 Modeling the adhesion bonding in full-polypropylene T-joint specimens ...	93
Investigation of the effect of the process parameters	93
Modeling of the adhesion bonding and calculation of the quadratic distance of diffusion.....	94
2.5.2 Welding resistance in hybrid T-joint specimens	98
Effect of the process parameters.....	98
Evaluation of the residual stress	99
Evaluation of the effect of the morphology.....	100

2.5.3	Lightflex Project	102
2.6	Approach to the Cohesive Zone Modeling	105
2.6.1	The modeling in Ansys	105
2.6.2	Sensitivity analysis	108
	Factors defined by the sensitivity analysis	108
	Operating principle of the script in Matlab®	110
2.7	Results and discussions	111
2.7.1	Modeling the adhesion bonding in full-polypropylene T-joint specimens .	111
	Investigation of the effect of the process parameters	111
	Modeling of the adhesion bonding and calculation of the quadratic distance of diffusion.....	113
2.7.2	Welding resistance in hybrid T-joint specimens	120
	Effect of the process parameters.....	120
	Evaluation of the residual stress	122
	Effect of a localized heating	124
	Effect of the morphology.....	127
2.7.3	Welding resistance in <i>functionalized</i> hybrid T-joint specimens.....	130
	Future improvements	132
2.8	Result of the structural simulation (CZM).....	135
2.8.1	Modeling of the behavior of specimens with uniform heating of the laminate	135
	The most performant specimens (uniform heating)	135
	The less performant specimens (uniform heating)	137
2.8.2	Modeling of the behavior of specimens with local heating of the laminate	138
	The most performant specimens (local heating)	138
	The less performant specimens (local heating)	139
2.8.3	Modeling of the behavior of specimens with local heating and cooling of the laminate	141
2.8.4	Modeling of the behavior of specimens with laminate “as provided”.	141
2.8.5	Delamination of the analytical model.....	143
2.9	General discussion about the experimental behavior and modeling.....	145
	Variability during the tensile test	145
	Consideration about strain energy release rate G_{IC}	147
Part 3	151
3	Measurement of the fiber length distribution	151
3.1	Dependency of polymer properties on the length of the fibers.....	153

3.2	Traditional experimental procedure for fiber length distribution measurement.	157
3.2.1	Pyrolysis	157
3.2.2	Ultrasound bath	157
3.2.3	Image acquisition.....	158
3.2.4	Image analysis	158
3.2.5	Critical aspect of measurement procedures	159
3.3	Other technique for measuring of fiber length.....	163
3.4	Materials and methods	167
3.4.1	Material.....	167
3.4.2	Experimental apparatus for the image acquisition	167
	Procedures for spreading of the fibers	168
	Measurement of the rate pixel/millimeter	169
	Image acquisition and processing.....	170
3.5	Industrial case study.....	175
3.5.1	Plasticating settings	176
3.6	Preliminary results	179
3.7	Uncertainty calculation	183
3.7.1	Experimental procedure with the reference sample	185
3.7.2	Extension of the uncertainty to a 50-fibers sample	187
3.7.3	Extension of the uncertainty to the full sample made of 35 images.....	188
3.8	Industrial case studies for validation.....	189
3.8.1	Reprocessing of the fibers of the plasticating experiment.....	189
3.8.2	Evaluation of the damage induced by the opening level of the hot-chamber nozzles	189
3.9	Results.....	191
3.9.1	Evaluation of the uncertainty with the 25 fibers sample	191
3.9.2	Extension of the uncertainty to a 50-fibers sample	196
3.9.3	Extension of the uncertainty to the full sample made of 35 images.....	198
3.9.4	Reprocessing of the fibers of the plasticating experiment.....	202
3.9.5	Evaluation of the damage induced by the opening level of the hot-chamber nozzles	206
3.10	Conclusions.....	217
	Bibliography.....	219
	Part 1	219
	Part 2	225
	Part 3	231

List of figures

Figure 1.1 Fuel efficiency of automobiles by year [9]	5
Figure 1.2 Material consumption-rate for light vehicles [9]	6
Figure 1.3 Process steps for the manufacturing of an automotive part in metal/polymer composites [59]	9
Figure 1.4 Details of the connection by use of undercuts (a) and by use of adhesives (b) [62].....	12
Figure 1.5 Comparison of then stiffness of FEMs at the latch location as measured by the Vertical Latch Pull Test [61].....	13
Figure 1.6 Evolution of the technology for the manufacturing of FEM in several types of car [61]	14
Figure 1.7 Examples of full-thermoplastic composite hybrid parts for automotive applications [66]	17
Figure 1.8 Seat pan of the Opel Astra OPC [67].....	18
Figure 1.9 Processing phases of the direct in mold forming process [68]	19
Figure 1.10 Processing phases for the two-step in mold forming, insert molding [69]	20
Figure 1.11 Manufacturing Technologies as function of the complexity of the parts and properties [70]	20
Figure 1.12 3D printed ribs-structure and functionalized laminate [72]	21
Figure 1.13 3D printing station, hating stations and forming station of the processing route [72]..	21
Figure 1.14 Main components of the forming station [72]	22
Figure 1.15 Steps of the forming/joining phase[72].....	22
Figure 1.16 3D supporting system and improving of the geometry [72]	23
Figure 1.17 The metal-polymer hybrid Front-End where the dark region indicates the metal-sheet parts and the blue region indicates the fiber reinforced inject part	25
Figure 1.18 Assembly of the frontal part of the car where the Front-End is joined to the frame and to the other components.	26
Figure 1.19 Back view of the assembly of the frontal part of the car where the Front-End is joined to the frame and to the other components.	26
Figure 1.20 Reduction of the interface area between the ribs of the injected part and the laminate	27
Figure 1.21 Reduction of the interface area between the ribs of the injected part and the laminate	28
Figure 1.22 Adding of the reinforcing ribs.....	28
Figure 1.23 Topological optimization of the front under the opening effect of the hood	29
Figure 1.24 Full-plastic composite hybrid Front-End with reinforcement beams	29
Figure 1.25 Load condition “Front Light Stiffness” (number 1).....	31
Figure 1.26 Load condition “Hood Lock Stiffness” (number 2).....	31
Figure 1.27 Load condition “Hood Stops Stiffness” (number 3)	32
Figure 1.28 Load condition “Yield Point Hood Lock Stiffness” (number 4)	32
Figure 1.29 Constraint conditions of the bolted joint.....	33
Figure 1.30 Graphic interpretation of the MPC formulation [75]	36
Figure 1.31 Graphic interpretation of the Pinball Region [75]	37

Figure 1.32 Graphic representation of the specific orientation of the elements of the transversal beam.	38
Figure 1.33 Graphic representation of the constraint conditions. The figure on the left represents the definition of the bolted joint where the intersection of the pinball region with the flange and the spring used for the definition of the stiffness are shown. The figure on the right represents the areas where the pinball region defines the bonded contact.	39
Figure 1.34 Graphic representation of the constraint conditions. The figure on the left represents the definition of the load through the remote point. The figure on the right represents the areas where the pinball region defines the bonded contact and the spider system for the application of the remote force.....	40
Figure 1.35 Results of the topological analysis under the load case “Front Light Stiffness” and the ribs system that was modelled.....	42
Figure 1.36 Performance of the Front-Ends under the loading condition “Front Light Stiffness” (load condition number 1, target: Stiffness > 54,64 N/mm).....	42
Figure 1.37 Performance of the Front-Ends under the loading condition “Front Light Stiffness” (load condition number 4, target: deformation < 6 mm).....	43
Figure 1.38 Von Mises Equivalent Stress referred to the laminate with layering 80(1mm).50(45°0,5mm).80(1mm) and injected part under the load condition C1 (Back).....	44
Figure 1.39 Von Mises Equivalent Stress referred to the laminate with layering 80(1mm).50(45°0,5mm).80(1mm) and injected part under the load condition C1 (Front).....	44
Figure 1.40 Von Mises Equivalent Stress referred to the laminate with layering 80(1mm).50(45°0,5mm).80(1mm) and injected part under the load condition C4 (Back).....	45
Figure 1.41 Von Mises Equivalent Stress referred to the laminate with layering 80(1mm).50(45°0,5mm).80(1mm) and injected part under the load condition C4 (Front).....	45
Figure 1.42 (a) Load 1: equivalent stress at interface, (b) stress-strain curve of Stamax.....	46
Figure 2.1 Representation of the length of the macromolecular motion [33].....	55
Figure 2.2 Representation of the distance of interdiffusion [33].....	55
Figure 2.3 Graphic representation of the “Temperature:XY Plot” of two node at interface: the red node belong to a part insert at environmental temperature, the black one, hidden by the red node, belongs to the injected material.....	62
Figure 2.4 Representation of the process zone.....	64
Figure 2.5 Graphical representation of the bilinear cohesive law.....	65
Figure 2.6 Graphical representation of the trilinear cohesive law.....	66
Figure 2.7 Representation of how the two laws contribute in the definition of the behaviour of the trilinear law.	67
Figure 2.8 Geometries of the plate : flat-plate (A) and cone-plate (B).....	69
Figure 2.9 Rotational Rheometer ARES G2.....	70
Figure 2.10 Scheme of the capillary rheometer.....	70
Figure 2.11 Reometro rotazionale RHEOLOGIC 2500.....	71
Figure 2.12 Differential scanning calorimeter DQ200 (TA Instrument).....	73
Figure 2.13 Viscosity plot - PP Buplen.....	74
Figure 2.14 WLF model for the effect of temperature on viscosity - PP Buplen.....	75
Figure 2.15 DSC ramp test - PP Buplen.....	75

Figure 2.16 Frequency sweep test on Buplen at 220°C	76
Figure 2.17 Viscosity plot – PP Extruded Laminate	77
Figure 2.18 WLF model for the effect of temperature on viscosity – PP Extruded Laminate.....	78
Figure 2.19 DSC ramp test – PP Extruded Laminate.....	78
Figure 2.20 Geometry of the T-joint specimen	85
Figure 2.21 Injection mold for the manufacturing of the hybrid T-joint specimens	86
Figure 2.22 Machine and devices used for the manufacturing of the hybrid T-joint specimens	86
Figure 2.23 Hasco thermometer and Hasco Z2512 probe for contact measurement	87
Figure 2.24 MTS environmental chamber used for the annealing treatment	88
Figure 2.25 Supporting system for the stems with 14 slots.....	89
Figure 2.26 Example of the geometries of the 4 mm thick stem.....	89
Figure 2.27 Rectangular frame with pneumatic clamps and detail of a single clamp.....	89
Figure 2.28 Heating system for melting of the external area of the stems.....	90
Figure 2.29 Values of the temperature on the interface of the stem after 10 seconds from the removal of the supporting system	90
Figure 2.30 Forming station with the supporting system under the pressure chamber and IR heating station with the laminate on the rectangular fram	91
Figure 2.31 Sensofar Plu Neos Profiler and Nikon Metrology X-Tek uCT225.....	92
Figure 2.32 Clamping systems for the base of the specimen that were used during the tensile test	92
Figure 2.33 Time-Temperature plot of the injection molding cycle of the mold cavity under the laminates. The colored upper line indicates the thermoregulation phases, the lower one indicates the injection molding phases.....	99
Figure 2.34 Lateral view of the screen assembly	100
Figure 2.35 Screen for the local heating of the interface.	101
Figure 2.36 Interface morphology on the laminate side before the filling phase.....	102
Figure 2.37 General idea that supports the use of the macrostructure for a better heating of the surface of the stem.....	102
Figure 2.38 Macrostructuring features at the interface: without features, with regular features and with mixed features	103
Figure 2.39 Process cycle and main operations for the forming of the T-joint specimen.....	103
Figure 2.40 Preliminary results from the comparison of experimental and numerical data [59]...	105
Figure 2.41 Modeling of the geometry and of the boundary conditions	106
Figure 2.42 Effect of the parameter α in the bilinear law	109
Figure 2.43 Effect of the parameters δn^* , δnfb and δnc in the trilinear law	110
Figure 2.44 Main effects and interaction plots for melt temperature and holding pressure on the UTS of the full-polypropylene T-joint specimen.....	111
Figure 2.45 Main effects and interaction plots for melt temperature and laminate temperature on the UTS of the full-polypropylene T-joint specimen.....	112

Figure 2.46 Fracture surface. Specimen manufactured with temperatures at the lower level (220°C_30°C), on the left, and specimens manufactured with temperature at the higher level (260°C_130°C), on the right.	113
Figure 2.47 Comparison of the experimental and analytical results	114
Figure 2.48 Calculation of the quadratic distance of diffusion across the interface	Errore. Il segnalibro non è definito.
Figure 2.49 Main effects plot for the process parameters on the UTS of the hybrid T-joint specimen	121
Figure 2.50 Interaction plot for mold temperature and laminate temperature on the UTS of the hybrid T-joint specimen.....	121
Figure 2.51 Main effects plot for the process parameters on the Average Von Mises equivalent stress at the interface of the hybrid T-joint specimen	122
Figure 2.52 Main effect and interaction plots of the annealing parameters on the UTS of the hybrid T-joint specimen.....	123
Figure 2.53 Main effect and interaction plots of the process and annealing on UTS	123
Figure 2.54 Mean values of the UTS of the specimens manufactured with a local and a uniform heating of the laminate	125
Figure 2.55 Main effects plot for the process parameters on the UTS of the hybrid T-joint specimen with the local heating of the laminate	126
Figure 2.56 Micro x-ray investigation at the interface that shows the penetration of the injected material inside the laminate.....	127
Figure 2.57 Interaction plot of melt temperature and mold temperature on UTS (local heating)..	127
Figure 2.58 Mean values of the UTS of the specimens manufactured with the laminate provided with the four conditions.....	128
Figure 2.59 Reconstruction of the surface starting from the point clouds	129
Figure 2.60 Micro x-ray investigation of the interface and profilometry along the medium plane	130
Figure 2.61 Specimens manufactured with the Lightflex technology and details of the interface	131
Figure 2.62 Main effect plot and interaction plot of the process parameters on UTS.....	131
Figure 2.63 Ultimate tensile strength results of the functionalized hybrid T-joint specimens.....	132
Figure 2.64 Example of process-induced rivetting after having removed the aluminium insert ...	132
Figure 2.65 First experimental trial with process induce rivetting.....	133
Figure 2.66 Analysis of the interface in the process induced rivetting	133
Figure 2.67 Variant proposed for the process-induced rivetting.....	133
Figure 2.68 Bilinear model for specimens of the level AC.....	136
Figure 2.69 Trilinear model for the specimens of the level AC.....	136
Figure 2.70 Bilinear model for the specimens of the level O.....	137
Figure 2.71 Trilinear model for the specimens of the level O.....	138
Figure 2.72 Bilinear model for the specimens of the level AC _{local}	139
Figure 2.73 Bilinear model for the level B _{local}	140
Figure 2.74 Trilinear model for the level B _{local}	140
Figure 2.75 Bilinear model for the specimens of the level M.....	141

Figure 2.76 Bilinear model for the specimens of the level V	142
Figure 2.77 Trapezoidal model for the specimens of the level V	143
Figure 2.78 Modeling of the crack propagation.....	144
Figure 2.79 Delamination of the matrix and slight presence of fiber-bridging.....	145
Figure 2.80 Fiber peeled out by the stem	146
Figure 2.81 Examples of overlapping of the interface on the woven fabric	146
Figure 2.82 Morphological details of the surface of the fracture	147
Figure 2.83 Surface of the fracture on the stem's side of the hybrid T-joint specimen manufactured with laminate "as provided".....	147
Figure 2.84 Influence of the opening mode on <i>GC</i> [43].....	148
Figure 3.1 Tensile strength (in blue) and flexural strength (in black) vs. fibers content [3].....	153
Figure 3.2 Charpy (in blue) and Izod (in black) resilience vs. fibers content [4].	153
Figure 3.3 Fitting of the Kelly Tyson model [8].....	154
Figure 3.4 Mechanical properties vs. normalized fiber length [8].	154
Figure 3.5 Effect of fiber length on tensile strength with and without compatibilizer [9].....	155
Figure 3.6 Example of image before and after digital filtering [10]	158
Figure 3.7 Scale factor determination with reference fiber [10]	159
Figure 3.8 Example of fibers measurement [10].....	159
Figure 3.9 Scheme of fiber disposition on the slide and example of captured areas.....	160
Figure 3.10 Example of fiber entanglement on the slide	161
Figure 3.11 Example of not processable image because the fibers are not completely contained in the field of view of the instrument [11].	163
Figure 3.12 Example of "image-mosaic" technique [11].....	163
Figure 3.13 Automatic identification and labeling of a sample image with numerous cross fibers, using the software application used by Purdue University for PNNL [14].....	165
Figure 3.14 Distribution of the length of the fibers expected from simulations and experimentally measured [13].....	165
Figure 3.15 Rubber grid	168
Figure 3.16 Black box	168
Figure 3.17 Sample acquisition. For illustrative purpose this is only a selected portion containing 4 of 35 images. It can be noted as the rubber grid allows space for cropping the images leaving a significant margin, in order not to cut any fiber.....	169
Figure 3.18 Werth Video-Check IP 40.....	170
Figure 3.19 The script in Matlab code provides this output screen to refine the subsequent cropping coordinates.	171
Figure 3.20 Cropped image. It is possible to notice the overlapping rectilinear fibers. The software has no problem in solving the crossings. A particular care is only required in not overlapping the images, which comes easier after a short training phase in acquisition operations.....	172
Figure 3.21 Three-zone (above) and Maxi Melt (below) screws employed in the case study	175
Figure 3.22 Fibers length distribution at 200mm from the hopper.	179

Figure 3.23 Fiber length distribution at 800mm from the hopper.....	179
Figure 3.24 Breakage progression along the screws.....	180
Figure 3.25 Experimental average length of the reinforcement along each screw in conditions A and B.....	180
Figure 3.26 Schematic view of the five zones: from the operator point of view and how the pictures are acquired.....	186
Figure 3.27 Defect created by the edges of the slide in the acquisition (left). The image is subjected to a high brightness threshold to make it evident. Mask fabric (right) on which, at the center, the slide is placed.....	186
Figure 3.28 (1) counting of the fiber in ctFIRE; (2) counting of the fiber in ctFIRE without the threshold on the number of pixels.....	187
Figure 3.29 Automotive spoiler where the analysed sample were cut.....	189
Figure 3.30 Standard deviation of the measurement of each fiber (25 bars) repeated 10 times in the first zone.....	192
Figure 3.31 Standard deviation of the measurement of each fiber (25 bars) repeated 10 times in the second zone.....	192
Figure 3.32 Standard deviation of the measurement of each fiber (25 bars) repeated 10 times in the third zone.....	192
Figure 3.33 Standard deviation of the measurement of each fiber (25 bars) repeated 10 times in the fourth zone.....	193
Figure 3.34 Standard deviation of the measurement of each fiber (25 bars) repeated 10 times in the fifth zone.....	193
Figure 3.35 Systematic error of the measurement of each fiber (25 bars) repeated 10 times in the first zone.....	193
Figure 3.36 Systematic error of the measurement of each fiber (25 bars) repeated 10 times in the second zone.....	194
Figure 3.37 Systematic error of the measurement of each fiber (25 bars) repeated 10 times in the third zone.....	194
Figure 3.38 Systematic error of the measurement of each fiber (25 bars) repeated 10 times in the fourth zone.....	194
Figure 3.39 Systematic error of the measurement of each fiber (25 bars) repeated 10 times in the fifth zone.....	195
Figure 3.40 Average of the Standard Deviation of the length of the fibers in each zone (1-5).....	195
Figure 3.41 Mean of the systematic error in each zone (1-5).....	196
Figure 3.42 Calculated uncertainty of each zone (1-5).....	196
Figure 3.43 Arithmetic mean of the length of the fibers in each zone (1-5).....	196
Figure 3.44 Comparison of the three average models that are applied without filtering the data from ctFIRE, on the data measured in ImageJ and by filtering the data from ctFIRE in Matlab.....	197
Figure 3.45 Deviation of the arithmetic mean calculated on the ctFIRE output from the arithmetic mean calculated with the measurement made in ImageJ (no filter).....	198
Figure 3.46 Deviation of the weighted average calculated on the ctFIRE output from the weighted average calculated with the measurement made in ImageJ (no filter).....	198

Figure 3.47 Deviation of the Huq-Azaiez model calculated on the ctFIRE output from the Huq-Azaiez model calculated with the measurement made in ImageJ (no filter).....	199
Figure 3.48 The same image is presented as ctFIRE output without any filter on the minimum length. The longer line is an example of the scratches on the scanner screen that are recognized as a fiber (1). In this case the lower filter is set equal to 30 pixel (2).....	199
Figure 3.49 Deviation of the arithmetic mean calculated with the ctFIRE output from the arithmetic mean calculated with the measurement made in ImageJ (filter).....	200
Figure 3.50 Deviation of the weighted average calculated with the ctFIRE output from the weighted average calculated with the measurement made in ImageJ (filter).....	200
Figure 3.51 Deviation of the Huq-Azaiez model calculated with the ctFIRE output from the Huq-Azaiez model calculated with the measurement made in ImageJ (filter).....	201
Figure 3.52 Comparison of the three average models that are applied without filtering the data from ctFIRE, on the data measured in ImageJ and by filtering the data from ctFIRE in Matlab.....	201
Figure 3.53 Example of the effect of the lower filter in recognizing the fibers.....	202
Figure 3.54 Comparison between the average values calculated with Huq-Azaiez model before and after the optimization.....	203
Figure 3.55 Comparison of the arithmetic mean calculated without any filter, with lower filter of 30 pixels (1.27 mm) and the upper of 10.5 mm, and with lower filter of 1.5 mm and the upper of 10.5 mm.....	204
Figure 3.56 Comparison of the weighted average calculated without any filter, with lower filter of 30 pixels (1.27 mm) and the upper of 10.5 mm, and with lower filter of 1.5 mm and the upper of 10.5 mm.....	204
Figure 3.57 Comparison of the mean calculated with the Huq-Azaiez model without any filter, with lower filter of 30 pixels (1.27 mm) and the upper of 10.5 mm, and with lower filter of 1.5 mm and the upper of 10.5 mm.....	205
Figure 3.58 Comparison of the mean calculated with the three model by applying a lower filter of 30 pixels (1.27 mm) and the upper one of 10.5 mm.....	205
Figure 3.59 Comparison between the average values calculated on a random sub-image for each zone. The uncertainty was directly applied.....	206
Figure 3.60 Example of the image processing with long fragments (M1A) on the left and short fragments (M3D) on the right. In the first row the images are presented with a light threshold. In the second and third.....	208
Figure 3.61 Average length in the zone M1 by reducing the overture of the hot nozzle. The lower filter at 30 pixels (1.27 mm) was applied.....	209
Figure 3.62 Average length in the zone M1 by reducing the overture of the hot nozzle. The lower filter at 2 mm was applied.....	209
Figure 3.63 Average length in the zone M3 by reducing the overture of the hot nozzle. The lower filter at 30 pixels (1.27 mm) was applied.....	210
Figure 3.64 Average length in the zone M3 by reducing the overture of the hot nozzle. The lower filter at 2 mm was applied.....	210
Figure 3.65 Average length of the fibers in the 10 samples by applying the lower filter at 30 pixels (1.27 mm).....	211
Figure 3.66 Average length of the fibers in the 10 samples by applying the lower filter at 2 mm..	211
Figure 3.67 Fibers counting in each class of the sample M1A with the values that are lower filtered at 30 pixels. The graph is representative of the frequency in a sample on 4000 fibers.....	213

Figure 3.68 Fibers counting in each class of the sample M1D with the values that are lower filtered at 30 pixels. The graph is representative of the frequency in a sample on 4000 fibers..... 213

Figure 3.69 Fibers counting in each class of the sample M1A with the values that are lower filtered at 2 mm. The graph is representative of the frequency in a sample on 3000 fibers 214

Figure 3.70 Fibers counting in each class of the sample M1D with the values that are lower filtered at 2 mm. The graph is representative of the frequency in a sample on 3000 fibers 214

List of tables

Table 1.1 Volume and weight reduction in the new models: with and without the reinforcing beams	30
Table 1.2 Load application points and direction of the condition “Front Light Stiffness”	31
Table 1.3 Load application points and direction of the condition “Hood Lock Stiffness”	31
Table 1.4 Load application points and direction of the condition “Hood Stops Stiffness”	32
Table 1.5 Load application points and direction of the condition “Yield Point Hood Lock Stiffness”	33
Table 1.6 Coordinates and Equivalent Stiffness of the bolted joint	34
Table 1.7 Mechanical properties of Stamax 30YM240 used for the simulations	40
Table 1.8 Layers arrangement in the analysed model where the plies arrangement is reported by angle and the balanced laminate is indicated with “X” and the unbalanced with “=”.	41
Table 1.9 Progressive increase of the thickness and relative results in stiffness and local deformation in Z measured on the transversal beam.	42
Table 2.1 Coefficient for the Mark-Houwink equation [46]	74
Table 2.2 Cross-WLF parameters – PP Buplen	75
Table 2.3 Rheological and thermal properties – PP Buplen.....	76
Table 2.4 Cross-WLF parameters - PP Extruded Laminate.....	78
Table 2.5 Rheological and thermal properties – PP Extruded Laminate	79
Table 2.6 Elastic and Shear Modulus.....	80
Table 2.7 Average values and standard deviation of <i>GIC</i>	82
Table 2.8 Investigated parameters for the manufacturing of full-polypropylene T-joint specimens	93
Table 2.9 Injection molding parameters for the manufacturing of full-polypropylene T-joint specimens	93
Table 2.10 Temperature levels of the rectangular cutouts	93
Table 2.11 Coefficient for the calculation of the quadratic distance of diffusion at 220°C (PP).....	98
Table 2.12 Factors levels of the in mold forming process	99
Table 2.13 Injection molding parameters for the manufacturing of the hybrid T-joint specimens..	99
Table 2.14 Factors levels of the annealing treatment.....	100
Table 2.15 Factors levels for the overall evaluation of as-molded and annealed T-samples	100
Table 2.16 Factors levels of the Lightflex production	102
Table 2.17 Elastic Isotropic Material parameters for modeling of the stem.....	107
Table 2.18 Elastic Orthotropic Material parameters for modeling of the base	107
Table 2.19 Analysis of variance results for the process parameters on the UTS of full-polypropylene T-joint specimen.....	111
Table 2.20 Analysis of variance results for the process parameters on the UTS of the full-polypropylene T-joint specimen.....	112
Table 2.21 Analysis of variance results for the process parameters on the UTS of the hybrid T-joint specimen.....	121

Table 2.22 Analysis of variance results for the annealing parameters on the UTS of the hybrid T-joint specimen	123
Table 2.23 Analysis of variance results for the process setting and the annealing treatment on the UTS of the hybrid T-joint specimen	124
Table 2.24 Comparison of the UTS of specimens with laminate uniformly heated and laminate locally heated	125
Table 2.25 Analysis of variance results for the process parameters on the UTS of the hybrid T-joint specimen with the local heating of the laminate	126
Table 2.26 Comparison of the interfacial area and of the welding performance	129
Table 2.27 Analysis of variance results for the process parameters on the UTS of the functionalized hybrid T-joint specimen	131
Table 2.28 Cohesive zone parameters for the level AC of the hybrid T-joint specimens manufactured with the laminates provided at 150°C (uniform heating).....	136
Table 2.29 Cohesive zone parameters for the level O of the hybrid T-joint specimens manufactured with the laminates provided at 150°C (uniform heating).....	137
Table 2.30 Cohesive zone parameters for the level AC _{local} of the hybrid T-joint specimens manufactured with the laminates provided at 135°C (local heating).....	138
Table 2.31 Cohesive zone parameters for the level B _{local} of the hybrid T-joint specimens manufactured with the laminates provided at 135°C (local heating).....	139
Table 2.32 Cohesive zone parameters for the level M of the hybrid T-joint specimens manufactured with the laminates provided after local heating and cooling down.....	141
Table 2.33 Cohesive zone parameters for the level M of the hybrid T-joint specimens manufactured with the laminates provided without heating (“As provided”).....	142
Table 2.34 Values of <i>GIC</i> for the specimens modeled with the bilinear law	148
Table 2.35 Values of <i>GC</i> for the specimens modeled with the trilinear law and the values of <i>GIC</i> for the specimens modeled with the trapezoidal law	149
Table 3.1 Comparison of the parameters modified in ctFIRE software.....	172
Table 3.2 Aspect ratio of the three-zone screw	175
Table 3.3 Aspect ratio of the Maxi Melt screw.....	176
Table 3.4 Comparison between optimal and sub-optimal parameters	176
Table 3.5 Set temperatures for optimal parameters.....	176
Table 3.6 Set temperatures for sub-optimal parameters.....	176
Table 3.7 Percentage reduction at section 200 mm.....	180
Table 3.8 Comparison of the maximum and minimum value at section 800 mm.....	181
Table 3.9 Comparison of weight in conditions A and B.....	181
Table 3.10 Variables used in the uncertainty calculation.....	185
Table 3.11 Setting of the parameter of ctFIRE used for the calculation of the uncertainty	191
Table 3.12 Setting of the parameters of ctFIRE that are used for the acquisition of the larger sample with 50 fibers	197
Table 3.13 Setting of the parameters of ctFIRE that are used for the acquisition of the fiber from the plasticating trials	202

Table 3.14 Comparison between the averages calculated with the Huq-Azaiez model before and after the optimization of the method	203
Table 3.15 Average length of the fiber with lower filter at 1.27 mm and upper filter at 10.5 mm .	205
Table 3.16 Rate between weighted average and arithmetic mean for each section of the screw ...	206
Table 3.17 Setting of the parameters of ctFIRE that are used for the acquisition of the fiber from INglass samples	207
Table 3.18 Average values of the fiber length that was measured with a lower filter at 30 pixels	212
Table 3.19 Rate between weighted average and arithmetic mean of the fiber length that was measured with a lower filter at 30 pixels.....	212
Table 3.20 Average values of the fiber length that was measured with a lower filter at 2 mm	215
Table 3.21 Rate between weighted average and arithmetic mean of the fiber length that was measured with a lower filter at 2 mm	215

Part 1

Lightweight design of a modular front-end

1.1. European Regulations

The raising demand of equipment for safety and comfort is responsible of the weight increase of the vehicle [1-4]. Every year an average increase of 20 kg is attained (Europe). Nevertheless, this trend is against the European regulations that ask for the reduction of fuel consumption for limiting the local emission and extend the fuel autonomy. The European Union, with the Regulation 443/2009, defined a program, which is based on subsequent cornerstone, for the reduction of the local emission of CO₂ that is enclosed in the laws package 20-20-20 (i.e. the reduction of the greenhouse gas emission up to the 20% and the increase of the energy efficiency from renewable source by year 2020) [5].

The directive impose to the carmaker industries to replace the inefficient models, with a criteria based on the emission of CO₂ grams, and simultaneously it fixed financial penalties for whom would not fulfill the protocol. The target of 130 grams of CO₂ emitted for kilometers would have been fulfilled before the 2015, with a further and progressive reduction until 95 grams for kilometer before the 2020. Being the 75% of the fuel consumption directly related to car weight, a reduction of 100 kg allows to avoid the emission of 11 grams of CO₂ at each kilometer [6]. How was said can be directly translate in a lightening of the car of 100 kg before the 2015 and an extra reduction of 200 kg before the 2020. Moreover, the directive 2000/53/EC, which provides the standard for the end-of-life treatment, is complementary to regulation 443/2009. The directive obliges the carmaker to design vehicles that can reused and recycled for the 95% of the total weight [7-8]. For this purpose, the thermoplastic composites materials play an important role in redesigning the parts of the car.

1.2. Lightweight design with polymer and polymer composites

Weight reduction of vehicle is always related to the reduction of fuel consumption and as consequence to the extension of the fuel distance. Lightweight applications with polymer and polymer composites are frequently aimed to replace metal parts with the purpose to increase the specific mechanical properties. Polymers used for lightweight vehicles are overall classified in high performance polymers, polymers for weight reduction, composite polymers, polymer sandwiches, polymer/metal hybrid systems and polymer continuously/discontinuously reinforced hybrid systems. Moreover, the kind of application of the high performances and composite polymer can be mainly divided in structural and semi-structural application. Unfortunately, the thermoplastic composite materials, are still enclosed in the latter group because the dependencies of the mechanical properties on the temperature if compared to the thermosetting ones. However, the use stabilizer additives and the continuous spreading of high performance strength matrix, even though is slow, can break the wall of this categorization. The use of polymer [9] in the production of current vehicles is still limited but the regional regulation on the reduction of the local emission and in providing a sustainable end-of-life treatment can reverse this tendency. Moreover, the green mobility, that is bound to the short range because of the limited battery charge, push on the lightweight design.

Vehicle weight directly affects energy consumption and a 10% reduction in weight increases fuel economy by approximately 7%. Figure 1.1 shows a trend of fuel efficiency of automobile by year [10].

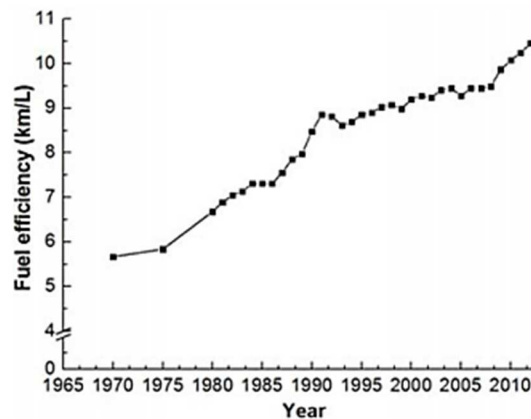


Figure 1.1 Fuel efficiency of automobiles by year [9]

Vehicle weight reduction can be achieved by various means employed simultaneously. These means involve reducing the size and number of engine-related parts by maximizing engine efficiency, producing structurally efficient body design, reducing overall vehicle size by maximizing interior room using space efficient designs, as well as employing lightweight materials. [11-13] Lightweight materials can be utilized by developing effectively advanced materials, pioneered molding processes, and construction technologies. The materials used for vehicle fabrication are largely classified as ferrous metals, non-ferrous metals, and polymers.

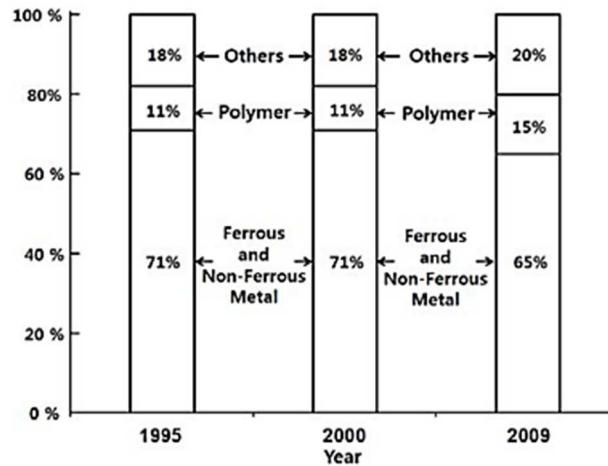


Figure 1.2 Material consumption-rate for light vehicles [9]

Figure 1.2 shows material consumption ratio for a light vehicle. [14] Currently, approximately 15 to 20% of the total weight of a vehicle is polymer materials. Typical parts that are being replaced with polymers are front ends, bumpers and fascia systems, grills, fenders, intake manifolds, engine mounts, door structures and panels, door impact beams, bonnet panels, under hood parts, pedal boxes, body structures, steering columns, wheel rims, seat backs and under parts, roof modules, sun roofs, interior trim components, instrument panel, and others. [15-18]

High performance polymer

Generally thermoplastics material are more popular than thermosets ones for manufacturing of automobile parts because shaping thermoplastics is simpler and faster. Materials to be applied near engine parts should have high thermal resistance, whereas exterior and structural parts should be fabricated from materials with high mechanical strengths. Thermoplastics, however, have limited thermal resistance and mechanical properties, and thus, can be applied only after they are modified for high performance application through reinforcements. The historical progress of polymers, from the PA in 1930 to the PPS, PEI and PEEK starting from 1970, reflects the fact that the synthesis technologies used for the preparations of novel polymers were developed in accordance with the needs for polymers with higher mechanical strengths and thermal resistances. More recently, other high temperature performing polymers were industrially manufactured as the PBI. These high performance polymers are used in automobile parts alone or as alloys, and with reinforcements. Another important advantage of thermoplastic material is to use additives in order to functionalize their properties. [19-23]

Polymer for the reduction of the weight

The walls of polymer parts, due to the lower density, can become thicker in order to increase the overall strength and in some case, also providing the same moment inertia results in a thicker wall because the limitation of the processing technology. Sometime, a high core density is not a requirement and it can be avoided thanks to some process variant. Forming foams, bubbles, or cells in a component's construction material can answer to this necessity. This method originated at MIT in the 1980s and now it is commercialized by Trexel Inc. with the name MuCell. In this method, microcellular foams are developed during the injection molding process. In the MuCell process, polymers are melted in the injection unit of the injection molding machine and then a supercritical fluid is dissolved in the melted polymer using a physical blowing agent (PBA), such as N₂ and CO₂. Then, the melted

polymer, containing the supercritical fluid, is injected using by high pressure, into the mold cavity and allowed to solidifying. Various polymers are used in this process, such as PPS, PS, POM, PET, TPE, PP, HDPE, PA, and PC. Weight reductions of approximately 10-60% can be achieved, depending on the material that is used. Products containing foams also demonstrate better thermal insulation properties. Some defects that limit the applicability of the process can arise during the foaming processing, as the swirl marks on the molded surface as a result of trapped air, silver streaks on the surface, as a result of bubbles breaking, surface blistering and post-blowing. Mechanical strength drops markedly when the size of the foam exceeds 0.25 mm, thus research into overcoming these problems is needed. One approach to overcoming these problems is to use injection compression molding that leads to enhanced control of microcellular structure or the core-back MuCell [24-27].

Reinforced polymer composite

Polymer composites exhibit a wide range of properties that can be achieved through various manufacturing processes. Polymer composites are achieved by compounding reinforcements with polymers or by impregnate a reinforcing preform directly in the mold cavity. Reinforcements are usually mineral fibers, such as glass fibers, carbon fibers, boron fibers, and basalt fibers. However, Polymer fibers such as aramid fibers and PE fibers are also used. The mechanical strength and stiffness of a polymer composite depend on the content, type, and shape of the reinforcement that is used. Fibers used in fiber reinforced polymer composites are designated as discontinuous fibers or continuous fibers, according to their forms. Discontinuous fibers are short fibers, long fibers, and chopped strand mats. Continuous fibers are continuous fiber mats, unidirectional or multiaxial laminates, woven fabrics, knitted fabrics, and braided fabrics [28-32]. Manufacturing processes for producing parts with fiber reinforced polymer composites are diverse. Each process is suitable for the manufacturing of specific kind of product on the basis of the required final length of the reinforcement. Short glass fibers (typically < 3 mm) reinforced polymer composites are used in conventional injection molding, long glass fibers (typically 3-25 mm in length) reinforced polymer composites are used in extrusion-compression and sheet extrusion processes. When reinforcement of such length are used in injection molding process, the fiber breakage is not avoidable and the final length of the fiber, depending on the plastication group and by the mold geometry, is reduced. Polymer composites that use continuous fiber and woven fabric are manufactured in pultrusion, thermostamping, and compression molding. The compression molding process is used for manufacturing parts with thermoset-matrix composites and uses sheet molding compounds (SMCs) as starting materials. A SMC is a thin sheet containing glass fibers, most of which are approximately 25 mm in length, in a thermosetting resin. When para-aramid fibers or carbon fibers are used as reinforcing fibers in SMC, these composites can be used for metal replacement application. Racing cars already use these composites [33-37]. Molding thermoset parts reinforced with glass fibers during reaction injection molding (RIM) is called reinforced reaction injection molding (RRIM). The most common thermoset resin systems are polyester, vinylester, epoxy, phenolic, and bismalyamide. The thermoset resins usually used are polyurethane and polyurea, and short glass fibers are used. When using long fiber materials in RIM, the perform is first inserted into the mold and then the resin is injected and cured. Reactants are feed separately to the mixing chamber, and then the mixed reactants are injected into the RIM mold. In contrast, in RTM, premixed reactants held in the reservoir, are fed into the mold by a plunger. RTM involves low flow velocity and low resin viscosity. Both RIM and RTM process was also adapted to thermoplastic matrix that must have low viscosity or that polymerizes directly in the cavity [38-40].

Polymer-sandwich panels

Polymer sandwich panels and structural composites have two types of core geometries, solid and spatial. Polymer sandwich panels with solid core are manufactured by RTM of thermosets resins after presetting of glass fiber laminates into the molds. Thermoset resins form skin layers during this process. The same process can be adapted to thermoplastic material with very low viscosity or that polymerize inside the cavity. In this case, the process is called T-RTM where the first T indicates the thermoplastic matrix. In general, RTM process has the advantages of lower processing costs and higher surface qualities, compared to Sheet Molding Compound SMC, and it is suitable for smaller numbers of products. Carbon fibers or para-aramid fibers can be used for reinforcement when core layers are manufactured using reinforced thermoset resin laminates (i.e. epoxy resin). Laminated core layered polymer sandwiches are similar to polymer composites and their rigidities are poor compared to structural core layered polymer sandwich panels [41-42]. Polymer sandwich panels consist of core and skin layers. The mechanical properties of polymer sandwich panels depend on the geometrical structures of their core layers and the mechanical properties of their skin layers. Using foam structures for core layers instead of the solid structures produced by RTM produces components with better mechanical properties and smoother surfaces than SMC does. The mechanical properties of foam cored polymer sandwich panels vary with the size and density of foam used, and those parameters should be well controlled during molding. The properties of structural composites depend on the properties of their core layers and the geometric arrangements of their core structures. Applications of polymer sandwich panels vary since sandwich panels with new functions can be achieved by imposing special properties onto core layers [43-48]. By using polymer sandwich panels that contain full three-dimensional core structures instead of two and a half dimensional structures, like in the case of the honeycomb shape, mechanical properties can be greatly improved. This kind of core design has been attempted on metal sandwich panels and recently it has been applied to polymer sandwich panels. The kagome structure is considered the best core structure design and polymer sandwich panels with such pyramidal cores show high rigidity, high-energy absorption, and high impact resistance. Thus this design is very attractive for vehicle materials. Complete adhesion between skin and core layers is very important for these structural sandwich panels and the strong points of these panels are only secure once perfect adhesion has been achieved. Also the technologies for manufacturing of sandwich panels are adapted to the forming of thermoplastic structure by using organosheet and thermoplastic core structure that are suitable for direct joining such as welding, or riveting [49-50].

Polymer/metal hybrid system

Polymer/metal hybrid systems are classified into two types: sheet metal/reinforced plastics (two layers or two components) and sheet metal/plastic foam/sheet metal (three layers). Joining plastics to metals is usually accomplished during the molding process. The most common approach is to use the insert injection molding process where the metal insert is placed and clamped in the mold cavity and then the thermoplastic is injected. The polymer is joined by means of undercut previously created on the insert or thanks to a preparation of the metal surface. Laser ablating, sandblasting, plasma activation can be used. Moreover, in some cases, some adhesive can be placed on the insert before the injection phase. The metal is buried and fixed in the thermoplastic. Semicrystalline materials, which are subjected to high volumetric shrinkage, need the pre-treatment of the metal insert. Otherwise, the use of reinforced matrix can overcome the detachment due to the process shrinkage and to the different thermal contraction/expansion during the operating conditions [51-54].

Thermosets/metal hybrid parts can be prepared also by reaction injection molding of P, as well with resin transfer molding of epoxy, vinylester resin-based systems, and PU [55].

Polymer/organosheet hybrid system

As already mentioned in the previous chapter, in recent years and especially thanks to Bond Laminates, many technologies were adapted to the use of thermoplastic composite laminate that are reinforced with continuous fiber. The In Mold Forming technologies, also known with other commercial names, is aimed to in-line couple the thermoforming and the injection molding process. This technology is directly aimed to replace the metal sheets of the polymer/metal composites with the organosheet. The joining between parts can be done with mechanical interlocking but in this case the healing phenomenon that takes place at the interface of two compatible polymer matrices ensures a direct adhesion [56-58]. The following paragraphs and, in general, all the work, are focused on this process variants.

The pioneering industrial case of an automotive metal/polymer composite

By the end of the 80s, Lanxess began to develop a new technology that was defined as “hybrid”, to contrast the reduction of metal-sheet parts of the car body. The technology aimed to compensate the thickness reduction by adding an internal rib structure through injection molding of glass fiber reinforced polymer and adhesive joining [59-60]. The innovative approach allowed to reduce the local reinforcement that was commonly made by welding of stiffener metal bands. The first hybrid metal/polymer composite was made by a metal sheet structure internally reinforced and stiffened with a composite rib-structure.

The synergy of the two materials also increased the metal performance by ensuring:

- *Excellent resistance to bending, compression and torsion;*
- *High energy absorption*
- *Dimensional stability*
- *Weight reduction with equal performances*

To realize the hybrid components Lanxess adopted a common injection process in which the reinforced thermoplastic resin is directly overinjected on the preformed sheet. The joining of the two materials takes place thanks to undercuts and holes strategically positioned on the metal sheet. This technology also allows to position the metal sheet only in specific areas, increasing design efficiency and cycle times for the complete manufacture by using the injection molding advantages. (Figure 1.3).



Figure 1.3 Process steps for the manufacturing of an automotive part in metal/polymer composites [59]

In addition, they are guaranteed:

- *High dimensional stability. The molding process ensures a good geometrical accuracy for the parts free to deflect and that are subject to external environmental variables*
- *Integration of functional elements. The plastic allows the creation of modules ready to be assembled, eliminating costs of pre- and post-process such as assembly or welding*
- *Easy recycling. With a grinding machine and a magnetic separator, or with a density separator, the plastic can be separated from the metal allowing a fast re-use of the materials.*

For structural components subjected to great mechanical static and dynamic stress, and thermal load is possible to overmold the most appropriate reinforced polymer on inserts of various material as titanium, aluminum, magnesium or even sheets of fiber-reinforced laminate. The materials most used for the overinjected part are polyamide (PA6 or PA66) or polypropylene (PP) matrices, 15-60% w reinforced with glass fibers. These materials ensure a good distribution of the tensions, as well as a good predisposition to modeling with CAE software.

The technology, which takes advantage of the variety of forms and solutions that the injection molding process provides, can be extended for the development and the manufacturing of components not only circumscribed to the automotive field. Besides to the anti-intrusion bars, modular front end, tailgate frame, door panels and other automotive parts, hybrid components are suitable for the frame of household appliances, body of scooters and for sports equipment. A consistent use of hybrid components in massive productions can allow a reduction of the manufacturing cost up to 30%, of the investment cost up to 50% and save up to the 40% of the weight while still providing the same mechanical characteristics.

1.3 Lightweight design of modular automotive front-end

The Front-End Modules (FEM) have revolutionized the design and the assembly phases of the automotive vehicles [61]. They are typically multiple pieces that integrate the frontal components of the car such as headlights group, air vents, radiators, condensers of air conditioning, hook for the hood, components of electronics etc. The opportunity in integrating all these parts make the front end suitable for complete the car frames having so-called open architecture that must be reinforced to support the weight of the entire assembly. Currently the modular front-end are mainly used on compact or small cars, and only in recent years were used on large sedans, all with monocoque architecture. They are also used on SUVs and pickups having a body-on-frame architecture construction. Unfortunately, they cannot be used for all the types of passenger cars but, for those in which this is possible, the benefits are certainly not negligible.

These modules not only eliminate a large number of assembly operations and secondary stations, but also reduce the processing costs thereby increasing the operating capital. The assembly of the modular front-end can be executed in the last instance, improving the ergonomics of the operations for mounting of all the other rear parts that can be added in line. Since the basic structure of the FEM can be standardized by leaving freedom of design for appearance and cosmetics, it can be used as common design solutions for many automotive models, with a direct estimated savings around 20-30%.

Not to be overlooked is also the greater easily in control of the dimensional accuracy. In fact, operating on a large scale on a component that incorporate more parts and not on punctual scale, there is a higher and spread quality control on each of the sub-component so that it can be correctly fitted without multiply the error.

The introduction of the Front End Modular is attributable to Volkswagen AG that in the first half of the 90's has equipped some of its VW and Audi models in a single module made entirely of sheet metal. Subsequently it is passed to a metal-plastic hybrid configuration and therefore to the completely thermoplastic composite and the hybrid thermoplastic composites. Although the adoption of FEM has shown great advantages in term of design and assembly operations, it is spread especially among European car manufacturers and not between the American and Asian where only Chrysler LLC, Ford Motor Co., Nissan Motor Co., Hyundai Motor Co. has developed this solution. General Motors Corp. and Toyota Motors Co. have not already considered it appropriate to make such a commitment. The reason for these strategies is clearly motivated by Conrad Zumhagen who is the president of Zumhagen Co. He declared that the European car manufacturers have always been the most innovative and early in the use of structural and functional components in plastic because of the higher cost of fuel in Europe than in North America, and for the most restrictions on the emission of exhaust gases issued by the governments. It should also add the fact that many companies have difficulty in quantifying the actual total cost to the assembly level, and do not perceive the indirect advantages of the integration of the components and the efficiency in the assembly due to the use of modular front end [61].

The structure of the modular front end, which is physically secured to the frame of the car and on which are fixed the front headlights, the bumper, the bonnet hook and other sub-components, can be produced completely in metal, in hybrid metal-plastic or in a full-plastic version with the use of thermoplastic composite. The choice of materials is affected by several factors, including the size of the vehicle, the loads that it must support, the stiffness of the adjacent components, the weight of the components that are fixed on it and the tolerances to be respected.

Usually the configuration of the front-end that ensure the complanarity between frame, radiator and hood hook are the most suitable for the replacement of metal parts with composite materials. Otherwise, if the fasteners to the frame are on other plans and are far from the main beam of the front end, a metal structure is necessary to ensure rigidity and strength. The first hybrid metal-plastic solutions bound the two materials by means of special adhesives produced by Dow Automotive, and only at in later time was adopted the metal-plastic hybrid technology patented by Lanxess that ensures a greater link between the two materials and avoids the delamination mutual collision. A comparison between the two principles is presented in Figure 1.4 Details of the connection by use of undercuts (a) and by use of adhesives (b) [62].

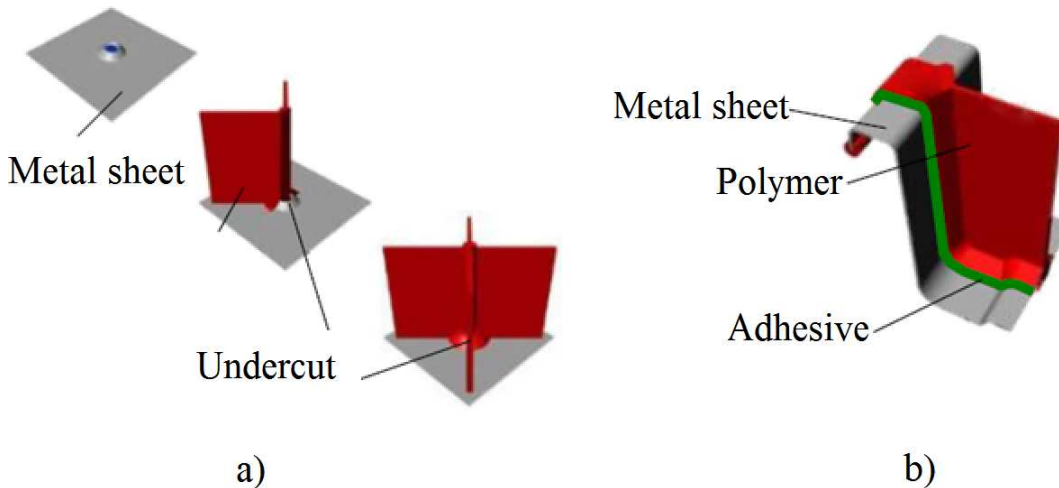


Figure 1.4 Details of the connection by use of undercuts (a) and by use of adhesives (b) [62]

Only recently, the structure was completely designed with plastic composite. The most common thermoplastic matrices are polypropylene and nylon. Initially the only technology suitable for the production of such component was the compression molding of GMT (moldable glass mat thermoplastic composite). With the rise of the injection molding technology, the use of short fiber reinforced polymer for injection molding process became of interest and it replaced the GMT technology. However, the use of short fiber was not suitable for high performance application and for this reason, the development of new technologies aimed to increase the length of the reinforcement in the parts growth even more. This trend aimed to the development of technologies for processing of the long glass fiber reinforced polymer such as the injection molding of LFT, the in-line compounding (ILC) and the Direct-LFT that ensure a lower manufacturing cost of the raw material if compared to the short glass fiber. In addition to the lower production costs of the long fiber reinforced polymers, they are guarantee:

- Most energy absorbed during the impact and good vibration absorption
- Higher elastic modulus
- Reduced volume shrinkage upon solidification in the mold and lower shrinkage anisotropy
- Excellent resistance to high temperatures and fatigue
- Extra soundproofing

Unlike, the short fiber reinforced polymers guarantee best surface properties, greater flexibility, and low sensitivity at the weld lines [63]. The graph in Figure 1.5 shows the stiffness of the various EMF developed in recent years by comparing the configurations in metal-plastic hybrid and full-thermoplastic composite completely. These values, for a tensile test performed on the hood-look area, show that the stiffness increases for not only hybrid

configurations reinforced with polypropylene rather than nylon, but also surprisingly increases the configurations for all plastic composite compared to metal-plastic. However, this does not mean that in some situations the high loads and the weight of the car itself leads automakers to incorporate metal inserts also on parts that are mainly made of plastic composite like on the Audi A8 (produced in collaboration with Lanxess) or in the most part of SUVs.

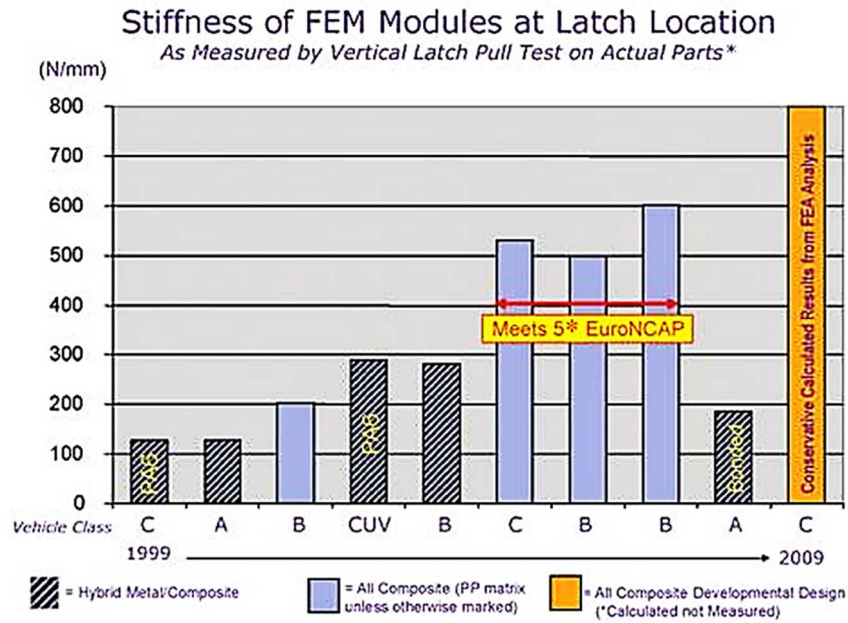


Figure 1.5 Comparison of then stiffness of FEMs at the latch location as measured by the Vertical Latch Pull Test [61]

Over the past decade there have been many developments in the FEM design in terms of materials and processes, as well as secondary operations and level of integration. In Figure 1.6 are shown for illustrative purposes some examples of configurations following one another over the years for different types of cars:

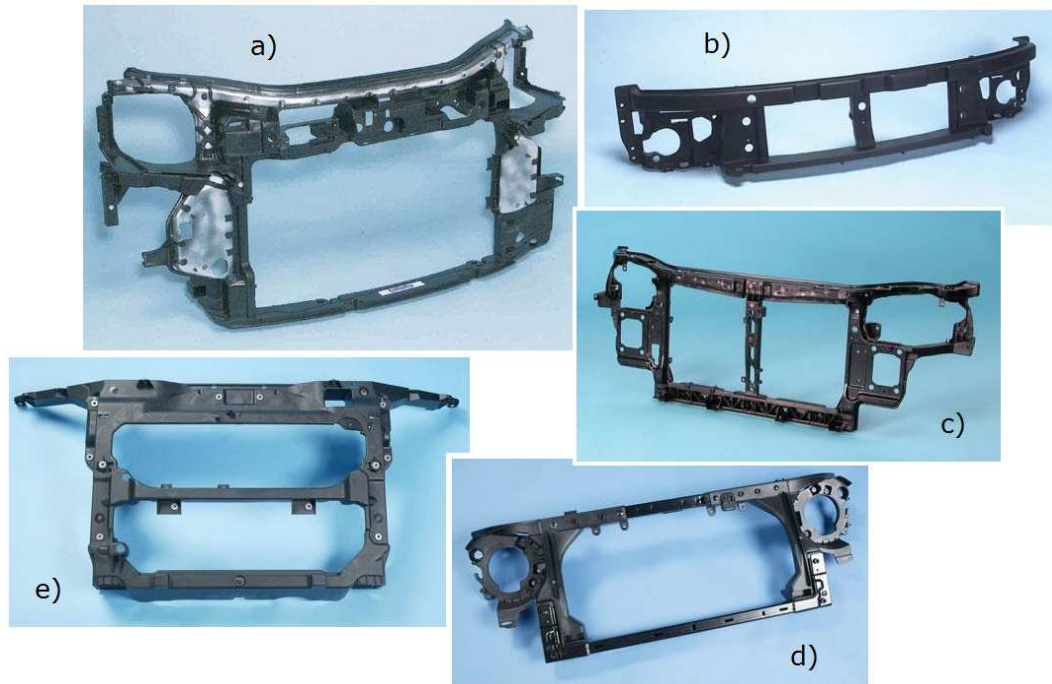


Figure 1.6 Evolution of the technology for the manufacturing of FEM in several types of car [61]

- a) Audi A2 (year 2000): the hybrid metal polymer configuration acquired the know-how from the bigger model A6 where the joining was made by mechanical interlocking. The steel sheet provides the structural performances and the plastic part, which was made by injection molding of short glass reinforced Nylon 6, absorbs the joining functions with the other parts of the assembly. The part allowed a saving in weight of 30% and a cost reduction of 20%.
- b) Mini Cooper (year 2002): it was the first FEM in a full-thermoplastic configuration. It was completely made of polypropylene reinforced 30% in weight with long glass fibers. The part allowed a saving in weight of 30% and a reduction of the cost of 25%. Moreover, a reduction of 20% of the total number of the components was evaluated. The NVH factor (Noise, vibration and harshness) resulted strongly reduced.
- c) Kia Cerrano (year 2004): it was the first case of close plastic-metal frame. The in mold assembly technology was used for the insert molding of 18 metal inserts with Nylon 6 30% in weight reinforced with glass fibers. The part showed a good adhesion between polymer and metal and it guaranteed a high stiffness/weight rate with a weight reduction of 40% and a saving of 30%. Also the NVH was improved.
- d) Jeep Wrangler (year 2007): it was the first case of application of FEM on body on frame vehicles. The front end was made by joining the metal frame and the polypropylene part with low energy adhesive. The innovation was in the adhesive that allowed to avoid the pre-treatment of the surfaces. The new solution allowed a weight reduction of 15% and a saving of 25%. All the metal-metal welding was eliminated.
- e) Ford Edge (year 2007): it was the first case of an all plastic FEM that allowed the use of the open-architecture vehicle build on SUV. A polypropylene long glass fiber reinforced was used. The assembly phase was improved and made leaner.

For the development and the structural analysis of the Front End Modules, especially for those made of thermoplastic composite, the computer-aided engineering and design with the use of FEA software are even more necessary. They are useful to accurately identify the most critical areas and thus to be reinforced as well as a faithful and accurate modeling of the mechanical behavior of the materials. In this regard, it becomes fundamental the correct characterization of materials. In addition, the use of computer simulations reduces the investment for specific mechanical tests on prototypes and greatly reduces the lead-time of the design. The metal replacement applications in the front end modules and in other parts of the car will experience a significant increase only when the designers will have more confidence in the design of composite structures, both with continuous and discontinuous fiber reinforced thermoplastic materials, and in the related manufacturing technologies.

1.4 In Mold Forming technology

At K2010 exhibition in Düsseldorf, for the first time, KraussMaffei and Engel, together with Lanxess and BASF, featured two highly automated production cells for presenting a new technology that promises to drastically change the rules for the production of automotive components. It is the in-mold forming of thermoplastic matrix composites, also called all-plastic "organic hybrid" composite technology. The technology in-line couples the thermoforming of composite laminate sheets, called organosheets, and the injection molding of reinforced polymers with a compatible matrix. In the heating station, the organosheet is heated up close to the melting temperature. Then, the organosheet is clamped and formed inside the injection mold and the injection phase is performed [64]. The woven fabric of the organosheet avoids the flowing of the matrix during the heating and the handling of the laminate.

This technology is the natural evolution of the hybrid metal-plastic composites. The connection between the metal and the plastic by means of spots where the matrix is attached in a discontinuous way to the substrate is replaced by a continuous weld of the rib to the substrate that, being of the same family, can ensure a better joining of the two components. Furthermore, the replacement of the metal with the fiber composite sheet contributes to the reduction of the overall weight of the component (Figure 1.7). In fact, the composite material can claim a module/density ratio up to eight times greater than the metal [57, 65].

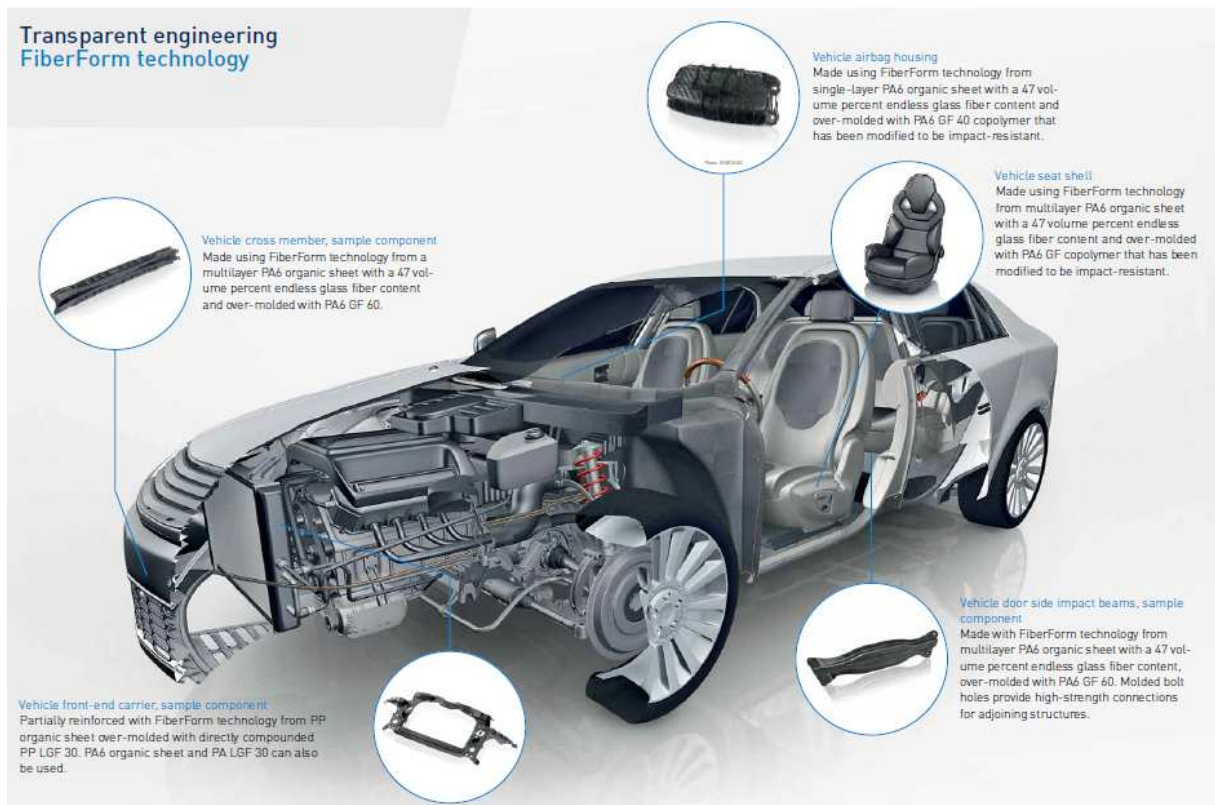


Figure 1.7 Examples of full-thermoplastic composite hybrid parts for automotive applications [66]

Engel presented the box of the steering group, while KraussMaffei presented the anti-intrusion bar of an automotive door. The demonstrative parts used sheets of composite Tepex of Bond-Laminates GmbH, over-molded by glass reinforced Nylon. The handling of the laminate was performed with linear robots with six axes and the preheating of the sheets taken place in an infrared oven at 300°C for 30-40 seconds. The long production cycle is

settled down between 33 and 55 seconds, mainly penalized by the time of the laminate heating and by the cooling time typical of the injection molding process.

In addition to these two demonstrations, Lanxess presented an improved version of the polymer/metal hybrid front-end of the Audi A8 produced by integrating in lower part of the structure a transversal beam in Tepex. The aim of the innovation was to answer to the safety of the pedestrian in case of collision. BASF, in collaboration with Faurecia, presented an automotive seat in full-thermoplastic composite manufactured by the overmolding of a Tepex laminates with a PA6 35%w reinforced polymer. The part presented stiffness, ductility, and finishing compatible to design requirement with a 20% weight saving compared to the other seats in the same category.

In 2012, at the Düsseldorf European Composites show and at the Paris JEC Composites exhibition, the great development of this technology aimed to present a redesigned air bags housing. The part was produced on a KraussMaffei system by overmolding of Durethan 40%w reinforced with glass fibers on a composite organosheet made of Tepex Dynalite RG600 102 47 %. Both the two composites have a polyamide matrix. It was possible to reduce the thickness from 3-4 mm of the former version, which was made by injection molding, to 0.5-1 mm with a consequent weight reduction of 30%.

Noteworthy were also a brake pedal, produced with the same materials of the airbag housing, which has halved the weight compared to the steel version (coming to weigh 355 g), and the base of the seat of the Opel Astra OPC sports coupe (Figure 1.8). The base of the seat was made by coupling laminated sheet 1 mm thick with a new high impact material for injection molding with a saving in weight of 45%.



Figure 1.8 Seat pan of the Opel Astra OPC [67]

The Organosheet Injection Overmolding

In relation to the complexity of the part to be produced, there are two possible variants of the process.

The first, shown schematically in Figure 1.9, is suitable for simple parts superficially and it consists in heating the laminate with infrared lamps above the melting temperature and in its direct insertion inside the mold. Here, the reinforcement parts and the various features for the installation are over-molded immediately at the end of the forming. At the end of cooling phase, the part can be extracted and directly transferred to the assembly line or, in particular cases, may be subjected to the cutting of irregular edges. The cycle time is almost equal to that of the injection process (60 seconds), and it is determined only by the total cooling time, proportional to the square of the maximum thickness of plastic.

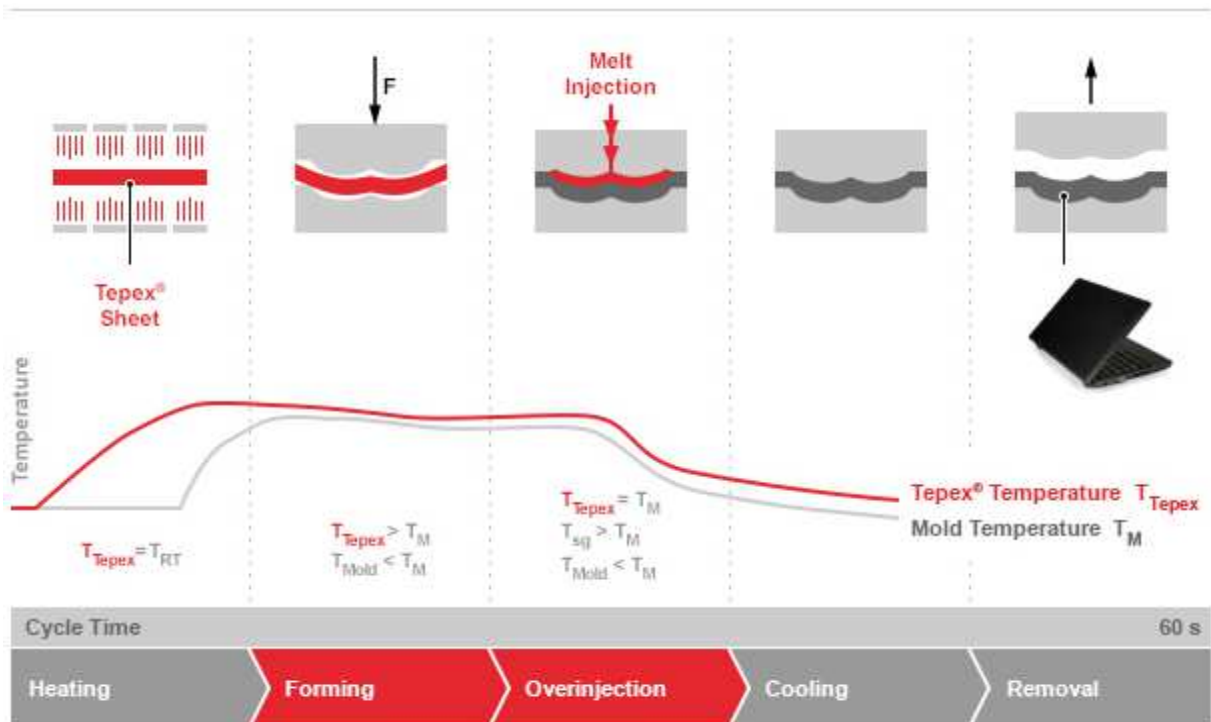


Figure 1.9 Processing phases of the direct in mold forming process [68]

The second method, presented in Figure 1.10, is used for the production of parts with shapes that are more complex and with reinforcement features that are more extended. This variant separates the forming phase of the laminate from the overmolding making necessary an automatic transport of the laminate across the two stations. Since the laminate is already fully impregnated, the forming phase does not require a strong pressure and a pressure of at least 5 bar is enough. This version has a cycle time longer than the previous one and it may present the cooling of the laminate during the forming and the subsequent handling. However, the high degree of automation reduces the effects and makes this solution still preferable to other technologies currently in use especially when applied to high-volume production components. Both the version are designed as complete production cells, with the advantage of being compact, fully automated and easily managed with integrated system controls.

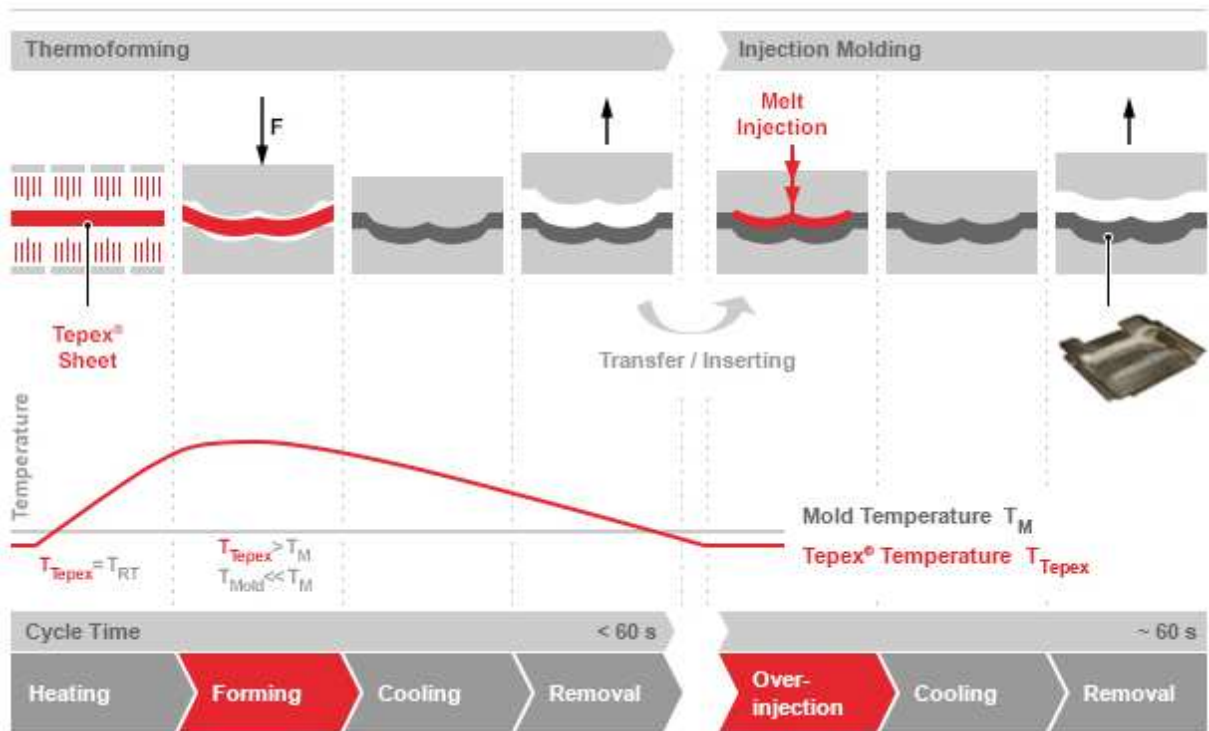


Figure 1.10 Processing phases for the two-step in mold forming, insert molding [69]

The parts produced in this way provide stiffness and unrivaled strength, being able to be designed appropriately by placing the fiber and reducing the thickness of the plastic and laminate where the stresses do not require it. Furthermore, the use of hot injection channels allows a better distribution of the molten polymer flow, which results in a better orientation of the reinforcement fibers and in a complete filling of the mold cavity.

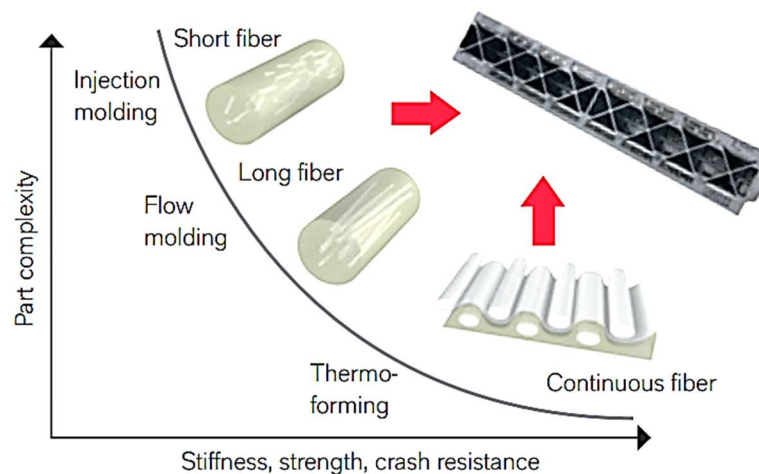


Figure 1.11 Manufacturing Technologies as function of the complexity of the parts and properties [70]

As shown in the graph of Figure 1.11 the mechanical properties mainly depends on the length of the fibers and on their orientation, a condition that can be ensured appropriately redesigning the feed channels to not break up the reinforcement. In some case, more intermedium phases must be integrated in the process and a redesign of the manufacturing process can be required with the consequent increase of the initial financial investments.

Individualized and functionalized production

Production of individualized parts with high variability or the productions of small volume lot are even more requested for the increasing demand of customization or for manufacturing of functional prototypes. The “Lightflex project”, which is a German national project funded by Federal Ministry of Education and Research, is aimed to provide an innovative processing route that combine the additive manufacturing of structures and the thermoforming of continuous reinforced laminate [71,72]. In practice, the injection molding phase of the in-mold-forming process is replaced by 3D printing of thermoplastic parts, which is preferably it is made of the same matrix of the laminates, and a local heating of the interface side (Figure 1.12). The project involves also the functionalization of the tape or of the composites laminate, by varying the matrix and the amount and the kind of the reinforcement. Moreover, commercial organosheet can be locally reinforced and the unidirectional sheet can be layered with different orientations according to the design requirements.

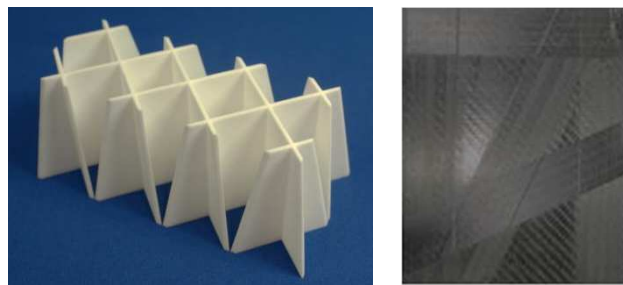


Figure 1.12 3D printed ribs-structure and functionalized laminate [72]

After the respective heating, the 3D printed part and the organosheet meet in the forming station, where a mold-free system forms the laminate on the functionalized part (Figure 1.13).

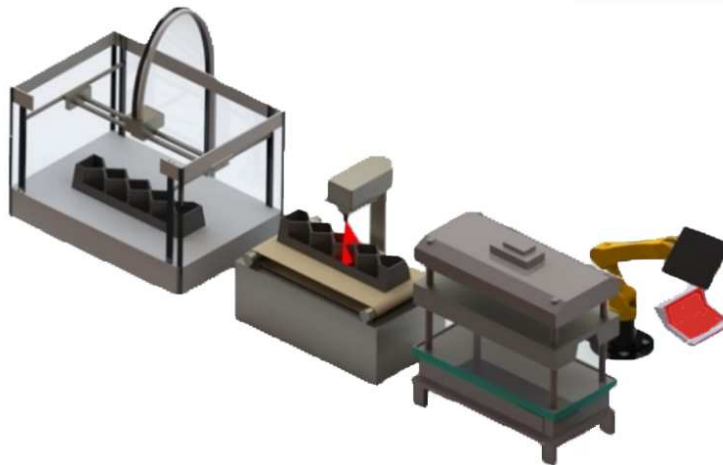


Figure 1.13 3D printing station, heating stations and forming station of the processing route [72]

The complete system is still under development, but the heating phase is assigned to a laser unit that is able to recognize the position of the 3D printed part and to local heat the welding area on it (Figure 1.14). However, infrared system or conformal hot plate can be suitable for the local heating but the geometry of the system is not adaptable to various geometries.

Main components of the system

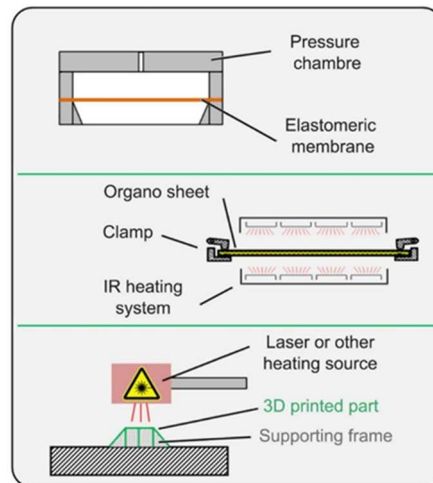


Figure 1.14 Main components of the forming station [72]

The process was designed with the aim to be tool-independent; in fact, the 3D printed part self-constitutes half of the mold while the other half is replaced with a diaphragm forming station. The welding between the rib structure made by 3D printing and the organosheet is made in the forming station after a previous local heating of the interface on the side of the stiffening parts as it clarified by Figure 1.15 where the most important steps of the forming phase are summarized.

Forming/Joining Phases

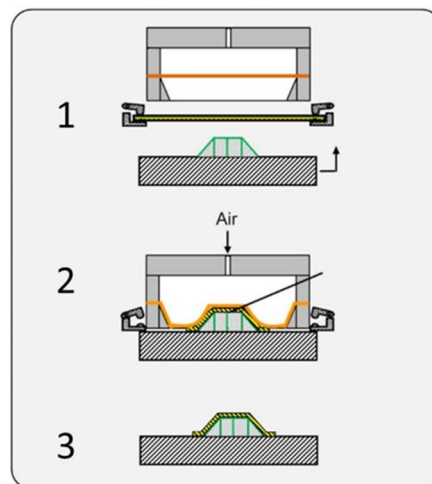


Figure 1.15 Steps of the forming/joining phase [72]

The first step represents the initial conditions before the forming. The organosheet moved from the IR station to the forming one, the 3D printed part was heated by the laser system and the pressure chamber is empty. In phase two, the forming station is closed and pressurized air blows the membrane for the forming of the composite sheet on the functionalized part and promotes the welding between the components. In phase three, the part can be removed. If the geometry of the 3D printed part is too thin, a low cost supporting system can be used for the avoid the deformation of the structure, otherwise the part can be redesigned with the addition of ribs or other features that support the laminate during the forming and avoid its wrinkling (Figure 1.16).

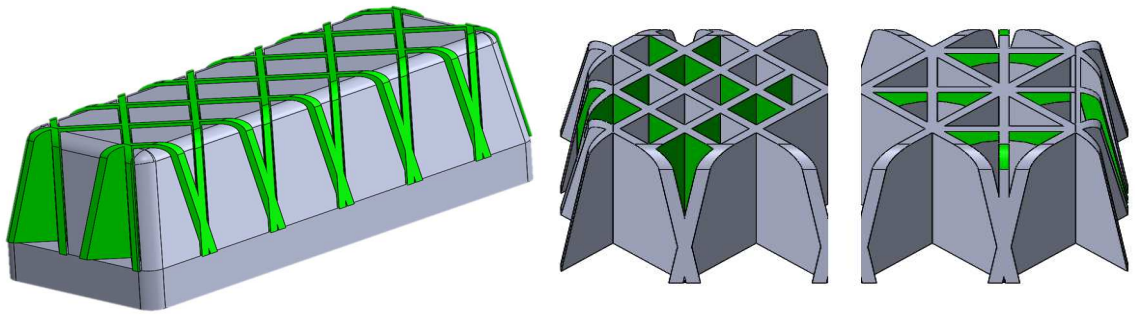


Figure 1.16 3D supporting system (on the left) and improving of the geometry (on the right) [72]

1.5 The case study of an automotive front-end (collaboration with Sole S.p.A.)

The presented work is aimed to the analysis and to the re-design of an automotive semi-structural part called front-end in order to be manufactured with the organosheet injection overmolding process. The objectives of the work are the structural static simulation of the part when it is loaded in four different conditions and the re-design of the geometry when the local stiffness of the part does not match the target.

The original version was a metal-plastic hybrid part with three metal sheet plates that were overmolded with short-fiber reinforced polypropylene. The transversal beam and the two plates are 1.2 mm thick and their main function was to withstand the loads while the injected part provide the continuity between the metal part and constitute the frame where other component such the radiator and the lights are fixed. Moreover, the composite part provide a lighter solution if compared to a full-metal frame. The polymer-metal hybrid configuration is shown in Figure 1.17, whereas the assembly of the front-end is shown in Figure 1.18 and Figure 1.19.

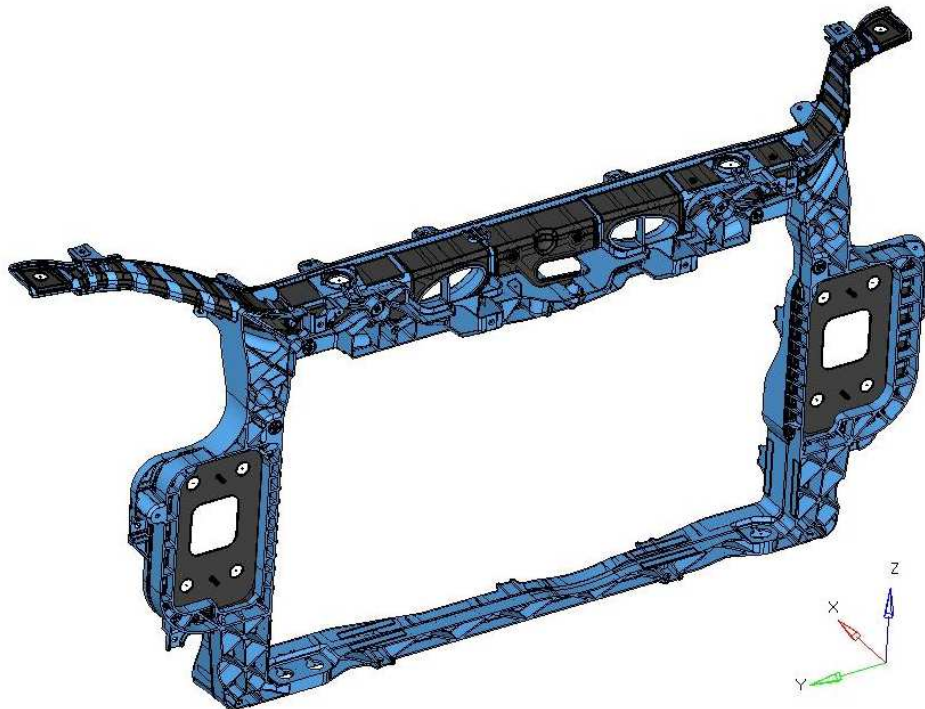


Figure 1.17 The metal-polymer hybrid Front-End where the dark region indicates the metal-sheet parts and the blue region indicates the fiber reinforced inject part

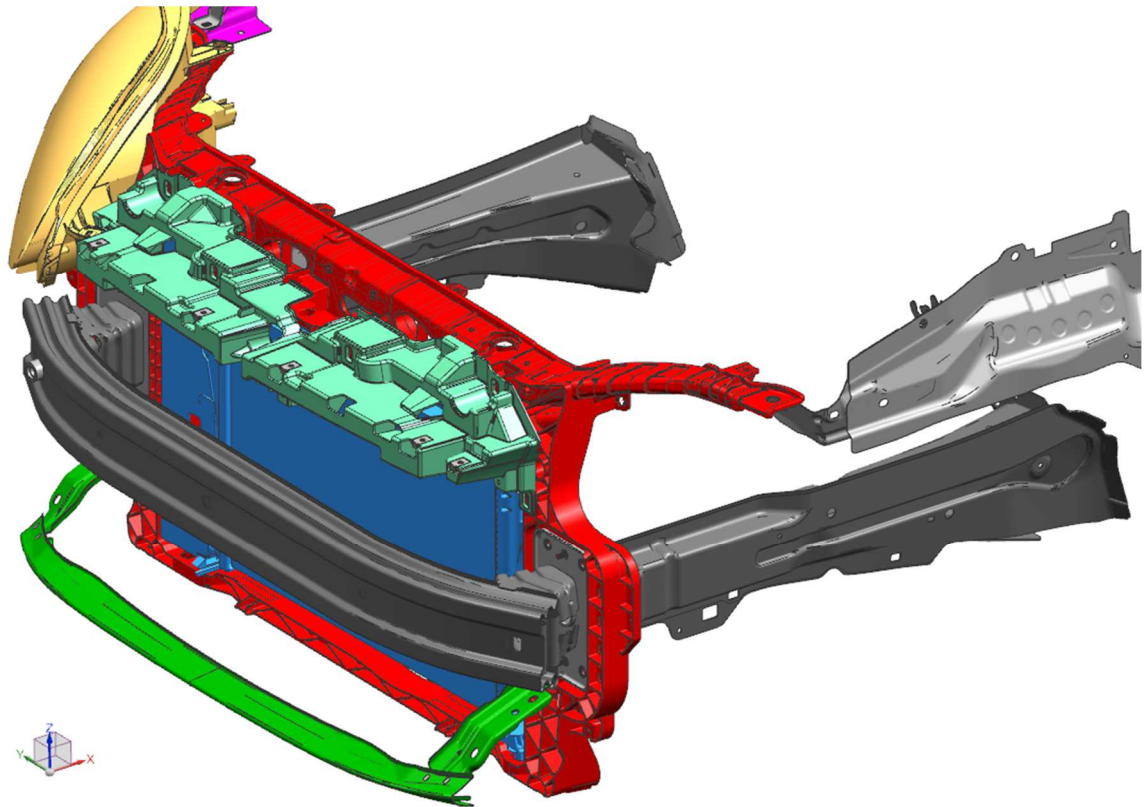


Figure 1.18 Assembly of the frontal part of the car where the Front-End is joined to the frame and to the other components.

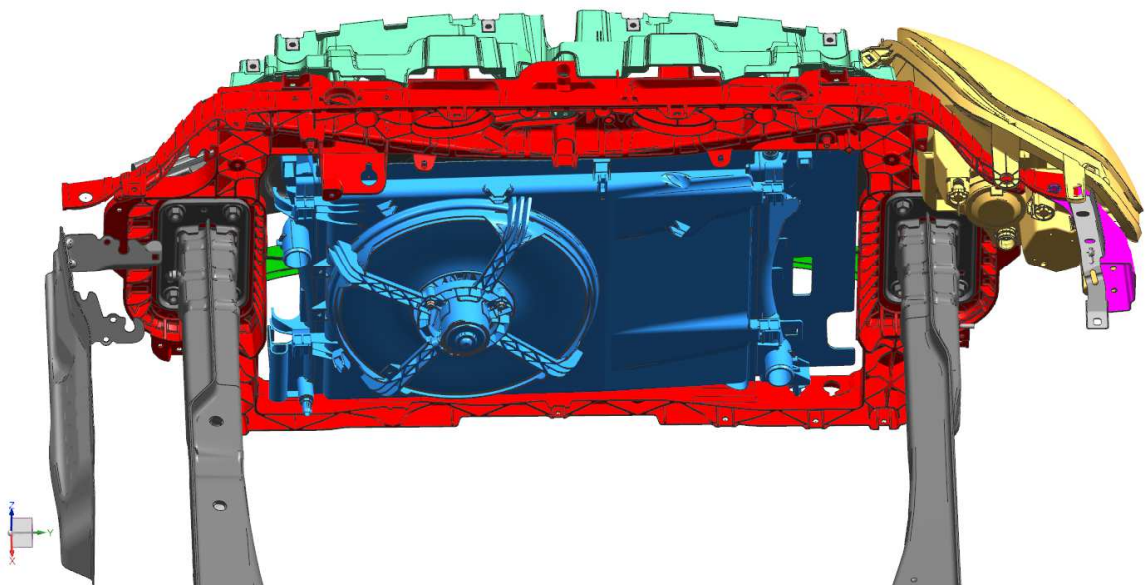


Figure 1.19 Back view of the assembly of the frontal part of the car where the Front-End is joined to the frame and to the other components.

The purpose of the project is to reduce the overall weight of the system by replacing the metal sheet with the organosheet (thermoplastic laminate reinforced with continuous glass-fiber woven) whilst ensuring the same structural specifications. It was not possible a complete redesign because the joining constraints and all the mathematical boundary must be maintained. The old points of joining to the frame and to the other components such as

lights group, hood lock, air vents, radiator etc. must be keep equal. This factor greatly reduces the possibility of optimization but the main constraint in CAD modeling allowed to directly compare the new models to the previous one.

The replacement of the composite material could have been a solution to increase the overall stiffness of the part. However, even if a Nylon matrix composite can provide a higher stiffness, the polypropylene has a lower density (0,90-0,91 g/cm³ of the Polypropylene compared to the 1,1-1,4 g/cm³ of the Nylon), a higher resistance to the humidity and a lower cost. For these reasons, a Polypropylene matrix organosheet was chose in order to guarantee a good process-induced welding between the shell and the ribs structure. Two different kinds of laminate, which are manufactured by Bond Laminates, were considered. The main differences between them is the fiber alignment and interlacing. The composite laminate and the injected material were mechanically characterized in order to properly define the material properties in the simulations.

1.5.1 Approach to the redesign of the Front-End

Since the stiffness of the composite is one tenth the stiffness of the steel, it was necessary to redefine the thickness of the part. Because the complexity of the geometry, an approximate approach that is based on the equivalence of the bending stiffness was used [73]. If the two materials are compared in guaranteeing the same bending stiffness, Equation 1.1 must be satisfied:

$$E_{metal} I_{metal} = E_{composite} I_{composite} \quad \text{Equation 1.1}$$

If the geometry of the two sections is similar, Equation 1.1 can be reduced to Equation 1.2:

$$E_{metal} h_{metal}^3 = E_{composite} h_{composite}^3 \quad \text{Equation 1.2}$$

By applying this equation to the case of the front-end, the thickness must be increased from the 1.2 mm of the steel sheet to the 2.7 mm of the polypropylene organosheet. Since the laminate is supplied in thickness multiple of 0.5 mm, which is the unitary thickness of a matrix-fabric layer, the thickness of the laminate was assumed equal to 2.5 mm.

An additional modification of the geometry and a weight redistribution to stiff the weaker areas was possible because of the principles that lead the welding in the organosheet over molding process. In Figure 1.20 are presented the main modifications: removing of several bands and reducing the width of ribs base. If before the base was intended to ensure greater surface area for the physical interlocking, now it serves as the interface for the chemical welding between the two polymers. Furthermore, reinforcement ribs were added to stiffen the hood lock.

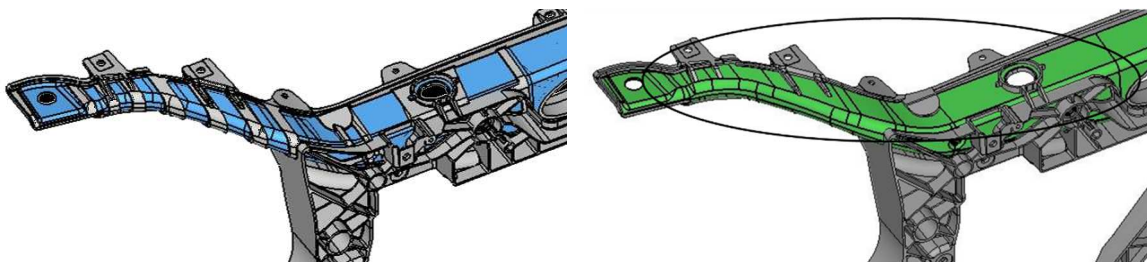


Figure 1.20 Reduction of the interface area between the ribs of the injected part and the laminate

With the same motivation, it was possible to reduce the width of the band of the ribs that are on the internal side of the transversal beam. As shown in Figure 1.21, the bands were not completely removed to ensure a larger surface of adhesion and to create a ribs system that allows the load distribution, avoiding the punctual concentration.

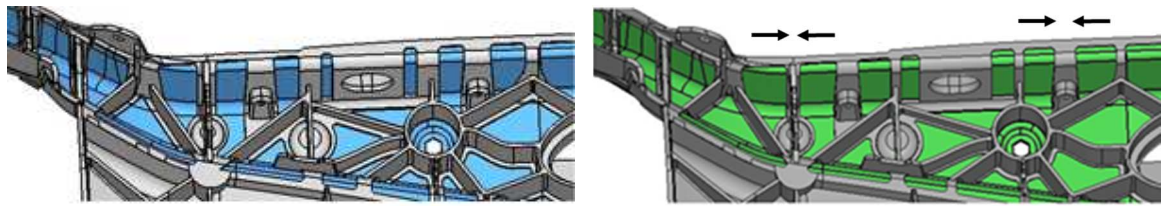


Figure 1.21 Reduction of the interface area between the ribs of the injected part and the laminate

The central part of the transversal beam was furtherly stiffen in correspondence of the air venting holes and of the hood lock system. Since this part is the most critical because of the high loading condition, some ribs were added in correspondence of the weaker zone as it shown in Figure 1.22.

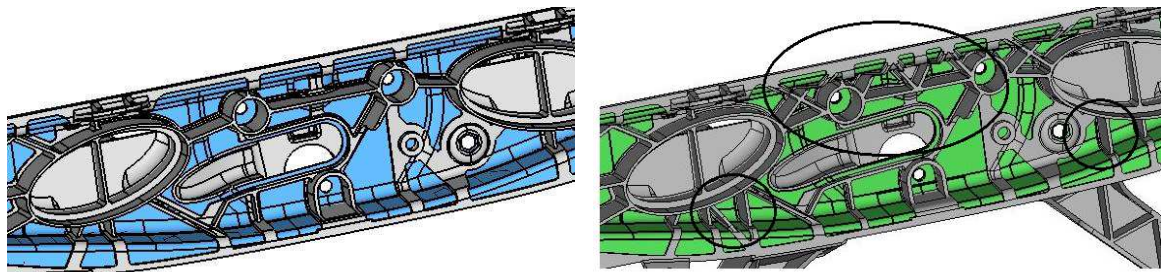


Figure 1.22 Adding of the reinforcing ribs

The redesign process involved a further investigation of the areas that are believed to be critical. A topological analysis was performed in Optistruct environment (Altair) in order to highlight the zones that should be stiffen with additional material under the load condition due to hood closure. This loading condition, which is better discussed in the following paragraph, was assumed to be the critical one because it acts on a highly loaded and weak area of the transversal beam due to the air venting holes and to the constrain that does not allow to add new material on the inner side.

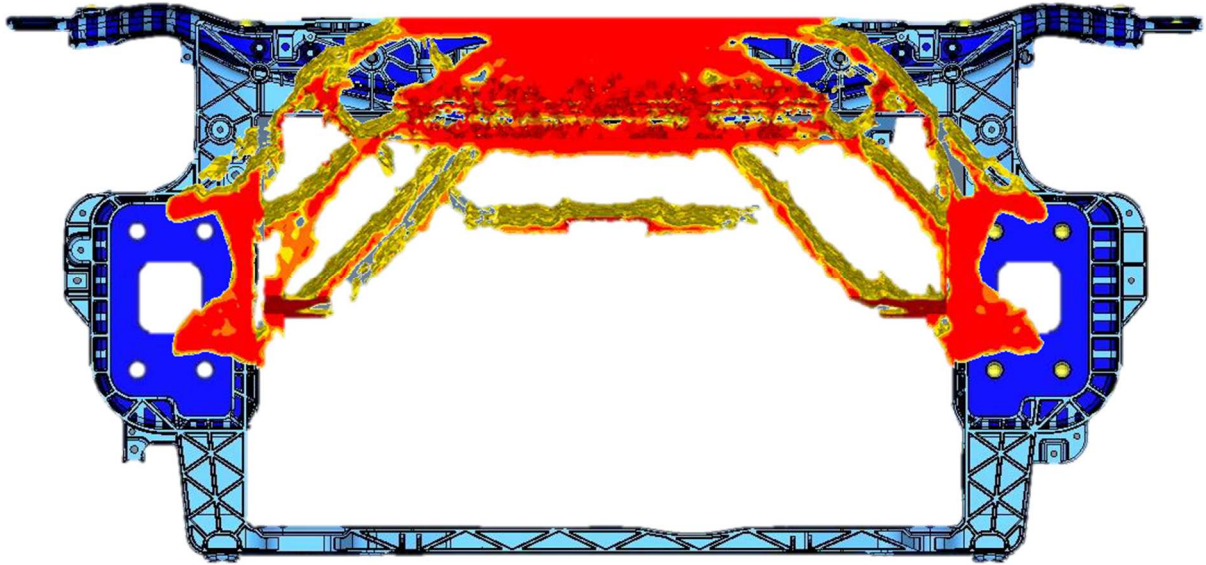


Figure 1.23 Topological optimization of the front under the opening effect of the hood

The topological analysis confirmed the intuition and indicated that additional material should be added in the hood-look area and to support it with additional beam aimed to redistribute the load on the body frame of the car (Figure 1.23).

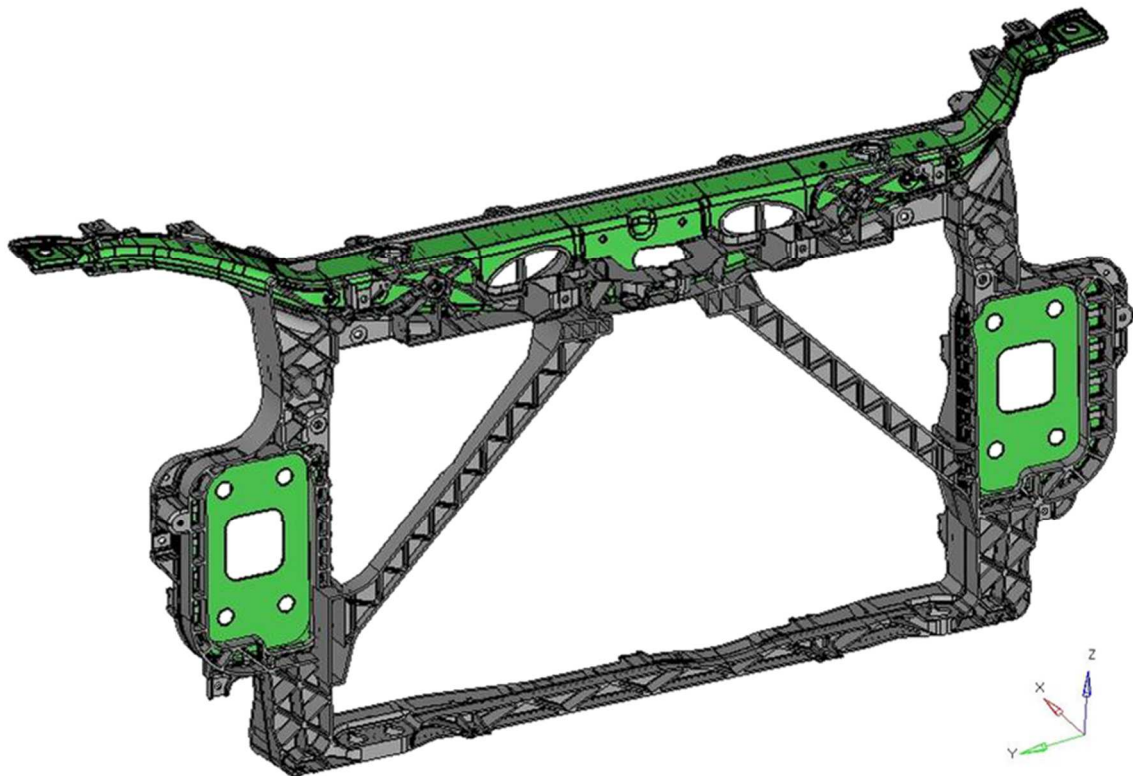


Figure 1.24 Full-plastic composite hybrid Front-End with reinforcement beams

In order to fulfill the results of the simulation, two diagonal beam was added to stiff the front-end structure as it shown in figure Figure 1.24. It must be highlight that the use of the new geometry needs a complete re-design of the assembly phase. In particular, the radiator, which is mounted by the frontal side, must be mounted from the backside. The structural

simulation will show if the proposed solution, which recall the one proposed and used on the Ford Fiesta and on some Skoda cars, could guarantee the target.

Now it is possible to compare the proposed solution in terms of weight reduction. The weight reduction provided by full-plastic hybrid version (with and without diagonal beams) when they are compared with the former plastic-metal hybrid one, is summarized in Table 1.1.

Table 1.1 Volume and weight reduction in the new models: with and without the reinforcing beams

Reference: Polymer-Metal hybrid Front-End				
	material	density [g/cm3]	volume [cm3]	weight [g]
Injected plastic part	PP-LGF30	1,12	2252	2522
Transversal beam	steel	7,81	189,5	1480
Flanges for joining	steel	7,81	83,5	652
			total	4654
Full-plastic Front-End with supporting beams				
	material	density [g/cm3]	volume [cm3]	weight [g]
Injected plastic part	PP-LGF30	1,12	2166	2426
Transversal beam	Tepex 104	1,68	395,8	665
Flanges for joining	Tepex 104	1,68	83,5	140
Reinforcing beams	PP-LGF30	1,12	362	405
			total	3636
Weight reduction	- 1018 g	(-21,9%)		
Full-plastic Front-End without supporting beams				
	material	density [g/cm3]	volume [cm3]	weight [g]
Injected plastic part	PP-LGF30	1,12	2166	2426
Transversal beam	Tepex 104	1,68	395,8	665
Flanges for joining	Tepex 104	1,68	83,5	140
			total	3231
Weight reduction	- 1423 g	(-30,6%)		

1.5.2 Structural target performances

The validation of the front-end requires the passing of 4 loading conditions. The local stiffness and the total displacement must be evaluate singularly and the performances must accomplish the target required by the customer without having the breakage of the part.

1. Front Lights Stiffness.

The condition is satisfied if the stiffness is higher than the required target when the front end is loaded by the action of the frontal lights. (Figure 1.25).

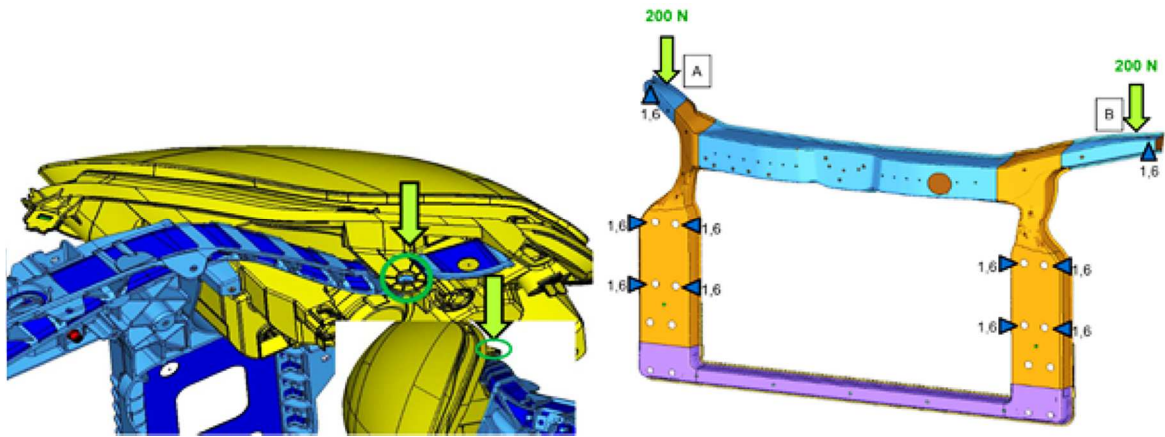


Figure 1.25 Load condition “Front Light Stiffness” (number 1)

In Table 1.2 are summarized the point where the load is applied and the direction of the load.

Table 1.2 Load application points and direction of the condition “Front Light Stiffness”

Direction of the loads: $i = 0, j = 0, k = -1$			
	COORD. X (mm)	COORD. Y (mm)	COORD. Z (mm)
Point A	-387	560	526
Point B	-387	560	526
Target: Stiffness > 54,64 N/mm			

2. Hood Lock Stiffness.

This is the stiffness that the structure must be guarantee when during the closure of the hood and it acts on the hood lock system. (Figure 1.26).

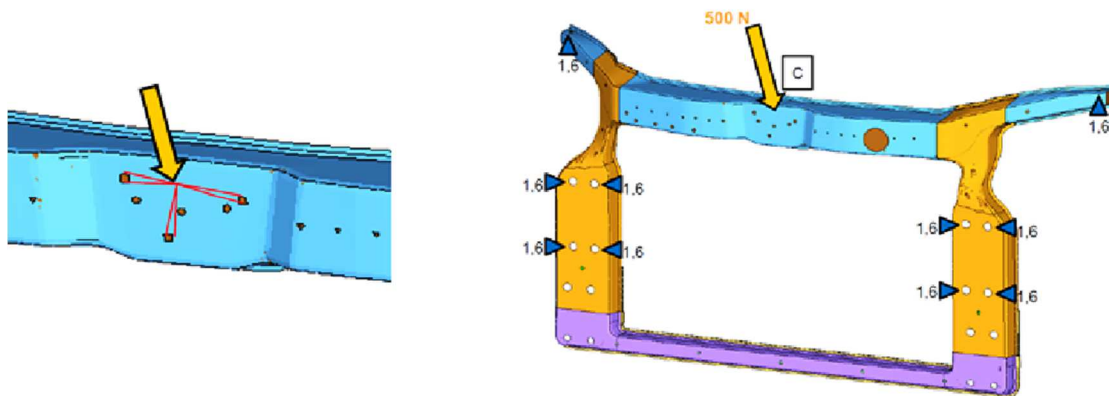


Figure 1.26 Load condition “Hood Lock Stiffness” (number 2)

Figure 1.26 shows how the hood lock system was simulated. Since the load is applied outside the system, the lock closure is simulated by a “spider” that connects the application point to the holes where the closure is bolted. In Table 1.3 are summarized the application point and the direction of the load.

Table 1.3 Load application points and direction of the condition “Hood Lock Stiffness”

Direction of the loads: $i = -0,127642, j = 0, k = -0,991133$			
	COORD. X (mm)	COORD. Y (mm)	COORD. Z (mm)
Point C	-595,44	0	464,2

Target: Stiffness > 350 N/mm

3. Hood Stops Stiffness.

The loads are due to closure of the hood and they that act on the hood-stop areas. The target is the stiffness that the system must guarantee. (Figure 1.27).

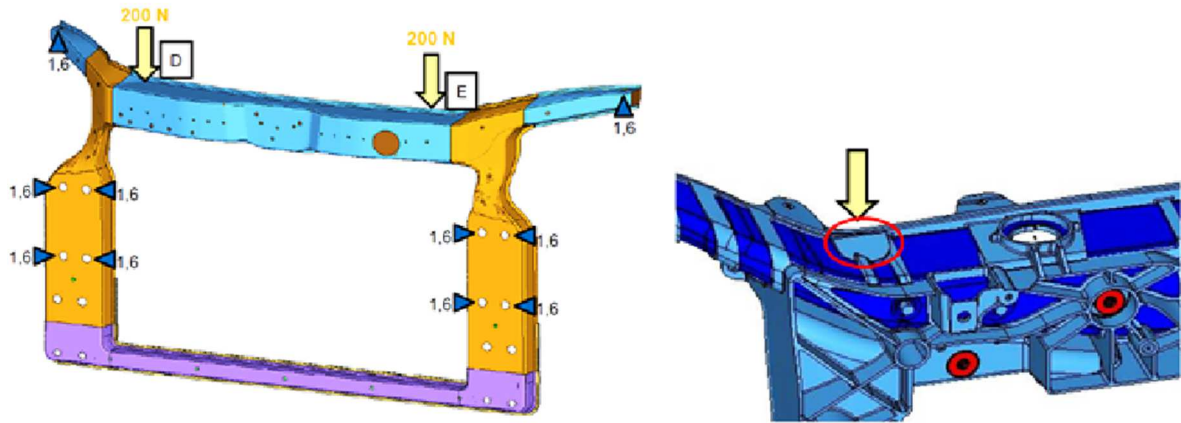


Figure 1.27 Load condition “Hood Stops Stiffness” (number 3)

In Table 1.4 are summarized the application point and the direction of the load.

Table 1.4 Load application points and direction of the condition “Hood Stops Stiffness”

Direction of the loads: $i = 0,26$, $j = 0$, $k = -0,97$			
	COORD. X (mm)	COORD. Y (mm)	COORD. Z (mm)
Point A	-555,42	392,05	509,89
Point B	-555,42	-392,05	509,89

Target: Stiffness > 400 N/mm

4. Yield Point Hood Lock Stiffness.

The loading condition is due to the force that acts on the front-end, through the closure system, when the car is moving at the top speed and the air is prone to open the hood. As it was done in the loading condition number 2, the closure system is simulated with a rigid “spider” system.

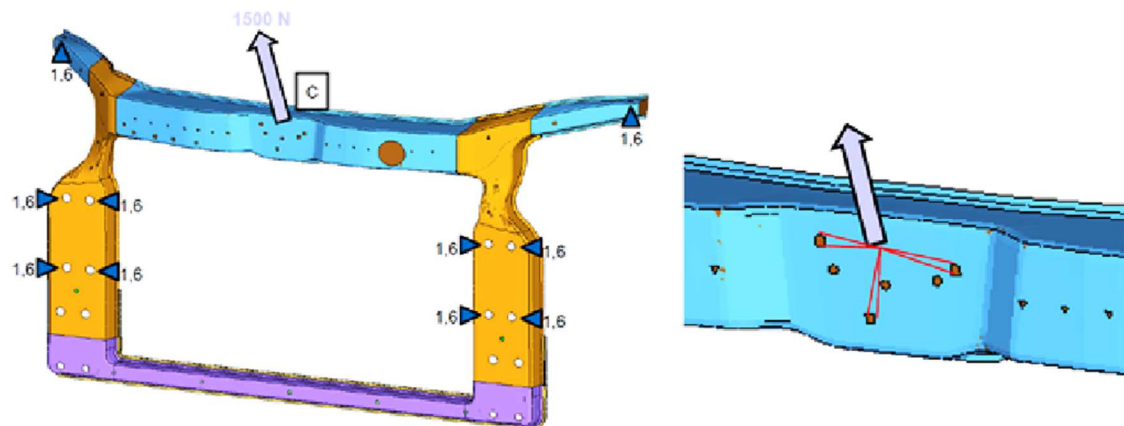


Figure 1.28 Load condition “Yield Point Hood Lock Stiffness” (number 4)

In Table 1.5 are summarized the application point and the direction of the load.

Table 1.5 Load application points and direction of the condition “Yield Point Hood Lock Stiffness”

Direction of the loads: $i = -0,127642$, $j = 0$, $k = -0,991133$			
	COORD. X (mm)	COORD. Y (mm)	COORD. Z (mm)
Point A	-595,44	0	464,2
Target: Total deformation < 6 mm			

The target were defined in order to guarantee the stiffness of the system both during the assembly operation and during the normal operations of the car. All the unwanted displacements of the parts that can be responsible of their deformation and of the other parts of the car, with consequent change of the geometry, must be avoided. The passing of the first loading condition is aimed to guarantee the correct supporting to front lights and avoid a wrong lighting of the road. The same reason is at the base of the loading condition number 4. In this case the front-end must be rigid in order to avoid the consequent deformation of the radiator and its incorrect operation. The stiffening effect due to the radiator is not considered in this work.

The boundary condition that simulate the fastening of the front-end to the ground are summarized in Table 1.6. The entire system is constrained to the car body in 10 points through the steel bolted connection. As reported in Figure 1.29. In order to simulate in a proper way the supporting of the parts due to the car frame, the constraint point are defined using three spring elements. Each spring simulate the equivalent stiffness in the principal direction x, y, z of the system. According to what was stated, the anchoring of the radiator was not considered not to overestimate the stiffness of the structure.

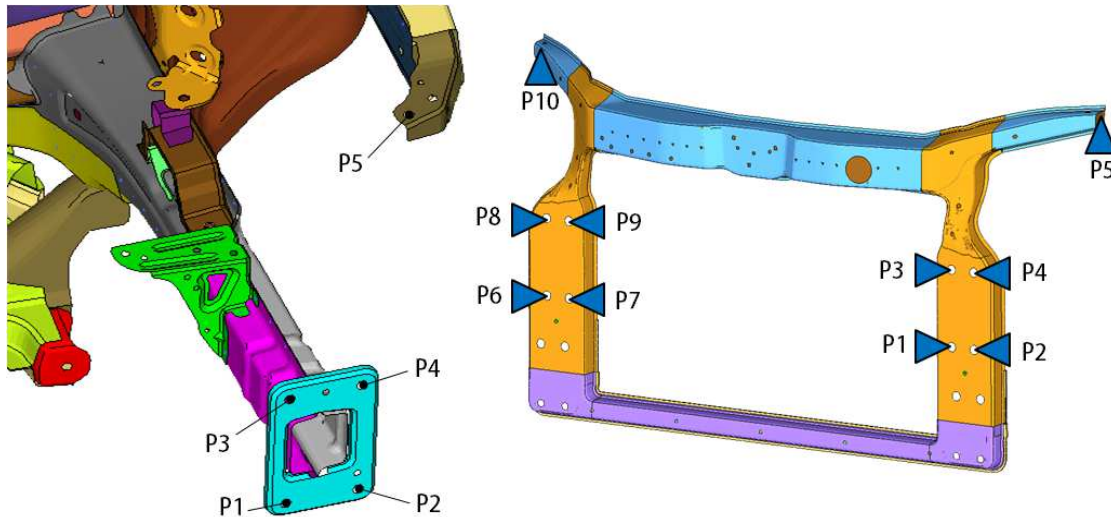


Figure 1.29 Constraint conditions of the bolted joint

In Table 1.6 are summarized the coordinates and the equivalent stiffness of the bolted joint.

Table 1.6 Coordinates and Equivalent Stiffness of the bolted joint

	Coordinates			Equivalent Stiffness		
	X [mm]	Y [mm]	Z [mm]	kx [N/mm]	ky [N/mm]	kz [N/mm]
P1	- 592,93	- 423,50	133,0	1470	370	1480
P2	- 592,93	- 497,0	133,0	1110	370	1300
P3	- 592,93	- 423,50	284,50	1590	380	1470
P4	- 592,93	- 497,0	284,50	960	380	1310
P5	- 390,0	- 622,0	508,50	260	110	50
P6	- 592,93	510,50	133,0	1110	370	1300
P7	- 592,93	437,0	133,0	1470	370	1480
P8	- 592,93	510,50	284,50	960	380	1310
P9	- 592,93	437,0	284,50	1590	380	1470
P10	- 390,0	622,0	508,50	260	110	50

1.5.3 Modeling of the Front-End

Meshing

After having designed the 3D geometry of the front-end, it is necessary to mesh the model before setting the simulation in the FEA environment. In this work, the Ansys Workbench 14.5 software was used [74, 75]. The meshing of model must be consistent with the requirements that the customer asked because it is used for other internal simulations in other environment aimed to the dynamic validation of the complete car.

The part was therefore modeled with shell elements since the thickness of the laminate and of the rib-structure are negligible if they are compared with the overall dimension of the part.

The nodes of the elements must belong to the middle plan of the solid with a tolerance of 1 mm with some exceptions that are allowed. The meshing of the part was consistent with the general requirements of the customer.

Two general criteria define the representation of the geometrical details. In particular, the significance of a geometric detail is linked to the structural importance of the zone in which the detail is. It is necessary to represent the detail whenever it is considered that it would have a significant structural contribution. Moreover, the representation of a geometrical details with limited size, if it is compared to the body size, is related to the degree of detail selected, and then to the average element size used in the surrounding of the detail.

The main specifications regarding the type and size of the mesh are due to the necessity of exporting the model in different simulation environments. The discretization of the sheets must be carried out with a shell-type elements (membrane behavior in bending) with 4 nodes and a linear formulation. It is admitted the local use of elements with three nodes for consistency reasons and to prevent geometric malformations. Use of triangular elements in the areas of interest or in their vicinity should be avoided and the number of triangular elements must not exceed 5% of the total. It is important to take as a maximum element size a dimension of 5 mm. In the areas where the evaluation of the stress-state is not important, the maximum size can be set to 8 mm. The size can go down as needed in the case of structural detail with high importance. The discretization must also observe the criteria of regularity and uniformity for which the ratio between the sizes of two neighboring elements must be less than 1.5 mm.

The connections between the injected part and the composite laminate will be simulated with elements of solid type that will bind together the nodes of the elements placed at the contact interface. It would also be possible to simulate the contact with spring-type elements (extensional flexibility) placed between coincident nodes. However, it would be necessary to provide an adequate documentation of the methods that are used to calculate the characteristics of the springs, as well as being outside the scope of this thesis, it would involve a study of the adhesion between the composite matrix and the overmolded polymer that is not defined uniquely by the scientific world.

Since the geometry of the overinjected part has draft angles, the thickness of the ribs was divided in classes (layers) based on the average thickness that contain increment of 0.2 mm. The geometry of the injected part was divided in 28 layers and the laminates are divided in 2 layers, one for transversal beam of 2.5 mm and one that contains the 2 plates of 1 mm.

Starting from this model that was provided in a format compatible with LsDyna, it was necessary to convert all the elements to make the model compatible with Ansys. The conversion required an intermedium passage in Ansys Mechanical APDL, otherwise, the Workbench environment was not able to recognize the layers. The intermedium steps required to save the meshed model in *.cdb format, to open it Ansys Mechanical APDL and to save it again. Then the model can be suitable for the Workbench environment with a direct and unambiguous recognition of the layers. The layers that are based on thickness were automatically recognized as named selections.

In the following section some features provided by Ansys for a correct simulation of the problem are presented. It starts with the presentation of the elements that were chosen for modeling the part. Then, it presents the various contacts offered for the simulation, how to define the parameters which describe the orientation of the laminate and the possible formulation for the definition of the loads and the deformations on their point of application. Finally, the properties of the material that were used are summarized.

Mesh element

The selected elements are shell181. These elements have four nodes, one for each vertex (unlike the shell281 that have an additional node to the midpoint of each side) and are suitable for both simulations with large deformations and that use materials with linear or non-linear behavior. Each node has 6 degrees of freedom. A characteristic feature of these elements is the ability to assign a thickness to each vertex in order to directly approximate the total thickness variation, without creating steps. The use of these elements suggests a full Newton-Raphson computational pattern.

Contacts

The contact is made when two distinct surfaces are touching becoming mutually tangent; the physical sense of the contact means that the surfaces do not interpenetrate and are able to transmit compressive normal forces, or traction if it specified, and tangential friction forces. The contact area is a non-linear change of state where the local stiffness of the system depends on the type of contact. The contacts in this thesis are essentially surface-to-surface and line-to-surface. By convention, in the contact definition, the two elements should be divided into target and contact: for contacts between rigid and flexible element, the rigid element is always the target whereas the deformable is the contact; for contacts between edges (lines) and surface, the edge must always be the contact whereas the surface is the target. In this case, with shell181 elements, the surface-to-surface contact is made between

TARGE170 and CONTA173 elements whereas, in the case of line-to-surface, the surface is the TARGE170 and the line is the CONTA177.

The nodes of the elements that are defined as contact cannot penetrate the target element, whereas the target nodes of the element can penetrate the contact element. More specifically, asymmetric contact is the most efficient in the contact surface-to-surface modeling and is preferred especially when there is a clear distinction between the contact surfaces and the target. When there is not a clear distinction between the definition of the two elements, or the meshes of the contact areas are inaccurate, it is preferable to use the symmetrical behavior (the algorithm in this case reinforces the contact constraints, and it covers most of the surface area). However, it is less accurate than the previous but it is more suitable to avoid the interpenetration of elements with a low surface stiffness. In this case study, which requires the Bonded contact with a MPC formulation, the behavior was exclusively set as asymmetrical.

In Bonded contact, both the faces are linked as glued without the possibility of separation or mutual sliding. The contact can also take place in the presence of gaps, penetration, and lack of load. This contact has a linear formulation and it is the default option in the automatic contact definition. It requires the least capacity and calculation time. For the specific case of Bonded contact and No-Separation contact between two surfaces, the formulation Multi-Point Constraint (MPC) is available and is strongly suggested (Figure 1.30). This formulation adds new constraint equations that "link" the movements between the contact surfaces and it is an additional option to the penalty-based and Lagrange multiplier-based formulations. It is a direct and efficient way to correlate the surfaces in contact. This formulation is compatible with the large deformation option.

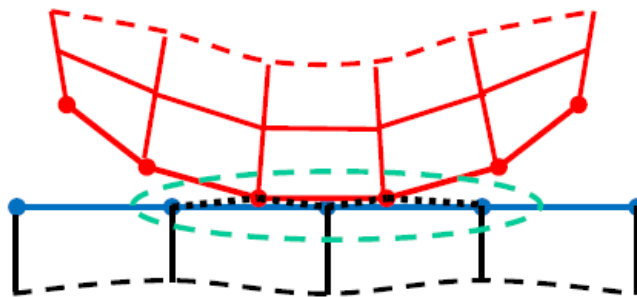


Figure 1.30 Graphic interpretation of the MPC formulation [75]

Since with shell elements it is not possible to ensure a constant distance between the elements and the nodes of the target and the contact surface, especially in correspondence of curved geometries, it is fundamental the definition and the use of the Pinball Region. This parameter is necessary to distinguish elements that need to be considered *far*, not in contact, and element that need to be considered *near* that are not physically connected but must be considered to actively participate in the contact.

Figuratively, the *Pinball* region is similar to a sphere that is defined by a radius imposed by the user on the basis of the desired effect, which include all the elements that participate to the type of the contact. In the case of Bonded contact, if there is a gap between the surface that is covered by the pinball regions, all the elements are considered as participating in the contact definition. The graphic interpretation of the pinball region is showed in Figure 1.31.

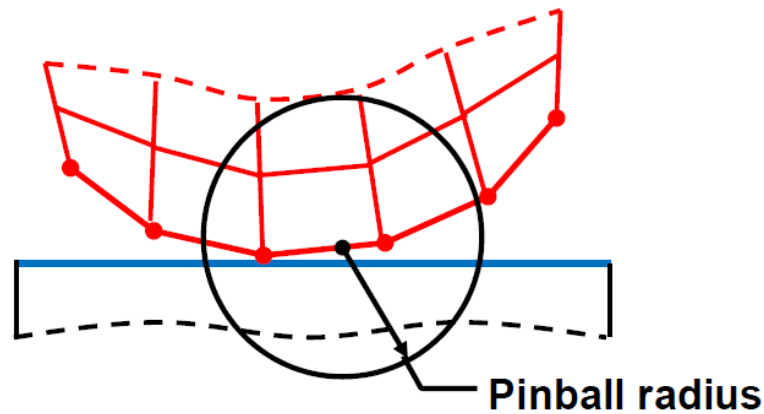


Figure 1.31 Graphic interpretation of the Pinball Region [75]

The advantage offered by this instrument is a greater flexibility in the identification of the elements to keep in contact, and if a formulation of MPC type is used, also in the possibility of considering the nodes. It is not even negligible that the radius determines the depth at which the interpenetration between the elements, if it is present, can be solved. The hardest part is to define the radius of Pinball Region that does not include the nodes of surrounding elements that are not directly participating in the physical contact: it is true that these nodes “in excess” does not affect the contact, but the higher the number of constraint equations is, the more the calculated stiffness is overestimated.

However, the definition of the radius cannot be avoided given the large variety of radii of curvature that are in the part and the general mesh size required by customer. For this reason, it is preferable to accept an overestimation of the calculated values rather than obtain a model in which there is no contact between the laminate and over-injected part.

The radius has been judiciously chosen and defined for each region of the part and then repeated and set for all the different configurations of the component that must be simulated. In so doing, although they may be present small inaccuracies, they are reproduced for all the simulation without creating source of random error that is not easily eliminable. The radius values used for the Pinball ranging from 1.5 mm in correspondence of the welding zones close to the side brackets where the thickness of the various components is small, up to 6.5 mm for the welds between the ribs and the upper beam where the thickness of the first and the curvatures of the second lead higher gap. It is recalled that shell elements are placed on the middle plane of the parties and the greater the thickness of the parties is, the more the distance between the target and contact increase, and thus the required radius of the Pinball. Instead, when the number of the constraint equations, which are visible at the level of *Graphics* in the *Solution Information* windows, becomes too high and it is no longer possible to act with the modification of the Pinball Region it will work by setting, where necessary, the *Constraint Type Target Normal, Uncouple U to ROT*

Orientation of the laminate

In order to correctly simulate the orthotropic behavior of the laminate and to allow the full recognition of the changes of orientation of the reinforcement fibers along the curvature of the part and of the geometric singularity, it is indispensable to refer the laminated composite parts to a specific coordinate system. This must be done in the definition of the geometrical specifications of the various components that constitute the part. The reference system can be placed in any point of the space, but it is preferable to center it on the part to which is referred for the viewing convenience reasons. The local reference system must have an

orientation consistent with the definition of the properties of the material that constitutes it. Moreover, the orientation of the normal of the each shell element that discretizes the part must be consistent both with the bordering elements and with the principal direction of the material's properties. After having defined the reference system, it is advisable to specify this in the *Geometry* window as *Coordinate System* of the part to which it is referred. To verify the correct orientation of the elements that are involved it is possible to have a global overview by adding the voice *Element Triads*, which can be found in the *Coordinate System* section, to the required *Solution*. The image that is obtained is shown in Figure 1.32 where, for a greater visual effect, only the orientation of the laminate elements on the upper transversal part is showed. The transversal beam was sectioned with a cutting plane for an easier understanding of also the x and y directions of the orientation of the elements. Note that the z direction is oriented according to the normal of the elements constituting the part in accordance with what was said before.

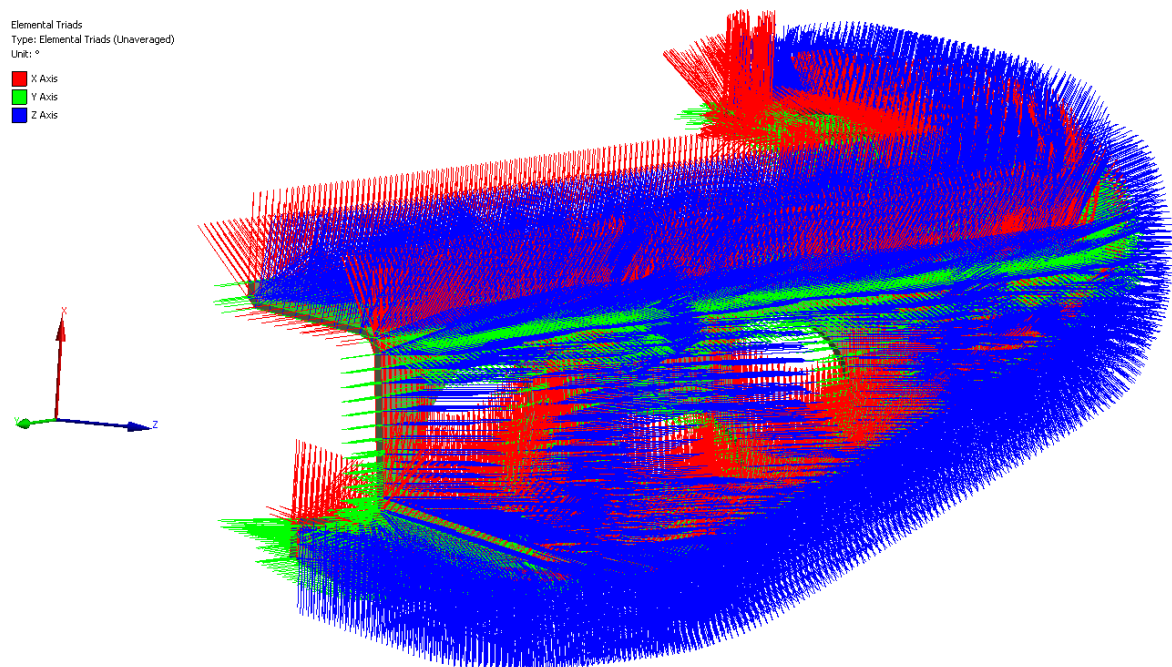


Figure 1.32 Graphic representation of the specific orientation of the elements of the transversal beam.

Definition of loads and constrains

With regard to the positioning of the loads and the definition of the stiffness of the constraints that are constitute by the chassis of the car, in the previous chapter the coordinates of the points of application of forces and the stiffness defined by the customer were presented. It is therefore necessary to define the *Remote Force* and *Boundary Conditions* body to ground. Respecting the sequence proposed by Ansys for the definition of the model it is necessary, after specifying the laminate-injected contacts, to set the stiffness exerted by the external constraints. In this regard, they must be placed the *Body-Ground springs* that have the elastic constant equal to the stiffness of the real constraint in that direction. For each point of the fastening of the system to the frame (P1, P2, P3, etc.), three springs were used each arranged along a main direction and with stiffness k_x , k_y , k_z . Then, it will be important to fix the coordinated of the fixed end (to the body) and the mobile one (to the ground).

The latter must be consistent with the coordinates of the constrain that were specified by the customer and that must be referred to the area where the component is affected by the strength of the constraint. The fixed point instead, can be chosen at will on condition not to be coincident with the mobile one for avoiding the modeling of the screw's head or of the rosette. The representation of the bond is shown in **Errore. L'origine riferimento non è stata trovata.**. On the left side, the representation of the spring it is almost invisible, but the point of application can be recognized inside the Pinball Region (semi-transparent) that intersects the surface of the laminate (blue). The area that results in dark blue indicates the effect of the bolting. On the right side, it is reported the representation of the bolting and of the constrain that is available in the *Constrain Equations* viewing mode, during the calculation phase of Ansys.

Regarding the definition of the *Remote Force*, just add it in the section *Static Structural* in the subsection *Loads*. In this subsection, the coordinates of the point of application are specified and the force is defined by setting the principal components. In Figure 1.33 are reported, as it was done for the springs, the *Constrain Equations* relating to the forces that act in the fourth loading condition. To get in the output values of the components of the displacement in the application point of the force, just switch the *Remote Force* in a *Remote Point* and set the *Remote Point* as *Location Method* of the output called *Deformation Probe* in the Solution section.

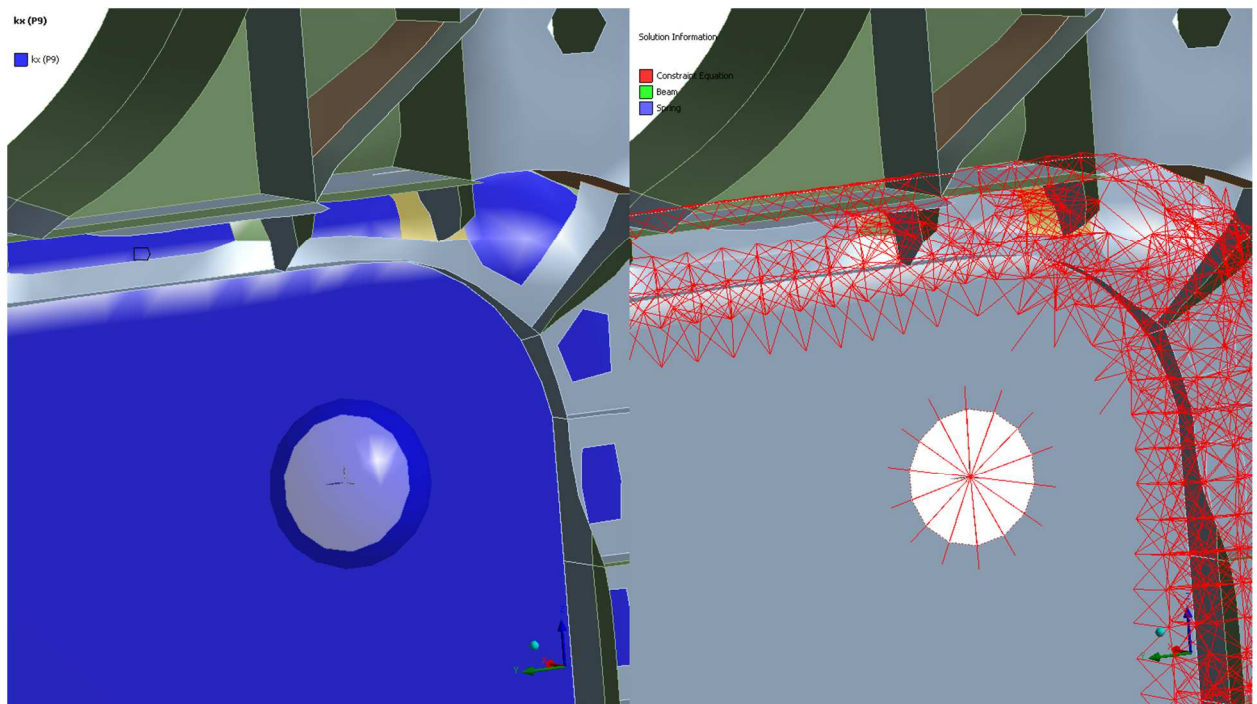


Figure 1.33 Graphic representation of the constraint conditions. The figure on the left represents the definition of the bolted joint where the intersection of the pinball region with the flange and the spring used for the definition of the stiffness are shown. The figure on the right represents the areas where the pinball region defines the bonded contact and the connection to the ground.

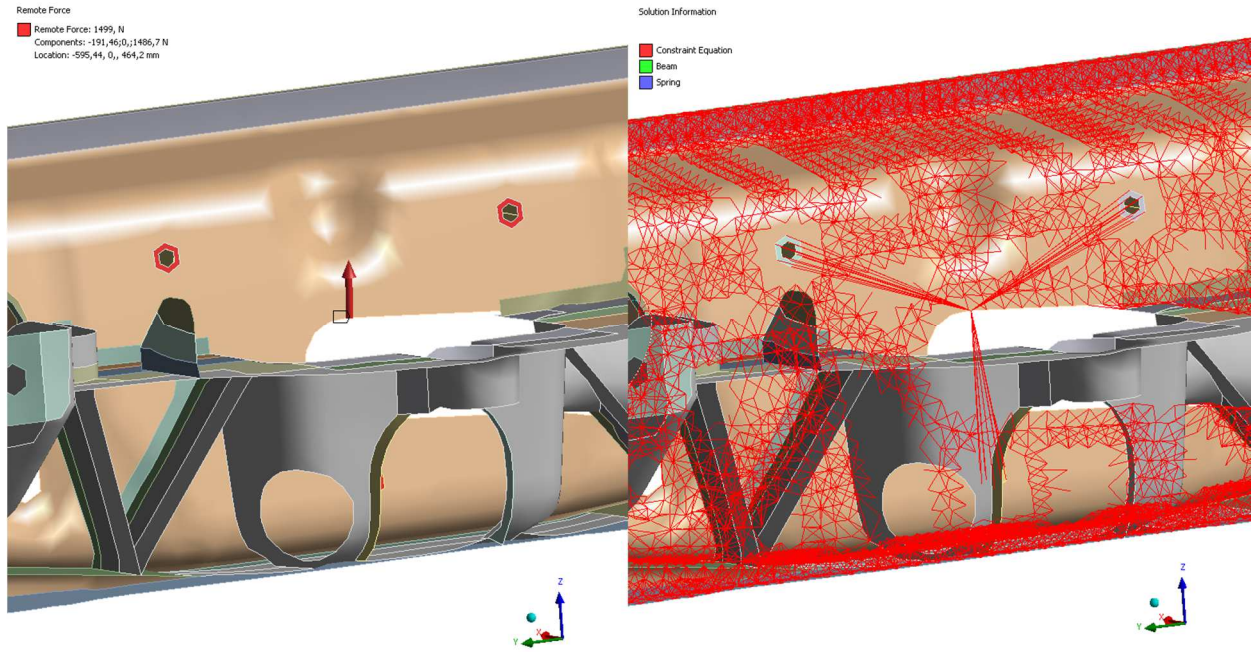


Figure 1.34 Graphic representation of the constraint conditions. The figure on the left represents the definition of the load through the remote point. The figure on the right represents the areas where the pinball region defines the bonded contact and the spider system for the application of the remote force.

After having set the orientation of the composite laminate, the contacts between parts and the fastening to ground, the loads are applied according to the directions presented in the previous paragraph. A simulation for each loading condition was performed. The setting of the properties of the material is now presented.

Materials

The materials were set in accordance to the result of the mechanical characterization of the specimens.

The overinjected part is made of Stamax 30YM240, a polypropylene 30%w reinforced with long glass fiber. The behavior of the material was modelled as isotropic. The main properties are described by the average values obtained from tensile testing of dog-bone specimens that were milled directly from an injection-molded plate. The reference standard is the UNI EN ISO 527. The cut from the injected plate was made to have a homogeneous distribution of the fibers and to avoid the dependence of the orientation by the filling of a cavity of fixed geometry. The test samples were cut out at 0°, 45° and 90° with respect to the direction of filling and were tested at the same test speed.

The values used in this work are choose in accordance to the Stamax 30YM240 datasheet for a strain of 10/s. The values are summarized in Table 1.7

Table 1.7 Mechanical properties of Stamax 30YM240 used for the simulations

Elastic Modulus E [MPa]	UTS [MPa]	Deformation at UTS [%]	Tangential Modulus G [MPa]	Compression Modulus K [MPa]	Poisson coefficient ν
4692	87	2,7	1629	1303	0,44

In addition, the organosheets that were chose for the design of the main transversal beam and the flanges were mechanically characterized. The results of this step, for a better reading of the work, are reported in the part 2 in the mechanical characterization of the organosheet. The behavior of the laminate was assumed as orthotropic.

1.5.4 Results, optimization and validation

All the analyzed models are summarized in Table 1.8. Preliminary analysis involves the front-end without transversal reinforced beams (models A and B) and with them (models C and D). Both RG600 and RGUD600 composite laminates were used. Full-plastic composite models A and B lead a weight reduction up to 3.38 kg (-27.75%), against a weight reduction up to 3.81 kg (-18.50%) of models C and D. Both the models had not met the target under the front-lights loading condition. In contrast, loading conditions 2 and 3 are largely complied with targets: they have been omitted from results. The effect of the reinforcement beams was appreciable especially under the loading condition 4. In addition, the metal/plastic front-end was tested to get a complete comparison. Because the addition of reinforcement beams increase the total weight and requires a review of the mounting sequence too, the stiffness of the part was improved in other ways. Since the worst performance is under the load 1, which acts in a torsional way due to light, the principal direction of the laminate was rotated of 45 degrees (model E). A deepening analysis shown improvements, under load 1, by rotating only the middle ply (model F) but the target stiffness has not yet been reached. In order to increase the stiffness of the front light area, a crossed ribs system was added (models G-L) inside the transversal bar.

Table 1.8 Layers arrangement in the analyzed model where the plies arrangement is reported by angle and the balanced laminate is indicated with “X” and the unbalanced with “=”.

Model ID	1°	2°	3°	4°	5°	6°	Weight [kg]	%	
A	Balanced RG600						/	3.38	- 27.8
B	Unbalanced RGUD600						/	3.38	- 27.8
C	Balanced RG600 (with beams)						/	3.81	- 18.6
D	Unbalanced RGUD600 (with beams)						/	3.81	- 18.6
E	x 45°	x 45°	x 45°	x 45°	x 45°	/	3.38	- 27.8	
F	x 0°	x 0°	x 45°	x 0°	x 0°	/	3.38	-27.8	
G	= 0°	= 0°	x 45°	= 0°	= 0°	/	3.46	- 26.0	
H	x 45°	= 0°	= 0°	= 0°	x 45°	/	3.46	- 26.0	
I	Unbalanced RGUD600						3.59	- 23.3	
L	x 45°	= 0°	= 0°	= 0°	= 0°	x 45°	3.59	- 23.3	
MP	Metal-plastic front-end						4.68	-----	

The ribs were placed between the vertical ones and their thickness was gradually varied between 2 and 4 mm. Optimization were performed under the front-light load condition and the results of the subsequent changes is reported in Table 1.9. The optimal configuration of the distribution of the thicknesses, which is represented in Figure 1.35, cannot be improved much more due to technological limitations of injection molding that discourage the manufacture of features thicker than 4 mm for the reasons related to the volumetric shrinkage and to cycle time. Notice that also the thickness of the outer profile of the entire injected part around the beam was increased according to the results of the topological analysis.

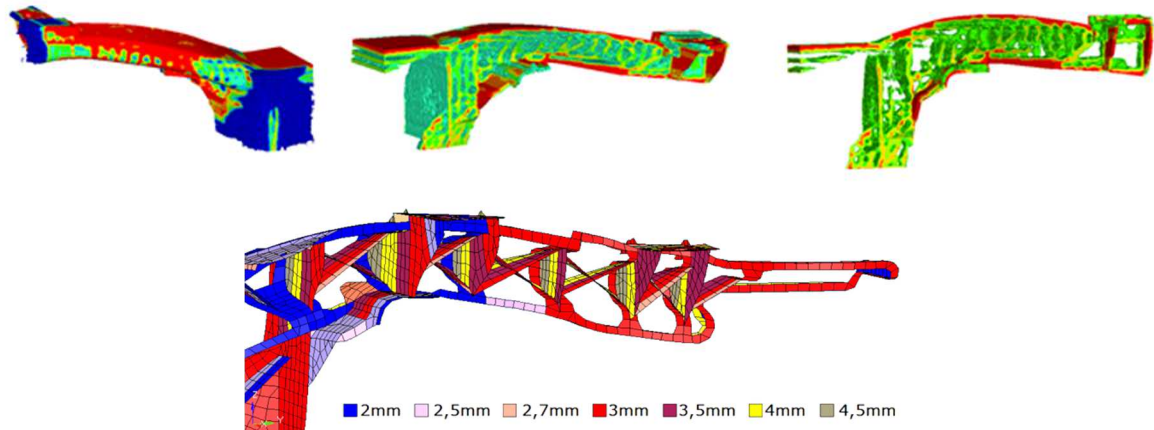


Figure 1.35 Results of the topological analysis under the load case “Front Light Stiffness” and the ribs system that was modelled.

Table 1.9 Progressive increase of the thickness and relative results in stiffness and local deformation in Z measured on the transversal beam.

Medium Thickness	No ribs	2 mm	3 mm	4 mm
Front Light Stiffness [N/mm]	38.09	51.28	52.35	54.05
(Z Deformation)	(-5.25 mm)	(-3.9 mm)	(-3.82 mm)	(-3.7 mm)

A deformation reduction of 29,5% against an increase of the total weight up to 3.46 kg (-26,1%) was attained. However, targets were not fully achieved: effects of layers arrangement were further deepened. Better performances were obtained coupling the higher torsional strength of the balanced laminate when is 45° oriented and the higher bending strength of unbalance laminate (models G and H). Standard RGUD600 composite (model I) and a layered structure (model L), both 3 mm thick, were analyzed. Increasing the thickness allowed to meet all the targets also avoiding the plies re-arrangements and a saving of 1.1 kg was achieved (-23.3%) compared to the original model. The overall comparison between the different geometries that were simulated and the polymer-metal hybrid configuration are reported in Figure 1.36 and in Figure 1.37 where the target value is represented with a red line. Since the load conditions 2 and 3 were largely satisfied, they are not reported.

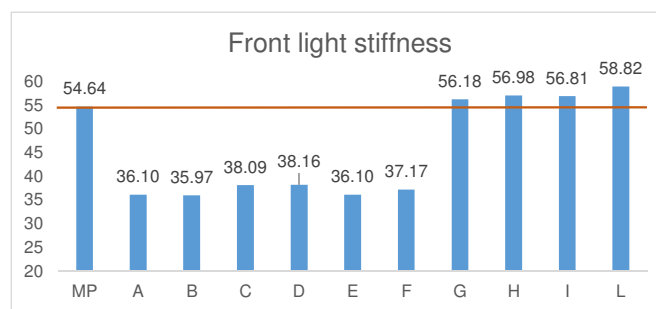


Figure 1.36 Performance of the Front-Ends under the loading condition “Front Light Stiffness” (load condition number 1, target: Stiffness > 54,64 N/mm)

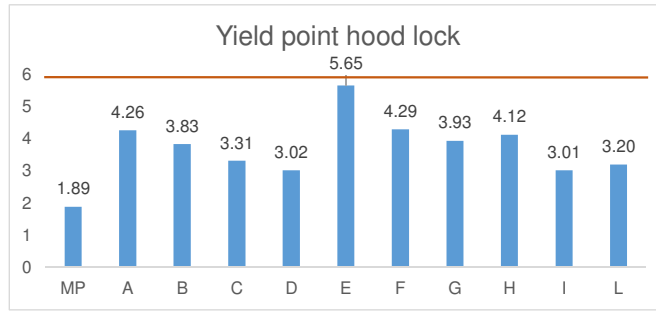


Figure 1.37 Performance of the Front-Ends under the loading condition “Front Light Stiffness” (load condition number 4, target: deformation < 6 mm)

For the G and H configurations, which are deemed the most valid under the aspect of the attainment of target, a preliminary check of the welding between the matrices of the injected part and of the laminated was performed. For quantifying the value of the maximum tensile strength of the weld were considered the experimental result from two main studies [76,77] where the welding strength was measured by tensile testing of hybrid T-joint specimens. From these works, the tensile strength of the specimens results about 1/3 of the maximum strength of the material that constitutes the matrix of the composite. For this reason, since the ultimate tensile strength of a polypropylene homopolymer varies between 25 and 50 MPa it was chose a reference value equal to 40 MPa and thus a permissible maximum crush strength of the weld equal to 16 MPa.

The results presented below were obtained by the creation of *Named Selection* that group the surfaces involved in contact-type surface-bonded surface and by querying the Von Mises' stress and strain results (Figure 1.38 – Figure 1.41). The edge-type surface contacts cannot be displayed in the set. With the view named "Back" is meant the surface in contact with the back of the composite beam that, for better clarity, is reported from the front side view.

L: VM WELD 80.50.80 C1 (relaz)
 VM Bonded Interface BACK
 Type: Equivalent (von-Mises) Stress - Top/Bottom - Layer 0
 Unit: MPa
 Time: 1
 16/04/2015 18:50

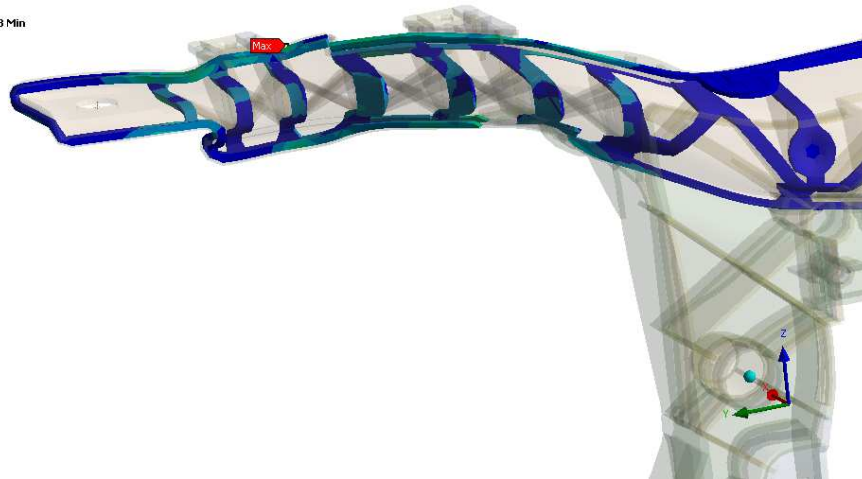
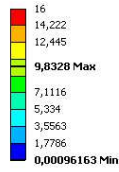


Figure 1.38 Von Mises Equivalent Stress referred to the laminate with layering 80(1mm).50(45°0,5mm).80(1mm) and injected part under the load condition C1 (Back)

L: VM WELD 80.50.80 C1 (relaz)
 VM Bonded Interface FRONT
 Type: Equivalent (von-Mises) Stress - Top/Bottom - Layer 0
 Unit: MPa
 Time: 1
 16/04/2015 18:52

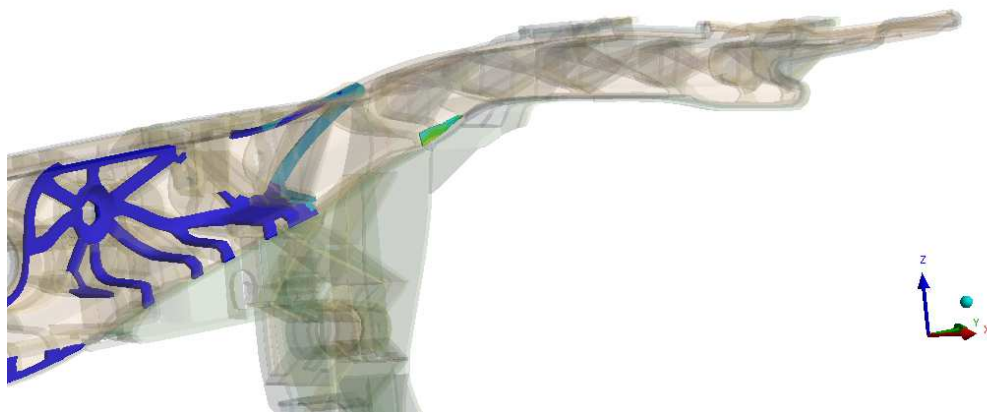
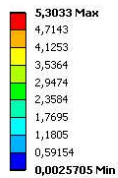


Figure 1.39 Von Mises Equivalent Stress referred to the laminate with layering 80(1mm).50(45°0,5mm).80(1mm) and injected part under the load condition C1 (Front)

T: VM WELD 80.50.80 C4 (relaz)
 VM Bonded Interface BACK
 Type: Equivalent (von-Mises) Stress - Top/Bottom - Layer 0
 Unit: MPa
 Time: 1
 16/04/2015 18:30

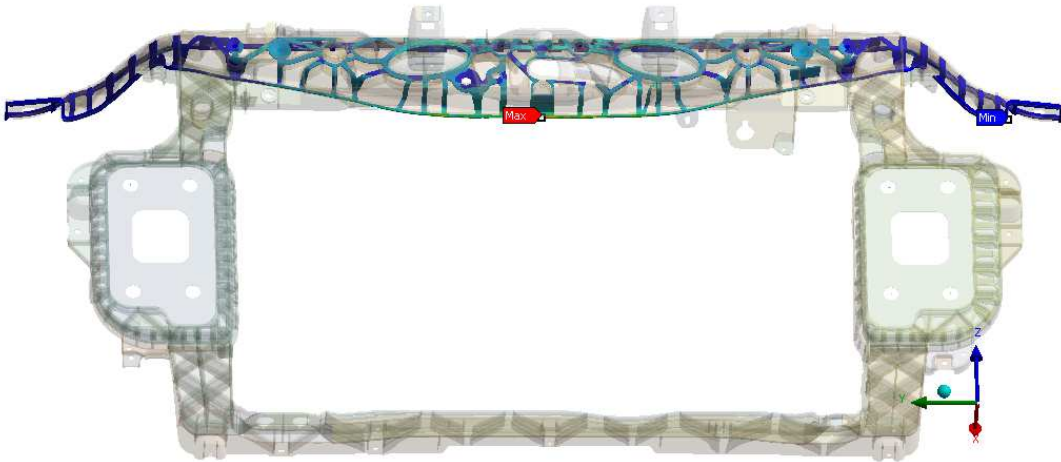
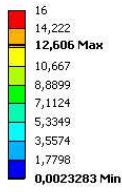


Figure 1.40 Von Mises Equivalent Stress referred to the laminate with layering 80(1mm).50(45°0,5mm).80(1mm) and injected part under the load condition C4 (Back)

T: VM WELD 80.50.80 C4 (relaz)
 VM Bonded Interface FRONT
 Type: Equivalent (von-Mises) Stress - Top/Bottom - Layer 0
 Unit: MPa
 Time: 1
 16/04/2015 18:36

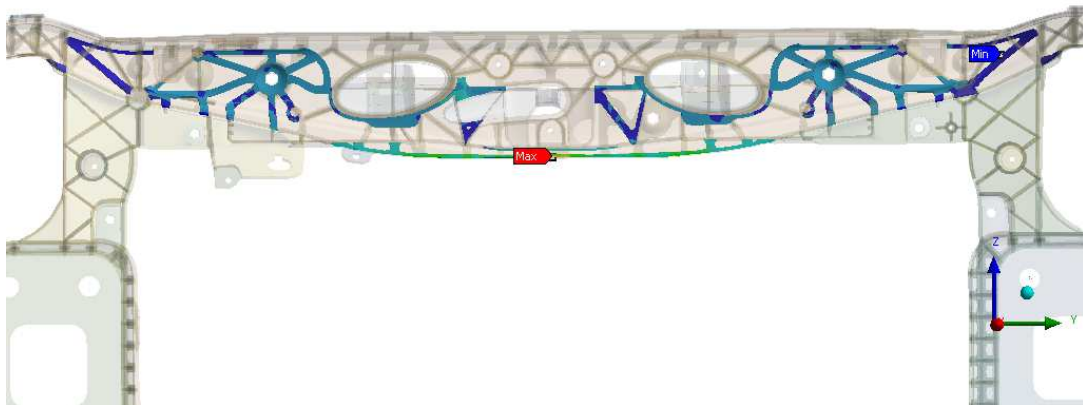
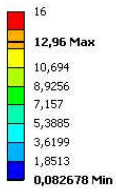


Figure 1.41 Von Mises Equivalent Stress referred to the laminate with layering 80(1mm).50(45°0,5mm).80(1mm) and injected part under the load condition C4 (Front)

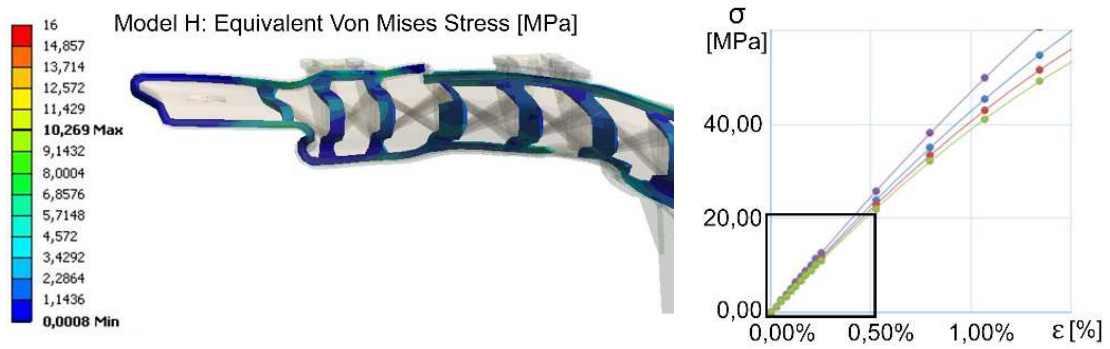


Figure 1.42 (a) Load 1: equivalent stress at interface, (b) stress-strain curve of Stamax

The maximum equivalent Von Mises stress at the interface is in below the limit of 16 MPa and so, the bonding resistance requirements was assumed as fulfilled. In the right side of Figure 1.42 the first part of the stress-strain curve is reported. Since the maximum strain of the parts was noticed under the loading condition 4 and it is equal to 0.0046, or 0.4%, assuming the injected material as an elastic material was an admissible choice.

1.6 General remarks: introduction to the following parts

The consultancy work was aimed to provide the customer with an overall idea about the static performance of an automotive front-end made of full thermoplastic hybrid composite. The approach to the modeling was strongly limited by the customer and all the work was done without consider the process effect to the global performances of the part. However, the effect of the metal sheet replacement with a layered organosheet was in deep evaluated. The main limit of the work is due to lack of knowledge about:

- *how to define the boundary condition between the laminate and overinjected part*
- *how the process parameters affect the welding resistance*
- *how the injection process affects the distribution of both the length and the distribution of the fiber (and how they reflects on the overall performance of the part)*

All of the listed points were subject of the investigation during the years of the Ph.D. In order to provide the reader with an organized work, the discussion continues in two different sections.

Part 2 is dedicated to the investigation of the effect of the process parameter on the welding resistance. A model for the prevision of the welding strength at the polymer-polymer interface was calibrated on the experimental results. Moreover, an approach to the modeling of the welding area as a boundary condition in FEA simulations was proposed to go beyond the limits.

Part 3 is dedicated to a complete measurement chain for the fiber length distribution. The system, which is based to the image analysis technique, was used for evaluating the effect of plasticating phase on the fiber length degradation. As a results, the measurement chain was optimized and the uncertainly of the measure was calculated. Finally, the measure chain was used on an additional case study.

2 Welding resistance in full-thermoplastic hybrid composites

2.1 Joining of polymers

The requirement of parts even more performant and lightweight implies the joining of different materials and sub-components that absolve different functions. This trend gives up the theoretical idea of a monolithic part free of joints that can deteriorate the mechanical strength but can answer to limitation of the production processes in manufacturing of complex geometries [1]. Therefore, the need of integrate technologies and parts leads to the constant understanding and development of available and new joining techniques. Since composite polymer play a key-role in the lightweight design, increasing attention is paid to the joining with dissimilar materials.

The methods for joining plastic components can be divided in three major categories: mechanical joining, adhesive bonding, and welding. [2]. Mechanical joining involves the use of separate fasteners, such as metallic or polymer screws, or take advantages of integrated design elements that are molded or overmolded into the part, such as snap-fit or press-fit joints. In adhesive bonding a third elements, which is the adhesive, is placed at the interface of the parts to joint them and serves to transmits the load between them. In welding or fusion bonding, heat is used to melt or soften the polymer at the interface to enable the molecular interdiffusion across the interface and to create chain entanglements to give the joint strength. Each of the listed categories comprises a variety of joining methods that can be used in a wide range of application. This dissertation is focused on process induced welding that takes advantages of the process conditions and that is based on the same principles that regulates the welding processes. Moreover, in the particular case of the injection overmolding of composites thermoplastic laminates (organosheets), the process can induce a modification of interface where, thanks to the surfacing of the reinforcement fibers, a local mechanical interlocking can take place.

As is better deeper explained in paragraph 2.1.2, when two interface of the same polymer are brought together in molten state, the interface will conform to each other to achieve intimate contact followed by intermolecular diffusion and chain entanglement and the weld takes place. The degree of welding is based on many parameter, including material properties, time-temperature history and interfacial pressure. In process that involves the injection process, the intimate contact it is almost instantaneous when the melting front meets the organosheet. Many researchers demonstrated that the macromolecules move between each other in a confined volume. The models generally assume that the interfaces are in intimate contact and a constant temperature. The complete healing of the interface is assumed completed after having been in contact at the molten state for time equal to a reference time, called reptation or diffusion time. Under ideal condition at complete healing, the polymer chains, from each side cross the interface so that the interface cannot be distinguish from the bulk material anymore. The models were initially developed for isothermal condition, but they can be adapted to the non-isothermal case that is typical for most of the industrial processes.

When the interface or the part solidify, respectively in welding processes or process-induced welding, residual stresses resulting from the nonlinear thermal contraction remain in the part. If the molecular alignment result parallel with the interface, the molecular orientation is frozen during the cooling stage, especially in high non-isothermal process and it can results in a pretensioning effect of the welding. [3, 4]. The analysis of residual stresses plays an important role for several reason linked to the decrease of the mechanical properties of the welding as static and dynamic performances, toughness and fatigue life. Moreover, the eventual presence of micro cracks increases the corrosive effects in presence of solvent [5-9].

2.1.1 Process-induced welding

With reference to the hybrid composites that were presented in the first part of the work, the technologies that are based on the injection molding process allow the joining or the welding between parts at the end of the cycle. This is an advantage in terms of direct and indirect cost because the molten state and the high temperature of the injection phase promote the bonding and the following assembly procedures are reduced. In particular, the direct joining is typical of the polymer/metal hybrid composite and the direct welding is typical of the polymer/polymer hybrid composites.

Polymer/metal hybrid (PMH)

The joining between the metal and thermoplastic sub-components is attained through direct-adhesion of injection-molded thermoplastics to the metal without using of undercuts or holes, which are created on the metal side, that are filled by molten polymer [10]. Otherwise, the joining can take place without the use of interlocking rivets and other features and by avoiding the structural adhesives [11]. The overview of the literature in the PMH direct-adhesion field revealed that within the micro-scale the required level of adhesion strength is attained via the infiltration of the micron-size roughness features of the metal substrate with thermoplastic melt [12]. To this aim, the metal substrate temperature has the largest effect on to the polymer-to-metal adhesion strength. If the metal substrate is not previously heated, the polymer melt would freeze upon touching it and failing to infiltrate its micron-size roughness features. Alternatively, the direct adhesion may be promoted without preheating or in addition through various surface treatments, such as etching or plasma or laser ablating [13-15]. In other work was highlighted the dependencies of the joining from the characteristics of the metal substrate such as roughness and temperature as well as the injection molding parameters such as injection temperature and pressure, which help the bonding process [16]. However, the filling percentage of the polymer is fundamental to reduce the volumetric shrinkage of the matrix and avoid the trigger of the detachment.

Polymer/polymer hybrid or thermoplastic hybrid composites (TPHC)

The joining between the polymer sheet (organosheet) and the thermoplastic stiffening system is attained through direct adhesion of the injection-molded material to the laminate. The welding is based on the healing that takes place at the interface of the two thermoplastic materials and that, in some cases, is accompanied by a mechanical interlocking between the inject material and the fiber yarns of the reinforced laminate when the process uncover them. Several researches were carried out to understand how the In-Mold-Forming process affect the welding strength [17-20]. All the works are in agreement with the positive effect of the injection temperature on the welding resistance. Aurrekoetxa et al. showed that holding pressure has a positive but non-significant effect of the welding strength [17]. Contrarily, Moritzer et al. [18] found a positive contribution of the holding pressure but it was related to the higher level of the injection velocity. Giusti et al. also found the positive effect of the injection velocity and they suppose it was related with both the consequent higher pressure and to a lower cooling of the flow front [19]. The same concept related to the flow front is expressed again in the work of Moritzer et al. where the distance from the injection point was investigate and a negative correlation of the performances with the distance was found. This confirm that the flow front cooling affect the resistance of the fairest areas.

Individualized and functionalized polymer/polymer hybrid (Lightflex concept)

The technology is aimed to answer to the increasing request of individuality and adaptability of the parts without losing of robustness and stability [21, 22]. The process couples the 3D printing and the thermoforming of tape, layered tapes and organosheet, individually or together. The process requires the local heating of the outer surface of the 3D printed parts that is subsequently used as lower frame for the direct thermoforming of the thermoplastic shell. The technology is still under development but is clear that the bonding mechanism is based on the process induced welding. The strength of the welding is directly related to the material characteristic as well as process parameters that regulated the forming. The healing of the interface is affected by the listed conditions and, as in the case of the In Mold Forming, they reflect on the welding strength of the joining and on the overall performances of the parts.

2.1.2 Analytical healing model

The welding process between two thermoplastic materials is characterized by two main phenomena that define the degree of the bonding. The first contribution is given by the intimate contact that indicates the physical contact between the two surfaces. For the thermoplastic materials that come into contact at temperatures close to the melting point and to the high pressures typical of injection molding process, thanks to their nature, it can be assumed that the intimate contact is achieved at the end of the filling phase. The second contribution is given by the phenomenon of self-diffusion of the macromolecules. In thermoplastic polymer matrix materials it can occur only when the macromolecules have enough energy for the motion, in particular the self-diffusion occur when the polymers are in contact above their glass transition temperature, or the crystallization temperature, respectively if they are amorphous or semi-crystalline.

The Reptation theory

The movement of a chain in amorphous materials was described by the reptation theory, developed by De Gennes [23] and based on the intuition of Edwards [24]. The theory allows to describe the motion of a macromolecule through the Brownian motion of chain segments. The motion of the macromolecules is constrained inside a tube with its conformation. The main assumptions of the theory are the following:

- *The chains move in a fixed network, and it is not allowed to cross the obstacles;*
- *The chains move between obstacles in a manner similar to that of a snake.*

The motion can occur only along the track of the tube and the first interested parties are the free-ends of the chain (Figure 2.1). This is because near the interface they have a non-equilibrium conformation, which allows it to diffuse. The time required to assume a new conformation and start the formation of new entanglements is said time of reptation t_{rep} . After a time longer than the reptation time, the complete adhesion that corresponds, in the industrial case, to the maximum resistance of the weld is obtained. Following, the theory was redefined by Edwards and Doi [25].

The reptation theory allows to predict the distance, which is represented in Figure 2.1, that is covered by the macromolecule after the time t . The distance l is called minor chain length and is defined in Equation 2.1.

$$\frac{l}{L} = \left(\frac{t}{t_{rep}} \right)^{1/2} \quad \text{Equation 2.1}$$

Where L is the length of the tube. The creation of a junction can be attributed to the minor chains crossing the interface and creating entanglement. The same theory can be used for predicting the distance of the average interdiffusion, which is assumed equal to the average distance between the end of the macromolecule and the interface.

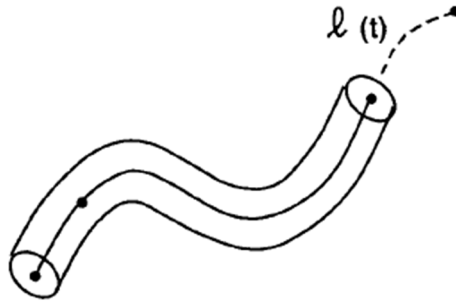


Figure 2.1 Representation of the length of the macromolecular motion [33]

Equation 2.2 allows the prediction of the average distance of interdiffusion χ , which is represented in Figure 2.2, at the time t .

$$\frac{\chi}{\chi_{\infty}} = \left(\frac{t}{t_{rep}} \right)^{1/4} \quad \text{Equation 2.2}$$

Where χ_{∞} is the radius of gyration R_g of the macromolecule.



Figure 2.2 Representation of the distance of interdiffusion [33]

As the time increases, the interface is going to disappear and the properties of the bulk material are reached for time longer than the reptation time. The creation of a junction can be attributed to the minor chains crossing the interface and creating entanglement

The healing theory, as presented by Kim and Wool [26], can relate microscopic parameters, such as l and χ , to macroscopic mechanical properties, such as strength and toughness. The models make the assumptions on the failure mechanism that can be due to chain pullout (stress based) or to chain breakage (energy based).

The healing model states that the fracture stress is proportional to the interpenetration distance and, according to (Equation 2.3), it is proportional to the fourth root of time. Based on similar considerations, the fracture energy G_C is proportional to the square root of the minor chain length and, according to (Equation 2.4), it is proportional to the square root of time. The proportionalities are presented in the following equations:

$$\frac{\sigma}{\sigma_{\infty}} = \frac{\chi}{\chi_{\infty}} = \left(\frac{l}{L} \right)^{1/2} = \left(\frac{t}{t_{rep}} \right)^{1/4} \quad \text{Equation 2.3}$$

$$\frac{G}{G_{\infty}} = \frac{l}{L} = \left(\frac{t}{t_{rep}} \right)^{1/2} \quad \text{Equation 2.4}$$

Where σ_{∞} e G_{∞} are the fracture stress and energy of the fully healed interface. These relations are valid for isothermal healing at a temperature T and for process times t less than

or equal to t_{rep} . The prediction of the real fracture stress and the real fracture energy, it is necessary to determine experimentally the maximum values under controlled conditions must be determined experimentally in controlled condition. Moreover, the reptation time which describe regulate the thermal control must be carefully evaluated.

Molecular interdiffusion

The interdiffusion into molten polymers, which have high molecular weight, has received a considerable experimental and theoretical attention. The link between the long molecular chains leads to differing restrictions on the dynamics of the chain. Most of the studies were focused on the case of larger diffusion lengths than the dimensions of the diffusing molecule. The reptation model that was proposed by de Gennes is a simple example and visual molecular dynamics in the presence of fixed obstacles, where the transverse motion is strongly limited by the contour of the tube. The main purpose of reptation theory is the evaluation of the interdiffusion that occurs at the interface of the two molten polymers that are put in contact. Here, the ends of the macromolecules are activated by the high local temperature and they can cross the interface and create a reciprocal link.

Graessley, on the base of the works of De Gennes, Edwards and Doi, proposed a self-diffusion coefficient that is based on the viscoelastic parameters of the polymer that participate to the healing [27].

The self-diffusion coefficient is described by the following equation:

$$D = \frac{G_N^0}{135} \left(\frac{\rho RT}{G_N^0} \right)^2 \left(\frac{\langle r^2 \rangle}{M_w} \right) \frac{M_c(T)}{M_w^2 \eta_{0,M_c(T)}} \quad \text{Equation 2.5}$$

where G_N^0 is the plateau modulus, ρ is the density of the polymer, R the universal gas constant, T is the absolute temperature, $\langle r^2 \rangle$ is mean square end-to-end distance of the macromolecules, M_w the molecular weight, $M_c(T)$ is the critical molecular weight at the temperature T and $\eta_{0,M_c(T)}$ is the zero shear viscosity at the critical molecular weight at the temperature T .

The plateau modulus G_n^0 for amorphous material can be obtained from dynamic rheology measurement and several methods are available in literature for the determination of such value as is largely discussed and highlighted in the work of Liu et al. [28]. Generally, the evaluation of the plateau modulus for amorphous material is easier than for semi-crystalline material. In Equation 2.6 is described a crossover modulus-based model for the indirect calculating of the plateau modulus of semi-crystalline material that is valid when the polydispersity is around 2.

$$\log\left(\frac{G_N^0}{G_c}\right) = 0.380 + \frac{2.63 (\log p)}{1 + 2.45(\log p)} \quad \text{Equation 2.6}$$

Where G_c is the value of the modules at the crossover point where the storage modulus and the loss modulus are equal, and p is the polydispersity index of the polymer. Unfortunately, the model is not valid for polymers that are synthesized with polydispersity higher than two as in the case of some polyolefins (Polyethylene and Polypropylene). For this reason, several other methods that are an extension of the model for the monodisperse polymer were proposed for the evaluation of the G_N^0 . The methods are called MAX-method, MIN-method, INT-method and, as in the case of Equation 2.6, crossover modulus-based methods. The modified MAX-method for polydisperse material, which was proposed by Marvin-Oser and

was discussed in the work of Liu et al. [28], is based on an old theory that considers a shifted Rouse model for the terminal spectrum of uniform entangled space, and the agreement with other methods was defined as a mere coincidence.

$$G_N^0 = 4.83 G_{max}'' \quad \text{Equation 2.7}$$

However, the constant 4.83 in Equation 2.7 that link the plateau modulus to the maximum of the storage modulus, is not completely wrong and in some real cases a correspondence is matched. For instance, in the work of Liu et al. are summarized a huge amount of experimental values that include also some syndiotactic polypropylene, where the constant is in the range 4.69÷5.08 even if the polydispersity index is around 2, and some polyisobutylene, where the constant is in the range 5.38÷6.65 with a polydispersity index between 2.08 and 6.12.

The critical molecular weight $M_c(T)$ is correlate to the molecular weight of the entanglement M_e [29]. Where M_e is correlate to the plateau modulus G_N^0 [30]. The relations are respectively resumed in Equation 2.8 and Equation 2.9.

$$M_c(T) = 2M_e(T) \quad \text{Equation 2.8} \quad M_e(T) = \frac{\rho RT}{G_N^0} \quad \text{Equation 2.9}$$

The mean end-to-end distance of the macromolecule, as the name indicates, is the average distance between the ends of the macromolecule. Since the experimental difficulties to determine this parameter, it is common to consider a particular value available from the literature.

The self-diffusion coefficient D can be used for the calculation of the quadratic distance of diffusion of the macromolecules that participate to the healing of the interface. By comparing the quadratic distance of diffusion $\langle l^2 \rangle$, which is defined in Equation 2.11, with the mean square end-to-end distance $\langle r^2 \rangle$ it is possible to establish if the interdiffusion of the macromolecules is occurred. The complete healing indeed occurs only if the quadratic distance of diffusion is higher than the mean square end-to-end distance [31].

The work carried out in this thesis takes as reference the approach proposed by Lafranche for evaluating the effect of the interdiffusion at the polymer-polymer interface in polyamide-matrix hybrid specimens [32]. The calculation of the self-diffusion coefficient was coupled with the thermal history across the thickness, which was determined with a one-dimensional thermal simulation. The model is defined by a thermo-dependent factor and has a domain of application that is limited inferiorly by the crystallization temperature. It is not clear how they calculate the time of diffusion at the interface but they propose the following equation:

$$T_Z(t_{diff}^Z) = T_c \quad \text{Equation 2.10}$$

Where T_Z is the temperature of the median plan, t_{diff}^Z is the diffusion time at the median plan and T_c is the crystallization temperature of the polymer. Then, the quadratic distance of diffusion was calculates as [31, 32]:

$$\langle l^2 \rangle_Z = 2 \int_0^{t_{diff}^Z} D(t) dt \quad \text{Equation 2.11}$$

In this work, in order to better understand how to apply the model, the model was proposed in a new formulation. The integration of the quadratic distance of diffusion was discretized in the sum of each isothermal contribution. The temporal domain of a non-isothermal healing process was divided into n time intervals and the process in each n -th interval was considered to be isothermal at the average temperatures T^* between t_i and t_{i+1} .

$$\Delta t = (t_{i+1} - t_i) = \frac{t_{healing}}{n} \quad \text{Equation 2.12}$$

Where $t_{healing}$ indicates the time-dominium of the model.

$$\langle l^2 \rangle = 2 \sum_{t=i}^n D(T^*) (t_{i+1} - t_i) \quad \text{Equation 2.13}$$

The self-diffusion coefficient was calculated at the average temperature T^* of the n -th interval. The thermos-depend and parameters were determined for each value of temperature by applying the WLF model.

Non-isothermal healing model

The healing model used in this work for the prevision of the bonding strength of the specimens is the non-isothermal healing model proposed by Bastien and Gillespie [33]. The model was developed for characterizing the bonding strength in the joining of semi-crystalline laminate in PEEK made by using the amorphous film technique, where a thin layer of PEI is placed on both the sides of the PEEK laminate during the consolidation process. This suggests that the adhesion bonding occurred between amorphous materials. The model, which is based on the healing theory for amorphous material, has been proposed for the prediction of the strength and the toughness as a function of thermal history of a non-isothermal hot press welding.

In the model development, the temporal domain of a non-isothermal healing process was divided into n time intervals and the process in each n -th interval was considered to be isothermal at the average temperatures T^* between t_i and t_{i+1} .

$$\Delta t = (t_{i+1} - t_i) = \frac{t_{healing}}{n} \quad \text{Equation 2.14}$$

Where $t_{healing}$ indicates the time-dominium of the model. The incremental bond strength provided within each Δt was derived from the isothermal reptation theory and the intent of the model was to determine the bond strength at any instant t as the summation of the incremental. The final expression of the non-isothermal model is reported in Equation 2.15.

$$\frac{\sigma}{\sigma_{\infty}} = \frac{\chi}{\chi_{\infty}} = \sum_{t=0}^{t/\Delta t} \left[\frac{t_{i+1}^{1/4} - t_i^{1/4}}{t_{rep}(T^*)^{1/4}} \right] \quad \text{Equation 2.15}$$

where $t_{rep}(T^*)^{1/4}$ is the reptation time referred to the average temperature of the n -th time intervals.

Consideration about the model

In the work of Yang and Pitchumani [34], the model proposed by Bastien and Gillespie and the subsequent improvement proposed by Sonmez and Hand [35], which was optimized for the tape placement technique of semi-crystalline materials, were critically discussed. In particular, it was highlight how the model was unsuitable for non-isothermal process especially of high molecular weight polymer, as the high performance semi-crystalline materials are. A new model suitable for the non-isothermal processing of semi-crystalline materials was proposed. The process welding time, which is lower than the reptation time, was considered long enough to get the maximum welding resistance and was assumed as reference value. In the same study, the three models were compared in predicting of the welding strength in hot press welding process in non-isothermal heating and cooling cycle. The result highlight that the time to reach the maximum degree of healing is shorter in the cooling phase and that all the models predict the same trend. However, the Bastien and Gillespie model predicts a longer time to get the maximum degree of healing in the heating cycle and the opposite happens in the cooling cycle, with a prevision of a shorter welding time.

However, they conclude that in the first stage of the non-isothermal process, below the 30% of the complete healing, all the models are comparable in predicting the healing development. Otherwise, at the end of the reference process time of 500 seconds for the non-isothermal cooling cycle, from 400°C to 340°C of a PEEK specimen, the Bastien and Gillespie's model overestimate the degree of healing up to the 25% (0.7 compared to 0.56).

The objective of the thesis is to take advantage of the simplicity of the Bastien and Gillespie's model for predicting the welding strength at the interface of full-polypropylene T-joint. The model was applied in the highly non-isothermal process of injection overmolding where the process temperatures are strongly higher than the crystallization and the melting temperatures. The general assumption and the procedure are summarized in the paragraph 2.3.1 where the characterization of the materials is presented and in paragraph 2.5 dedicated to the scheduling of the experiments.

The non-isothermal model for the self-diffusion calculation and for the prevision of the welding strength was applied on the time-temperature history of the interface in the injection overmolding process.

To this aim, the simulation of the process performed in a CAE environment allows to evaluate the time-temperature interval for the application of the model. Since domain of the models is lower-bounded by the crystallization temperature or by the glass transition temperature, respectively if the material is semi-crystalline or amorphous, the simulation allows determining the dominium of the time. The interval of application considered in this work, thanks to the design of the specimens, starts at the end of the filling phase and end when the interface temperature reach the crystallization value.

Correlation between the quadratic distance of diffusion and the healing model

Thanks to the following equation [36]:

$$R_g^2 = \frac{1}{6} \langle r^2 \rangle \quad \text{Equation 2.16}$$

It is possible to relate the quadratic distance of diffusion $\langle l^2 \rangle$, which is expresses in Equation 2.17 as a function of the self-diffusion coefficient D , to the distance of diffusion χ , which allows the calculation of the welding strength in Equation 2.19.

$$\langle l^2 \rangle = 2 \sum_{t=i}^n D(T^*) (t_{i+1} - t_i) \quad \text{Equation 2.17}$$

$$D = \frac{G_N^0}{135} \left(\frac{\rho RT}{G_N^0} \right)^2 \left(\frac{\langle r^2 \rangle}{M_w} \right) \frac{M_c(T)}{M_w^2 \eta_{0,M_c(T)}} \quad \text{Equation 2.18}$$

$$\frac{\sigma}{\sigma_\infty} = \frac{\chi}{\chi_\infty} = \sum_{t=0}^{t/\Delta t} \left[\frac{t_{i+1}^{1/4} - t_i^{1/4}}{t_{rep}(T^*)^{1/4}} \right] \quad \text{Equation 2.19}$$

Where χ_∞ is equal to radius of gyration R_g .

The two model are not directly likable but the relation in Equation 2.16 is helpful for providing a general overview about the macromolecular movement across the interface by following two different approaches.

2.2 Finite Elements Analysis

In order to full-fill the needs of data for the validation of the models and for the evaluation of experimental data that are difficult to be evaluate, several FEA environment are use.

The CAE software Autodesk Moldflow was involved in predicting the interface temperature in the overmolding of full-polypropylene T-joint specimens and the average volumetric shrinkage in the full-composite ones. The FEA software Autodesk Simulation Mechanical was used to have a general idea about the residual stress induced at the interface by the injection molding phase. Ansys APDL was finally used in order to apply the Cohesive Zone Modeling (CZM) approach in defining the cohesive zone material that fit the experimental behavior of the hybrid composite T-joint specimens.

Autodesk Moldflow environment

The simulation of the injection overmolding process where performed in order to acquire the time-temperature history on the nodes at the welding area. The analysis sequence that was used is the *Cool(FEM)+Fill+Pack*. Moldflow offers two different temperature output that are the result from the *cool* and the *flow* analysis respectively. The main differences from the two output are due to the boundary conditions that are used in the two phases.

In the case of the *cool* simulation, the cavity is considered as instantaneously filled at melt temperature, and this is the starting condition for *cool* iterations. In the advanced option is possible to choose the kind of solver between the option *conduction* and *flow*. The diffencies between the two is the cooling gradient. In particular, it was highlighted that with *flow* solver the entire flow solution in the part, passes the data across the calculation of the mold temperature distribution, then takes the temperature information from the mold and recalculates the entire flow solution in the part. This process is reiterated many times over until the convergence of the results. This means more accurate results and longer calculation time. In the *flow* simulation are considered the filling effects on melt, and the changes of melt temperature due to injection process. By performing the analysis sequence *Cool(FEM)+Fill+ Pack* it is possible to have accurate results close to the case of usage of the *flow* solver.

As discussed in paragraph 2.4, the cycle time for the production of the specimen is long and the preparatory stages require time. For this reason, the mold is never in a regime condition, but in a transitory condition. The “*Temperature, part (transient):XY plot*” is the output from the *cool* analysis and the output is available only with a *Cool(FEM)* analysis that allows to consider the transitory phase. The “*Temperature:XY plot*” is the output from the *flow* analysis and its graphical representation is presented in figure 2.3 where the time-temperature history of two overlapping node at the interface that respectively belong to two different parts is shows.

The advanced option panel allows requiring the information in a specific interval of time by setting the number of steps for the process phase of interest or by specifying the time of interest at which getting the results. In the *flow* analysis, it is possible to select the *number of part heat flux time steps* between 7 and 500. For this reason, if the results are needed for a regular interval of time, it is necessary to play with number of steps. Otherwise, if there is interest exclusively in the cooling results of the first stages of the simulation, since the high gradient of cooling, it is possible to reduce the total cycle time (by reducing the holding time in the *pack* analysis) and get a regular division. Otherwise, the advanced option for the *flow* analysis, which is divided in the sub-phases *fill* and *pack*, allows two different opportunities about writing the intermediate results. After having selected the time step in the filling phase

and in the packing phase, which are done respectively by selecting the *maximum % volume to fill per time steps* between 0 and 100% and the *maximum packing time step* between 1 and 100, it is possible to select how to write the intermediate results between the options *write at specified times* and *write at constant interval*. If the resolution of the step is a sub-multiple of the time that was selected for the intermediate results, it is possible to have a regular time-temperature history and the output can be exported as text file. Because of the highlighted options, it is possible to have a high-resolution time-temperature history that describes the operability windows in which the prevision models can be applied.

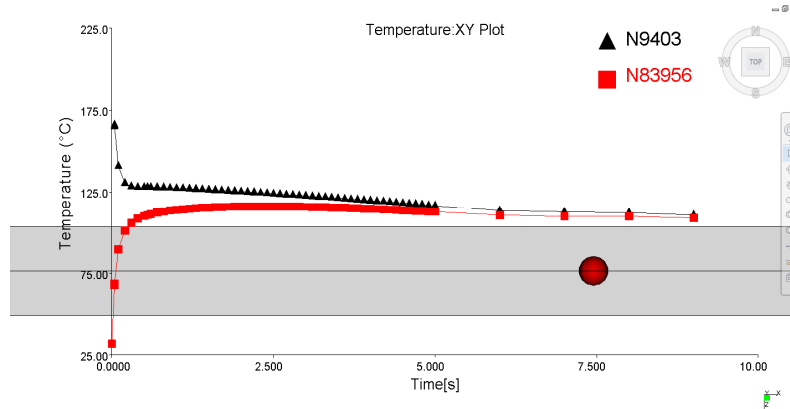


Figure 2.3 Graphic representation of the “Temperature:XY Plot” of two node at interface: the red node belong to a part insert at environmental temperature, the black one, hidden by the red node, belongs to the injected material.

Another interesting output provided by *flow analysis* is the result “*Re-melt zone part insert*” that shows areas where the insert may not have completely frozen, or has re-melted, when the second component is injected. Re-melting occurs when the first component has not cooled enough before the second component is injected, or when the melt temperature of the second component is sufficient to heat the material in the first component above its transition temperature. However, it must be highlighted that the software considers the re-melting if the temperature at the interface is over the transition temperature of the material. When semi-crystalline material are involved, the *T_{trans}* value is assumed equal to the crystallization temperature.

From the same kind of simulation, also the “*Average Volumetric Shrinkage*” was used. The output is directly use from the software Autodesk Simulation Mechanical for evaluating the residual stress induced at the joining area by the injection molding process. The average volumetric shrinkage result shows the average value of volumetric shrinkage over the half-gap thickness for 3D models. The volumetric shrinkage is the percentage increase in local density from the end of the packing phase to when the part has cooled to the ambient reference temperature (default value of 25°C).

Its calculations begin once the cavity is filled, based on the difference between the current *pVT* state and the reference state:

$$VS = \frac{\rho_{av}(t)}{\rho(T_{amb}, p_{atm})} \quad \text{Equation 2.20}$$

Where:

- *VS* is the volumetric shrinkage
- $\rho_{av}(t)$ is the average density

- $\rho(T_{amb}, p_{atm})$ is the density
- the pressure p is zero and temperature T is the specified ambient temperature

As the mass of an element changes, shrinkage continues to change with each change in the $p\nu T$ -state of the element. Once the mass stops changing, the current $p\nu T$ -state of the element is fixed in the shrinkage calculation as the reference state. The mass of an element stops changing when the cavity pressure has decayed to zero and the volumetric shrinkage becomes a constant.

Autodesk Simulation Mechanical environment

Autodesk Simulation Mechanical is a software for finite element analysis that is provided for the interoperability with Autodesk Moldflow. Thanks to the direct interface between the two software, it is possible the direct transferring of the nodal and elemental information. The interoperability was used in order to convert the volumetric shrinkage due the injection process in a residual stress distribution at the interface between the two parts.

Unfortunately, the boundary conditions that define the contact type at the interface are not customizable and it is not possible to describe the real interface condition. For the overmolding process the most realistic type of contact is “Bonded” that connects the nodes at the interface with a one-to-one correspondence. During the cooling phase, the welding can shrink and pre-tensioning takes place to maintain the continuity.

2.2.1 Structural simulation

In multi-material systems, the interfaces play an important role in the definition of the mechanical performance of a part, and very often are the weaker link in the whole structure. One of the main and frequent phenomena that occur at the interface between two materials is the phenomenon of delamination. Delamination consist is the progressive detachment of the surfaces constituting the interface itself. The study of structural failures in multi-material systems is generally carried out through the mechanical criteria of the interfacial fracture.

The use of these approaches requires the presence of an initial crack at the interface that is rarely knowable a priori. The same happens for the path of propagation of the crack that it is implicitly assumed. Sometimes these issues can be an important limitation for the application of the criterion. An alternative method to examine the delamination at the interface without the need of having to know in principle or estimate the initial crack is offered by the cohesive zone model, otherwise known as CZM.

The basic concept of the method consists in considering the mechanism of fracture as a gradual phenomenon during which the separation between the interface surfaces develops in a narrow region at the crack tip (cohesive zone) that is counteracted by the presence of forces of cohesive nature. The cohesive law, better known as traction-separation law, governs the relationship between these forces and the separation of the surfaces near the apex of the crack.

Cohesive Zone Modeling (CZM)

The CZM historical formulations have been defined by Barenblatt [37] and Dugdale [38]. The first proposed the CZM as a possible alternative to the fracture mechanics in a perfectly brittle material, while the second extended the concept also to perfectly plastic materials. The technique consists in modeling the fracture process zone (Figure 2.4):

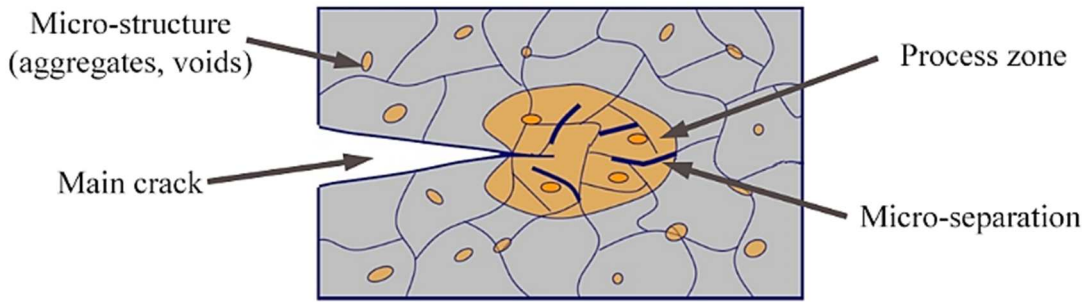


Figure 2.4 Representation of the process zone

The cohesive zone will be governed from a relationship that defines the progress of the cohesive tension with increasing separation between the virtual surfaces that surround it. More than a constitutive law, it is better referable as a phenomenological relationship. The fracture process can be interpreted as a progressive decay of the material properties as a function of the separation of these virtual surfaces. More precisely, up to a certain threshold of separation, the cohesive stress (traction) follows an increasing trend and reaches its maximum. After that, the further increase of the separation, the voltage reverses its trend and decreases towards a zero value, reaching a total debonding of the surface. It is therefore of a non-linear law which provides the progressive damage to the material. It is called cohesive law, also known as traction-separation law.

There are different types of cohesive laws and each of them has an initial portion in which the cohesive stress (cohesive traction) is growing and a separation level in which the value of the tension is maximum and then is followed by a decreasing trend indicating the damage of the material and the decay of its strength. When the value of the traction becomes a zero value, the material is no longer able to offer any resistance. The crack tip remains defined during the progressive delamination. This theory leads to a new numerical approach that can predict the nucleation of the crack in a structure without any defect and determine its evolution. In fact, the area under the traction-separation curve expresses the work of separation per unit area accomplished for opening the two virtual surfaces. It is therefore evident the link of this quantity to the fracture toughness of the material or of the interface. In the case of pure opening, the area under the curve (normal traction-separation law) represents the critical strain energy release rate in mode I opening (G_{IC}), while in the case of pure sliding, the area under the curve represent the critical strain energy release rate in mode II opening (G_{IIC}).

Bilinear and Trilinear traction separation law

During the development of CZM, they have been developed various forms of cohesive laws including polynomial, exponential, bilinear, trapezoidal and trilinear law [39]. In general, every kind of law that can describe the experimental curve of a test can be used as cohesive law.

Bilinear law

The bilinear law (or triangular law) is the first traction-separation law used in this work and deserves a more detailed description. The law was initially proposed by Geubelle and Baylor to describe the delamination in composites and it is represented in Figure 2.5, assuming that it refers to the pure mode I opening [40].

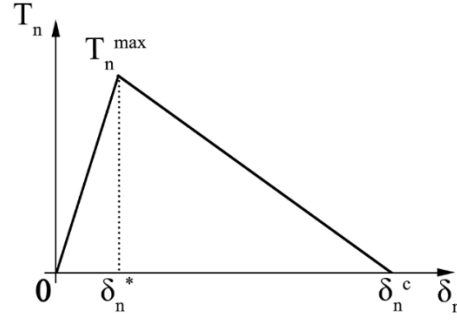


Figure 2.5 Graphical representation of the bilinear cohesive law.

The behavior is perfectly linear elastic between $\delta_n = 0$ and $\delta_n = \delta_n^*$. In this zone there is a complete reversibility of the cohesive zone.

The behavior is linear elastic between $\delta_n = 0$ and $\delta_n = \delta_n^*$. In this zone there is a total reversibility of the cohesive zone. The critical value of the stress is reached for $\delta_n = \delta_n^*$. The damage of the interface starts after this value and it is regulated by the dimensionless parameter D . The damage is zero for $\delta_n = \delta_n^*$ and equal to unity for $\delta_n = \delta_n^c$. In the range between δ_n^* and δ_n^c the damage is defined by Equation 2.21:

$$D = \left(\frac{\delta_n - \delta_n^*}{\delta_n} \right) \left(\frac{\delta_c}{\delta_n^c - \delta_n} \right) \quad \text{for } \delta_n^* < \delta_n < \delta_n^c \quad \text{Equation 2.21}$$

In the separation range, the cohesive traction can be determined by Equation 2.22:

$$T_n = \frac{T_n^{max}}{\delta_n^*} (1 - D) \delta_n \quad \text{Equation 2.22}$$

The area under the traction-separation curve expresses the unitary work of the separation that represent the *critical energy release rate* G_{IC} .

$$G_{IC} = \frac{1}{2} T_n^{max} \delta_n^c \quad \text{Equation 2.23}$$

When T_n^{max} and δ_n^c are know, the value of G_{IC} is defined. The formulation of the bilinear law is uniquely defined after defining the rate α in Equation 2.24.

$$\alpha = \frac{\delta_n^*}{\delta_n^c} \quad \text{Equation 2.24}$$

The model assume, as the subscript indicates, that the fracture is dominated by the normal separation of the interface.

T_n^{max} : maximum normal cohesive traction

δ_n^* : normal separation in correspondence for $T_n = T_n^{max}$

δ_n^c : normal separation for $D = 1$

K_n : normal cohesive stiffness ($K_n = T_n^{max} / \delta_n^*$)

α : rate between δ_n^* and δ_n^c

D_n : damage

The general correlation between the normal cohesive stress T_n and the normal separation δ_n , is expressed by Equation 2.25:

$$T_n = K_n \delta_n (1 - D_n) \quad \text{Equation 2.25}$$

The subscript n , means that the mode I (normal) is considered as dominant. The only way to create in Ansys a material that satisfies this law, is to use the APDL command TB, CZM,, BILI. This command prepares a table that must be completed by entering the parameters, through the TBDATA command, which are so defined:

$$C_1 = T_n^{max}; C_2 = \delta_n^c; C_3 = -T_t^{max}, C_4 = \delta_t^{max}, C_5 = \alpha$$

Where $-T_t^{max}$ is the maximum cohesive shear stress. The negative sign identifies that the analysis is performed in the dominant mode I. δ_t^{max} is the tangential separation in correspondence of T_t^{max} . When the mode I is dominant, the value C4 and C5 are irrelevant for the model. However they must be inserted in to the command line and using a reasonable value is sufficient to run the program without error.

Trilinear law

The trilinear cohesive law was subsequently introduced and it has proved particularly suitable to describe the behavior of polymeric materials with reinforcing fibers. The trilinear law was used especially when the propagation of the crack front was accompanied by a significant leakage of the fibers from the matrix [41-43]. The phenomenon is generally indicated as “fiber bridging”. From a simplistic point of view, the trilinear cohesive law can be seen as the sum of two bilinear laws that are merged together to form a single law as represented in Figure 2.6 and Figure 2.7. A law is associated with the breaking of the matrix, whereas the latter represent the fiber-bridging.

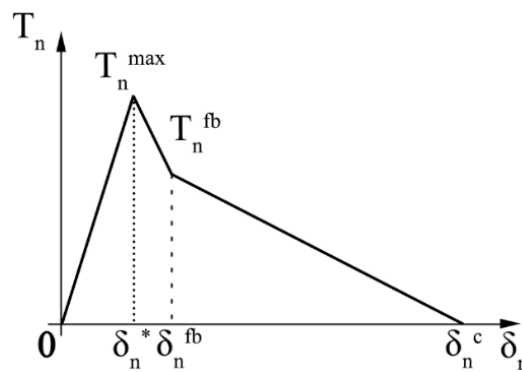


Figure 2.6 Graphical representation of the trilinear cohesive law.

The law shows many similarities with the law of bilinear type, there are in fact the maximum cohesive stress T_n^{max} , the separation δ_n^* in correspondence of T_n^{max} and the maximum separation δ_n^c in correspondence of the unitary damage. In addition there are two other parameters that are T_n^{fb} and δ_n^{fb} that identify the phenomenon of the fiber-bridging. The area under the curve is equal to the strain energy release rate G_{Ic} of the material that, as said before, can be seen as the sum of two fracture mechanisms. The two contributions are represented in Figure 2.7.

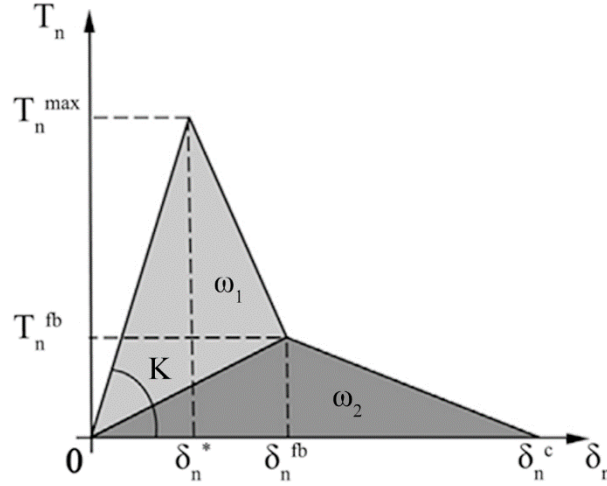


Figure 2.7 Representation of how the two laws contribute in the definition of the behavior of the trilinear law.

The figure shows that there are two components that compose the area under the curve, the ω_1 area is related to failure of the matrix, while the area is ω_2 relative to fiber bridging.

The behavior is linear elastic between $\delta_n = 0$ and $\delta_n = \delta_n^*$. In this zone there is a total reversibility of the cohesive zone. The critical value of the stress is reached for $\delta_n = \delta_n^*$. The damage of the interface starts after this value and is regulated by the dimensionless parameter D . The damage is zero for $\delta_n = \delta_n^*$ and equal to unity for $\delta_n = \delta_n^c$. In the range between δ_n^* and δ_n^c the damage is defined by two different equations: the first is valid until the beginning of the fiber-bridging:

$$D = (\delta_0 - \delta_n) \frac{\delta_n^* - \alpha_\sigma \delta_0}{\delta(\delta_0 - \delta_n^*)} \quad \text{for } \delta_n^* < \delta_n \leq \delta_n^{fb} \quad \text{Equation 2.26}$$

$$D = \frac{\delta_n(\delta_n^* - \delta_n^{fb}) - \alpha_\sigma \delta_0(\delta_n^{fb} - \delta_n)}{\delta_n(\delta_n^* - \delta_n^{fb})} \quad \text{for } \delta_n^{fb} < \delta_n \leq \delta_n^c \quad \text{Equation 2.27}$$

The Equation 2.26 and Equation 2.27 are expressed by parameter α_σ that represent the rate between the maximum cohesive stress T_n^{max} and the cohesive stress at the beginning of the fiber-bridging T_n^{fb} in correspondence of the changing of the slope of the displacement.

$$\alpha_\sigma = \frac{T_n^{fb}}{T_n^{max}} \quad \text{Equation 2.28}$$

After having evaluated the damage, the calculation of the cohesive stress can be performed applying Equation 2.29:

$$T_n = \frac{T_n^{max}}{\delta_n^*} (1 - D) \delta_n \quad \text{Equation 2.29}$$

The strain energy release rate G_{Ic} has a different formulation, but for an easier reading is omitted.

The trilinear cohesive law is not available by default in Ansys and it was necessary to build and implement the software by using some advanced option. ANSYS provides the customization of the software, using the User Programmable Feature (UPF). UPF are powerful tools and require a thorough understanding of the software and the basic math behind the theories that are considered. Through the various available UPF, it is possible to build new elements, materials, etc. There is a particular UPF called UserCZM, which allows the user to customize the cohesive law. Through the creation of a subroutine in Intel Fortran® (it is the only software that has a direct interface with ANSYS) was possible to write and use the cohesive trilinear law according to the analytical basis that was previously treated.

The subroutine that define the law is recall by the command TB control, CZM ,, USER. The software prepares a table that must be completed by entering the parameters, through the TBDATA command, which are so defined:

$$C_1 = T_n^{max}, C_2 = \delta_n^c, C_3 = -T_t^{max}, C_4 = \delta_t^{max}, C_5 = \delta_n^{max}, C_6 = \delta_n^*, C_7 = \alpha_\sigma$$

The TBDATA must be used twice because it can contain a maximum of seven parameters.

2.3 Materials and their characterization

The materials used for the experiment are selected in accordance to the industry trends. The work is aimed to the investigation of the welding strength at the interface between the two composite materials. As previously reported, the breakage moves from the interface between the matrices to the interface between the matrix and the glass-woven inside the laminate and it takes place as a delamination.

In order to define a reference optimum, it was necessary to investigate the maximum strength of a full thermoplastic specimens manufactured through injection overmolding of two homopolymer polypropylene. The chemical nature of the polymer was choose in accordance to polymeric matrix of the composite material. Since it is hard to get specific information about the material from the producer, it was decided to use two commercially available polypropylenes. The T-joint specimens was manufactured by the injection molding of a commercial polypropylene (Buplen 6331-Lukoil) on a rectangular cut-out from a commercial polypropylene sheet. Both the material were characterized from the rheological and thermal point of view.

The final hybrid T-joint specimens is made by the overmolding of a polypropylene 30%w reinforced with long glass fibers on rectangular cutout from a commercial organosheet (Tepex 104 RG600-Bond Laminates). The organosheet was mechanically characterized. Tensile test in the direction 0° , 90° , 45° were performed. In addition, Mode I opening test were performed on a series of DCB specimens obtained by two different procedure.

2.3.1 Materials and their characterization

Rheological characterization: rotational rheometer

The rheometer is constituted by two plates, one fixed and the other moving, among them is interposed the fluid. An engine allows to impose a given speed of rotation to one of the two plates and imposing a shear flow within the fluid under examination. A second device located on the other plate, the transducer, provides to measure the torque necessary to maintain the plate in motion. From the measurement of the torque, it is possible to identify the stress applied to the fluid and, from the measurement of the rotation speed, it is possible to identify the sliding gradient. These measures lead to the determination of the viscosity of the test material. The geometries of the plate that are mainly used are flat-plate (A) and cone-plate (B) (Figure 2.8).

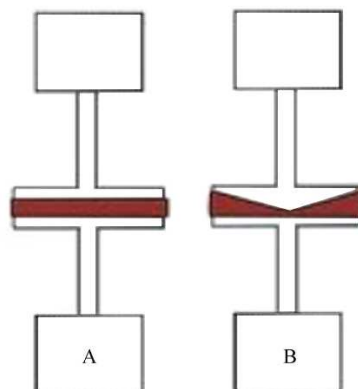


Figure 2.8 Geometries of the plate: flat-plate (A) and cone-plate (B)

The rotational rheometer used for the low shear rate behavior of the polymer is the ARES G2 configured with the cone-plate geometry (Figure 2.9).



Figure 2.9 Rotational Rheometer ARES G2

Rheological characterization: capillary rheometer

The rheometer, which is schematically represented in Figure 2.10, consists of a cylindrical chamber (4) where is placed the material to be characterized. Afterwards, it is extruded through the nozzle (3), which has cylindrical geometry with a calibrate L/D ratio, by means of the pushing force of the piston (2). The material is maintained at the test temperature thanks to a series of resistances placed around the cylindrical chamber (1). Before the inlet nozzle, it is placed a pressure sensor for measuring the pressure. The test is performed after having set the piston speed. The parameters necessary for the measurement of the viscosity depend from the geometry of the die, from the values of the pressure at the entrance of the nozzle and the force that is measured on the head of piston.

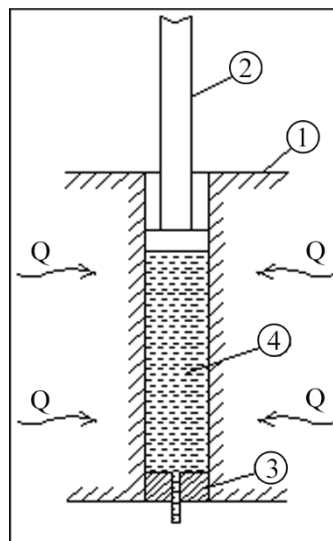


Figure 2.10 Scheme of the capillary rheometer

The measure of the force on the piston is carried by a load cell working in the range 0 to 2000 daN and that is housed on the piston head. The change in pressure between the entrance and the exit of the nozzle is measured by a pressure sensors with an adequate capacity and sensitivity. Known the geometry of the die and known the flow rate, which is determined by the advancement of the piston speed, it is possible to measure the viscosity of the fluid.

For the tests at high strain rate the capillary rheometer Rheo 2500 CEAST was used (Figure 2.11). The geometries of the die have L / D ratios of 0.5 (0.25 / 0.5) and 10 (5 / 0.5).



Figure 2.11 Rotation rheometer RHEOLOGIC 2500

The difference of pressure between the inlet and the outlet region of the capillary is given by the sum of the distributed drop of pressure along the capillary and the concentrated drop of pressure in the inlet region. The latter can be very important, and even exceed the former, especially in the case of short capillaries. The situation worsens in the case of polymeric fluids, in which the elongation viscosity can assume very high values. For these reasons, in order to determine the correct value of viscosity it is necessary to assess the inlet losses. The evaluation of the drop of pressure at inlet region can be performed by applying the Bagley's correction.

The drop of pressure ΔP through the capillary rheometer can be expressed as:

$$\Delta P_{tot} = \Delta P_{imb} + \left(\frac{\Delta P}{L}\right)_{cap} L \quad \text{Equation 2.30}$$

where $\left(\frac{\Delta P}{L}\right)_{cap}$ is the drop of pressure for unit length in the capillary.

The drops of pressure increase linearly with the length of the capillary. When the length of the capillary tends to zero, as for example in the case of efflux through a hole, it is always necessary to spend a certain amount of energy, precisely equal to the inlet losses. The Bagley correction consists in performing at each assigned speed, different measurement of pressure drop performed with capillaries of different length. Plotting the pressure loss as a function of the capillary length, the data should be interpolated by a straight line.

Extrapolating to zero length of the capillary, the ordinate at the origin is the value of ΔP_{imb} and then is possible to calculate the value of the pressure drop for unitary length $\left(\frac{\Delta P}{L}\right)_{cap}$ for every flow. Finally, the correct value of the viscosity is defined.

The Rabinowitsch correction is applied to the measured shear rate, which is called apparent, to eliminate the error.

$$\dot{\gamma}_{corr} = \dot{\gamma}_{app} \frac{3n + 1}{4n} \quad \text{Equation 2.31}$$

In the characterization of the materials considered in this work, the experimental data were interpolated with a third degree polynomial, whose the first derivative provides the flow rate value, n . The following assumptions were made:

- *the flow is incompressible, isothermal and established;*
- *the viscosity is not pressure dependent;*
- *the melt sticks to the wall.*

Rheological characterization: the Cross-WLF model

The Cross-WLF model allows to draw the complete graph of the viscosity of a material combining the values obtained by the rotational rheometer that constitute the horizontal portion of the chart, said Newtonian Plateau, to the values obtained by the capillary rheometer which constitutes the portion of oblique curve, said Shear Thinning. The Cross model allows to calculate the viscosity by means of the formula:

$$\eta = \frac{\eta_0}{1 + \left(\frac{\eta_0 \dot{\gamma}}{\tau^*}\right)^{1-n}} \quad \text{Equation 2.32}$$

where η_0 is the zero shear viscosity, $\dot{\gamma}$ is the shear rate, τ^* the critical stress and n the power law coefficient.

The Williams–Landel–Ferry model (WLF) allows to calculate the shear viscosity by:

$$\eta_0(T) = D_1 \exp \left[-\frac{A_1 (T - T^*)}{A_2 + (T - T^*)} \right] \quad \text{Equation 2.33}$$

$$A_2 = A_3 + D_3 p \quad \text{Equation 2.34}$$

Where T indicates the temperature at which the value of the viscosity must be evaluate, T^* is the reference temperature that is commonly assumed equal to the glass transition temperature T_g of the material. A_1 , A_2 , D_1 and D_3 are empirical constant, p is the pressure of the material.

For polypropylene and semicrystalline materials, the glass transition temperature is replaced by the crystallization temperature. This is because the transition temperature for this polymer is below 0°C, precisely equal to -18.58°C, and it would conflict with the Cross-WLF model. The Cross-WLF model, by definition, is valid between T_g and T_g+100 . The mobility of the chain below the crystallization temperature is almost inexistent for semicrystalline materials.

Before applying the correction and the correlation, the number of data points from the rotational (plateau) and the capillary (shear thinning) rheometers was equaled for not having the constraint of the model in any of the two directions.

Using an Excel spreadsheet, the parameters $A1$, $D1$, τ and n^* can be optimized. This is possible by minimizing the quadratic sum of the errors obtained from the difference between the value derived from the Cross model and the value of viscosity obtained experimentally by rheometers. The parameter values were determined by fitting the model with the minimization of errors on experimental values obtained at the intermediate temperature,

T=220°C. Subsequently, the model result were overlaid with the experimental values at the other temperatures, T=190°C and T=250°C, using the Cross-WLF model.

Thermal characterization: DSC

The differential scanning calorimetry, also known as DSC (Figure 2.12), is a thermal analysis technique used to measure the temperature and the heat flow associated with the transitions that occur in a sample such as the enthalpies of fusion, the glass transitions and the kinetics of crystallization of polymeric materials



Figure 2.12 Differential scanning calorimeter DQ200 (TA Instrument)

The operating principle of this technique consists in extract information on the material heating or cooling in a controlled manner. The DSC is based on the measurement of heat flow difference between the testing sample and a reference one, both subjected to a predetermined temperature variation.

Molecular weight and MFI: bibliography research

Without the instrumentation for a direct and accurate evaluation of the molecular weight such GPC (Gel permeation chromatography), a literature search was performed in order to find an indirect assessment evaluation through the experimental data that were already available. The Mark-Houwink equation was used in a first approximation for the calculation of the molecular weight [44]. The parameters in the equation can be determined by size-exclusion chromatography technique such as the gel permeation chromatography [45]:

$$\eta_0 = K M_w^a \quad \text{Equation 2.35}$$

The equation relates the zero shear viscosity to an exponential law of the average molecular weight. The constant K depend on the kind of solvent used during the test and the exponent a is related to the kind of polymer. The exponent a is generally lower than the unitary value when the molecular weight is lower than the critical molecular weight value and it is in the range 3.4÷4.2 when the molecular weight is higher than the critical value. For the polymer used in injection molding or in extrusion process, the melt flow index can change and this means a change of viscosity and of molecular weight. Since the molecular weight is defined by the polymerization process and the viscosity is a function of the temperature, the value K and a are temperature dependent too.

Thanks to the thermal characterization of the material carried to the differential scanning calorimeter, it was possible to identify the type of the polypropylene molecules under investigation on the base of the glass transition temperature. Both the materials have an isotactic configuration, which has a glass transition temperature $T_g = -20^\circ\text{C}$. For an isotactic polypropylene, the coefficient values that are available from the literature are summarized in table 2.1:

Table 2.1 Coefficient for the Mark-Houwink equation [46]

Kind of polymer	Solvent	Testing Temperature	a	K (dl/gm)
Isotactic Polypropylene	TCB	145°C	0,76	0,0000156
Isotactic Polypropylene	TCB	130°C	0,76	0,0000152

However, the calculation of the molecular weight through the Equation 2.35 provides values that are sensitive to the tested material and affected by the procedure of the test. The value of the molecular weight of the materials that were used in this work was chosen from the literature based on the data that were experimentally determined. In particular, the value of the molecular weight was chosen in literature by knowing the process for which the material is designed and after having determined the polydispersity index, which is defined by cross-over modulus G_c . The zero shear viscosity was evaluated for the temperature 190°C, 220°C and 250°C by covering the range of temperature that are the most used in the practice. All the procedure in order to determine the coefficient K and the exponent a that are valid for molecular weight higher than the critical value are explained in paragraph 2.5.1.

2.3.2 Lukoil Buplen 6331

Buplen 6331 is a homopolymer polypropylene for general purpose, for the production of home appliances, medical devices, technical products, packaging products for the food industry, rough textile and parts for the electrical industry. It is provided in granules in neutral and stabilized form.

The material was characterized using both the rotational rheometer and the capillary rheometer for the Newtonian and pseudoplastic region respectively.

The rotational rheometer was used in dynamic oscillatory mode at an imposed strain. Measurements were performed in a frequency sweep mode (0.1 to 100 s⁻¹), for temperatures between 190°C and 250°C.

The capillary rheometer was used with two different dies (L/D of 0.5 and 10) and an imposed shear rate ranged from 50 to 5000 s⁻¹. The data were fitted to the Cross model by minimizing the sum of squares between experimental and Cross points. The variables that were changed by the solver are τ^* , n . The comparison between experimental data and the model is reported in Figure 2.13.

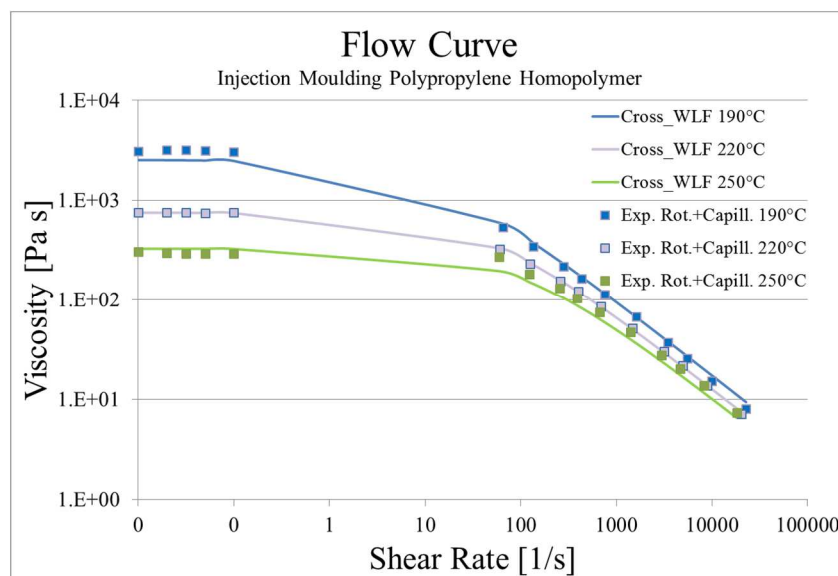


Figure 2.13 Viscosity plot - PP Buplen

The effects of temperature on viscosity was accounted by means of the William-Landel-Ferry (WLF) model. The constants of the WLF model for the tested material were determined and are resumed in Table 2.2. The fitting of the WLF model on the experimental data is shown in Figure 2.14.

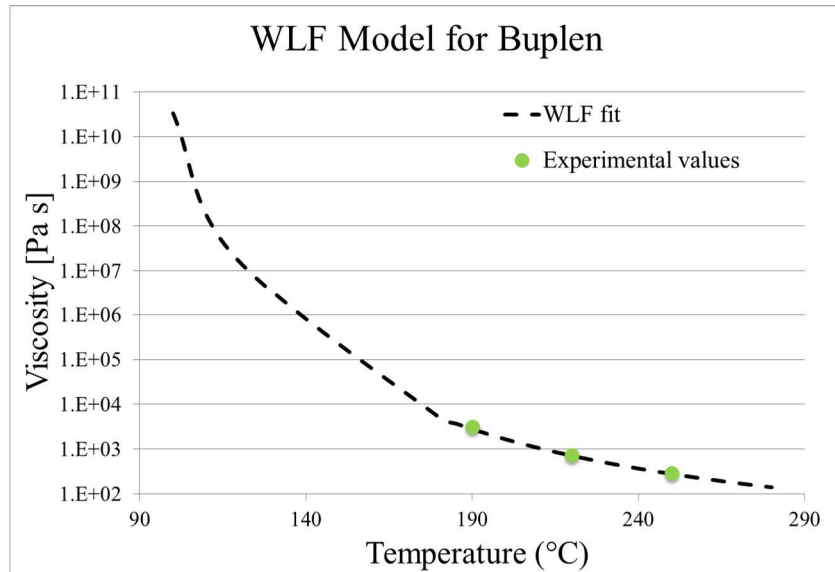


Figure 2.14 WLF model for the effect of temperature on viscosity - PP Buplen.

The melting temperature, the crystallization temperature and the glass transition temperature were determined by performing a complete heating and cooling cycle with a ramp of 10°C/min (Figure 2.15).

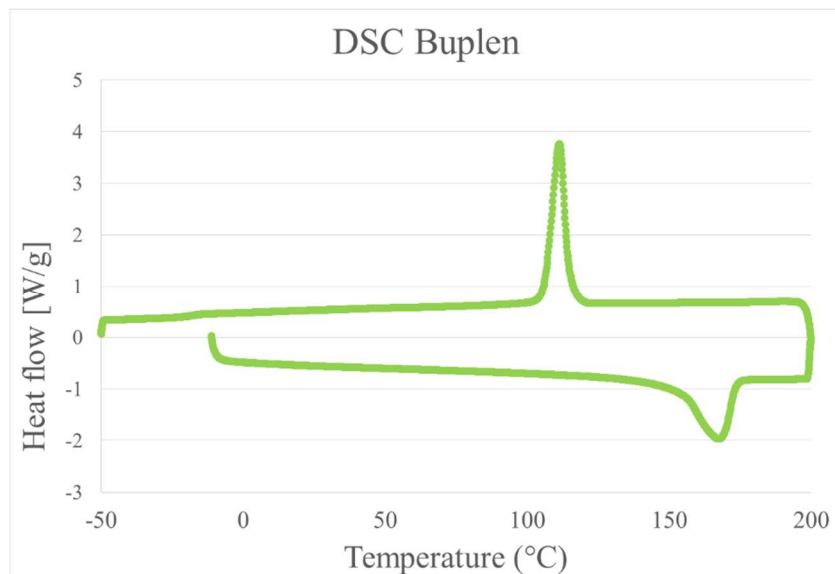


Figure 2.15 DSC ramp test - PP Buplen

The results of the characterization are summarized in in the following table (Table 2.2 and Table 2.3):

Table 2.2 Cross-WLF parameters – PP Buplen

Cross-WLF parameters	
n []	0.251
τ [Pa]	3273.59

D ₁ [Pa·s]	5.15E+07
D ₂ [K]	384.45
A ₁ []	16.41
A ₂ [K]	51.6

Table 2.3 Rheological and thermal properties – PP Buplen

Rheological and thermal properties	
Crystallization temperature (°C)	111.3
Transition temperature (°C)	-18.6
Melting temperature (°C)	167.5
Molecular weight [g/mol]	3.40E+05
MFI (T=230°C) g/10min	11.7

The characterization of the reptation time has been made using a TA Ares rotational rheometer, performing a frequency sweep test in the range 1-100 rad/s at temperatures between 190°C and 260°C with step of 10°C. The dynamic shear response was analyzed to determine the crossover frequency that, for the tested PP (Buplen) material at 220°C, is 64 rad/s and correspond to the time of 0.01 s (Equation 2.17).

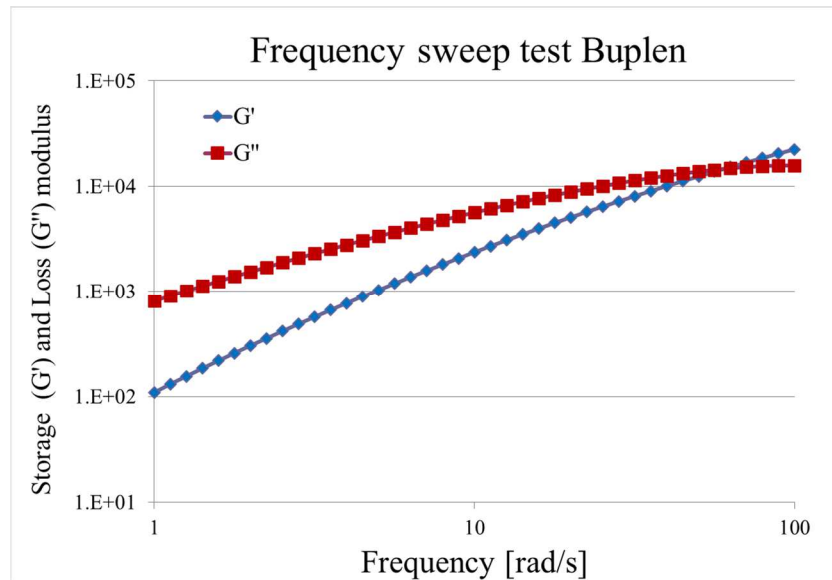


Figure 2.16 Frequency sweep test on Buplen at 220°C

The same test allowed to determine the value of the crossover modulus that is inversely related to the polydispersity index through the relation in Equation 2.36:

	$PI = \frac{100000}{G_c}$	Equation 2.36
--	---------------------------	---------------

Since it was noticed a slight dependency of the cross over modulus from the temperature, the TTS curve were created and the constants of the Arrhenius model were determined. By comparing the experimental values with the analytical values from the Arrhenius model, it was noticed that the last work well with the calculation of reptation time calculation but not for the crossover modulus. For this reason, in order to consider the increasing of the crossover modulus with the temperature, and therefore of the polydispersity index, the value

of the energy of activation was calibrated in order to reduce the sum of squared error. The value for the material Buplen are summarized in Table 2.4

Table 2.4 Constants of the Arrhenius model

Variable	Experimental value	$T_{ref} (^{\circ}C)$	E_a [J/mol]
t_{rep} [s]	0.099	220	64856 (TTS)
G_c [Pa]	12580	220	17150 (Adjusted)

2.3.3 Commercial laminate in homopolymer polypropylene

The extruded laminate is made of homopolymer polypropylene and was bought from a local supplier. Since the material was not provided with a datasheet, part of the laminate was grinded and the granules were characterized following the same procedure. The material was characterized using both the rotational rheometer and the capillary rheometer for the Newtonian and pseudoplastic region respectively.

The rotational rheometer was used in dynamic oscillatory mode at an imposed strain. Measurements were performed in a frequency sweep mode (0.1 to 100 s^{-1}), for temperatures between $190^{\circ}C$ and $250^{\circ}C$.

The capillary rheometer was used with two different dies (L/D of 0.5 and 10) and an imposed shear rate ranged from 50 to 5000 s^{-1} . The data were fitted to the Cross model by minimizing the sum of squares between experimental and Cross points. The variables that were changed by the solver are τ^* , n. The comparison between experimental data and the model is reported in Figure 2.17.

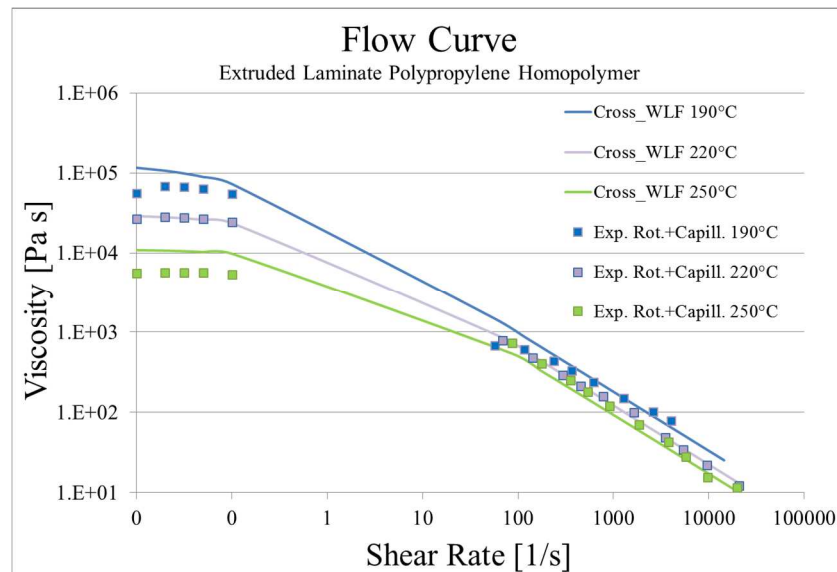


Figure 2.17 Viscosity plot – PP Extruded Laminate

The extruded material showed a very high viscosity, up to three orders of magnitude larger than the polypropylene for injection molding applications. The tests, although they were repeated several time, showed a moderate variability due to limits of the machine. In the case of the capillary rheometer, it has been required forces close to the flow rate of the machine.

The effects of temperature on viscosity was accounted by means of the William-Landel-Ferry (WLF) model. The constants of the WLF model for the tested material were determined and are resumed in Table 2.5 and the fitting of the WLF model on the experimental data is shown in Figure 2.18.

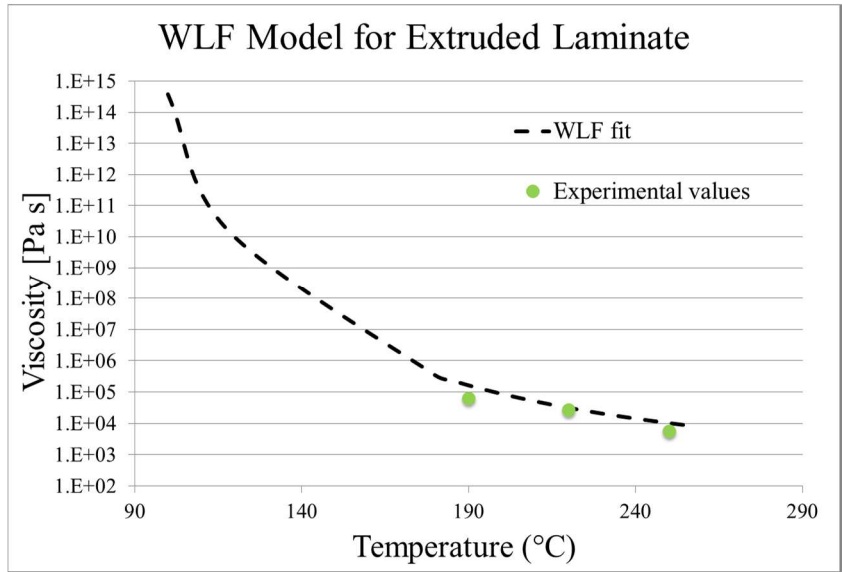


Figure 2.18 WLF model for the effect of temperature on viscosity – PP Extruded Laminate

The melting temperature, the crystallization temperature and the glass transition temperature were determined by performing a complete heating and cooling cycle with a ramp of 10°C/min (Figure 2.19).

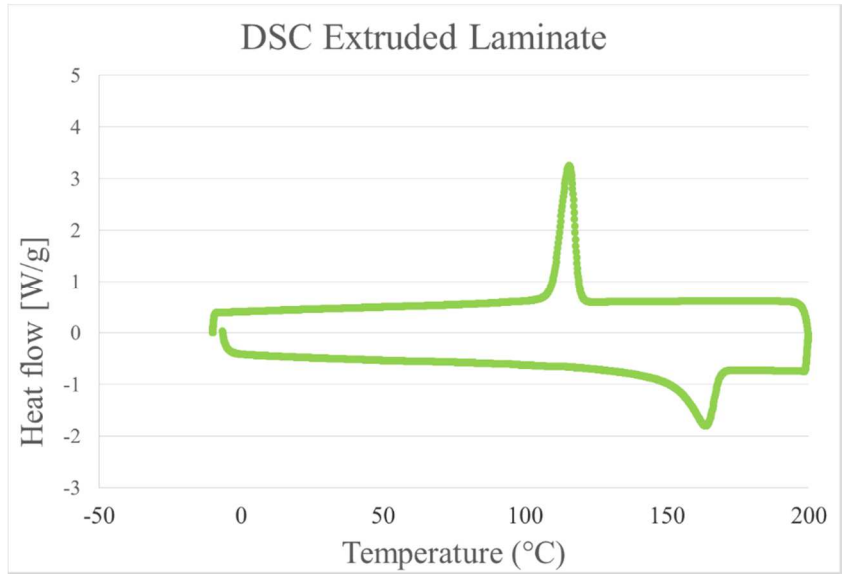


Figure 2.19 DSC ramp test – PP Extruded Laminate

The results of the characterization are summarized in the following table (Table 2.5 and Table 2.6)

Table 2.5 Cross-WLF parameters - PP Extruded Laminate

Cross-WLF parameters	
n []	0.234
τ [Pa]	18382.68
D ₁ [Pa·s]	7.21E+09
D ₂ [K]	388.75
A ₁ []	18.51
A ₂ [K]	51.6

Table 2.6 Rheological and thermal properties – PP Extruded Laminate

Extruded	
Crystallization temperature (°C)	115.6
Transition temperature (°C)	-18.6
Melting temperature (°C)	161.6
Molecular weight [g/mol]	7.40E+05
MFI (T=230°C) g/10min	0.5

2.3.4 Mechanical characterization of the organosheet

Tensile testing in the 0°, 90°, and 45° direction.

To perform the tensile test of composite laminates have been applied the guidelines of ASTM D3039 standard [48] while, to get the shear modulus, the regulations of ASTM D3518 standard [49] were applied. The standard allows to obtain the value through tensile tests on specimens with the fibers 45° oriented at 45° angle to the testing direction.

The tests were carried out on a test machine MTS 322 servo-hydraulic. This device is equipped with:

- A stationary head and a movable head
- A gripping system for the specimen able to measure and calibrate the clamping force
- A drive mechanism of the mobile head that is able to move with a controlled speed of displacement from the fixed head
- An indicator of the total force that was applied to obtain the required displacement

For all the tests, performed under displacement control, the test speed was set at 2 mm/min and the sampling frequency at 50 Hz.

For the evaluation of the shear modulus, it was considered a more appropriate formula proposed by Genta and reported in Equation 2.37 [50]:

$$G_{0-90} = \left[\frac{2 \nu_{0-90}}{E_{90}} + \frac{\left(\frac{1}{E_{\theta}} - \frac{\cos^4 \theta}{E_0} - \frac{\sin^4 \theta}{E_{90}} \right)}{\cos^2 \theta \sin^2 \theta} \right]^{-1} \quad \text{Equation 2.37}$$

For $\theta = 45^\circ$ the equation change as:

$$G_{0-90} = \left[\frac{2 \nu_{0-90}}{E_{90}} + \frac{4}{E_{\theta}} - \frac{1}{E_0} - \frac{1}{E_{90}} \right]^{-1} \quad \text{Equation 2.38}$$

The value of the Poisson coefficient, given the limited influence to the purposes of the calculation, is calculated with the general theoretical formula for fiber reinforced composites:

$$\nu = f \nu_f + (1 - f) \nu_m \quad \text{Equation 2.39}$$

where $f = 0.47$ is the percentage of the reinforcement, $\nu_f = 0.18 \div 0.30$ is the Poisson coefficient of the glass, $\nu_m = 0.45$ the Poisson coefficient of the polypropylene. The calculate value of the Poisson coefficient is $\nu = 0.32$. In the following table are summarized the values of the Elastic modulus in the three directions and the shear modulus of the organosheets.

Table 2.7 Elastic and Shear Modulus

	E 0° [MPa]	E 90° [MPa]	E 45° [MPa]	G [MPa]
RG600-104	17350	17669	5384	1505
RGUD600-104	24082	8247	5789	1649

Manufacturing and testing of DCB specimens

The reinforced composite laminates can suffer interlaminar delamination that leads to the delamination between adjacent layers. The application of the criteria of fracture mechanics to this phenomenon, as well as the use of CZM, requires the knowledge of the interlaminar fracture toughness of the composite.

The test that requires the use of the double cantilever beam specimen (DCB) is the most used for the determination of the interlaminar fracture toughness for mode I opening load (G_{IC}). Different standards that regulates this test are available but, usually, the relevant legislation in this area is given by ASTM D5528 [51], which was upgraded the last time in the year 2013. The standard is created to describe the behavior of polymer matrix composite laminates with unidirectional reinforcement but it is also used for laminates with fabric reinforcement. By working in displacement control, the reference value is the strain energy release rate (SERR) and it is indicated with G_I in Equation 2.40.

$$G_I = -\frac{1}{b} \cdot \frac{dU}{da} \quad \text{Equation 2.40}$$

The critical value at the crack propagation provides the interlaminar fracture toughness in mode I, G_{IC} .

The standard ASTM D5528 suggest three different methods for calculating of G_{IC} :

- *Modified Beam Theory (MBT)*
- *Compliance Calibration method (CC)*
- *Modified Compliance Calibration method (MCC)*

Under normal conditions, each criterion provides results similar to others. In most cases the MBT method has proved the most conservative relatively to G_{IC} values, therefore it may be preferred.

The preparation of the DCB was a quite critical part of the thesis because it was not possible to have samples that were directly manufactured by the supplier of the laminate. Moreover, the value is not provide in the commercial datasheet. It was therefore decided to carry out self-made specimens, trying to follow as closely as possible the legislation requirements and to use the resources that were available.

Initially, only 2 mm thick laminate were available. These laminates had a plain weave glass woven reinforcement (104-RG601(4)/47%). Two rectangular-strip cutouts were combined after being appropriately heated. A PTFE tape was placed between them in order to recreate the initial crack tip of length a_0 . When 4 mm thick laminate which have a twill woven fabric (104-RG600(8)/47%) were available, the crack tip was obtained by heating one side of the laminate and opening the cutout in the middle plane. After having removed the end zone, which was deformed and thermally degraded, the specimen was subjected to a preliminary test in which the crack has been propagate up to a length of 50 mm.

It is explained below and in detail the procedure followed for the production of test specimens by coupling two plain weave laminate 2 mm thick (2 mm + 2 mm) and the specimens obtained from the twill laminate 4 mm.

DCB made by coupling of two plain weave laminate 2 mm + 2 mm (104-RG601(4)/47%)

Five specimens were manufactured in accordance to the following procedure:

- *cutting of two stripes of plain wave laminate 104-RG601(4)/47% 2 mm thick and with dimensions $b=25$ mm and $L=200$ mm*
- *fastening of hinges to each stripe by bolting*
- *grinding of the countersunk head of the screws up to make them to the laminate level*
- *filing of the areas where it will placed the Teflon tape (thickness of 0.2 mm) in order to realize the slots*
- *cleaning of the surfaces with acetone*
- *positioning of the ribbon of PTFE on a line at about 50 mm from the load line a_0*
- *positioning of the lower strip template*
- *heating of the surfaces with a heat gun until the softening of the matrix*
- *overlap of the heated surfaces one on the other*
- *transfer of the specimen in a vice*
- *further heating along the edges of the specimen simultaneously to the application of clamping pressure*
- *measuring the exact length of the initial crack a_0*
- *filing the edges and subsequent painting of the same with white paint*
- *tracking of the notches along the edge to track the delamination (starting from a_0 were signed the first 5 mm at every mm, the next 20-25 mm every 5 mm: these lines allow to determine the propagation values of the fracture toughness in correspondence of precise lengths of delamination)*

Obviously, it was not sure to have accurately replicated the actual process conditions that occur during the manufacture of these laminates. The purpose of these specimens was only to have in advance an estimate, even coarser, in fracture toughness that can be expected with these materials. However, the laminate used in hybrid specimens will not be the plain weave reinforcement, but the twill one.

DCB made by opening of the 4 mm thick twill laminate (104-RG600(8)/47%)

The supply of twill laminate of 4 mm (104-RG600(8)/47%) has enabled a process of realization of the DCB specimens totally different and far more representative of the real conditions of adhesion between the layers that compose it. In fact it has been engraved a crack tip on a virgin laminate stripe without compromising the material.

Five specimens were manufactured in accordance to the following procedure:

- *cutting of a 4 mm thick laminate with dimensions $b = 25$ mm and $L = 230$ mm*
- *filing of the side edges*
- *opening of the laminate in correspondence of the semi-thickness for a length of 30 mm (The operation was accomplished by heating with a heat gun and using a sharp box cutter)*
- *fixing of the hinges on the two ends by bolting*

- manual application of an opening load in order to extend the crack over the thermally degraded area for about 35-40 mm
- cutting of the deformed and thermally degraded part (approximately 40-50 mm)
- repositioning of the hinges on the new ends of the sample by bolting. (The present crack tip allowed to open the specimen and to place, on both the sides, the short countersunk screws into the holes that were previously done on the laminate)
- tracking of the notches along the edge to track the delamination (starting from a_0 were signed the first 5 mm at every mm, the next 20-25 mm every 5 mm: these lines allow to determine the propagation values of the fracture toughness in correspondence of precise lengths of delamination)
- execution of an opening stroke in the test machine to an imposed displacement rate of 0.5 mm/min in order to extend the crack to an initial length of delamination equal to 50 mm (a_0)

The procedure required a certain manual skill, especially in the engraving of the crack exactly in the middle of the thickness between the two central layers. After the first initial attempts, a sufficient experience to perform an opening effective and repeatable was reached. They were produced and tested five samples as the standard recommends.

Testing of the DCB specimens

The tests were conducted at the UMT universal machine CETR Multi-Specimen Test System. The force sensor used has a maximum range of 1000 N

The tests were conducted under displacement control at a rate of 0.5 mm/min, as the regulation requires. The acquisition frequency was equal to 5 Hz that is a value more than adequate because of the slowness of the trial. The rate of the displacement could be increased after the first 5 mm of delamination over a_0 , but in this case it was decided to keep the rate of 0.5 mm/min until the end of the test.

The strain energy release rate G_{IC} was calculated based on the optical observation. G_{IC} was calculated in correspondence of the crack initiation and during its propagation at each defined steps (5 steps of 1 mm and subsequent step of 5 mm up to a total propagation of 25 mm). The value of each step results from the mathematical mean of the three model that are proposed by the ASTM standard: Modified Beam Theory (MBT), Compliance Calibration method (CC) and Modified Compliance Calibration method (MCC). The representative value of every single specimen is the global mean of each step. The final value of G_{IC} is the overall mean of the 5 specimens and it is summarized in Table 2.8.

Table 2.8 Average values and standard deviation of G_{IC}

DCB specimen	G_{IC} [J/m ²]	
	mean	st. dev.
2x104-RG601(4)	1214	280
1x104-RG601(8)	1062	105

Although the specimens were manufactured by following a different procedure and starting from different laminates, the experimental results led to obtain a very similar value of G_{IC} .

2.3.5 Materials used for Individualized production

The materials used for the manufacturing of hybrid T-joint specimens by the new process for individualized production have a polyamide matrix. The choice of a different family of material was due to a temporary unavailability of the 3D printer for the processing of polypropylene material.

The stems of the specimens were manufactured by selective laser sintering of PA2200 on a EOS P380 printer.

The thermoformed organosheet is a Tepex 102-RG600(4)/47% that is a polypropylene-matrix laminated reinforced with a twill glass fiber woven with a total thickness of 2 mm.

2.4 Experimental apparatus

2.4.1 T-joint specimens

The hybrid T-joint specimen is made of a 2 mm thick composite laminate base with area of 22 mm x 42 mm and an overinjected stem with area of 4 mm x 20 mm and height of 50 mm. The interface has a nominal area of 4 mm x 20 mm. The geometry is represented in Figure 2.20.

Depending on the aim of the investigation, the specimens was in full-polypropylene material or in full-composite material.

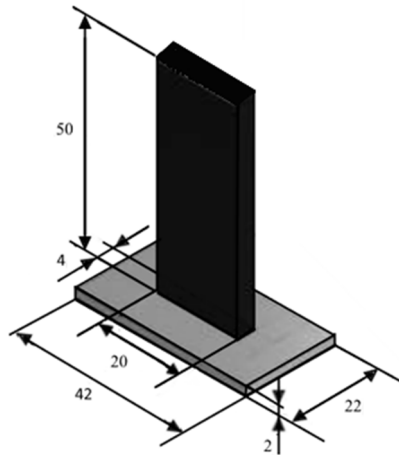


Figure 2.20 Geometry of the T-joint specimen

In the specimens used in the experimental campaign for modeling of the adhesion bonding between the matrices, the stem was made of Buplen 6331 and the base was made of a rectangular cut-out from the polypropylene laminate. In the specimens used for the mechanical evaluation of the welding strength of the hybrid joint, the stem is made of Celstran PP-GF30-0304, which is a polypropylene matrix reinforced with 30-wt% long glass fiber, that is manufactured by Celanese. The base is made of a rectangular cut-out from a Tepex Dynalite 104-RG600(4) laminate, which is a polypropylene matrix reinforced with 50-wt% glass with balanced woven fabrics, manufactured by Bond Laminate.

Finally, the production of the “functionalized” specimens, was performed with a dedicated technology on a different system. The process involve the use of stem manufactured by Selective Laser Sintering (3D printing) of PA2200, which is a polyamide 12 material manufacture by EOS and the thermoforming of a Tepex Dynalite 102-RG600(4) laminate, which is a polyamide 6 matrix reinforced with 50-wt% glass with balanced woven fabric, manufactured by Bond Laminate. At the end of the process, the base was trimmed in order to have the area of 22mm x 42 mm.

2.4.2 Injection over molding of the T-joint specimens

A two-cavity mold was designed in order to realize a T-welding joint at the end of the filling phase (Figure 2.21). The mold is provided with a transversal beam with 2 cavity slots that contain the rectangular cut-out laminates. The slots are perpendicular to the parting plane to allow the manual handling and the in-cavity positioning of the laminate after a preliminary IR heating.

In order to avoid the shear loading of the welding area during the extraction of the part, a mutual ejection system was designed. During the ejection phase, the pins push both the stems and the transversal beam allowing an easy handling of the part.

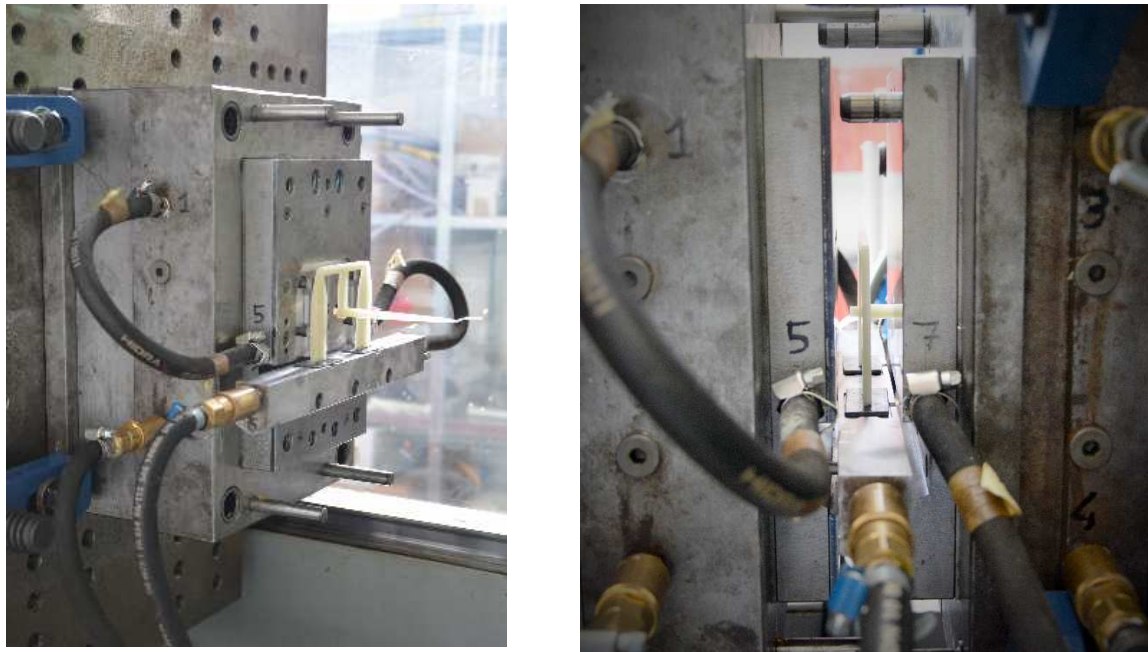


Figure 2.21 Injection mold for the manufacturing of the hybrid T-joint specimens

Three 8 mm diameter heating/cooling channels were added close to the interface area in order to provide a better heat exchange efficiency. The mold was controlled with a variothermal control unit (Wittmann Battenfeld TEMPRO plus D 180 Vario). All the samples were manufactured on a 1000 kN electrical injection molding machine (Engel E-Motion 440/100). The machine and the devices used for the manufacturing of the hybrid T-joint specimens are shown in Figure 2.22.



Figure 2.22 Machine and devices used for the manufacturing of the hybrid T-joint specimens

The heating system is mainly composed by an IR lamp (200 mm x 200 mm) manufactured by Krelus AG. The lamp was installed at the top of a tower frame with a lower grid tray wherein the laminates were placed. The heating phase was controlled by setting a combination of power heating supply, residence time and distance from the IR source of the

rectangular cutouts. In order to check the temperature of the interface an IR pyrometer (PorTerBir by Seitron) was calibrated by comparing the measurement with a type K thermocouple that was placed inside the laminate and connected to a Hasco Z251/2 thermometer (Figure 2.23). After the calibration, the emissivity was set equal of 0.94. During the heating phase of the process, the two cutouts were placed on a small tray that allows a comfortable manual handling inside the mold cavity.

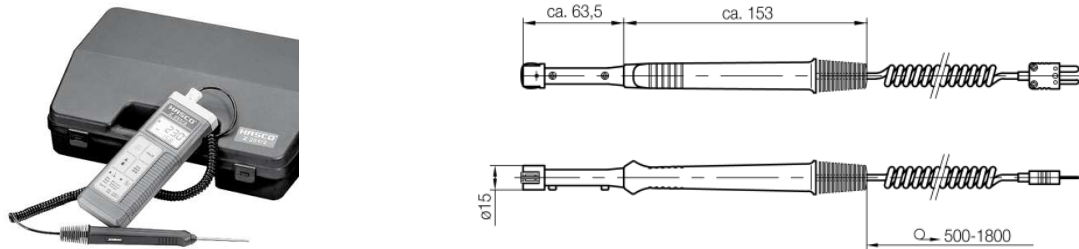


Figure 2.23 Hasco thermometer and Hasco Z2512 probe for contact measurement

Before starting the production, also the decrease of the temperature due to handling and the movement of the laminate until the filling phase was measured. The heating and the handling cycle were calibrated on single cutout. The handling of the cutout before the in-cavity placing took 20 seconds and then the temperature of the interface was measured after 10 second, which is the time necessary to close the mold before the injection phase. This checking was performed by using a probe Hasco Z2512 for contact measurement on flat surface. The procedure was repeated for each of the scheduled experiment.

2.4.3 Annealing treatment on hybrid T-joint

The post-forming annealing treatment on the hybrid T-joint specimens was performed in order to have an experimental feedback about the presence of residual stresses induced by the process. Recent studies aimed to understand the effect of the annealing treatment applied after the forming process. Kim et al [52] and Wang et al. [53] studied the effect on the annealing treatment respectively applied for the relaxation of the residual stress in Polycarbonate and Polypropylene injected molded parts.

The injection molding of polypropylene homopolymer leads to the formation of two distinct phases in the material: a more ordered α phase, in which the polymer chains have a helical form and a β -phase that is obtained if the cooling from the crystallization temperature to the solidification takes place suddenly [54]. The α -phase is the more thermodynamically stable phase and it starts to form as soon as it drops below the crystallization temperature. The helical chains are aligned to create crystals that come together in creating lamellae. Thereafter the chains grow perpendicularly to the primary structure and are arranged radially to form spherulite α . In the β -phase, the polymer chains do not have sufficient time to arrange themselves in an orderly manner. This results in a lower thermodynamic stability than in the α -phase and a lower density that have repercussions on the mechanical properties of the material. Moreover, the β -phase has lower melting temperature. Since the cooling occurs more quickly for the material that is in direct contact with the mold, it can be stated that, in the molded part, the crystallinity is not uniform. The training of β -phase on the outer surfaces there is therefore unavoidable. Since the lower melting temperature of the β -phase compared to that of α -phase, it is possible to obtain, through a suitable thermal relaxation process, a homogeneous material in which the crystallinity is entirely reordered. The heat cycle that is carried out on the specimens for the relaxation of residual stresses is aimed to the

homogenization of the β -phase without altering its crystal structure. Afterwards you want to evaluate the effect of relaxation on the mechanical properties of the material.

The studies conducted by Wang et al. [53] on the effect of annealing in polypropylene materials have shown that, while maintaining the temperature below 130°C for a time not exceeding 30 minutes, it is possible to obtain a relaxing of residual stresses. This process avoid a significantly altering of the average intensity of the crystallization and the overall morphology of the crystals (the phases remain almost unchanged). The distension in this case is to be attributed exclusively to the elimination of defects in the structure of the phase β because of the reorganization of the crystals. This process therefore does not involve the elimination of the residual stress within the material but allows its redistribution making uniformly tensioned (both in surface and in the interior of the matrix layers).

The levels of the parameters for the annealing treatment were chose according to the work of Wang et al. to allow the relaxation of crystals with imperfect space conformation avoiding any change of the crystallinity phase-distribution.



Figure 2.24 MTS environmental chamber used for the annealing treatment

The post-forming treatment was carried out in an environmental chamber MTS 65105F that is able to operate up to 350°C (Figure 2.24). The device allows to reach the target temperature in short time and to keep it constant.

2.4.4 Individualized manufacturing process (Lightflex Project)

The investigation of the potential of the “Lightflex” technology aims to determine the process parameters that maximize the welding strength in hybrid T-joint specimens made by 3D printing and thermoforming of polyamide-matrix materials. Although the process is aimed to avoid the use of molds, a supporting system for the stems was use in the preliminary phase. The supporting system was realized in aluminum and 14 slots were realized with the aim to provide flexibility with the geometry of the stems (Figure 2.25).



Figure 2.25 Supporting system for the stems with 14 slots

Changes in the geometry of the stems are possible in thickness, in width and in adding a base to increase the area of the interface. The supporting system is capable to contain stems with thickness up to 4 mm and width up to 40 mm (Figure 2.26). The modularity was possible by changing the aluminum insert on the upper part of the supporting system.

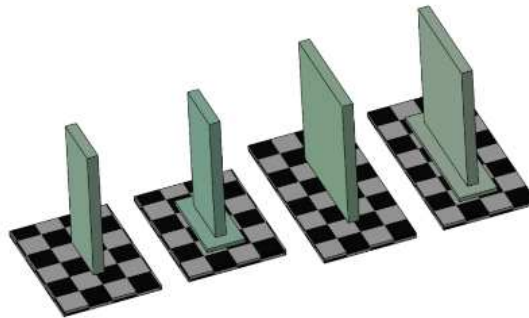


Figure 2.26 Example of the geometries of the 4 mm thick stem

The forming cycle require the heating of both the two component. The organosheet is supported by pneumatic clamps that are positioned on a rectangular frame (Figure 2.27). Before the forming, the organosheet is placed in the IR heating station where the temperature on both the sides is checked by two integrated pyrometers.

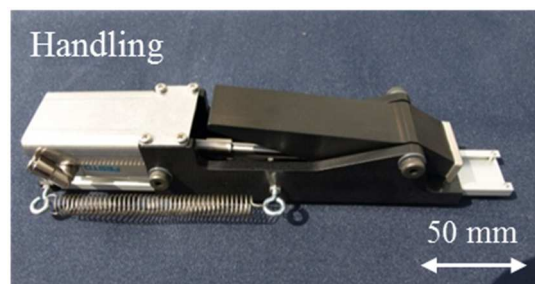


Figure 2.27 Rectangular frame with pneumatic clamps and detail of a single clamp

Whilst the heating of the organosheet can be performed in the same way as in the in mold forming process, the heating phase of the 3D printed side requires a dedicated station. To this purpose, the heating station was provided with 4 ceramic IR lamps with an area of 125

mm x 125 mm (Elstein-Werk HRS 1000W) that were controlled separately with a type K thermocouple. The power supply were back-controlled by a Hasco Z12930 power unit thank to 4 type-K thermocouples that were directly glued with water-glass on the external surface of the lamps. The heating station was closed with an aluminum box aimed to reduce the heat dispersion due to air convection. A movable front panel allows the handling of the supporting system (Figure 2.28).



Figure 2.28 Heating system for melting of the external area of the stems

The heating cycle of the interface on the stem side was calibrated and a thermocam FLIR A630 was used to check the temperature during the handling of the supporting system. The value of the emissivity was set equal to 1 because it was the only possible setting that allowed to replicate the temperature value measured by the contact probe Z5212. Since the aluminum block spread the heat quickly, the supporting system with the stems was heated for 15 minutes. Then, the time between the removals of the supporting system from the heating station to the starting of the forming process was determined as a value of 50 seconds and it was assumed as reference time. The temperature drop was monitored from the initial value of 180°C (after removing) to 140°C at the starting of the forming phase (after 50 seconds). It was found that the final temperature of the interface is close to the external value of the supporting system that is at 135°C. In Figure 2.28 are shown the temperature measured with a thermocam A-series after 10 seconds from the removal of the supporting system. The SP1 pointer indicates a local temperature of 168°C and the investigation on the area AR01 shows a maximum temperature of 175°C and a lower one of 160°C.

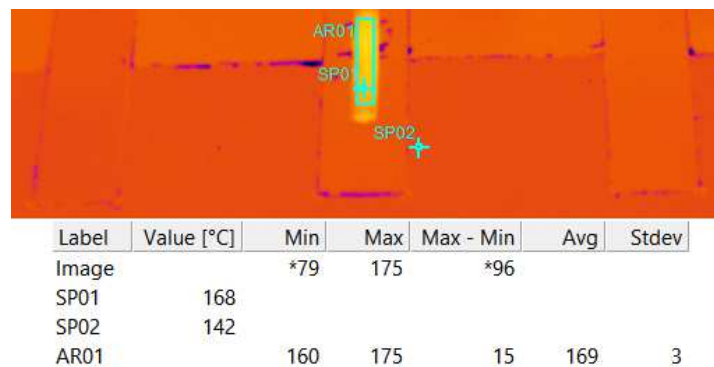


Figure 2.29 Values of the temperature on the interface of the stem after 10 seconds from the removal of the supporting system

It must be highlighted that a movable laser-heating unit will replace the heating system used for the preliminary experiments. The unit uses a modular laser grid that locally heats only the interface on the 3D printed structure. The heating flux is better controllable and the supply can be localized exclusively at the interface. As direct consequence, the heating time will be reduced and the supporting system can be directly placed on the forming station while the laser is movable. In this way, the heating cycle is faster and can ensure higher temperature at the joining interface with a direct optimization of the manufacturing process. The stems with the heated interface and the organosheet meet each other under the forming station as showed in Figure 2.30.

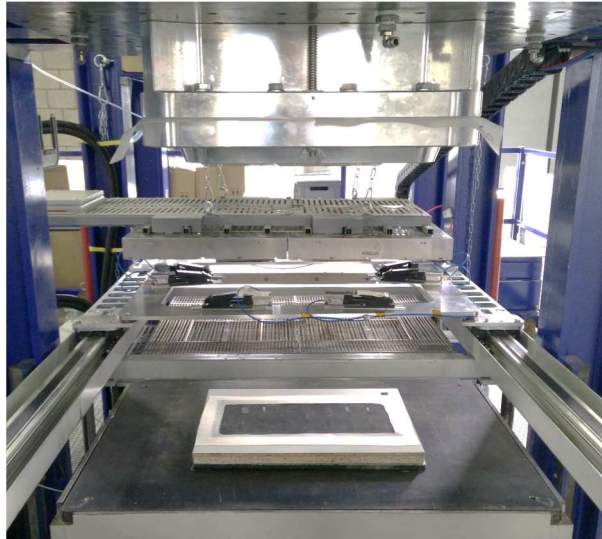


Figure 2.30 Forming station with the supporting system under the pressure chamber and IR heating station with the laminate on the rectangular frame

Here the lower plate of the press moves up to the pressure chamber. The pressure chamber frame is made of aluminum and is designed for working pressures up to 10 bar. However, the maximum pressure is limited by the cut-resistance of the silicon membrane. The silicon membrane, thanks to its deformability, is able to conform the supporting system and distribute the air pressure on the part.

2.4.5 Morphological characterization of the interface

A state-of-the-art 3D optical profiler (Sensofar Plu Neox optical profiler) was used for performing the morphological characterization of the surface on the laminate-side after the mold clamping (Figure 2.31). The instrument was used in confocal mode with 20X-magnification lens. All the interface area 4 mm x 20 mm was scanned.

The point-cloud output provided by the software was used for the reconstruction of the surface and the measurement of the area. The last step was performed in SolidWorks 3D CAD environment. By tracking a profile along the middle line in the width direction, it was possible to understand how the combined effect of the laminate temperature and the clamping phase contribute in increasing the roughness at interface. The area of the acquisition was assumed lower than the nominal area of the interface, 72.5 mm² compared to the 80 mm². This expedient ensured a quicker placement of the laminate on the table of the profiler and allowed an easier alignment of the optical with the border of the interface.



Figure 2.31 Sensofar Plu Neos Profiler and Nikon Metrology X-Tek uCT225

Moreover, a Nikon Metrology X-Tek MCT225 system was used for investigating the morphology at the real interface in four different T-joint specimens (Figure 2.31). The purpose of the investigation was the evaluation of the interface borders with a focus on the conformation of the fibers and the local macroscopic mixing of the matrices.

2.4.6 Mechanical testing of T-joint

The tensile tests of the T-specimens were performed on a universal tensile testing machine MTS 322 with a load cell of 5 kN. The basis was not clamped but it was secured using a steel plate with a central rectangular hole having sides 1 mm longer than the sides of the interface area (Figure 2.32). The lateral surfaces of the stem were free to slide without interference with the steel plate. This device allowed the stem clamping and prevented any kind of bulk loading of the sample during the closing of the clamps. Each test was displacement controlled with a rate of 0.5 mm/min and a frequency acquisition of 20 Hz. The same principle was followed for the tensile test of the “individualized” specimens, but in that case the clamping system was made of aluminum and a 1kN load cell was used.



Figure 2.32 Clamping systems for the base of the specimen that were used during the tensile test

2.5 Scheduling of the experiments

The scheduling of experiment is reported by following the chronological order. In particular, some experimental campaigns have the purpose to deep the investigation of the intermediate results.

2.5.1 Modeling the adhesion bonding in full-polypropylene T-joint specimens

Investigation of the effect of the process parameters

The process parameters effects on the ultimate tensile strength were evaluated in accordance to a design of experiments approach. More specifically, a full factorial design was selected with two parameters at two levels as scheduled in Table 2.9. The investigated parameters are injection temperature and the holding pressure. All the other process parameter were kept constant as summarized in Table 2.10. The laminate cutout was provided to the forming process after the local heating of the interface. The heating and handling cycle was calibrated in order to have a surface temperature of 130°C at the beginning of the filling phase. All the experiments were repeated 9 times and the resistance of the welding was determined through tensile tests and the ultimate tensile strength UTS was assumed as response.

Table 2.9 Investigated parameters for the manufacturing of full-polypropylene T-joint specimens

Investigated parameters (DoE)			
Levels		low	high
A	Melt temperature (°C)	220	260
B	Holding pressure [bar]	100	200

Table 2.10 Injection molding parameters for the manufacturing of full-polypropylene T-joint specimens

Injection molding parameters (Constant)	
Injection flow [cm ³ /s]	63
Back pressure [bar]	30
Holding time [s]	35
Coolant temperature (°C)	80
Cooling time (total) [s]	65
Contact time before closure [s]	5

The investigation was deepened by investigating the effect of the temperature of the polypropylene laminate. The rectangular cutouts were provided to the process at two temperature levels as summarized in Table 2.11. The lower level reflects the temperature of laminate cutouts provided to the forming process at environment temperature at the beginning of the filling phase. The value of the temperature of the laminate takes in to account of the heating provided by the mold (80°C) during the closing time. The effect of the melting temperature was considered by combining the temperature levels of the laminate with the levels to the melting temperature (220°C and 260°C). The holding pressure was kept constant at 200 bar.

Table 2.11 Temperature levels of the rectangular cutouts

Investigated parameters			
Levels		low	high
C	Insert temperature °C	32	130

Modeling of the adhesion bonding and calculation of the quadratic distance of diffusion

For both the modeling of the adhesion bonding and the calculation of the quadratic distance of diffusion it was assumed a higher mobility of the injected material (Buplen) than the extruded insert (homo-PP) because a lower molecular weight and slightly lower crystallization temperature.

To obtain a prevision of the weld strength, the Bastien and Gillespie's model was applied (Equation 2.15). Analyzing the model it is possible to define three macro parameters: strength at the theoretical maximum interdiffusion (σ_{∞}), time-temperature interval ($\Delta t = t_{i+1} - t_i$) and relaxation time (t_{rep}) evaluated at the medium temperature of the i -th interval.

The maximum theoretical strength was assumed equal to the strength of the homopolymer polypropylene. Numerical simulations of the overmolding process have been conducted in Autodesk Moldflow where the process conditions were set as simulation input and the *Cool+Fill+Pack* analysis was performed. The temperature evolution at the interface upon reaching the crystallization temperature of the matrix, which was assumed at 115°C and imposed by the crystallization temperature of the insert made of the extruded material, was estimated using the “*Temperature: XY Plot*” results (from *Flow* analysis). The output allowed to define the time-temperature interval of the contact of the molten material with the composite sheet.

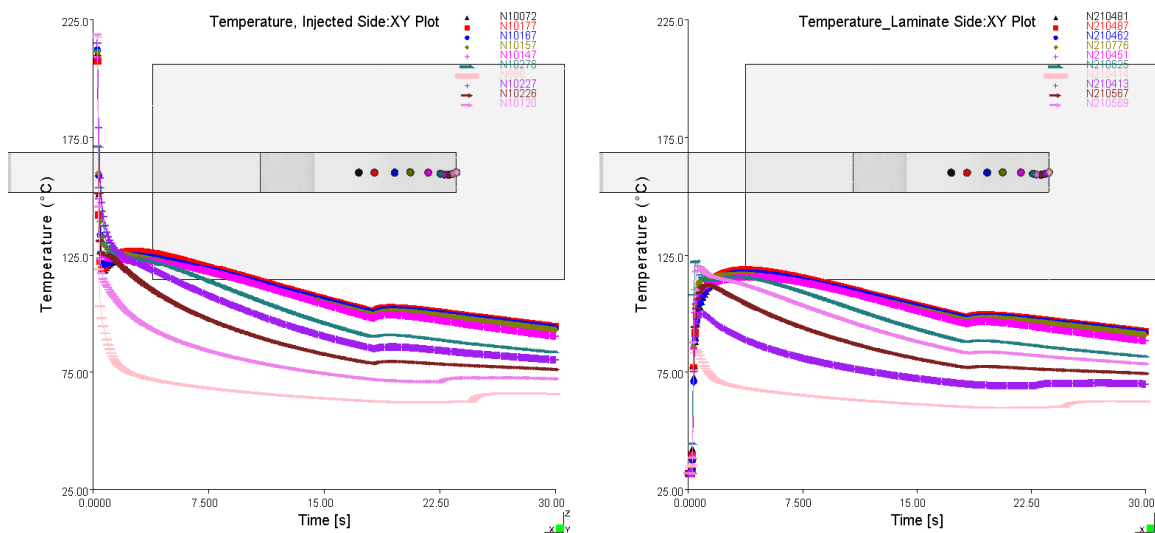


Figure 2.33 Example of output “*Temperature:XY Plot*” for the nodes on the injected part (L) and on the part insert (R)

The average value between the “*Temperature: XY Plot*” of the part and the insert was considered in accordance to the best practice for this topic as a mathematic mean. In this way, it is possible to take into account the re-melting of the interface area where the interdiffusion takes place and eventually the effect of the skin, which acts as a barrier for the interdiffusion, due to the sudden lowering of temperature for low injection speed. The time-temperature history that was used is the interface temperature and it was discretized in sub-intervals of equal duration that are characterized by an average temperature. The discretization in sub-intervals of equal duration was done by tuning the parameter of the solver under the advanced options panel. It was set a *maximum %volume to fill per timestep* of 5% and a *maximum packing time step* of 0.05 s. In order to have a good resolution, the writing of the intermediate results were set at specified time every 0.1 s on a total time of interest of 30 s. Some trials were done also for *cool* analysis and, since the high gradient in

the cooling phase, the total cycle time was set equal to 4 s with a holding time of 4 s and the *number of part heat flux time steps* was set equal to 100. This configuration allowed to obtain regular results every 0.04 s.

The relaxation time of an amorphous material is equivalent to the reptation time [32]. For a semicrystalline material, the assumption remains valid when the degree of crystallinity is approximately constant [55]. In accordance to this consideration, the crystallization temperature of the laminate was taken as the lower limit because it is higher than the one of the Buplen. The reptation time was determined by performing a frequency sweep test in the range 1-100 rad/s at temperatures between 190°C and 260°C. The main difficulties in evaluating the reptation time are evident at temperatures between the crystallization point and 190°C. In the work of Bastien and Gillespie, which was taken as reference [33], the reptation time of the amorphous material that they used was determined in the range $T_g + (20 \div 70)$ using three different methods that allow them to highlight a sudden increase of the time with decreasing temperature. In this work, the values of the relaxation time between 190°C and 260°C, in the range $T_{melt} + (25 \div 95)$, are all of the same order of magnitude. Below 190°C the test requires long time of preparation of the instrumentation and for this reason, several approach for estimate the reptation time at the average temperature of the intervals were used. First, it was created the TTS curve of the material and the relaxation time corresponding to the average temperature T^* of each interval was determined applying the Arrhenius model and then, the WLF model (both are from paragraph 2.3.2). The constants A_1 and A_2 from the rheological characterization, that are valid for a reference temperature of 111.13°C were used for determining the value of the constant D_1 , equal to 6702.4 s. Two more approaches were investigated: the first is the use of the power function in Equation 2.41 that interpolates the experimental values of the reptation temperature (from 190°C up to 260°C) considering also the value D_1 .

$$T_{rep} = 2E31 * T(^{\circ}C)^{-13.68} \quad \text{Equation 2.41}$$

The second one is an empirical method that makes the WLF shift factor miss the rheological sense. In this case, the model is forced on the experimental results by changing the value of the constant D_1 . This kind of approach needs several time-temperature histories in order to make the model work on a wide range of cases based on the reference couple of materials that are under investigation. In this study, the calibration for the last method was done on the stronger specimens that were manufactured with the process settings that maximize the interdiffusion of the macromolecules.

The comparison between the four method that are proposed and the experimental data is shown in Figure 2.34.

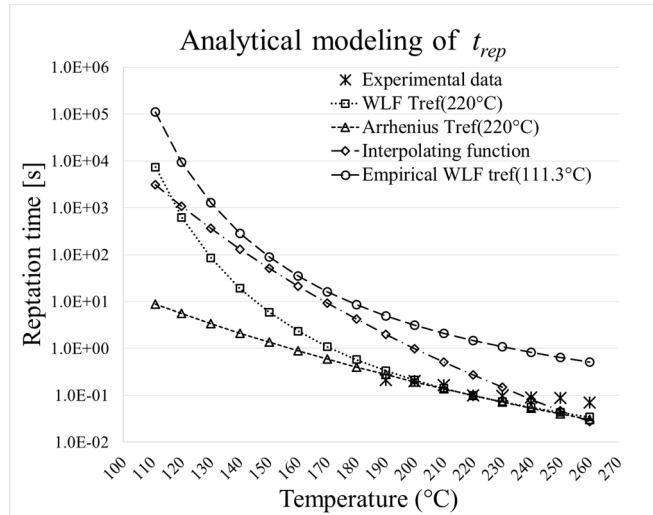


Figure 2.34 Comparison of the four model used for the analytical modeling of t_{rep} and experimental data

It is possible to see the difference in the prediction of the reptation time between 190°C and the crystallization temperature. Even if the WLF and the Arrhenius model show a good agreement in interpolating the experimental results in the range 190°C÷260°C, the Arrhenius model shows a slighter decrease of the reptation temperature with the temperature drop, otherwise, the WLF model shows a sudden increase. Differently, the empirical approach is not able to interpolate the experimental results. The sudden increase of the reptation time with decreasing temperatures provided by the WLF model and the power function agree with the trend proposed by Bastien and Gillespie [33]. However, the experimental determination of the reptation time that they proposed in [33], which was used as reference for the comparison of their previsions, is the results of the interpolation with an Arrhenius equation of three reptation-time values that were determined with three different methods. In fact they extrapolated the value from the results on lap shear specimens that were obtained by hot press welding for long time at temperature close to the transition temperature, then they evaluate the creep compliance through dynamic mechanical test at intermedium temperature and finally, they studied the dynamic shear response at higher temperature.

In this study the quadratic distance of diffusion was calculated in accordance to Equation 2.13 and the required parameter that regulate the motion of the macromolecules and define the self-diffusion coefficient in Equation 2.5 were extrapolated from the available experimental data or they were assumed from the literature and are summarized in Table 2.13 [55-58].

$$D = \frac{G_N^0}{135} \left(\frac{\rho RT}{G_N^0} \right)^2 \left(\frac{\langle r^2 \rangle}{M_w} \right) \frac{M_c(T)}{M_w^2 \eta_{0,M_c(T)}} \quad \text{Equation 2.5}$$

All the parameters that are temperature dependent were evaluated by applying the Arrhenius model. The value of the plateau modulus G_N^0 was calculated in accordance to both Equation 2.6, which is directly based on the cross-over modulus and on the polydispersity index, and Equation 2.7, which is based on the MAX-method and needs the determination of G''_{max} . Because of the difficulties in precisely determining the value of G''_{max} it was considered $G''_{max} = G_c$. The results in the frequency sweep test in Figure 2.16, show that he assumption could be done because the small discrepancy. The value of G_c , which was slightly dependant

from the temperature, was predicted using an energy of activation of 17150 J/mol with a reference temperature of 220°C (Table 2.4).

Based on the results summarized by Liu et al. [28], which were shortly reported in paragraph 2.1.2, the constant for the Equation 2.7 that link the plateau modulus to the maximum of the storage modulus, was assumed equal to 5.

Another important parameter which is not easy to be evaluated and that is strongly dependent from the kind of the material, from its rheological properties and then by the temperatures, is the zero shear viscosity at the critical molecular weight $\eta_{0,M_c(T)}$. The values was determined in accordance to Equation 2.35. The procedure that was used is aimed to the definition of the coefficient K and the exponent a that define the zero shear rate values. The procedure involve the plotting the zero shear viscosity value for every testing temperatures (190°C, 220°C and 250°C) versus the estimated molecular weight

Only the zero shear viscosity and the crossover modulus for the injection molding material (Buplen) at 220°C material was slightly tuned for obtain three parallel lines in the plot of Figure 2.35.

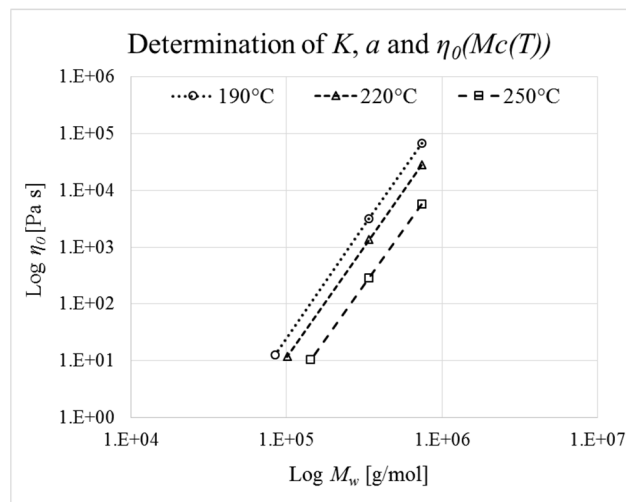


Figure 2.35 Log-Log plot of zero shear stress versus the molecular weight

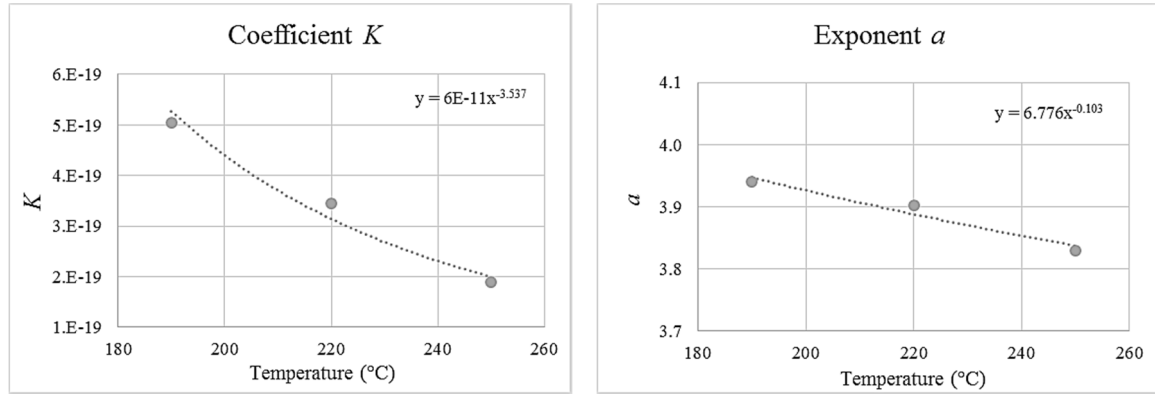
All the experimental values are resumed in Table 2.12.

Table 2.12 Experimental values of K and a

Temperature (°C)	Material	η_0	M_w	K	a
190	Buplen	3160	340000	5.05E-19	3.95
	Extruded	67700	740000		
220	Buplen	1350	340000	3.46E-19	3.90
	Extruded	28100	740000		
250	Buplen	290	340000	1.90E-19	3.83
	Extruded	5700	740000		

The last step was aimed to the definition of the functions that interpolate the values of the coefficient K and the exponent a . The three values of K and a were plotted and a power law was used to interpolate the experimental data. The plots are show in Figure 2.36

Figure 2.36 Plot and interpolation of the coefficient K and of the exponent a



And the equation are summarized by Equation 2.42 and Equation 2.43

$$K = 6.776E - 11 T(^{\circ}C)^{-3.537} \quad \text{Equation 2.42}$$

$$a = 6.776 T(^{\circ}C)^{-0.103} \quad \text{Equation 2.43}$$

Finally, the value of the mean square end-to-end distance $\langle r^2 \rangle$, which define the lower limit for having a complete self-diffusion, can be determined from a rate that is available in literature and expressed in relation to the molecular weight. The available value is the rate between mean square end-to-end distance and the average molecular weight [57]. The rate for a polypropylene is reported in Equation 2.44

$$\frac{\langle r^2 \rangle}{M_w} = 0.694 \text{ \AA}^2 \quad \text{Equation 2.44}$$

Table 2.13 Coefficient for the calculation of the quadratic distance of diffusion at 220°C (PP)

Coefficient			PP
Plateau modulus	G_N^0	[Pa]	6.30E+04
Modulus for $G'=G''=G_c$	G_c	[Pa]	1.26E+04
Polydispersity index	p	[]	7
Density	ρ	[g/mol ³]	9.00E+05
Universal gas constant	R	[J/molK]	8.314
Mean square end-to-end distance	$\langle r^2 \rangle$	[m ²]	2.34E-15
Numerical average molecular weight	M_n	[g/mol]	4.85E+04
Molecular weight	M_w	[g/mol]	3.40E+05
Critical molecular weight	M_c	[g/mol]	1.17E+05
Molecular weight of the entanglements	M_e	[g/mol]	5.86E+04

2.5.2 Welding resistance in hybrid T-joint specimens

Effect of the process parameters

The process parameters effects on the ultimate tensile strength were evaluated in accordance to a design of experiments approach. More specifically, a full factorial design was selected with three parameters at two levels as scheduled in Table 2.14. The investigated parameters are injection temperature, holding pressure and mold temperature. The mold temperature was regulated in two ways: a constant temperature was set at the lower level, whereas a

variothermal system (Wittmann-Battenfeld VARIOMOLD) was used at the upper level. The variothermal cycle was calibrated in order to heat the entire mold block and the transversal mold insert before the placing of the laminate so that the part cooling was counteracted. The thermal cycle is reported in Figure 2.37. Each experiment was replicated 7 times and the resistance of the welding was determined through tensile tests. The UTS value was assumed as response.

Table 2.14 Factors levels of the in mold forming process

Investigated parameters (DoE)		
Levels	Low	High
Melt temperature (°C)	220	260
Packing pressure [bar]	100	200
Mold temperature (°C)	80	130/80 (Vario)

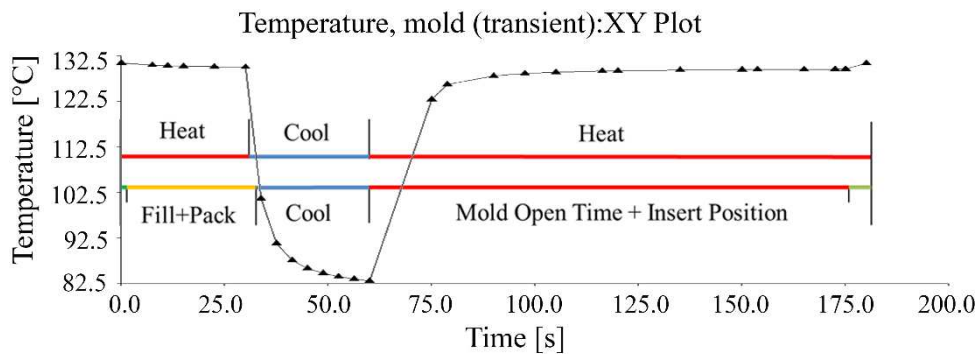


Figure 2.37 Time-Temperature plot of the injection molding cycle of the mold cavity under the laminates. The colored upper line indicates the thermoregulation phases, the lower one indicates the injection molding phases.

The laminate cutout was uniformly heated up to 220°C. The heating and the handling cycle were calibrated in order to provide the forming process with cutouts that have a surface temperature of 160°C and 150°C at the beginning of the filling phase respectively reached with a mold temperature of 130°C and 80°C. All the other process parameters, reported in Table 2.15 were kept constant.

Table 2.15 Injection molding parameters for the manufacturing of the hybrid T-joint specimens

Injection molding parameters (Constant)	
Injection flow [cm ³ /s]	63
Back pressure [bar]	30
Holding time [s]	35
Cooling time (total) [s]	65
Contact time before closure [s]	10

Evaluation of the residual stress

According to this experimental plan, each level was numerically simulated using Autodesk Moldflow. A cooling 3D analysis was set in order to consider both the variothermal cycle and the part-insert cooling after placing the insert in the mold at the heating temperature. The calculated residual stress distribution was analyzed by transferring the Moldflow results to Autodesk Simulation Mechanical environment. The contact between stem and laminate was set as bonded to guarantee a continuity between the interfacial nodes. An intermedium ANOVA was performed in order to evaluate the process parameters effect on the residual stress, which is based on the Von Mises average value on the stem-side interface, according

to Table 2.14. This approach allowed to qualitatively evaluate the effect of residual stresses on the mechanical performance of the T-joint sample.

On the basis of the first ANOVA results, the parameter level combination which provided the higher and the lower tensile strength were involved in a further analysis based in a post-forming annealing treatment. The second experimental plan is based on the annealing temperature and on the in-oven residence time. The scheduling of the treatments is summarized in Table 2.16. The treatments were first carried out on the most performant sample.

Table 2.16 Factors levels of the annealing treatment

Investigated parameters (DoE)		
Levels	Low	High
Annealing temperature (°C)	90	125
Holding time (min)	15	30

Finally, the relation between samples before and after annealing treatment was deepened following the third experimental plan, as it is resumed in Table 2.17. The annealing treatment (125°C for 30 min) was performed also on the less performant sample.

Table 2.17 Factors levels for the overall evaluation of as-molded and annealed T-samples

Investigated parameters (DoE)		
Levels	Low	High
Annealing	no	yes
Process parameters	worst	best
	(Tmelt-, Pp-, Tmold-)	(Tmelt+, Pp+, Tmold-)

Evaluation of the effect of the morphology

The conditions of the interface on the laminate side were considered in accordance to some variants of the In Mold Forming process. The newest variant of the process is completely automatized and energetically optimized. As highlighted by the name of the process, the forming of the laminate takes place inside the mold cavity. However, there are some other variants that split the two phases. If the laminate is thermoformed and fully re-compacted before the overmolding phase, it can happen that the temperature at the interface drop above the crystallization temperature and the welding strength results far from the optimum values. Moreover, if the thermoformed parts are stored before the overinjection phase, the laminate is provided to the process at environmental temperature. In this work, the effect of a local heating before the injection phase was evaluated by using a steel screen that is reported in Figure 2.38 and Figure 2.39.



Figure 2.38 Lateral view of the screen assembly

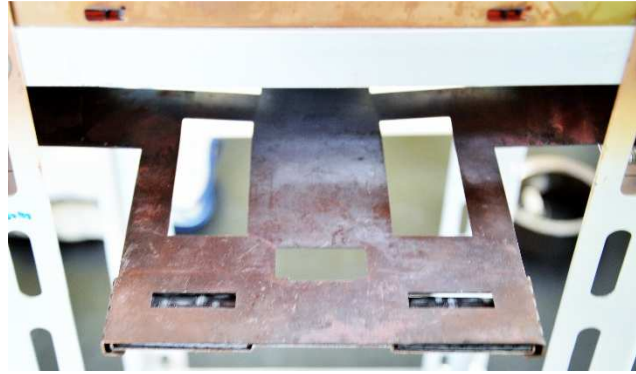


Figure 2.39 Screen for the local heating of the interface.

By using the screen, it was not possible to reach the same temperature of the uniform heating. For this reason, it was decided to run the full factorial design described at the beginning of this paragraph (Table 2.14) also for overmolding of the laminates that were locally heated.

The laminate cutout was uniformly heated up to 170°C. The heating and the handling cycle were calibrated in order to provide the forming process with cutouts that have a surface temperature of 142°C and 135°C at the beginning of the filling phase respectively reached with a mold temperature of 130°C and 80°C. Further improvement of the heating phase would be responsible of an extended heating of the interface by conduction and the aim of this investigation would be lost. Each factorial level was repeated 7 times.

In order to understand the effect of a lower temperature, a further comparison was performed by considering the laminate provided in three different conditions before the overmolding phase:

- *locally heated (135°C before the filling phase)*
- *uniformly heated (135°C before the filling phase)*
- *uniformly heated (150°C before the filling phase)*

The process setting that maximized the welding resistance in the first investigation (Melt temperature 260°C, mold temperature 80°C and holding pressure 200 bar) with the laminate provided at 150°C, were used and kept constant for manufacturing of the specimens. The resistance of the welding was determined through tensile tests and the UTS was assumed as response for comparing the effect of the morphology on the laminate side.

The investigation was deepened by evaluating the effect of the laminate condition before the filling phase. Four different conditions were investigated and each experiment was replicated 7 times.

- *As provided, without heating before the positioning*
- *After local heating and cooling down before the positioning*
- *After local heating and in cavity positioning (135°C before the filling phase)*
- *After uniform heating and in-cavity positioning (150°C before the filling phase)*

The interfaces that were investigated are obtained by stopping the cycle before the injection phase and removing the laminate from the cavity. The 4 morphology are shown in Figure 2.40.

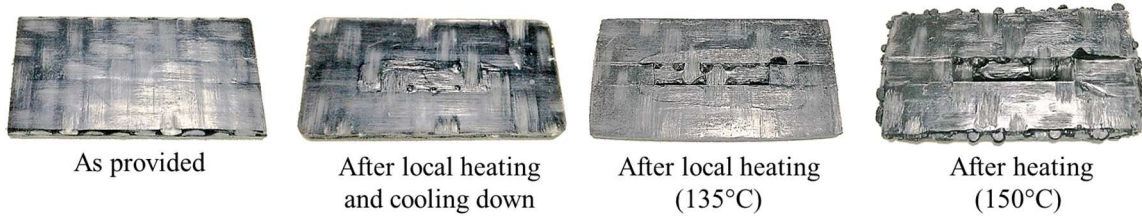


Figure 2.40 Interface morphology on the laminate side before the filling phase.

The morphological aspect of the two specimens provided at 135°C, heated by using a local screen or uniformly heated, was almost identical and for this reason is not presented.

2.5.3 Lightflex Project

Since the lack of the high heat flux at the interface and the holding pressure of the injection molding process, the pressure of the air in the forming chamber and the melting temperature of the interface were investigated and optimized. Moreover, the effect of the macro structuring of the interface was evaluate by following the principles that an extended surface for the intermediate heating phase resulted in an increased amount of melted material provided to the welding area. The general idea is schematized in Figure 2.41. The process parameters effects on the ultimate tensile strength were evaluated in accordance to a design of experiments approach. More specifically, a full factorial design was selected with two parameters at two levels as scheduled in Table 2.18. The investigated parameters are the heating temperature and the air pressure. The heating temperature was referenced to the heating time for the reason highlighted in the previous paragraph. Each experiment was replicated 7 times and the resistance of the welding was determined through tensile tests and the UTS was assumed as response

Table 2.18 Factors levels of the Lightflex production

Investigated parameters (DoE)			
Levels		low	high
A	Heating time (min)	10	15
B	Forming pressure [bar]	2.5	3.5

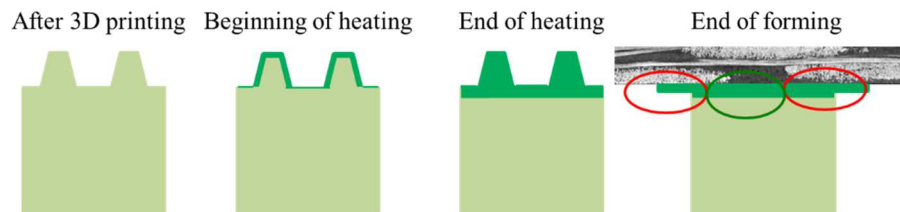


Figure 2.41 General idea that supports the use of the macrostructure for a better heating of the surface of the stem

The macro structuring of the surface was made by adding pins with a diameter of 0.5 mm. Two different kinds of structure were considered: a regular structure with constant pitch between pins that were 0.5 mm height and a mixed structure with variable pitch between pins with variable height from 0.5 mm to 1 mm. The geometries of the macrostructure are shown in Figure 2.42.

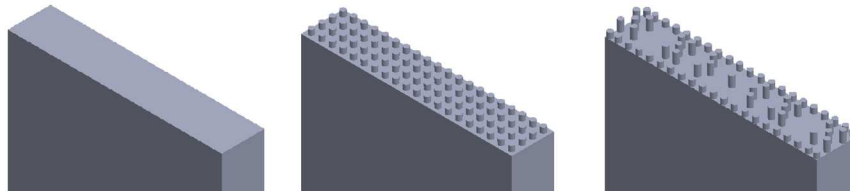


Figure 2.42 Macro structuring features at the interface: without features, with regular features and with mixed features

The timing of process cycle and the main operations are summarized in Figure 2.43. The timing highlights how the long heating time of the surface of the stems affect the cycle.

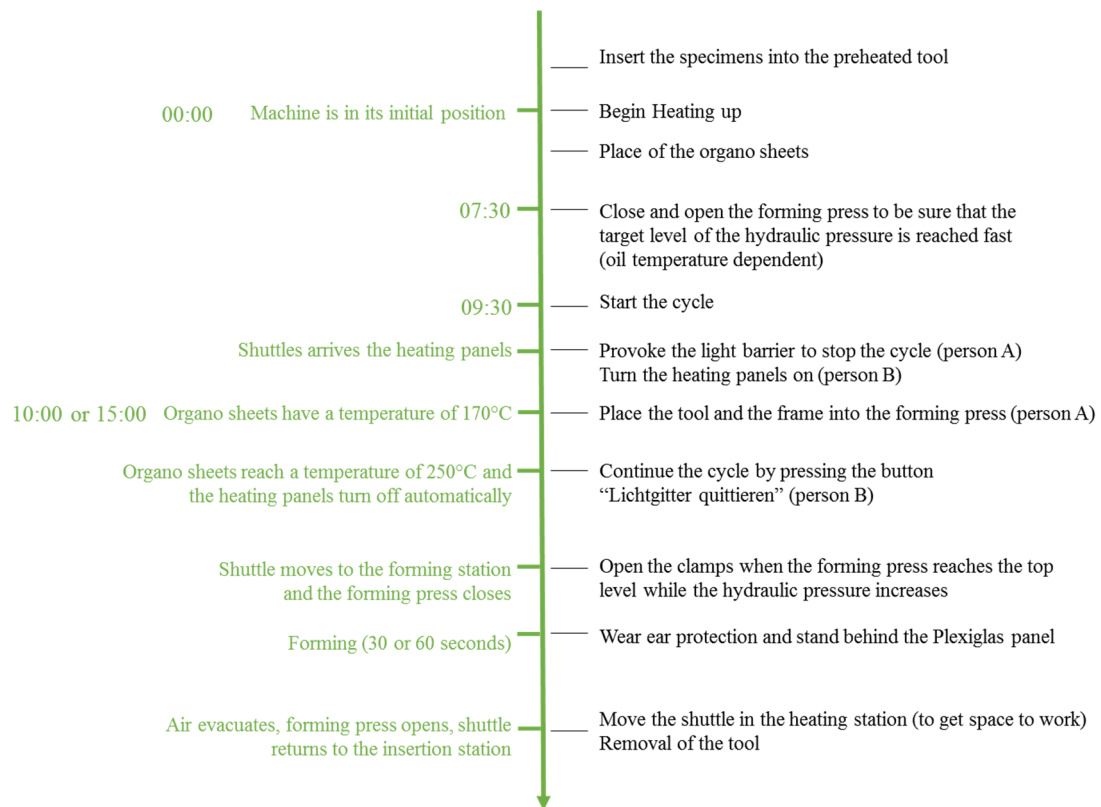


Figure 2.43 Process cycle and main operations for the forming of the T-joint specimen

2.6 Approach to the Cohesive Zone Modeling

2.6.1 The modeling in Ansys

The preliminary result of the modeling of the cohesive behavior of the T-joint are considered for the description of the approach to the simulation [59]. The software used for modeling of the behavior of the specimens is Ansys APDL. The programming phases are divided and described step by step.

Before treating the discussion, the traction-separation graph in Figure 2.44 summarizes the most critical aspect of the preliminary work.

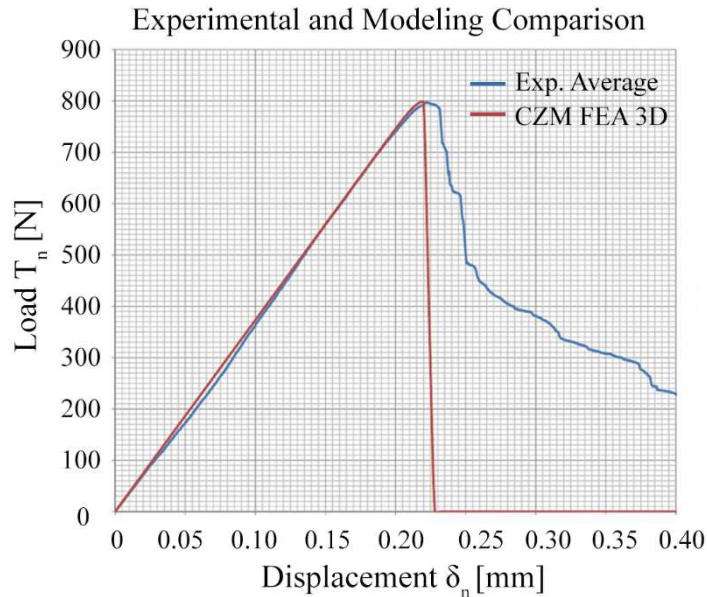


Figure 2.44 Preliminary results from the comparison of experimental and numerical data [59]

The figure shows how the model interpolates very well the elastic behavior (traction), while it is unable to obtain a good fitting during the delamination (separation) of the curve. The main reason lies in having considered the value of the strain energy release rate constant and identical to the value G_{IC} that was obtained experimentally by the opening tests performed on the DCB specimens. The final separation was then constrained to a constant value that does not allow to appreciate any increases of the energy absorbed by the specimen before the separation, which graphically is proportional to the area under the experimental curve. In the work of this thesis, the G_{IC} of the DCB specimens is neglected and the other parameters that describe the cohesive law was evaluated by a preliminary analysis that was directly performed on the experimental data. The initial analysis was performed by running a script in Matlab and then, it was refined in Ansys.

It is evident how the shape of the experimental curve has not a bilinear type trend, but it has a shape which approaches the trilinear law. Furthermore, the experimental curve was obtained by operating the average of all the experiments that were carried out. As explained in section 2.8, the behavior of the sample during the testing phase was not identical but it shown two different types. They were detected purely bilinear behavior, due to the propagation of delamination within the matrix in the case of brittle breakage, and the trilinear behavior due to the fiber-bridging. It is possible to understand that the average curve make losing the information that may be useful to appreciate the behavior of the weld in the T-joint specimens. It was necessary to modify the model created in order to recognize and divide the behavior of the interfacial fracture in the two main categories. Moreover, it was

considered important to add to the model the dispersion band, in order to consider the variability of results both in the type of behavior and in the absolute values of performance.

Definition of the geometry

The model that is now presented, thanks to the regular geometry of the profile, uses all the symmetry of the structure to allow a reduction of the computation time. The finite element analysis is performed on a quarter of the structure. The approach used consists in creating two volumes, which are then joined together by creating a mating interface. The size of the volumes involved are shown in Figure 2.45, which shows two views of the geometric model. The figure also present the constraints and the loads applied to the structure.

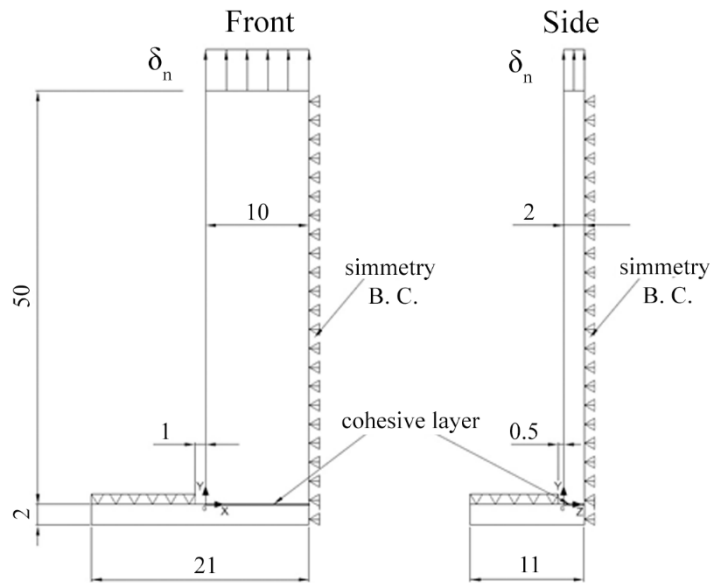


Figure 2.45 Modeling of the geometry and of the boundary conditions

Element type

The elements used in the model are of two types:

SOLID 185: they are three-dimensional elements having 8 nodes, each of which possesses three degrees of freedom, corresponding to the three available spatial offsets. The elements are used for the two volumes in the model, the base and the stem.

INTER 205: they have eight nodes. The lower four nodes are attached to the nodes of the laminate, while the upper ones are attached to the nodes of the overmolded. These elements have the opportunity to use the user-created cohesive laws. The elements are used in the interface between the two volumes.

Materials

This model involves the use of three materials which are listed below:

- A homogeneous isotropic material that was used for the over-injected stem. The properties entered into the model summarized in Table 2.19:

Table 2.19 Elastic Isotropic Material parameters for modeling of the stem

Elastic Isotropic Material Parameters: stem	
Elastic Modulus [GPa]	E = 4.2
Poisson coefficient	$\nu = 0.4$

- An orthotropic homogeneous material that was used for the base, which is the laminate. The properties entered into the model summarized in Table 2.20:

Table 2.20 Elastic Orthotropic Material parameters for modeling of the base

Elastic Orthotropic Material Parameters: base			
Elastic Modulus [GPa]	$E_x = 17.5$	$E_y = 2.5$	$E_z = 17.5$
Shear Modulus [GPa]	$G_{xy} = 2$	$G_{xz} = 1.5$	$G_{yz} = 2$
Poisson coefficient	$\nu_{xy} = 0.4$	$\nu_{xz} = 0.25$	$\nu_{yz} = 0.05$

- Cohesive material, which is invoked by the APDL command TB, CZM and where properties are defined by using the TBDATA command. As described in paragraph 2.2, by the BILI or USER options you can define the type of cohesive law that you want to use: the BILI command for the bilinear behavior, and the USER command to the trilinear behavior. The parameters that define the cohesive law, which have been preliminarily determined by the script in Matlab, are then refined to get the best model possible as long as the output results do not fit the experimental behavior.

Meshing

The model uses a three-dimensional mesh and the meshing option mapped was used. The interface was discretized in order to have a higher resolution in correspondence with the short side of the interface that has been divided in 80 parts. The elements that constitute the interface elements have size $\Delta x = 0.25$ mm (long side), $\Delta z = 0.05$ mm (short side) and Δy (height) resulting from an equal discretization of the thickness of the laminate (2 mm) in 4 parts. The other volumes possess elements of equal size along the common sides and a dimensions that is multiple of these along the direction orthogonal the interface. The mapped mode helps to get a homogeneous and regular mesh and allows to meet the desired geometry at the interface.

Loads and Constrains

With reference to the Figure 2.45, the top of the laminate floor has been constrained in every node along the Y direction. 1 mm along the x-direction and 0.5 mm along the z-direction, that represent the free space given by the metal plate of the supporting that was used during the tensile test, were excluded from the selection of the frame. Each node which lies on the plane of symmetry at $x = 10$ mm was bound with the appropriate symmetry constraint ($u_x=0$), as well as for each node of the second plane of symmetry at $z = 2$ mm ($u_z = 0$) in accordance to their symmetry condition. For the nodes of the upper surface of the stem it has been applied an imposed displacement (δ_n) $u = 0.4$ mm.

Solution

Inherently to the control of the solution, it is kept active the option of large deflection effects as well as recommended by the Ansys® manual for the execution of non-linear analysis. The number of substep used was equal to 40. The increased load is evaluated for each substep, corresponding to a movement of 0.01 mm, while the management phase of the numerical results is evaluated at each substep of the sum of the reaction forces of the individual nodes to which was applied the imposed displacement. Such amount, multiplied by 4, provides the overall strength of the complete structure rat any instant. This operation repeated for each interval allows obtaining the traction-separation law. The iterative algorithm recommended and used for the resolution of non-linear analysis is the method of Newton-Raphson

Post processing

In order to compare the results from the simulation to the experimental data, the normal cohesive stress, the tangential cohesive stress, the normal separation and the tangential separation were expressly request.

2.6.2 Sensitivity analysis

Through the sensitivity analysis it is possible to derive the parameters that describe the behavior of the sample, and which define the geometry of the cohesive law. The sensitivity analysis was performed with the help of a script in Matlab, which was specifically written for this purpose. By performing this procedure, is possible to operate without the dependencies from the G_{IC} value during the modeling phase. Later, the G_{IC} value obtained from the DCB specimens is used to discuss the results of the model by making assessments on the effects of the process parameters and on the morphological conditions of the interface. Following, it is presented the principle of operation of the script.

Factors defined by the sensitivity analysis

The cohesive parameters that are determined by performing the sensitivity analysis are dependent from the cohesive law that is used for modeling of the experimental results. In the case of the bilinear cohesive law that was used in Ansys, as seen from Figure 2.46, the increase in the α parameter is responsible for the decrease of the points calculated in the debonding section.

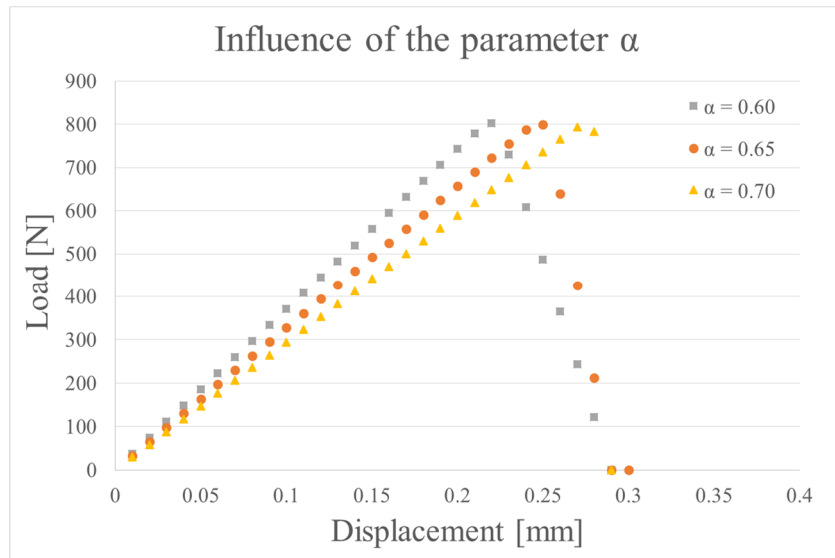


Figure 2.46 Effect of the parameter α in the bilinear law

The parameter α play an important role in accurately modeling of the separation mechanism and for this reason it is important to use values not too high. However, the phenomenon is attenuated by the value of T_n^{max} , in fact the lower the value, the smaller the influence of the parameter alpha. However, the graph shows how the software is not able to detect a delamination almost instantaneous. When this situation occurred, it was managed to approximate as best as possible the experimental behavior. The direct consequence is the obtaining of a larger value G_{IC} .

In the case of trilinear cohesive law, the parameters assessed by the sensitivity analysis, for a fixed T_n^{max} that defines the elastic range, are related to the displacement corresponding to the change of the slope due to the fiber bridging δ_n^{fb} and to the complete delamination δ_n^c . The effect of δ_n^* , δ_n^{fb} and δ_n^c are presented in Figure 2.47. The parameter δ_n^{fb} control the slope between the end of the elastic range and the beginning of the fiber bridging.

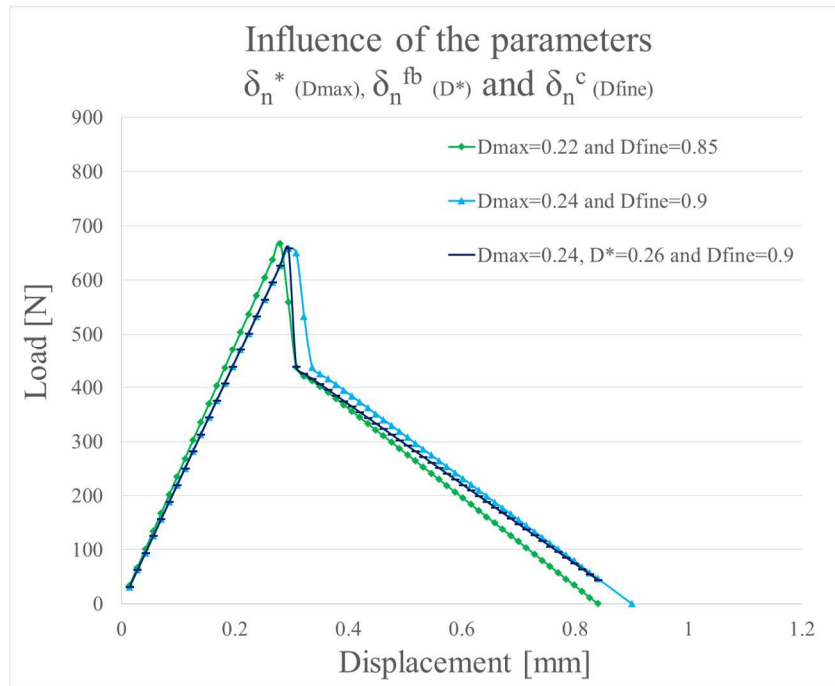


Figure 2.47 Effect of the parameters δ_n^* , δ_n^{fb} and δ_n^c in the trilinear law

Operating principle of the script in Matlab®

This cycle allows to perform the sensitivity analysis to determine each parameter that must be used in the simulation programmed and performed in Ansys APDL for the modeling of the experimental behavior. The script in Matlab provides the user with the main parameters that must be set as input in the simulation by running through the experimental points and recognizing the main changes. The first step of the cycle is to identify the initial slope of the curve. The starting value of the load is assumed equal to 100 N in order to neglect any adjustments of the specimen at the beginning of the tests. The analysis continues along the linear elastic section until it is detected the maximum value T_n^{max} in correspondence of δ_n^* . Then, the values that correspond to the critical displacement δ_n^c is assumed in correspondence on a residual traction force of 200 N.

The scrip detects the law that best describes the experimental behavior minimizing the sum of squared residual between the triggering of the break and the total damage.

The internal cycle creates a vectors that allows the assessment of the sum of the squared residual. In the case of trilinear law, the second change in slope must be evaluated and it is necessary to determine the value of T_n^{fb} , in correspondence of δ_n^{fb} , where the change of slope occurs. The T_n^{fb} value of is assumed equal to the 70%, 65%, 60%, 55% of the maximum value of the traction force T_n^{max} . After having evaluate the range in which the sum of squares is minimized, the scrip in Matlab provides the user with a text document where the basic data of the sensitivity analysis are stored and that are subsequently read by the script in Ansys.

The post-processing section of the simulation creates a text document with the numerical results and the relative plot that the user can use for assessing their quality. If the comparison of the numerical data from the simulation and the experimental result are not consistent, the user can continue the sensitivity analysis changing the input parameters for the following simulation.

2.7 Results and discussions

The results and their discussions are reported according to the chronological order of the execution of the experimental campaign, as it was reported in the paragraph 2.5.

2.7.1 Modeling the adhesion bonding in full-polypropylene T-joint specimens

Investigation of the effect of the process parameters

The analysis of variance (ANOVA) results (Table 2.21) of the screening plan on the tensile tested samples indicate that both the melt temperature and the holding pressure significantly affect the bonding resistance (Figure 2.48). However, only the melt temperature has a positive effect on the ultimate tensile strength.

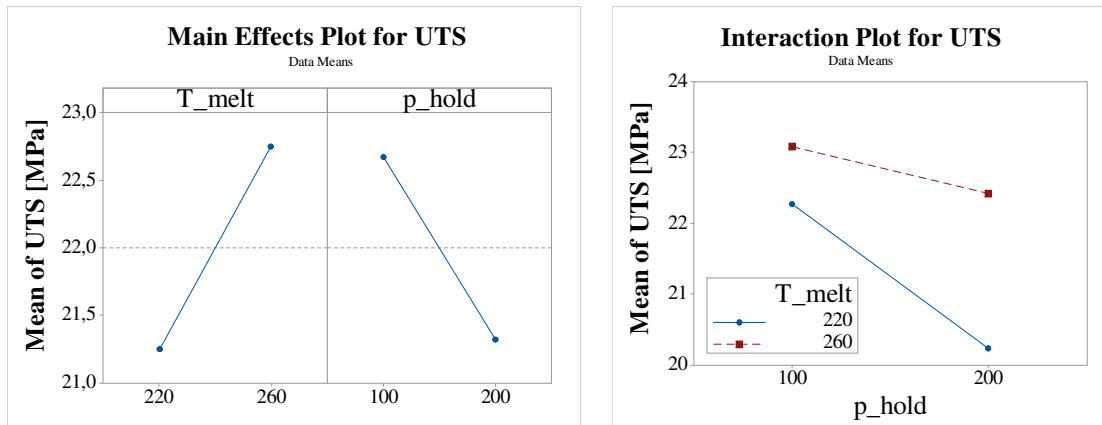


Figure 2.48 Main effects and interaction plots for melt temperature and holding pressure on the UTS of the full-polypropylene T-joint specimen

Table 2.21 Analysis of variance results for the process parameters on the UTS of full-polypropylene T-joint specimen

Factor	Sum of Square	Mean Square	F-Value	P-Value
T_melt	20.372	20.372	6.49	0.016
p_hold	16.443	16.443	5.24	0.029
T_melt*p_hold	4.277	4.277	1.36	0.252
Error	100.46	3.140		

$$\text{UTS} = 27,4 - 0,0141 \text{ T_melt} - 0,0962 \text{ p_hold} + 0,000345 \text{ T_melt*p_hold}$$

The positive effect of the melting temperature directly affects the macromolecular interdiffusion. The interface is provided with a higher amount of heat and the medium temperature at the welding area is directly increased. The negative effect of the packing pressure was unexpected since it is known that pressure contributes in increasing the degree of intimate contact [34]. However, it was supposed that the higher values of the holding pressure are responsible of a higher amount of residual stress induced by process. With a reference to the literature [18], it was observed that the positive contribution in reaching the optimal degree of intimate contact can be obtained for a certain levels of pressure and beyond this level, the holding pressure start in negatively contribute in the welding resistance. It was concluded that the temperature at the interface allow a good intimate contact for lower level of pressure. Beyond this limit, higher values of holding pressure only contribute in increasing the residual stress at the interface.

The second analysis of variance (ANOVA) results (Table 2.22) of the screening plan on the tensile tested samples indicate that both the melt temperature and the laminate temperature

significantly affect the bonding resistance. The positive contribute it is also confirmed by interaction between the two parameter. The main effects and the significant interaction are respectively resume in Figure 2.49.

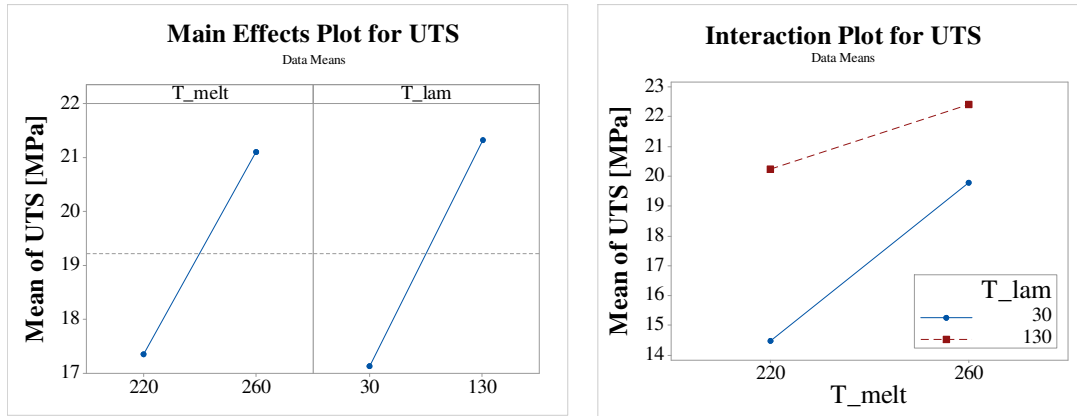


Figure 2.49 Main effects and interaction plots for melt temperature and laminate temperature on the UTS of the full-polypropylene T-joint specimen

Table 2.22 Analysis of variance results for the process parameters on the UTS of the full-polypropylene T-joint specimen

Factor	Sum of Square	Mean Square	F-Value	P-Value
T_melt	126.68	20.372	36.68	0.000
T_lam	159.53	16.443	46.19	0.000
T_melt*p_hold	21.84	4.277	1.36	0.017
Error	100.52	3.454		

UTS = -21,62 + 0,1561 T_melt + 0,2290 T_lam - 0,000779 T_melt*T_lam

The interaction plot allows to understand the principles of the macromolecular interdiffusion that is promoted by the higher temperature at interface. Considering the approximated value of the temperature at the interface

$$T_i = \frac{T_{melt} + T_{lam}}{2} \quad \text{Equation 2.45}$$

when the temperatures are at the lower level, the temperature at the interface is 125°C and increase up to the higher value of 195°C when the temperatures are at the higher level.

The quality of the welding can be macroscopically evaluate by observing the fracture surface after performing of the tensile test. In Figure 2.50, the fracture area on the left is typical of the specimens manufactured with temperature at the lower level and shows a weak and brittle welding between base and stem. However, a small portion of the laminate remained joined to the stem. The fracture area on the right is typical of the specimens manufactured with temperature at the higher level and shows a strong welding between base and stem, indeed the base is prone to follow the stem and to deform.

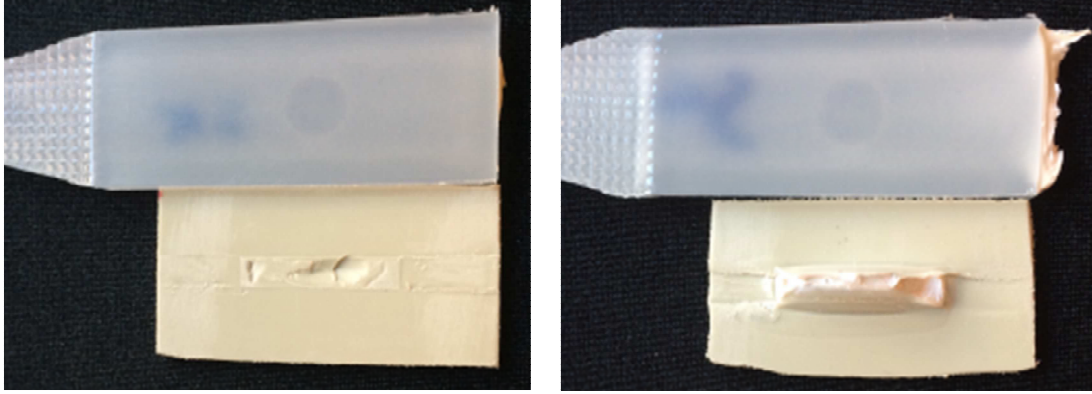


Figure 2.50 Fracture surface. Specimen manufactured with temperatures at the lower level (220°C_30°C), on the left, and specimens manufactured with temperature at the higher level (260°C_130°C), on the right.

Modeling of the adhesion bonding and calculation of the quadratic distance of diffusion

In this section are presented the results of the prevision of the strength that are obtained by applying the model proposed by Bastien and Gillespie [33] and then the calculation of the quadratic distance of diffusion in accordance to the model of Graessley [27] and applied by Lafranche et al. [32]. The interdiffusion of the injected material was considered as general condition because of the lower molecular weight.

The first approach in applying the analytical modeling proposed by Bastien and Gillespie was to evaluate the effect of the model for the calculation of the reptation time at the local temperature. The time-temperature history of the central node of the interface was used and the temperature values are lower-bounded by the crystallization temperature of the laminate (115°C). In the following graphs are reported the comparison between experimental results, analytical modeling and maximum theoretical strength. The analytical modeling in Figure 2.51 is based on the complete time-temperature history and it possible to see how none of the prevision is able to approximate the strength of the weaker specimens. This is probably due to difficulties in determining the reptation time at low temperatures as in the case where the laminate is provided at 32°C and the melt temperature is 220°C with a consequent temperature at the center point of 126°C. On the contrary, the models over predict the welding strength when the temperatures at the interface are higher for longer time. The green bars represent the analytical modeling made with the constant D_I empirically determined. This approach has the only effect to shift the modeling done with the WLF model to lower values.

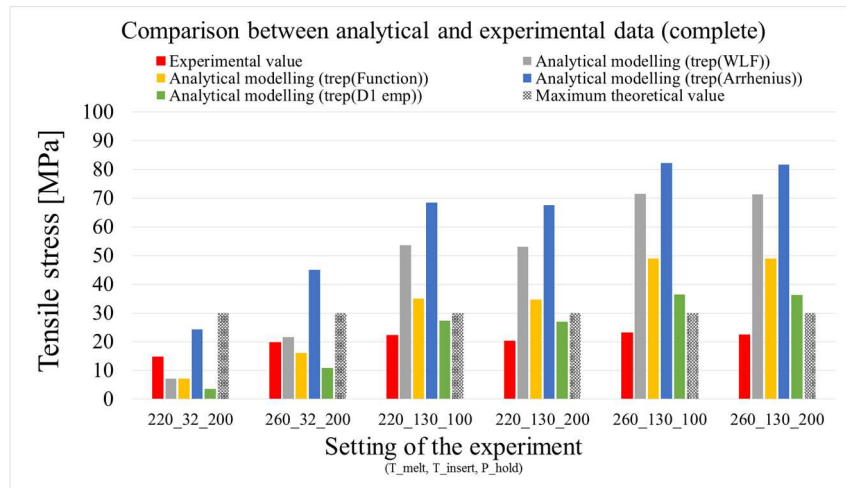


Figure 2.51 Comparison between analytical modeling on the complete thermal history that is based on four different approach and the experimental data

Table 2.23 Percent error of the four approach in modeling the welding resistance with the complete thermal history

Exp.	Exp. value	Analyt. (WLF)	% err	Analyt. (Func.)	% err	Analyt. (Arrh.)	% err	Analyt. (emp.)	% err
220_32_200	14.8	7.1	-51.8	7.1	-51.9	24.4	65.1	3.6	-75.5
260_32_200	19.8	21.5	9.0	16.1	-18.6	45.1	128.0	11.0	-44.6
220_130_100	22.3	53.6	140.5	35.0	-57.4	68.5	207.6	27.3	22.4
220_130_200	20.2	53.0	162.2	34.7	71.5	67.5	234.0	27.0	33.4
260_130_100	23.1	71.5	209.9	49.0	112.4	82.3	256.4	36.4	57.7
260_130_200	22.4	71.2	217.8	49.0	118.6	81.8	264.7	36.2	61.7

In Table 2.23 are summarized the percent error and it is clear that the previsions underestimate or overestimate the strength for low and high temperatures respectively, with the exception of the Arrhenius model that always overestimate the result. The reason of this over prediction is still related to the unsuitability of the model to predict the reptation time for temperature lower and farer from the reference value. The increase of the reptation time should decrease the contribution in the summation of the interval with low average temperature. However, it was found a strong agreement with the consideration in [33] where the hot plate welding process is discussed and it is stated that the mechanism of intimate contact and diffusion occurs simultaneously when temperature are high and, consequently, reptation time is low. The agreement was supported by applying the model on shorter time-temperature history of 0.9 s and 0.09 s that correspond to the contribution of the first 9 time-intervals and of the single time-interval respectively. Moreover is it important to notify that the first contribution of the summation in Equation 2.15 highly affect the modeling because its formulation. In fact, the second term of the numerator is equal to zero (initial instant) and contributes in a higher value if compared with the subsequent contributions of the summation. This characteristic contributes in supporting the consideration in [33] about the highly non-isothermal process that starts at high temperature.

The results of the analytical modeling in Figure 2.52 are based on the initial second of the thermal history and it possible to see that the trend of the previsions is still the same even if a reduction in the percent error is noticeable.

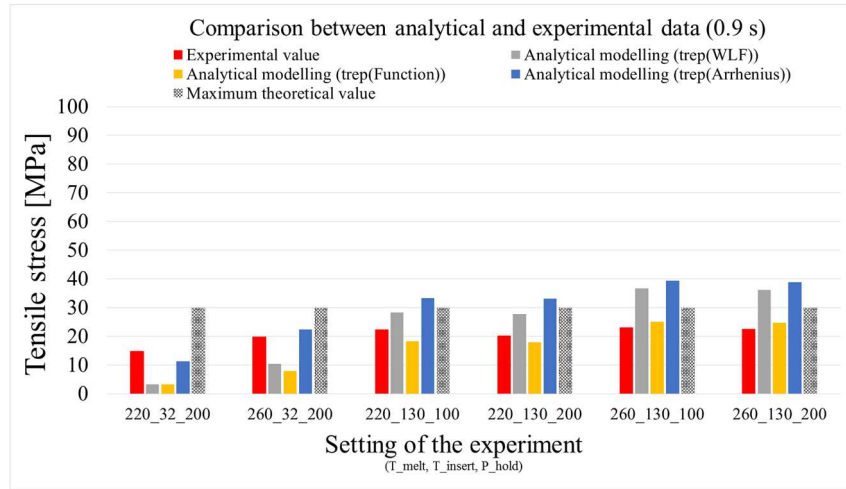


Figure 2.52 Comparison between analytical modeling on the first part of the thermal history (considering 0.9 s) made with four different approach and experimental data

In Table 2.24 are summarized the percent error and it is clear that the previsions still underestimate or overestimate the strength for low and high temperatures respectively. The Arrhenius model still overestimate the result but it shows the same trend of the experimental results.

Table 2.24 Percent error of the four approach in modeling the welding resistance considering the first part of the thermal history (0.9 s)

Exp.	Exp. value	Analyt. (WLF)	% err	Analyt. (Func.)	% err	Analyt. (Arrh.)	% err
220_32_200	14.8	3.3	-77.9	3.3	-77.7	11.4	-23.1
260_32_200	19.8	10.5	-47.0	7.9	-60.0	22.4	13.2
220_130_100	22.3	28.2	26.8	18.2	-18.1	33.4	50.0
220_130_200	20.2	27.9	37.7	18.0	-11.2	33.2	63.9
260_130_100	23.1	36.6	58.8	25.1	8.7	39.4	70.9
260_130_200	22.4	36.1	61.2	24.7	10.4	38.9	73.4

Finally, the first instant of the thermal history was considered and the graph in Figure 2.53 highlight that the analytical modeling based on the reptation time calculated with the Arrhenius model is suitable for a good prediction of the welding strength.

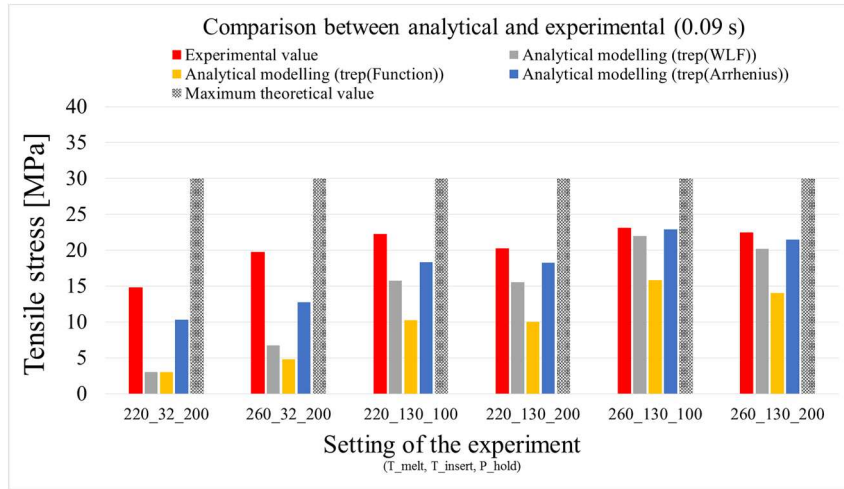


Figure 2.53 Comparison between analytical modeling made with four different approach on the first interval of the thermal history (considering 0.09 s) and experimental data

Table 2.25 Percent error of the four approach in modeling the welding resistance considering the first interval of the thermal history (0.09 s)

Exp.	Exp. value	Analyt. (WLF)	% err	Analyt. (Func.)	% err	Analyt. (Arrh.)	% err
220_32_200	14.8	3.0	-79.6	3.0	-79.6	10.3	-29.9
260_32_200	19.8	6.8	-65.7	4.8	-75.7	12.7	-35.5
220_130_100	22.3	15.8	-29.2	10.2	-54.1	18.4	-17.6
220_130_200	20.2	15.6	-23.0	10.1	-50.2	18.3	-9.8
260_130_100	23.1	22.0	-4.7	15.8	-31.5	22.9	-0.7
260_130_200	22.4	20.2	-9.8	14.0	-37.5	21.5	-4.1

From Table 2.25 reduction of the percent error is noticeable and its values are between 35%, that affects the modeling of the specimens with a shorter thermal history (lower temperature and lower time over the crystallization point), and 1% for the specimen with a longer thermal history.

The results of the evaluation of the quadratic distance of diffusion through the calculation of the Self-Diffusion coefficient proposed by Graessley are presented in the following section. A complete self-diffusion is obtained when the quadratic distance of diffusion is higher than the mean square end-to-end distance. The first step that was performed was the evaluation of how the thermal history and the plateau modulus affect the model. In Figure 2.54 and Figure 2.55 are reported the sensitivity analysis that was done on the less and the most performant configuration respectively. The histogram reports the mean square end-to-end distance and the calculated quadratic distance of diffusion with the plateau modulus calculated both Equation 2.6, by considering the slightly dependence of the polydispersity index from the temperature. The thermal history of the nodes of the part-insert, of the part and their mean were compared. Moreover, by considering the average temperature at the interface, it was assumed a plateau modulus calculated with a constant polydispersity index ($PI = 7$) and with a plateau modulus calculated with Equation 2.7.

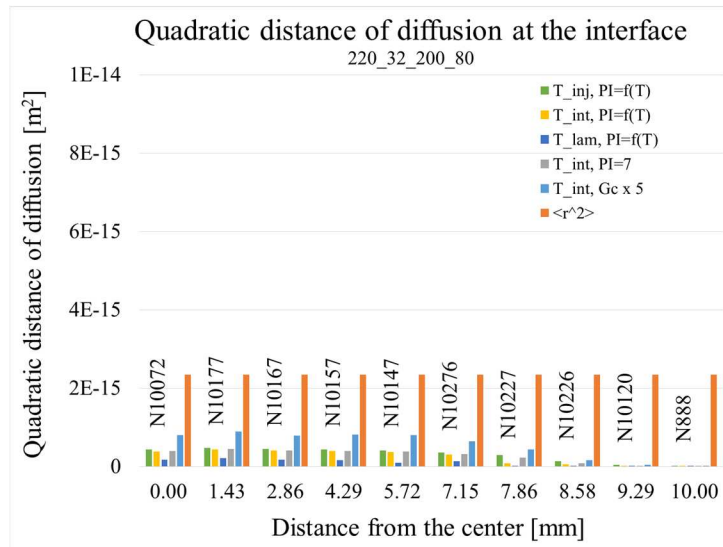


Figure 2.54 Representation of the quadratic distance of diffusion through several approaches during the sensitivity analysis of the model for the level 220_32_200_80

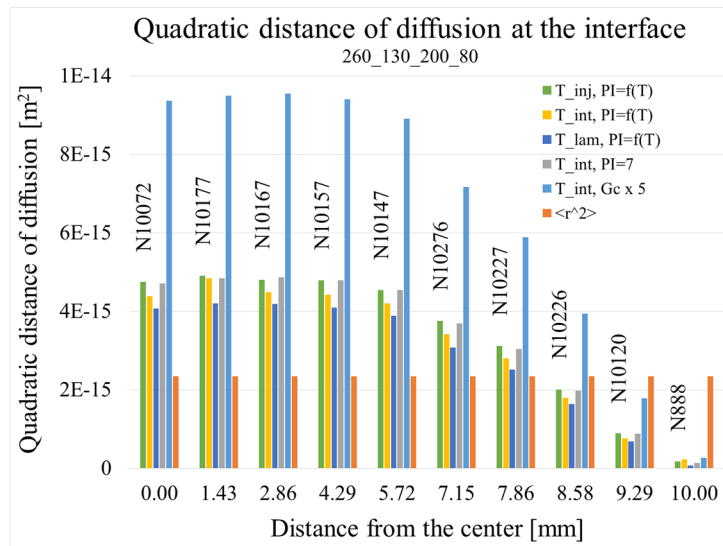


Figure 2.55 Representation of the quadratic distance of diffusion through several approaches during the sensitivity analysis of the model for the level 260_130_200_80

From the graph above, it is clear that all the approach are able to predict a constant value of quadratic distance on the node at the core of the stem and that is prone to decrease by getting closer to the mold wall where the skin, due to the lower temperature, act as barrier for the interdiffusion. In the less performant specimen, is it clear that a complete self-diffusion did not take place, on the contrary a complete diffusion characterized the most performant one. However, the modeling performed with the plateau module calculated with Equation 2.7 shows a better agreement with the simulation output *Re-Melt zone part insert* and with the morphology of fracture in Figure 2.50

In order to provide a better overview about the quadratic distance of diffusion, all the six specimens are compared by considering the model that use the plateau module that is calculated with Equation 2.7.

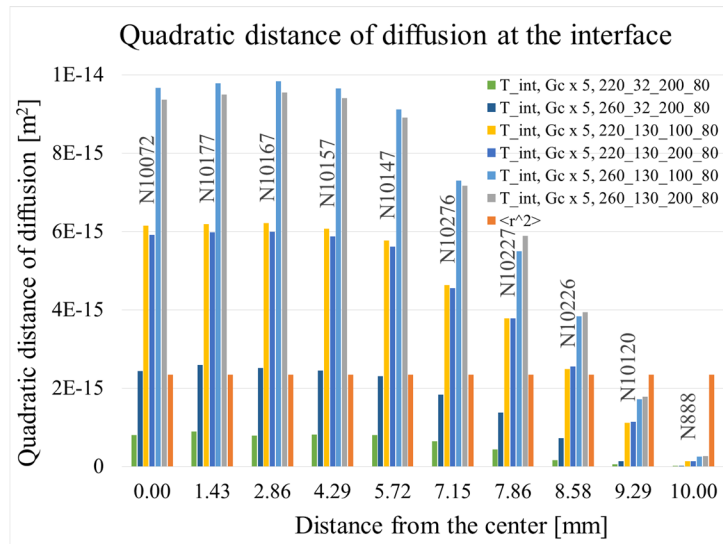


Figure 2.56 Overall comparison between the specimens produced with a different thermal histories

The graphs in Figure 2.56 highlight small discrepancies between the quadratic distance of diffusion calculated for the specimen manufactured with a holding pressure of 200 and 100 bar. In order to provide an explanation, the thermal history was investigated. It was noticed that a lower holding pressure is responsible of a different thermal history due to an earlier detachment of the part from the mold surface. The concept is represented in Figure 2.57 that provides a comparison between the thermal histories of the central nodes from both the specimen manufactured with low and high level of holding pressure. In Figure 2.57 are compared also the thermal history of the nodes on the part-insert, on the part and their average that is considered as the temperature at the interface.

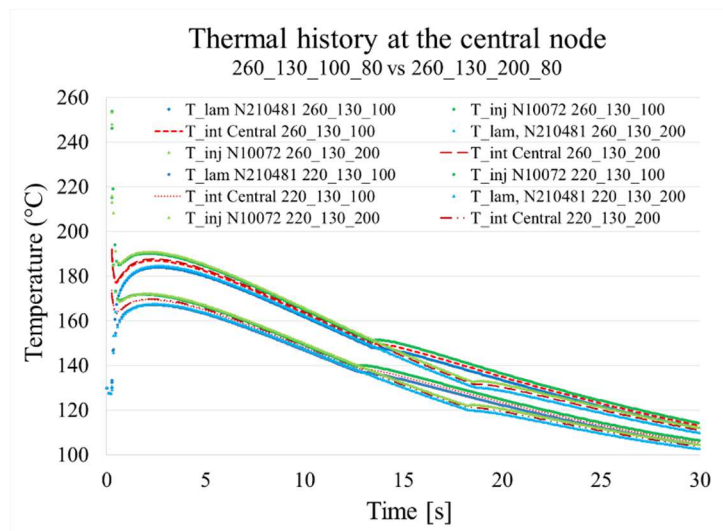


Figure 2.57 Comparison of the thermal histories between the specimen manufacture with low and high level of holding pressure

Figure 2.57 shows that the specimens manufactured with lower holding pressure have a lower gradient of temperature starting after 13 second from the filling.

Another useful output from the finite element analysis that shows a correlation with graphs in Figure 2.56 is the output *Re-Melt zone part insert*. The output is available only for the specimens that shows partial re-melt at the interface. In this study, a partial re-melt took place only when the laminate (part insert) was provided at 32°C.

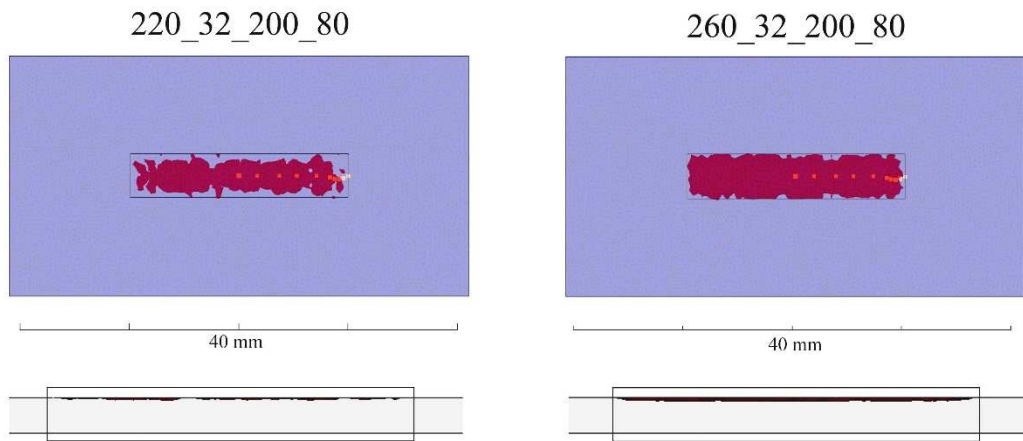


Figure 2.58 Re-melt zone part insert output with the position of the node investigated. For lower injection temperature the re-melt zone is smaller and thinner (L) for higher injection temperature the re-melt zone is larger and deeper (R)

The overall comparison between the graphs in Figure 2.56 and the output *re-melt zone part insert* in Figure 2.58 highlights a correspondence in the decrease of the quadratic distance of diffusion in the area close to the mold wall.

The summary graph in Figure 2.59 compares the analytical modeling of the welding strength, which was done with the Bastien and Gillespie's model and evaluating the reptation-time through the Arrhenius model, with the experimental data and provide the graphical representation of the quadratic distance of diffusion. The theoretical maximum strength and the mean square end to end distance are provided too. The final comparison involves only the central node of the interface.

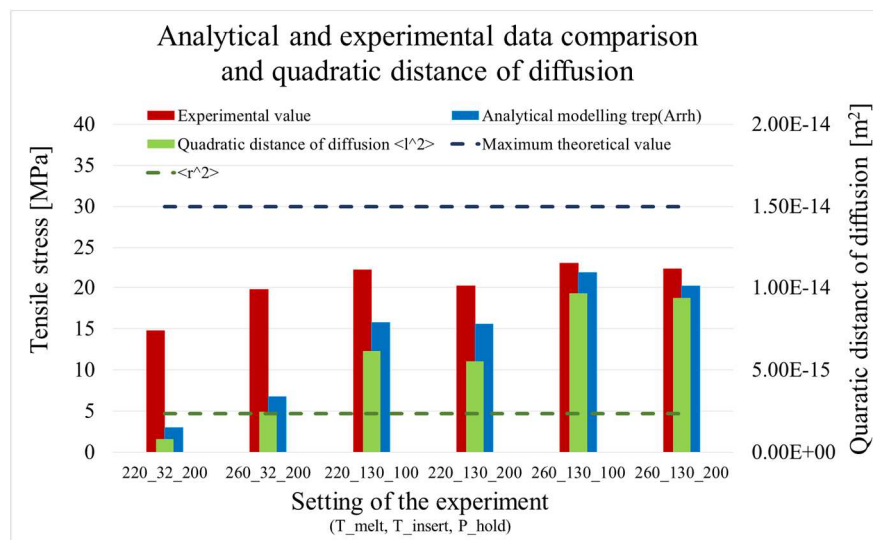


Figure 2.59 Comparison of the analytical and experimental results

The graph in Figure 2.59 shows high correlation between the mobility of macromolecules and the local time-temperature history. The analytical results from the model and the values of quadratic distance of diffusion are summarized in Table 2.26. The two different approaches are linked by Equation 2.46 where the interpenetration distance χ and the quadratic distance of diffusion $\langle l^2 \rangle$ are used.

$$\chi^2 = \frac{1}{6} \langle l^2 \rangle \quad \text{Equation 2.46}$$

Table 2.26 Summary of the experimental data and of the results of the analytical modeling with the Bastien and Gillespie's model and Graessley Self-Diffusion coefficient

Exp.	Bastien and Gillespie					Graessley			
	σ_{∞} [MPa]	σ_{exp} [MPa]	σ_{pre} [MPa]	% err	χ_{∞} (Rg) [m ²]	χ [m ²]	χ [m ²]	$\langle r^2 \rangle$ [m ²]	$\langle l^2 \rangle$ [m ²]
220_32_200	30	14.46	10.35	29.9	2.0E-08	6.8E-09	1.2E-08	2.3E-15	8.0E-16
260_32_200	30	19.77	12.74	35.5	2.0E-08	8.4E-09	2.0E-08	2.3E-15	2.5E-15
220_130_100	30	22.27	18.35	17.6	2.0E-08	1.2E-08	3.2E-08	2.3E-15	6.2E-15
220_130_200	30	20.22	18.25	9.8	2.0E-08	1.2E-08	3.0E-08	2.3E-15	5.5E-15
260_130_100	30	23.08	22.91	0.7	2.0E-08	1.5E-08	4.0E-08	2.3E-15	9.7E-15
260_130_200	30	22.42	21.50	4.1	2.0E-08	1.4E-08	3.9E-08	2.3E-15	9.4E-15

The analytical prevision of the welding strength is in a good agreement with the experimental results. An interesting outcome is the comparability of the interpenetration distance χ evaluated with two different approach that are of the same order of magnitude.

In general both the model are highly sensitive to time-temperature history at the interface. The Bastien and Gillespie model is suitable to predict the welding resistance with a percentage error below the 35%. And it confirms the hypothesis formulated on the result of the ANOVA. The negative effect of the pressure seems to be related to a more efficient heat exchange when it is at the higher level. The modeling of the quadratic distance of diffusion showed a correlation to the *re-melt zone part insert* that highlight a correspondence to the morphology noticed in the real surface fracture. This aspect directly reflects on the prevision of the welding strength and makes the modeling not completely accurate, even if it has an acceptable percentage error (on the central node). The discrepancies between experimental and analytical value could be related to the high deformability of the part-insert during the tensile test and the measure of a lower experimental strength. Moreover, as direct consequence of the results of the simulation, which highlight an incomplete remelting, the nominal area used in the calculation of the engineering strength could induce to a higher error. For this reason a weighted average should be best suited for the calculating of the experimental result. The general concept is to divide the area in sub-areas each characterized by a welding resistance that is analytically modelled by using the thermal history of the nodes.

2.7.2 Welding resistance in hybrid T-joint specimens

Effect of the process parameters

The analysis of variance (ANOVA) results (Table 2.27) of the screening plan on the tensile tested samples indicate that both the melt temperature and the packing pressure positively and significantly affect the bonding resistance being agree with literature results [17-19]. Contrarily, the interaction between melt temperature and mold temperature negatively affects the experimental ultimate tensile stress. The main effects and the significant interaction are respectively resume in Figure 2.60 and Figure 2.61.

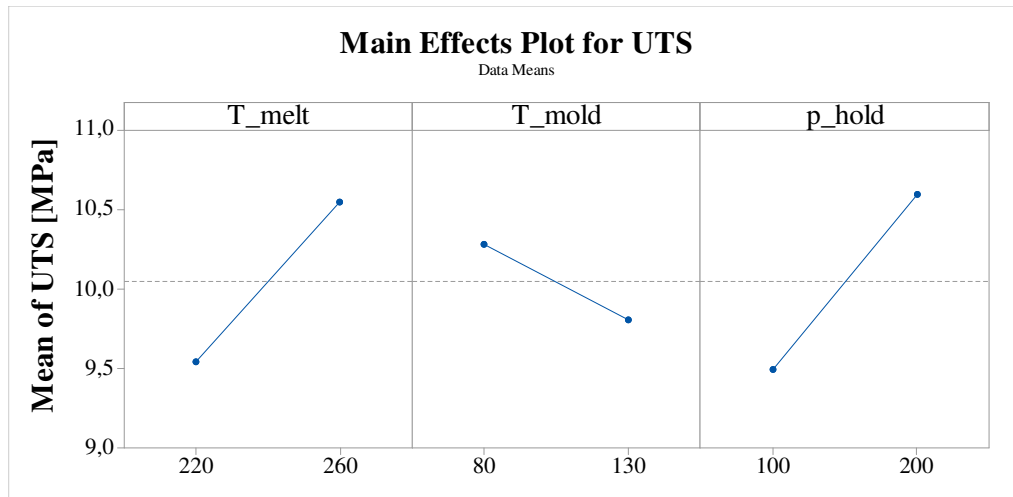


Figure 2.60 Main effects plot for the process parameters on the UTS of the hybrid T-joint specimen

Table 2.27 Analysis of variance results for the process parameters on the UTS of the hybrid T-joint specimen

Factor	Sum of Square	Mean Square	F-Value	P-Value
T_melt	14.060	14.060	5.79	0.020
T_mold	3.912	3.912	1.61	0.211
p_hold	16.966	16.966	6.98	0.011
T_melt*T_mold	10.090	10.090	4.15	0.047
T_melt*p_hold	1.213	1.213	0.50	0.483
T_mold*p_hold	2.392	2.392	0.98	0.326
T_melt*T_mold*p_hold	2.643	2.643	1.09	0.302
Error	116.61	2.429		

$UTS = 10,046 + 0,501 T_melt - 0,264 T_mold + 0,550 p_hold$
 $- 0,424 T_melt*T_mold - 0,147 T_melt*p_hold + 0,207 T_mold*p_hold - 0,217 T_melt*T_mold*p_hold$

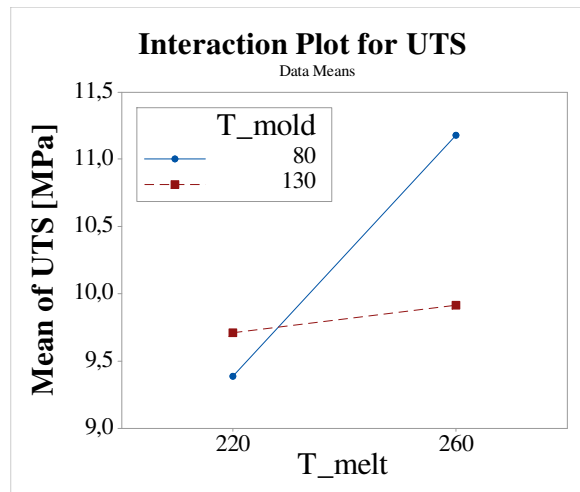


Figure 2.61 Interaction plot for mold temperature and laminate temperature on the UTS of the hybrid T-joint specimen

By varying only the melt temperature from 220 to 260°C, the UTS increase from 9.11 MPa to 10.82 MPa. Conversely, varying the only packing pressure from 100 bar up to 200 bar, the increase was from 9.11 MPa to 9.65 MPa. The combined effect of the two parameters allows to reach the best performance of 11.65 MPa.

Evaluation of the residual stress

With reference to the interaction plot of the previous section (Figure 2.61), it was supposed that the negative effect on the UTS is related to a higher residual stress induced by and proportional to a higher shrinkage of the interface. The shrinkage of the matrix can weaken the adhesion to the woven glass fabric. Moreover, a second hypothesis can be related to a geometrical issue. During the heating of the rectangular cutout, the matrix is prone to swell the laminate because of the increase of the specific volume and then, the higher temperature of the transversal beam reduces the cooling rate making the laminate thicker during the clamping of the mold. As consequence, the laminate is prone to interfere with the upper wall of the cavity during the closing phase and to be pinched by the edges of the two parts of the mold. However, the latter effect can contribute in a positive way as it will be discussed in the following section.

The influence of the process variables on the average of the Von Mises equivalent stress on the stem-side interface was investigated by using the same full factorial design reported in Table 2.14. The main effects plot of the process parameter on the average Von Mises equivalent stress is shown in Figure 2.62

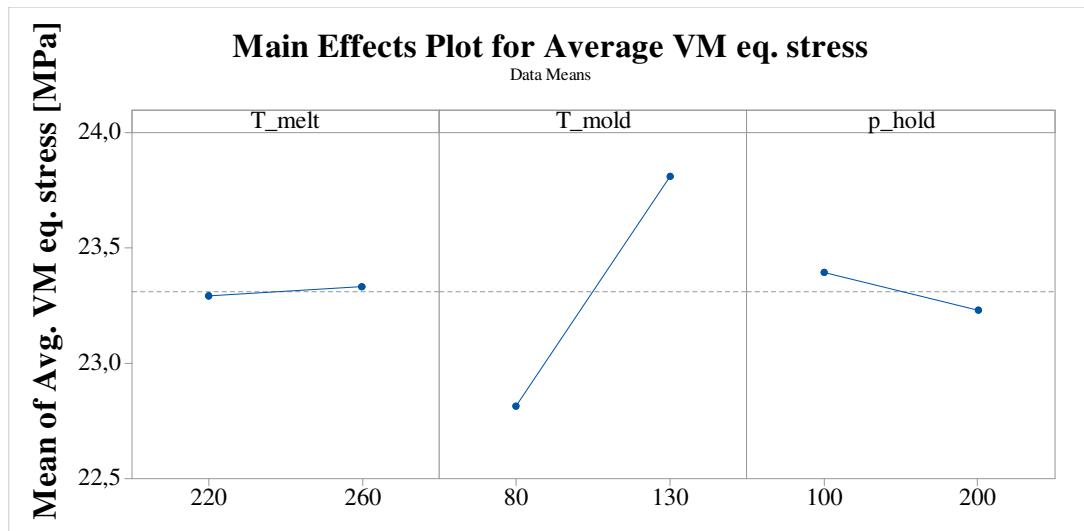


Figure 2.62 Main effects plot for the process parameters on the Average Von Mises equivalent stress at the interface of the hybrid T-joint specimen

The first hypothesis about the volumetric shrinkage was supported by the FEA analysis in Autodesk Moldflow that shows a strong dependency from the mold temperature. Moreover, the presence of residual stress was confirmed by the FEA analysis in Autodesk Simulation Mechanical, which converts the Moldflow outputs in a distribution of the residual stress at the end of the injection phase. The transferring of the information between the two software allows to visualize the “Initial Stresses” output, which is not directly available in the original environment. The analysis of variance results has not a real statistical significance because of the lack of repetitions due to the nature of the “experiments” that are the results of numerical simulation, anyway the plot of the main effects can help in evaluating how the process parameters affect the residual stress at the interface.

Since it is well known that the temperature promotes the macromolecular interdiffusion, the following investigation was focused on relaxing of the residual stress. Nevertheless, the treatment was applied to the setting of parameters that maximized the welding resistance (Melt temperature 260°C, mold temperature 80°C and holding pressure 200 bar). It was supposed that an annealing treatment oriented to the stress relaxation could improve the

welding resistance. The annealing treatment was designed as a full two-levels factorial plane. The ANOVA results of the experimental screening plan (Table 2.28) on the ultimate tensile test indicate that both the annealing temperature and the time have a positive effect (Figure 2.63) but they did not significantly affect the bonding resistance.

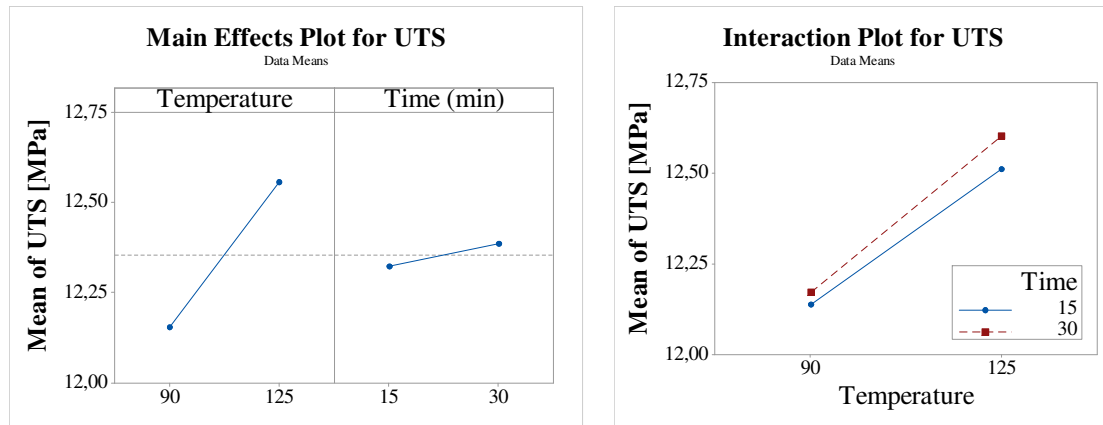


Figure 2.63 Main effect and interaction plots of the annealing parameters on the UTS of the hybrid T-joint specimen

Table 2.28 Analysis of variance results for the annealing parameters on the UTS of the hybrid T-joint specimen

Factor	Sum of Square	Mean Square	F-Value	P-Value
Temperature	0.0277	0.0277	0.13	0.943
Time	1.1428	1.1428	0.37	0.548
Temperature*Time	0.0057	0.0057	0.00	0.966
Error	100.52	3.454		

$$UTS = 12.355 + 0.031 \text{ Time} + 0.202 \text{ Temperature} + 0.014 \text{ Time*Temperature}$$

However, the main effect of the annealing temperature leads an increase of the UTS. Therefore, the evaluation of the annealing treatment was extended also the less performant setting (Melt temperature 220°C, Mold temperature 80°C and holding pressure 200 bar).

The ANOVA results of the experimental screening plan (Table 2.29) on the ultimate tensile test remarks the positive effect of both the melt temperature and the holding pressure, which are considered as a process setting, and highlight the positive effect of the annealing treatment as it is shown in Figure 2.64.

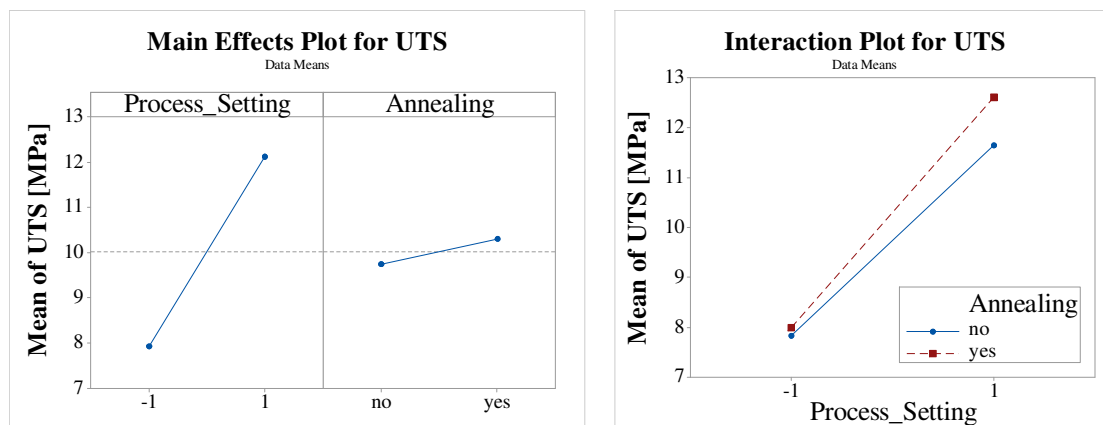


Figure 2.64 Main effect and interaction plots of the process and annealing on UTS

Table 2.29 Analysis of variance results for the process setting and the annealing treatment on the UTS of the hybrid T-joint specimen

Factor	Sum of Square	Mean Square	F-Value	P-Value
Process setting	124.324	124.424	34.97	0.000
Annealing	2.178	2.178	0.61	0.441
Process*Annealing	1.093	1.093	0.31	0.584
Error	85.326	3.555		
UTS = 10.019 + 2.107 Process + 0.279 Annealing+ 0.198 Process*Annealing				

The remarkable aspect is better appreciable by the interaction plot of Figure 2.64 where the effect of the annealing is more pronounced in the specimens manufactured at higher temperature. The last experiment indirectly confirmed the simulation results: although higher melt temperature can increase the residual stresses, the annealing treatment relaxes the pre-tensioning status and leads an improvement of the overall welding performances of 7%, from 11.65 MPa up to 12.60 MPa.

Effect of a localized heating

The graph in Figure 2.65, shows the ultimate tensile strength of the specimens that were locally and uniformly heated.

Considering the UTS of the most performant specimen from the first DOE as reference value for welding strength (11.65 MPa), which is the last bar on the right, the local heating of the interface is responsible of a reduction of the 24% (8.86 MPa). The laminate uniformly heated and provided at 135°C leads a lower reduction of the 7.3% (10.74 MPa).

Although the reduction in temperature leads to a modest reduction of the UTS, the localized heating results in a significant reduction of the mechanical strength at the interface. With a localized heating, only the top layers were softened while the rest of the base remains in the solid state. This has facilitated the placement of the laminate in the cavity because the unmelted area did not show any interference with the edges of the mold. However, this is a marginal limitation due to the experimental apparatus.

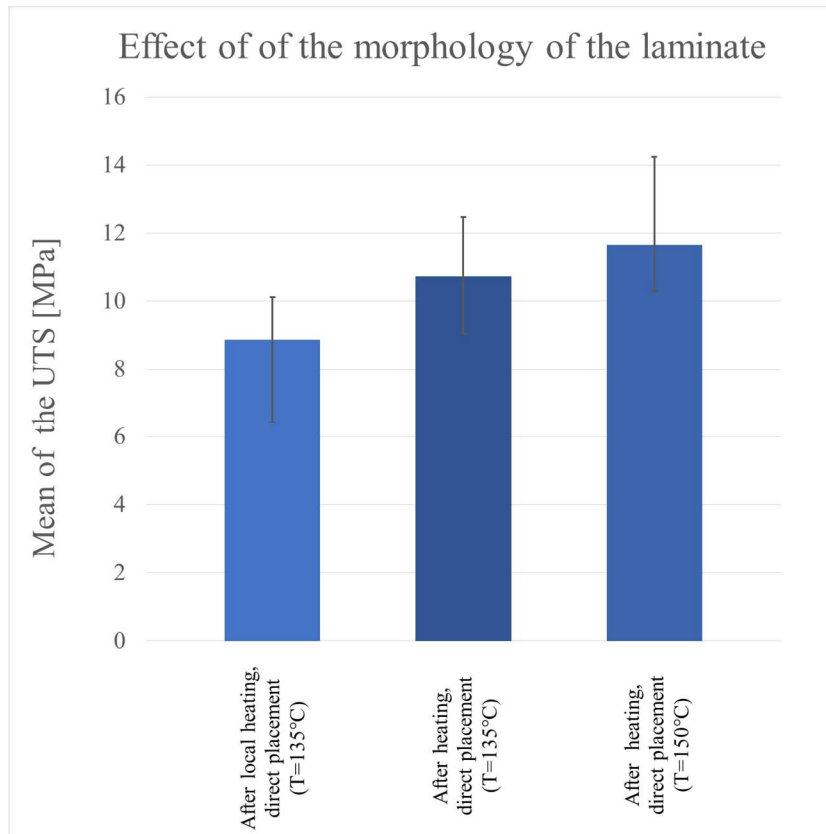


Figure 2.65 Mean values of the UTS of the specimens manufactured with a local and a uniform heating of the laminate

A first comparison between the mean value of the UTS of the specimens manufactured with the laminate uniformly heated at the higher temperature and the ones manufactured with the laminate locally heated, helps in understanding the general trend of the decrease of the welding resistance. The mean data are reported in Table 2.30 where the capital letters A, B and C indicate respectively the melt temperature, the mold temperature and the holding pressure at their higher level. All the parameters are at their lower level at level 0.

Table 2.30 Comparison of the UTS of specimens with laminate uniformly heated and laminate locally heated

Level	Uniform heating (150°C) [MPa]	Local heating (135°C) [MPa]	Variation [%]
A	10.82	8.77	-19.0
AB	9.47	6.77	-28.5
AC	11.65	8.86	-23.9
B	8.58	6.06	-29.4
BC	10.83	6.43	-40.5
C	9.66	7.61	-21.2
ABC	10.25	6.67	-34.9
0	7.83	6.36	-18.7

The comparison highlights that the most and the less performant level, matches in both the designed experiments, and correspond respectively to the level AC and the level B. The tests performed with the mold temperature equal to 130 °C, show the greatest percentage reductions.

The analysis of variance (ANOVA) results (Table 2.6) of the screening plan on the tensile tested samples show that the melting temperature and mold temperature significantly affect the welding resistance when the laminate is locally heated. The main effects plot in Figure 2.66 shows the same influence of the process parameter on the welding strength that was noticed with the laminate uniformly heated.

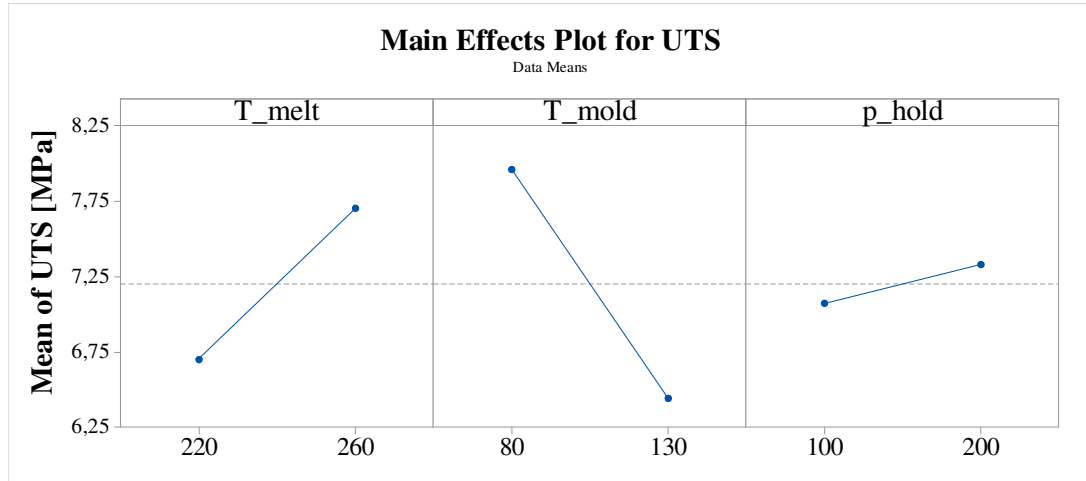


Figure 2.66 Main effects plot for the process parameters on the UTS of the hybrid T-joint specimen with the local heating of the laminate

The main difference from the previous results on the full-thermoplastic hybrid specimens is the higher, significant, and negative effect of the mold temperature. Nevertheless, the negative effect of the mold temperature is consistent with result of the process simulation that showed how the mold temperature leads the increase of the residual stress.

Table 2.31 Analysis of variance results for the process parameters on the UTS of the hybrid T-joint specimen with the local heating of the laminate

Factor	Sum of Square	Mean Square	F-Value	P-Value
T_melt	14.105	14.105	7.88	0.007
T_mold	32.923	32.923	18.10	0.000
p_hold	0.921	0.921	0.51	0.477
T_melt*T_mold	5.273	5.273	2.95	0.92
T_melt*p_hold	2.110	2.110	1.18	0.283
T_mold*p_hold	0.580	0.580	0.32	0.572
T_melt*T_mold*p_hold	0.056	0.056	0.03	0.861
Error	85.87	1.789		

$$\text{UTS} = -24,5 + 0,138 T_{\text{melt}} + 0,174 T_{\text{mold}} + 0,089 p_{\text{hold}} - 0,00080 T_{\text{melt}}*T_{\text{mold}} - 0,000326 T_{\text{melt}}*p_{\text{hold}} - 0,00038 T_{\text{mold}}*p_{\text{hold}} + 0,000001 T_{\text{melt}}*T_{\text{mold}}*p_{\text{hold}}$$

The melt temperature always contributes in increasing of the welding strength. Higher temperatures at the interface promote macromolecules interdiffusion and help in replicate the laminate surface. In addition, the holding pressure contributes positively in replicating the interface on the laminate side but it provides a stronger contribute when the laminate is heated at higher temperature. When the laminate is uniformly heated at higher temperature, the overinjected material can penetrate the laminate and replace the matrix. As consequence of this phenomenon, the two material are provided with a higher density of physical interlocking and an extended region where the macromolecules can interdiffuse. This observation is supported by the some x-ray investigation carried out a micro-computed tomography in Figure 2.67. In this case, the laminates were at temperature close to melting

point and the solid matrix around the heated area could not block the flowing of the overinjected material.

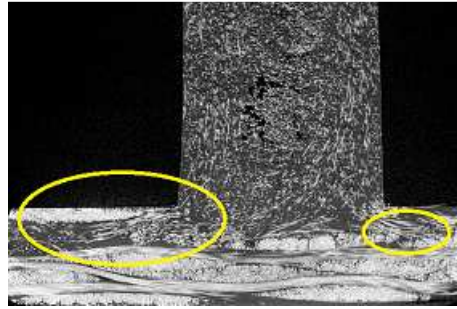


Figure 2.67 Micro x-ray investigation at the interface that shows the penetration of the injected material inside the laminate

In addition, the plot in Figure 2.68 shows that the interaction between melt temperature and mold temperature has a significant effect on the welding strength. The effect is consistent with the previous results and shows how the mold temperature leads the decrease of the welding performance.

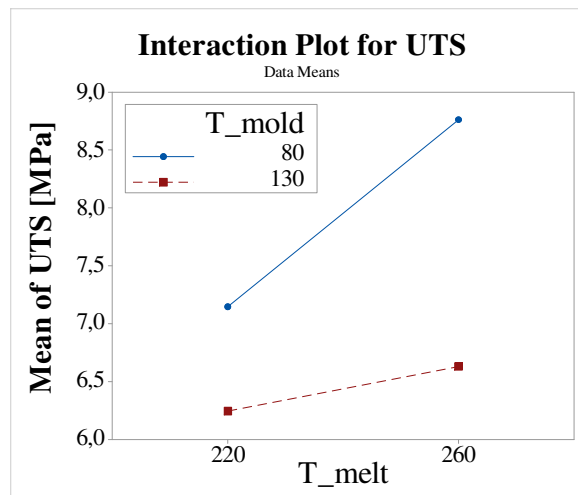


Figure 2.68 Interaction plot of melt temperature and mold temperature on UTS (local heating)

It is important to highlight that the negative effects is still present even with the localized heating. This observation allows to neglect the hypothesis of the pinching of the laminate during the mold closing.

Effect of the morphology

Before presenting the morphological characterization, an overall comparison of the welding performance of the four different specimens is provided in Figure 2.69. The condition of laminate that were investigated are:

1. As provided, without heating before the positioning
2. After local heating and cooling down before the positioning
3. After local heating and in cavity positioning (135°C before the filling phase)
4. After uniform heating and in-cavity positioning (150°C before the filling phase)

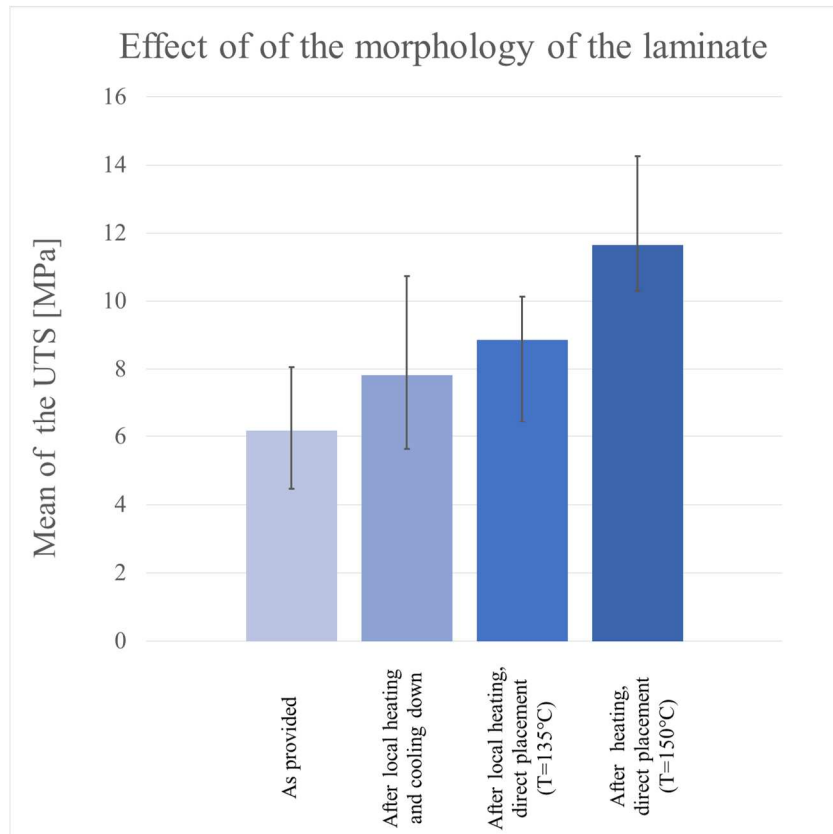


Figure 2.69 Mean values of the UTS of the specimens manufactured with the laminate provided with the four conditions

The comparison in Figure 2.69 shows that the change of the morphology leads a progressive increase of the welding strength. The increase of the area of the interface was evaluated through the surface reconstruction carried out in SolidWorks starting from the point clouds that were acquired with the optical profiler. The investigated area, 72.5 mm², is slightly lower than the nominal value of the interface 80 mm² for the reason already explained. The four conditions of the laminate are shown in Figure 2.70 whit the respective surface scanning, which was performed by using the profiler, and the surface reconstruction starting from the point cloud, which was performed in SolidWorks.

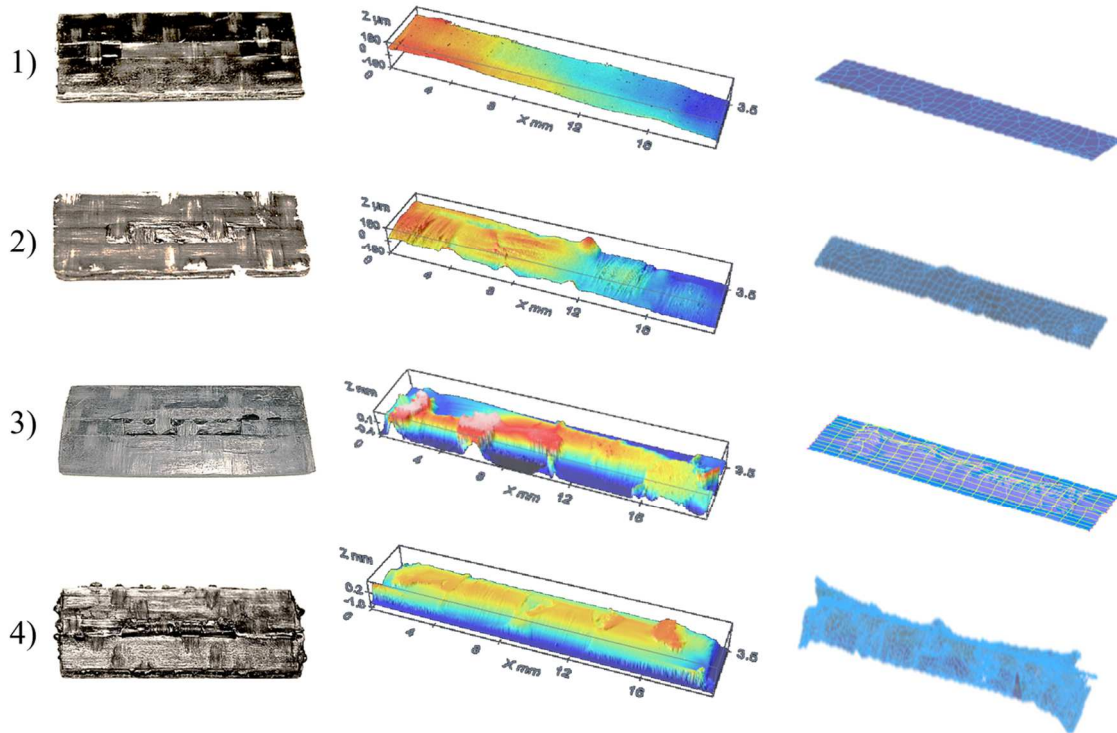


Figure 2.70 Reconstruction of the surface starting from the point clouds

The measured area and the relative percentage increase, which is obtained by the comparison to the first condition, are summarized in Table 2.32 and are accompanied by percentage increase of the welding strength.

Table 2.32 Comparison of the interfacial area and of the welding performance

Condition	Area [mm ²]	% Increase	Strength [MPa]	% Increase
1	72.9	reference	6.20	reference
2	73.2	0.4	7.80	26
3	84.1	15.4	8.80	42
4	94.1	29.1	11.65	89

The area of the interface was respectively 72.92 mm² for the as-provided laminate, 73.22 mm² for the laminate heated by using the mask and cooled down, 84.1 mm² for the laminate heated by using the mask and clamped in the cavity (T = 135°C) and 94.09 mm² for the laminate uniformly heated and clamped in the cavity (T = 150°C).

The investigation aims to understand how the process affects the morphology change on the laminate side before the filling phase and how it is reflected on the welding strength, nevertheless the welding strength is also affected by a different average temperature of the interface. Considering the average temperature before the filling phase T_i (Equation 2.45), the temperature at the interface was respectively 145°C for the as-provided laminate and for the laminate heated by using the mask and cooled down. The average temperature was of 197.5°C for the laminate heated by using the mask and clamped in the cavity and 205°C for the laminate uniformly heated and clamped in the cavity. However, the first and the second condition involve the laminates provided at the environmental temperature. The increase of the area in the second condition is due exclusively to the swelling of the matrix outside the woven glass fabric induce by the heating cycle and it provides an increase of the welding resistance of the 26%. The effect can be explained by a conforming status of the matrix

before the injection phase that eventually release some stress induce by the manufacturing process of the composite laminate. Moreover, the interdiffusion of the macromolecules is provided with an extended area. The same effects are present in the third and in the fourth conditions but in these cases, the increased area and the swelling of the woven fibers promote the opportunity in creating physical interlocking. Finally, when the laminate is provided at the highest temperature, the overinjected material can penetrate the laminate and replace the matrix. The discussion is supported by the micro x-ray investigation and by a profilometry along the medium line of the interface at half the thickness that are shown in Figure 2.71.

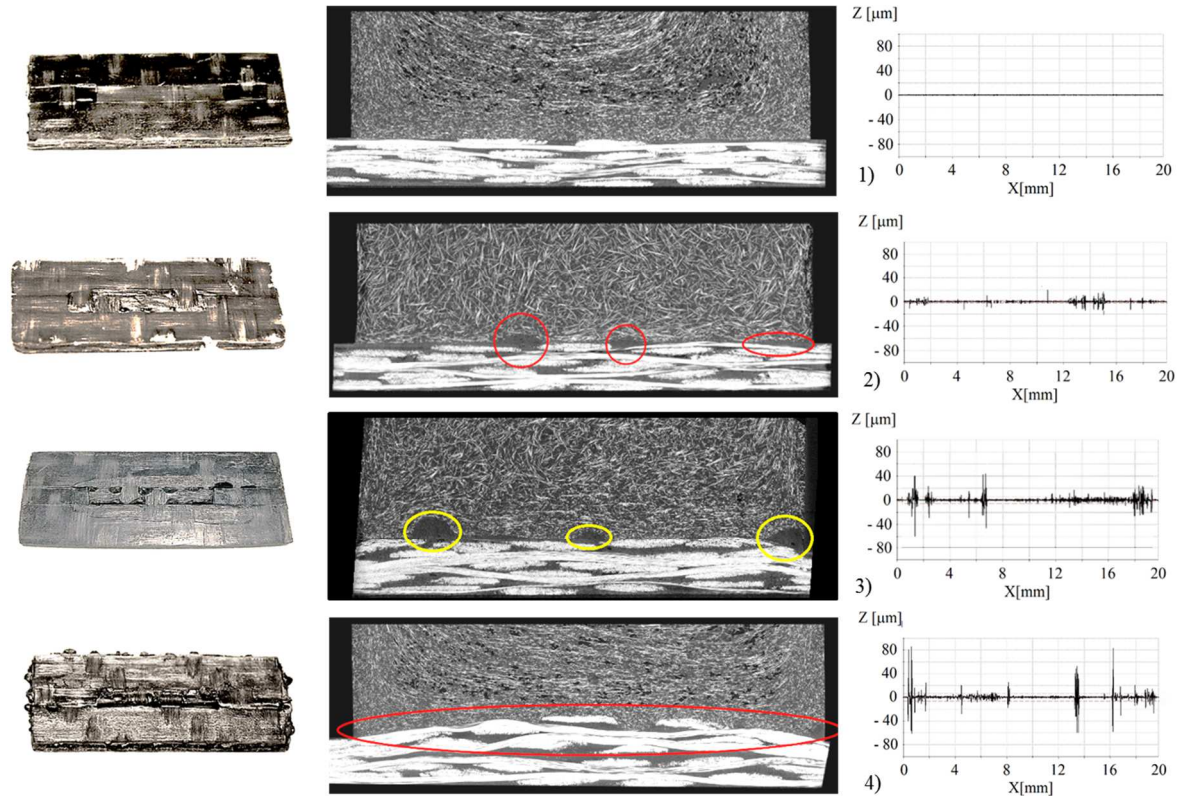


Figure 2.71 Micro x-ray investigation of the interface and profilometry along the medium plane

However, the CT scans and the morphology investigation highlight the problem related to the structural integrity of a hybrid composite part during the closing of the mold. Even if the morphological modification promote an increase of the welding resistance, it could act as a local defect. Being the matrix weaker and the layers subject to external forces in the direction parallel to the plane on which they are arranged, the layer are free to move one another and the fabric is able to deform. If this occurs, the mechanical properties of the laminate undergo a sharp deterioration because the stresses are no longer parallel to the fibers in the areas in which the laminate have been deformed. Therefore, the stresses are no longer supported exclusively by the reinforcement but they distribute within the matrix.

2.7.3 Welding resistance in *functionalized* hybrid T-joint specimens

The work carried out during the research period abroad at the Institute für Kunststoffverarbeitung (IKV) allows the manufacturing of the first specimens with the Lightflex technology for the individualize production of full-thermoplastic composite parts.

The specimens after the forming process and before having cut the perimeter of the base, are shown in Figure 2.72. In the same picture are presented also the details of the joining area.

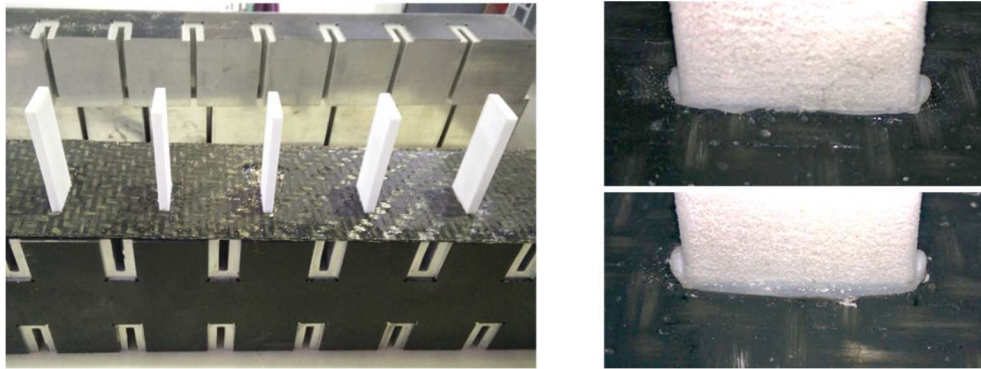


Figure 2.72 Specimens manufactured with the Lightflex technology and details of the interface

The analysis of variance results in Table 2.33 show, in accordance to previous activities, that the temperature leads the welding between parts and that there is a strongly positive correlation between temperature and pressure as it is graphically shown in Figure 2.73. On the other hand, the effect of the forming pressure has a negative effect. It was supposed that in case of low heating time, which results in a lower melted mass, the thin fused film is evacuated from the interface with a consequent reduction of the material that participate to the welding.

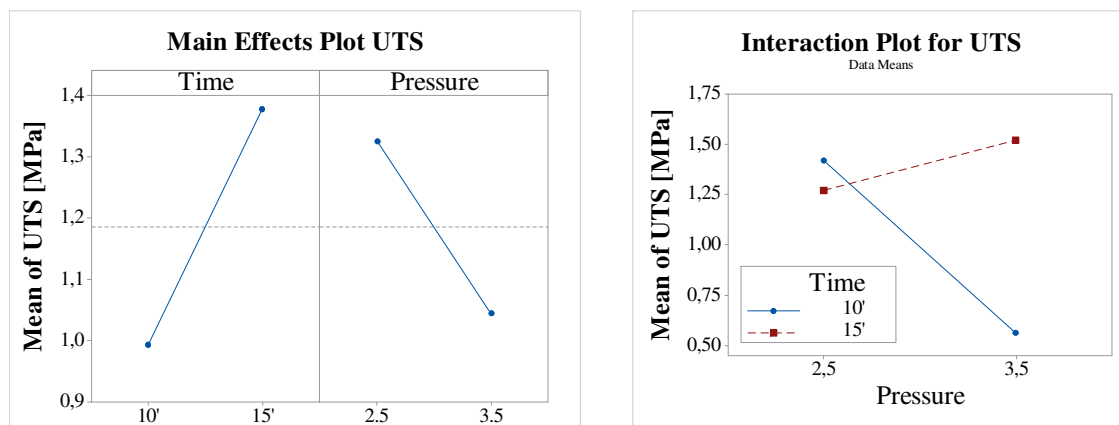


Figure 2.73 Main effect plot and interaction plot of the process parameters on UTS

Table 2.33 Analysis of variance results for the process parameters on the UTS of the functionalized hybrid T-joint specimen

Factor	Sum of Square	Mean Square	F-Value	P-Value
Heating Time	1.0430	1.0430	6.52	0.017
Pressure	0.5544	0.5544	3.47	0.075
Heating Time*Pressure	2.3098	2.3098	14.45	0.001
Error	3.8370	0.1599		

$$UTS = 1,1848 + 0,1930 \text{ Time} - 0,1407 \text{ Pressure} + 0,2872 \text{ Time*Pressure}$$

The average value of the ultimate tensile strength of the specimens from the levels of the design of the experiment and the specimens with a structured surface are resumed in Figure 2.74. The best performances were obtained with pins with irregular geometry and pitch. Provide the interface with a higher amount of melted material, especially where the stress is concentrated and the breakage starts, positively affects the resistance of the welding.

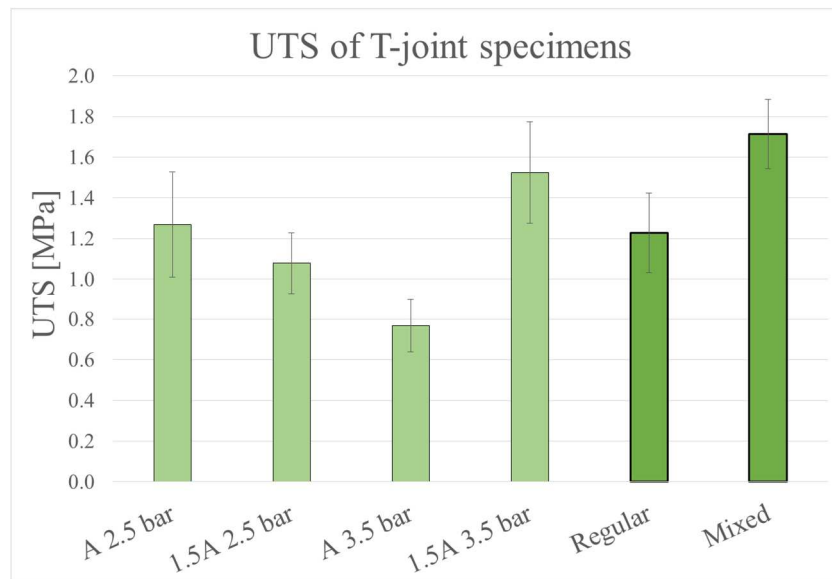


Figure 2.74 Ultimate tensile strength results of the functionalized hybrid T-joint specimens

The maximum average ultimate tensile strength of the specimens is one tenth of the reference value that was assumed the injected overmolded specimens (28 MPa). The reasons of the gap are related to main difference between the processes: currently, the forming pressure is one hundredth of the holding pressure and the small amount of melted material on the interface side of the stem is prone to provide heat also to the solid material. Furthermore, the manual handling of the stems and the closing time of the forming plate are responsible of the cooling of the interface that stops the chain mobility. The main reason it related to the nature of the polyamide and in particular, to the high rate of crystallization that reduces the processing windows. An automated and rapid heating system could help to reduce the heat dispersion. Likewise, a thermally insulated supporting system, especially in the region close to stem, would contribute in preserving the heat from the lower side of the stem. The replication of the experiments with a less sensitive material, such as polypropylene, could help in the optimization of the process.

Future improvements

Following, two general ideas aimed to increase the welding resistance during the forming process are proposed.

- Use the supporting system as device that helps in having a process induced riveting:



Figure 2.75 Example of process-induced riveting after having removed the aluminum insert

During the forming, the pressure is concentrated only on a small portion material. The supporting system cools down all the material almost instantaneously and it cannot participate to the welding process since the macromolecules are not enough activated.



Figure 2.76 First experimental trial with process induce riveting

This solution was quickly investigate by producing only two specimens in Figure 2.76. During the heating phase, the aluminum insert was removed and all the material out from to supporting system was exposed to IR heating as shown in Figure 2.75. Unfortunately, the external matrix was oxidized and signs of degradation were present as shown in Figure 2.77. If degradation takes place, the mobility of the macromolecules is compromised. Before use the following alternative, try to optimize the heating cycle being sure to avoid the degradation. After tensile testing of the specimen, the presence of some powder on the rupture surface suggests a bad adhesion due to the already explained reason. The powder is the result of the cutting of the specimen before performing the test. The PA6 and glass fiber powder flowed inside the voids.



Figure 2.77 Analysis of the interface in the process induced riveting

In order to improve the process-induced riveting, a higher amount of material can be considered as shown in Figure 2.78. During the forming, the pressure is concentrated on a higher amount of material. The supporting system cools down the edges and stops the flowing of the melted material. The volume of the “extra-material” should be at least equal to the empty volume of the cavity.

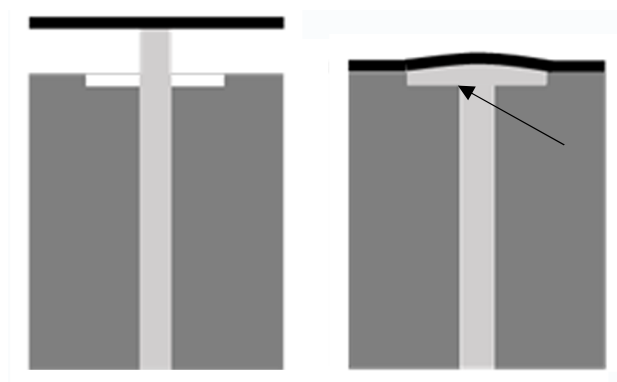


Figure 2.78 Variant proposed for the process-induced riveting

Moreover, in order to decrease the cooling of the interface, the supporting system should be heated up to 10-20°C below the melting temperature of the stem. After having reached the target temperature, the sample can be inserted and heated up to the required temperature. With an aluminum supporting system, a thermal insulation can help in keeping the temperature of the interface high for longer time. The following heating phase of the stems must be recalibrated. It is strongly recommended to calibrate also the cooling down of the supporting system, until the start of the forming. In the previous experiments, the supporting system dissipation acted as an uncontrollable variable.

2.8 Result of the structural simulation (CZM)

The models that are presented and widely discussed are related to the experiments planned with the DOE that showed the best and the worst performances. They were also examined the experimental behavior of the specimen manufactured by using the laminate without heating, with the laminate locally heated and cooled prior to placement in the mold and the laminate locally heated and direct placement in the mold. For every level that was modelled are presented:

- *Analysis of the sensitivity, i.e. the determination of the optimum parameters that allow to obtaining a good modeling and the other parameter that describe the cohesive law.*
- *Graph of the model that is obtained with assigned the scatter bands that contain and represent the experimental variability.*

In the following table, the value of the strain energy release rate G_{IC} is reported for all the experiments that are modelled with the bilinear law. However, for the reason that are discussed in the paragraph 2.8.5, it should be more appropriate to indicate the value as G_C when the process modifies the condition of the interface.

By applying the script in Matlab it is possible to define automatically the law that describes the cohesive zone model. The script defines the value T_n^{max} in correspondence of δ_n^* and the final displacement δ_n^c , and after calculating the sum of squared residual it defines the law that best fit the experimental data. In order to recognize the change of the slope during the fiber bridging, the script assumes four hypothetical value of T_n^{fb} respectively equal to 0.7, 0.65, 0.60 and 0.55 the value of T_n^{max} . When a bilinear law describes the behavior of the specimen, the rate α is consequently defined. When a trilinear law describes the behavior of the specimen, the parameters T_n^{fb} and the displacement δ_n^{fb} are defined and the rate α_σ is consequently defined.

After having performed a first simulation in Ansys with the parameters that were determined through the preliminary sensitivity analysis, the post-processing provides the user with the file that contains the numerical data of the cohesive model. If the result of the simulation does not fit the experimental results, the user can manually modify the Ansys's input parameters in order to get a better fitting.

The scatter bands are defined by standard deviation of the traction force T_n^{max} while the other parameters are defined by keeping constant the rate α for describing the bilinear law and the rate α_σ for describing the trilinear law. In the latter case, the value of the final displacement are defined by the standard deviation of the critical displacement δ_n^c .

2.8.1 Modeling of the behavior of specimens with uniform heating of the laminate

The most performant specimens (uniform heating)

The experimental results shown that the most performant specimens, where the welding strength was the higher, were manufactured by providing the laminate uniformly heated. The laminate were overmolded with a melt temperature of 260°C, a mold temperature of 80°C and an holding pressure of 200 bar. This level is called AC. Seven specimens were tested and they show two different experimental behavior:

- *3 repetitions showed a brittle breakage and they were modeled with a bilinear law*
- *4 repetitions showed the fiber-bridging and they were modeled with a bilinear law*

The results of the sensitivity analysis and the G_{IC} are summarized in Table 2.34 by T_n^{max} , α and δ_n^c when the behavior is described with the bilinear law, and by T_n^{max} , δ_n^* , α_σ and δ_n^c .

when the behavior is described with the trilinear law. All the other cohesive parameters and the G_{IC} are reported.

Table 2.34 Cohesive zone parameters for the level AC of the hybrid T-joint specimens manufactured with the laminates provided at 150°C (uniform heating)

Level	Law	G_{IC} [J/mm ²]	T_n^{max} [MPa]	δ_n^c [mm]	α δ_n^*/δ_n^c	δ_n^* [mm]	δ_n^{fb} [mm]	α_σ T_n^{fb}/T_n^{max}	
AC	Bilinear	2.43	Low	10.5	0.35	0.60	\	\	
			Mean	12.3	0.40	0.60	\	\	
			High	14.3	0.45	0.60	\	\	
	Trilinear	3.48	Low	10.5	0.64	\	0.16	0.23	0.65
			Mean	11.5	0.74	\	0.18	0.25	0.65
			High	12.5	0.84	\	0.2	0.27	0.65

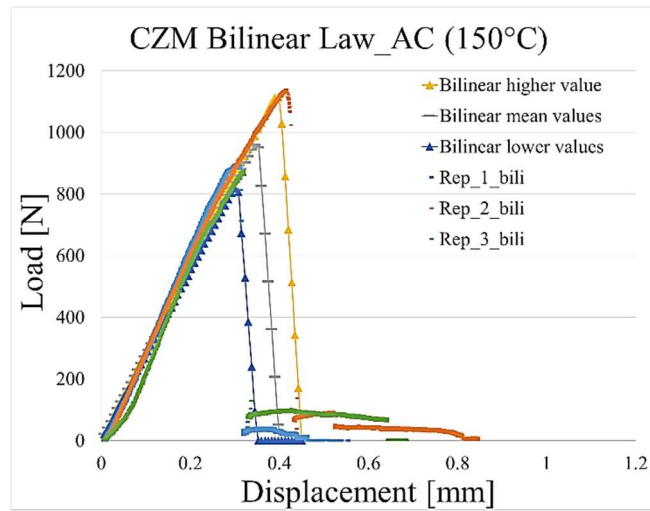


Figure 2.79 Bilinear model for specimens of the level AC

The comparison in Figure 2.79 between experimental and the bilinear cohesive zone model showed high variability of the maximum strength T_n^{max} . However, this trend was recognized in all the experimental trials. The model fits well the linear elastic range.

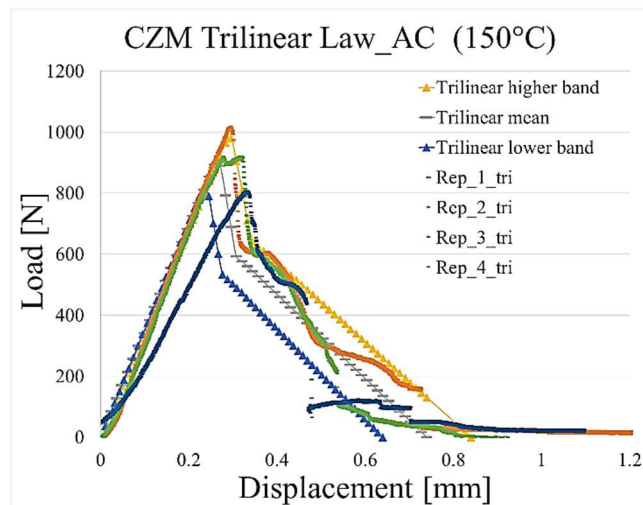


Figure 2.80 Trilinear model for the specimens of the level AC

The comparison in Figure 2.80 between experimental and the trilinear cohesive zone model showed high variability of the maximum strength T_n^{max} . However, this trend was recognized in all the experimental trials. The model fit well the linear elastic range except one trials that showed a longer adjustment and a slope less steep. Although the experimental behavior in the fiber bridging range is not linear, the model is prone to linearize the trend because of its formulation. The experimental curve is included within the scatter bands.

The variability in the experimental graph could be due to the limited and thin area where the stem overlaps the laminate. Since the thickness of the stem and the width of the yarn have the same dimension, the interface can overlays a random portion of the laminate that can include areas where the yarn is exposed and other that are occupied by the matrix that are located at the edge of the zones where the weft cross the warp. The above consideration are valid for all the trials and are deepened in the paragraph 2.9.

The less performant specimens (uniform heating)

The experimental results shown that the less performant specimens, where the welding strength was the lower, were overmolded with a melt temperature of 220°C, a mold temperature of 80°C and a holding pressure of 100 bar. This level is called O. Seven specimens were tested and they show two different experimental behavior:

- 4 repetitions showed a brittle breakage and they were modeled with a bilinear law
- 3 repetitions showed the fiber-bridging and they were modeled with a bilinear law

The results of the sensitivity analysis and the G_{IC} are summarized in Table 2.35.

Table 2.35 Cohesive zone parameters for the level O of the hybrid T-joint specimens manufactured with the laminates provided at 150°C (uniform heating)

Level	Law	G_{IC} [J/mm ²]		T_n^{max} [MPa]	δ_n^c [mm]	α δ_n^*/δ_n^c	δ_n^* [mm]	δ_n^{fb} [mm]	α_σ T_n^{fb}/T_n^{max}
O	Bilinear	1.51	Low	7.3	0.32	0.55	\	\	\
			Mean	8.8	0.35	0.55	\	\	\
			High	10.3	0.38	0.55	\	\	\
	Trilinear	2.46	Low	7.8	0.75	\	0.21	0.26	0.65
			Mean	8.5	0.9	\	0.24	0.29	0.65
			High	9.2	1.05	\	0.25	0.31	0.65

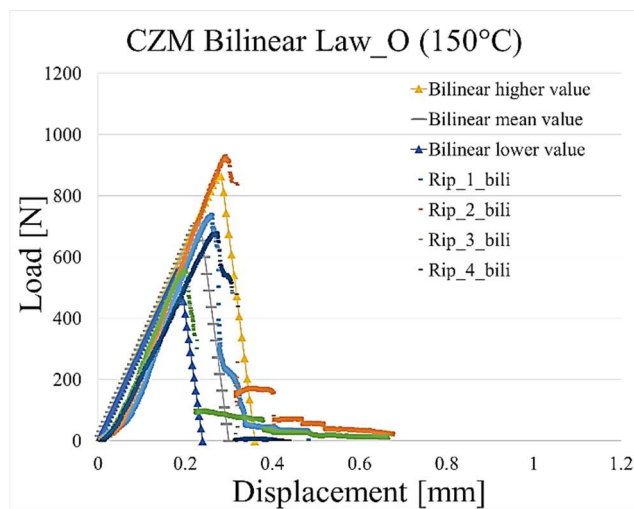


Figure 2.81 Bilinear model for the specimens of the level O

The first part of the elastic range in Figure 2.81 shows the adjustment of the specimen on the lower plane of the clamping system. However, the model fits well the linear elastic range and the scatter bands are able to contain the experimental variability. The comparison shows that the final parts of the experimental data are cut-off by the cohesive model. This choice allows to avoid more complex laws for the modeling of the behavior and it is on the safe side.

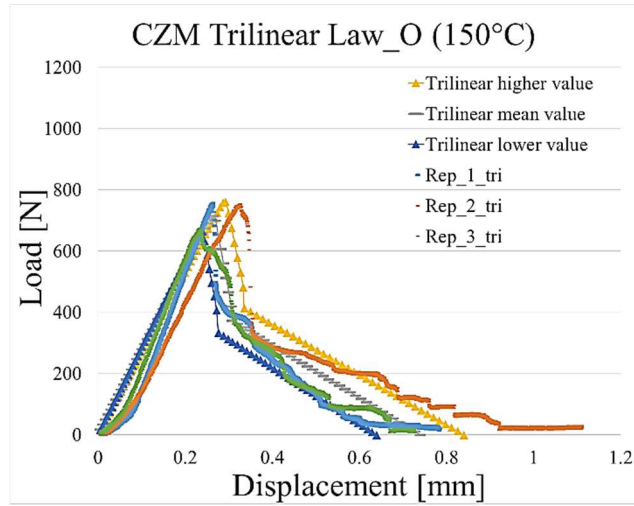


Figure 2.82 Trilinear model for the specimens of the level O

The model in Figure 2.82 fits well the linear elastic range. Although experimental behavior in the fiber bridging range is not linear, the model is prone to linearize the trend because of its formulation. The experimental curve is included within the scatter band.

The comparison of the experimental results, which were modelled and simulated by the bilinear and the trilinear law, highlights that the specimen that showed a brittle fracture have higher values of maximum traction force T_n^{max} whereas the specimens that shoed fiber bridging have higher value of the strain energy release rate G_{IC}

2.8.2 Modeling of the behavior of specimens with local heating of the laminate

The most performant specimens (local heating)

The experimental results shown that the most performant specimens, where the welding strength was the higher, were manufactured by providing the laminate after local heating and overmolding with a melt temperature of 260°C, a mold temperature of 80°C and an holding pressure of 200 bar. This level is called AC_{local}. Seven specimens were tested and they show the same experimental behavior:

- 7 repetitions showed a brittle breakage and they were modelled with a bilinear law

The results of the sensitivity analysis and the G_{IC} are summarized in Table 2.36.

Table 2.36 Cohesive zone parameters for the level AC_{local} of the hybrid T-joint specimens manufactured with the laminates provided at 135°C (local heating)

Level	Law	G_{IC} [J/mm ²]	T_n^{max} [MPa]	δ_n^c [mm]	α δ_n^*/δ_n^c	δ_n^* [mm]	δ_n^{fb} [mm]	α_σ T_n^{fb}/T_n^{max}
AC _{local}	Bilinear	1.42	Low	6.95	0.29	0.55	\	\
			Mean	8.25	0.35	0.55	\	\
			High	9.55	0.41	0.55	\	\

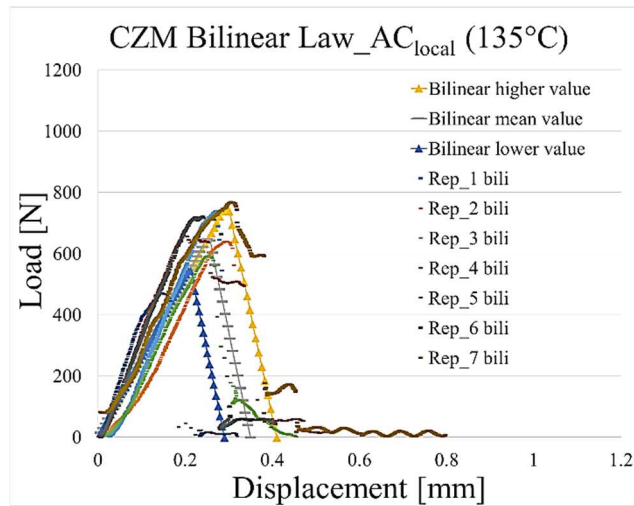


Figure 2.83 Bilinear model for the specimens of the level AC_{local}

The comparison in Figure 2.83 between experimental and cohesive zone model showed high variability of the maximum strength T_n^{max} . The model averagely fits the linear elastic range and the scatter bands are able to include most of the delamination ranges.

The less performant specimens (local heating)

The experimental results shown that the less performant specimens, where the welding strength was the lower, were manufactured by providing the laminate after local heating and overmolding with a melt temperature of 220°C, a mold temperature of 130°C and an holding pressure of 100 bar. This level is called B_{local} . Seven specimens were tested and they show two different experimental behavior:

- 3 repetitions showed a brittle breakage and they were modeled with a bilinear law
- 4 repetitions showed the fiber-bridging and they were modeled with a bilinear law

The results of the sensitivity analysis and the value of G_{IC} are summarized in Table 2.37.

Table 2.37 Cohesive zone parameters for the level B_{local} of the hybrid T-joint specimens manufactured with the laminates provided at 135°C (local heating)

Level	Law	G_{IC} [J/mm ²]	T_n^{max} [MPa]	δ_n^c [mm]	α δ_n^*/δ_n^c	δ_n^* [mm]	δ_n^{fb} [mm]	α_σ T_n^{fb}/T_n^{max}	
B_{local}	Bilinear	1.31	Low	4.8	0.45	0.45	\	\	
			Mean	5.3	0.5	0.45	\	\	
			High	5.8	0.55	0.43	\	\	
	Trilinear	1.54	Low	5.2	0.14	\	0.14	0.2	0.65
			Mean	6.6	0.18	\	0.18	0.23	0.65
			High	8	0.22	\	0.22	0.26	0.65

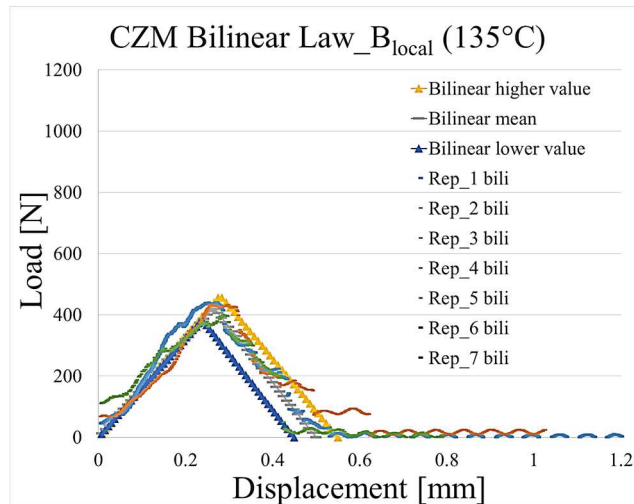


Figure 2.84 Bilinear model for the level B_{local}

The graph in Figure 2.84 presents an obvious initial adjustment of the load, while the delamination is not abrupt, but rather gradual. The model fit well the experimental data. One of the trials has an atypical trend in the elastic range that presumed to be due to the upper surface of the laminate that did not fit the lower plane of the clamping system. A second test shows a hint of trapezoidal behavior, but given the shortness of the constant section, it was decided to fit the data with a bilinear law. In this case, the interfacial mechanical strength is slightly underestimated. The dispersion band in the delamination range can include all the data. It is noteworthy how the experimental data of some trials, in the range of delamination, show several sudden drops. It is supposed that it may be due to the gradual distribution of the mechanical strength between the matrix and the fibers.

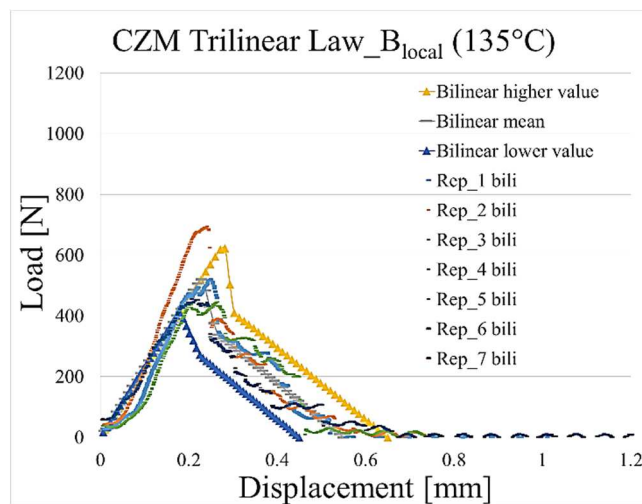


Figure 2.85 Trilinear model for the level B_{local}

The graph in Figure 2.85 shows the presence of an outlier. The first part of the elastic range shows the adjustment of the specimen on the lower plane of the clamping system. However, the model can fit well the experimental data. The dispersion band in the delamination range can include all the experimental data.

In this case, the comparison of the experimental results that were modeled and simulated by the bilinear and the trilinear law is in contrast with the previous results. By neglecting the outlier, the comparison highlights that the specimens that showed a brittle fracture and

the one that showed the fiber bridging have a similar values of the maximum traction force T_n^{max} whereas the latter showed a higher values of the strain energy release rate G_{IC} .

2.8.3 Modeling of the behavior of specimens with local heating and cooling of the laminate

The experimental data are the results of the tensile test of the specimens manufactured by providing the laminate after local heating and subsequent cooling down. The laminate were overmolded with melt temperature of 260°C, mold temperature of 80°C and holding pressure of 200 bar. This level is called M. Seven specimens were tested and they show the same experimental behavior:

- 7 repetitions showed a brittle breakage and they were modeled with a bilinear law

The results of the sensitivity analysis and the G_{IC} are summarized in Table 2.38.

Table 2.38 Cohesive zone parameters for the level M of the hybrid T-joint specimens manufactured with the laminates provided after local heating and cooling down

Level	Law	G_{IC} [J/mm ²]	T_n^{max} [MPa]	δ_n^c [mm]	α δ_n^*/δ_n^c	δ_n^* [mm]	δ_n^{fb} [mm]	α_σ T_n^{fb}/T_n^{max}
M	Bilinear	1.22	Low	6	0.26	0.55	\	\
			Mean	7.8	0.32	0.55	\	\
			High	9.6	0.38	0.55	\	\

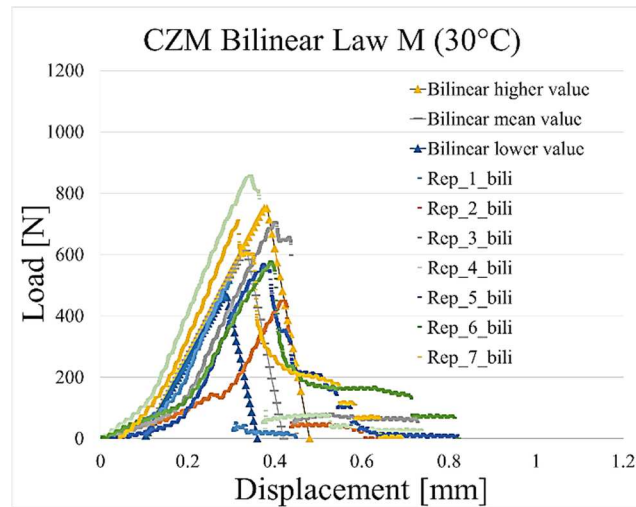


Figure 2.86 Bilinear model for the specimens of the level M

In this case, the longer adjustment phase is due to laminate surface because the heated and cooled area is larger than the real interface and the matrix that is surfaced interferes with the lower plan of the reference plate of the clamping system. However, thanks to the Matlab script, this occurrence was neglected by translating the cohesive zone model on each experimental graph. The model in Figure 2.86 well replicates the linear elastic range and the scatter bands are able to include most of the experimental data but the maximum and the minimum values of T_n^{max} are outside them.

2.8.4 Modeling of the behavior of specimens with laminate “as provided”.

The experimental data are the results of the tensile test of the specimens manufactured by providing the laminate without heating. The laminate were overmolded with melt temperature of 260°C, mold temperature of 80°C and holding pressure of 200 bar. This level

is called V. Seven specimens were tested and they show two different experimental behaviors:

- 5 repetitions showed a brittle breakage and they were modeled with a bilinear law
- 2 repetitions showed the fiber-bridging and they were modeled with a trapezoidal law

The results of the sensitivity analysis and the G_{IC} are summarized in Table 2.39. The trapezoidal law, differently from the laws used until now, require the sensitivity analysis for the definition of the horizontal section that is defined by α_σ and δ_n^{fb} . The trilinear law can be equated to a particular formulation of the trilinear law where the damage initiation is postponed and $T_n^{fb} = T_n^{max}$. The fictitious value is indicated with the apex. The sensitivity analysis was performed by the user varying T_n^{max} and δ_n^{fb} .

Table 2.39 Cohesive zone parameters for the level M of the hybrid T-joint specimens manufactured with the laminates provided without heating (“As provided”)

Level	Law	G_{IC} [J/mm ²]		T_n^{max} [MPa]	δ_n^c [mm]	α δ_n^*/δ_n^c	δ_n^* [mm]	δ_n^{fb} [mm]	α_σ T_n^{fb}/T_n^{max}
V	Bilinear	1.15	Low	4.1	0.26	0.7	\	\	\
			Mean	6.5	0.36	0.65	\	\	\
			High	7.4	0.46	0.6	\	\	\
	Trapezoidal.	1.15	Low	5.40	0.35	\	0.14	0.20	1
			Mean	6.65	0.40	\	0.15	0.23	1
			High	8.90	0.45	\	0.16	0.26	1

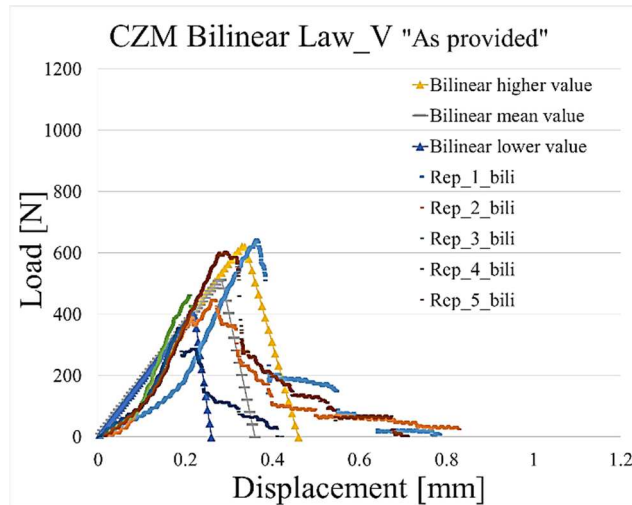


Figure 2.87 Bilinear model for the specimens of the level V

The first part of the elastic range in Figure 2.87 shows the adjustment of the specimen on the lower plane of the clamping system. However, the model can fit well the experimental data. The dispersion band in the delamination range can include all the experimental data until loads of 200 N. Given the small size of the load that the weld is still able to withstand, it was decided not to use the trilinear law.

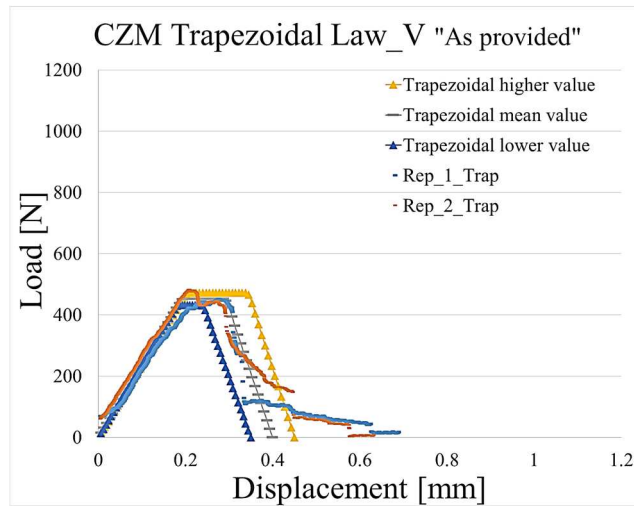


Figure 2.88 Trapezoidal model for the specimens of the level V

The trapezoidal model in Figure 2.88 is the only one that is able to fit well the experimental data. In this case, the trapezoidal model shows a small dispersion of the data and for the mathematical formulation it is not suitable to fit the rounded edges typical of experimental behavior. Despite the availability of only two experimental curves, it was decided to still provide a scatter band to uniform the discussion of the results.

2.8.5 Delamination of the analytical model

The series of pictures in Figure 2.89 describe the propagation of the normal cohesive stress at the interface related to the displacement of the tensile test. To the aim of this discussion, the displacement δ_n in the direction of the tensile test, which is called u by the program, test was discretized in sub-step of 0.004 mm.

The figure shows the born and the propagation of the crack until the complete separation that correspond to a displacement of 0.232 mm when the area is completely blue. The simulation allows to stop the displacement at each sub-steps and to evaluate the residual strength of the specimen. The higher the number of sub-steps the higher is the calculation time. If the delamination shows a brittle behavior, the dimension of the sub-step must be refined.

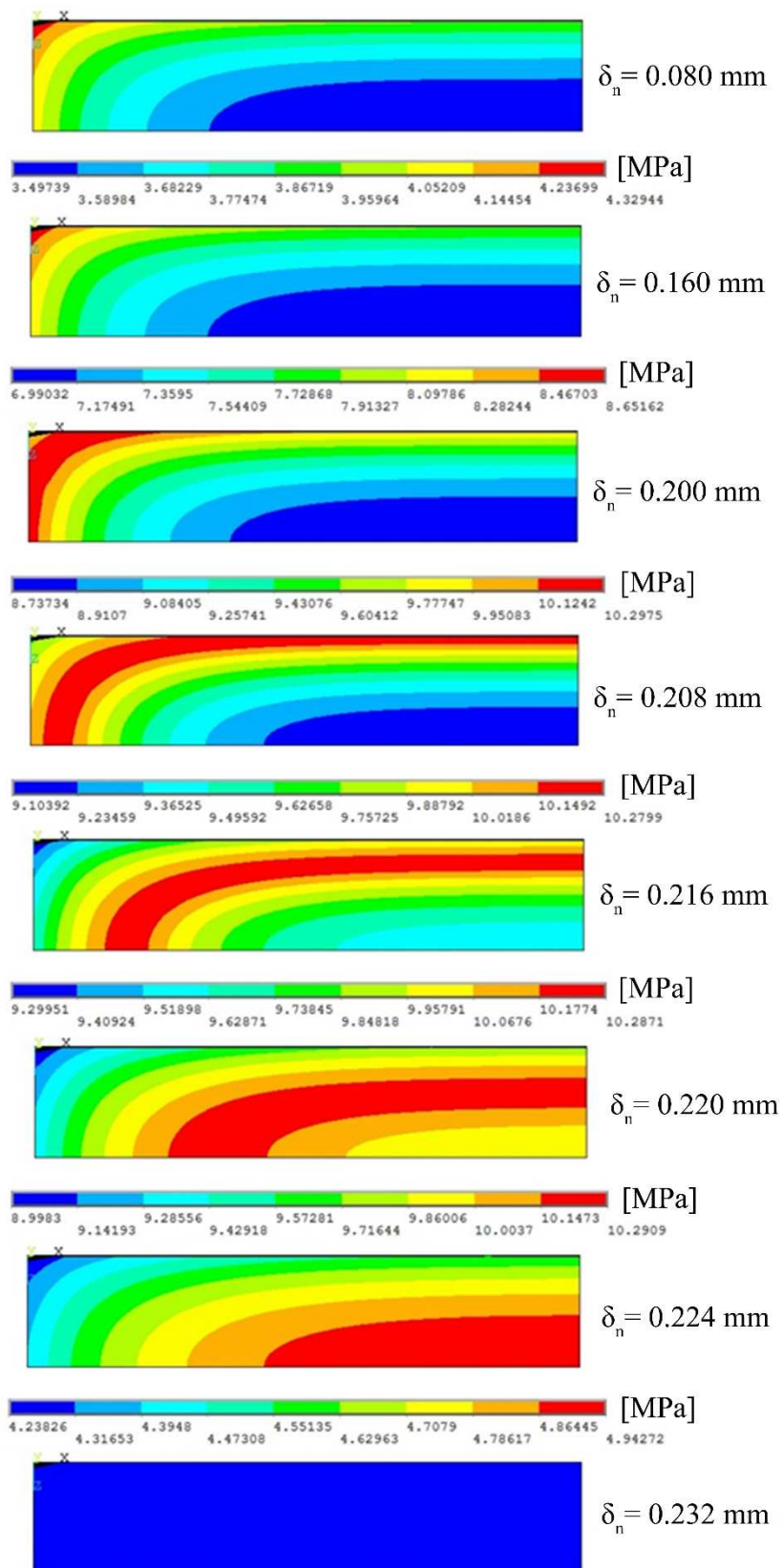


Figure 2.89 Modeling of the crack propagation

2.9 General discussion about the experimental behavior and modeling

Variability during the tensile test

The load-displacement graphs of the tensile test show high variability. The variability is noticeable both in the maximum load and in the behavior during the fracture propagation. The cohesive zone model were calibrated on the experimental results in order to describe the different behaviors and they are provided with a scatter band that include the data dispersion. However, the total number of the samples was limited to seven specimens or less, in dependence of the different kind of behavior that they showed during the test. The fracture area was investigated in order to understand the variability of the results and to highlight the factors that affect the behavior of the welding during the test. Two different typology of fracture area are shown in Figure 2.90 and in Figure 2.91. The laminate in Figure 2.90 results deprived of the matrix surface revealing a complete delamination of the first layer. Only a small portion of the yarn results cut and peeled in lower left-side corner.

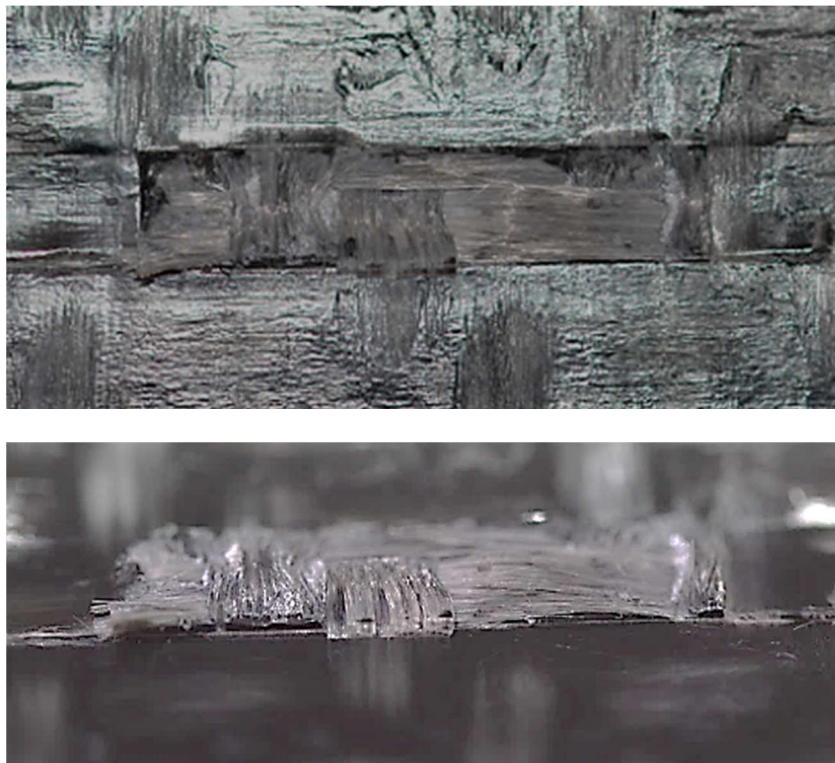


Figure 2.90 Delamination of the matrix and slight presence of fiber-bridging

The interface in Figure 2.91 shows a fiber yarn that was peeled by the stem. In this case is not clear the cause of the breakage of the yarn. The causes can be related both to the edge of the mold cavity, where the laminate is pushed during the mold closing, or directly due to the shear stress induced by traction of the stem. Moreover, it can be noticed that the weft is surfaced in correspondence of the shorter side of the interface (yellow circle). However, the experimental behavior of this specimen was modelled with a trilinear law.

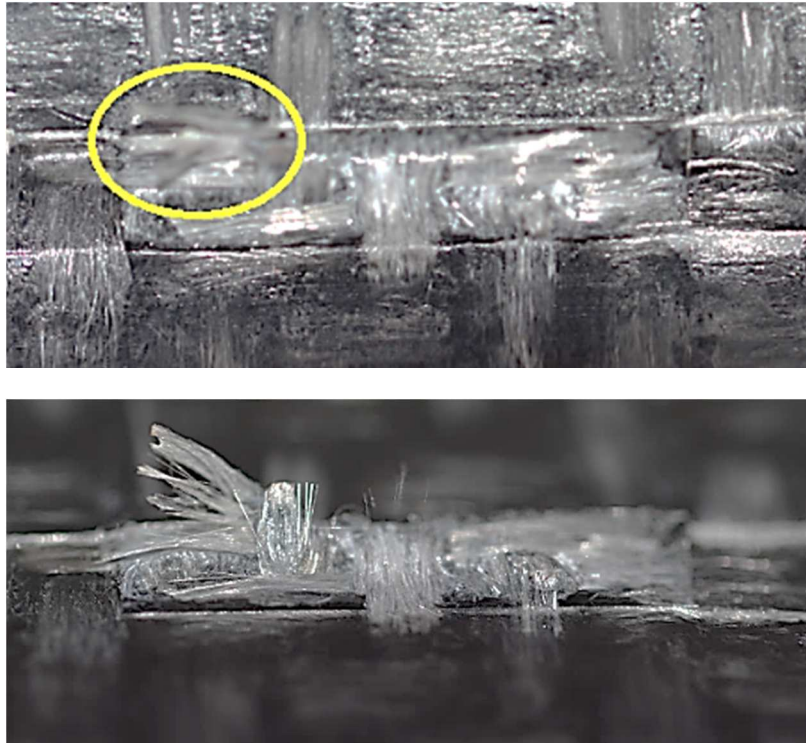


Figure 2.91 Fiber peeled out by the stem

The overlapping of the stem with the laminate, and in particular with the woven morphology, highly affects the behavior of interface during the test and it is crucial for determining the welding resistance. Since the thickness of the stem and the width of the yarn have the same dimensions, the interface can overlays a random portion of the laminate that can include areas where the yarn surfaces and some other that are occupied by the matrix, which are located at the edge of the zones where the weft cross the warp. In Figure 2.92 is provided an example of 6 different overlapping cases. The high variability of behavior, in the maximum strength T_n^{max} and in the delamination propagation, can be explained by a gradual distribution of the mechanical strength between the fibers and the matrix.

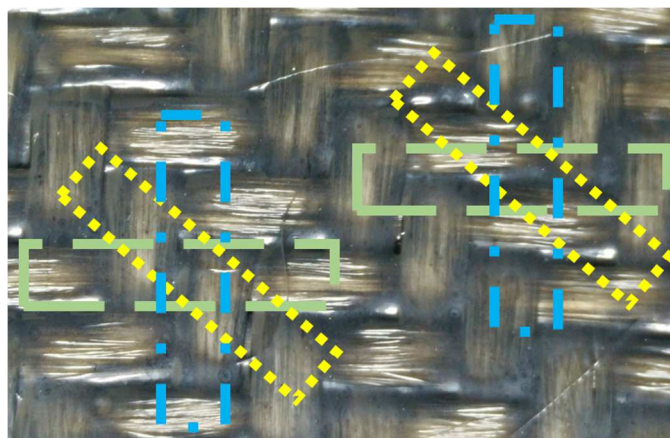


Figure 2.92 Examples of overlapping of the interface on the woven fabric

With reference to Figure 2.93, two typical area can be distinguished. The zones marked with green indicator represent the portion rich of matrix, where the injected stem can create a deeper welding. The red indicators highlight the area where the weft yarn surfaces in

correspondence of the shorter side of the interface. In this area, where the stress is higher and concentrated, the welding is poor of matrix and the delamination is promoted.

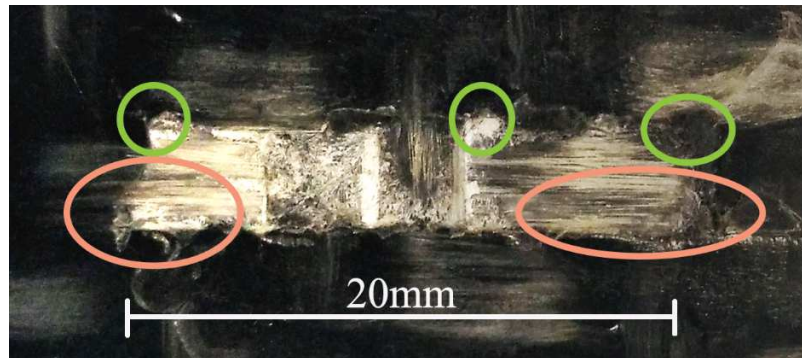


Figure 2.93 Morphological details of the surface of the fracture

Depending on how the overinjected material can create a physical interlocking between the fibers of the yarn, the fiber bridging is promoted. Indeed it is promoted especially when the laminate is provided to the cycle at temperature above the crystallization point (local heating with the screen and uniform heating). In this case, the laminate can swell inside the cavity and the small void produced inside the yarns and between the fibers are filled by the overinjected material. During the tensile test, the interlocking applies a shear stress to the fiber and provoke the fiber bridging. High stress can break the fibers.

Contrarily, when the laminate was provided at environmental temperature, the delamination phenomenon was promoted as is shown in Figure 2.94. The modeling of the experimental behavior of the specimens manufactured with the “as provided” laminate and with the laminate after heating and cooling used only the bilinear and the trapezoidal law.

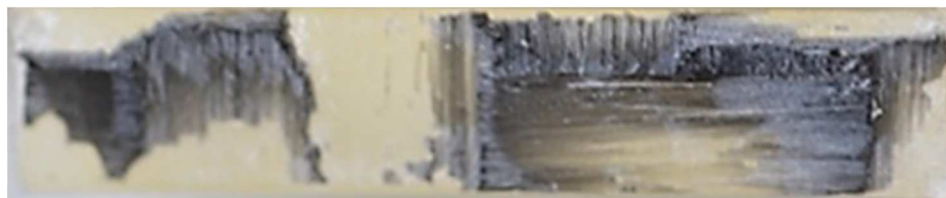


Figure 2.94 Surface of the fracture on the stem's side of the hybrid T-joint specimen manufactured with laminate “as provided”.

In the industrial practice, the edges at the base of the overinjected ribs are rounded. Otherwise, the interface is provided with an extended base. In this work, the nominal area was kept constant along the stem in order to investigate the real behavior of the interface and provide a careful description. However, the consideration could be helpful if it were used in the design of the area of the part where the delamination can start.

Consideration about strain energy release rate G_{IC}

In this work, it was determined the strain energy release rate by mode I opening test that were performed on DCB specimen. In a preliminary work, the same energy was attributed to the T-joint specimen because of the theoretical pure mode I opening. The choice was justified by the presence of the black matrix of the laminate on the stem-side interface.

The reference value was:

$$G_{IC} = 1.05 \pm 0.10 \text{ J/mm}^2$$

The hypothesis of a mode I fracture was based on the reciprocal movement during the tensile test that is orthogonal to the interface. In Table 2.40 Values of G_{IC} for the specimens modeled with the bilinear law are summarized the G_{IC} value that are determined by the finite element analysis of the specimens that was modelled with a bilinear law. Otherwise, the trilinear law is discussed later because it differs from the behavior that was noticed in the DCB specimens.

Table 2.40 Values of G_{IC} for the specimens modeled with the bilinear law

Level	V	M	A local	B local	A	B
G_{IC} [J/mm ²]	1.15	1.22	1.42	1.31	2.43	1.51

The G_{IC} values differs from the DCB result except in the case of the specimens manufactured by overmolding of laminates that were provided without significant modification of the interface. The discrepancy from the reference value is due to the change of the morphology induced by the mold closing. Because of this observation, with the exception of the levels V and M, is appropriate to indicate the strain energy release rate with the notation G_C . The micro x-ray investigation that were presented in the paragraph 2.7.2, show a progressive increase of the interface area due the higher swelling of the woven inside the cavity. Higher the temperature of the laminate, higher the swelling is during the mold closing. The increased curvature of the interface where the drops of unreinforced material are present, differ from the CZM interface morphology where the crack propagation is confined between two regular ply of glass woven.

The changes of the morphology induce a delamination that is better described by a mixed-mode. The G_C can describe the increase of energy dissipated during the test. The increase of G_C due to the variation of the opening mode is resumed in Figure 2.95 where the graph shows an example with the trilinear law.

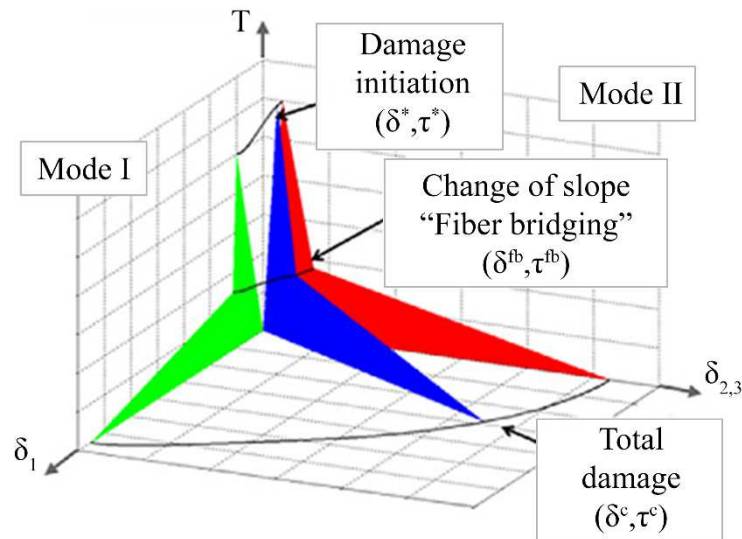


Figure 2.95 Influence of the opening mode on G_C [43]

The value of G_C increases gradually from mode I opening to mode II. The blue area, which represents G_C , is higher than the green one that represents G_{IC} . The same concept was expressed and experimentally verified also in [61] where it is reported that the strain energy release rate for mode II G_{IIC} can be from 2 up to 10 times the values for mode I G_{IC} . As concluded in [62] the lower values are referred to ductile materials, as in the case of

thermoplastic material such the polypropylene, and the higher one are referred to the thermosetting materials.

Moreover, as shown in [63] the residual stress, which is induced by the process, can play a significant role in promoting the fracture propagation and decrease the value of the G_C . In Table 2.41 Values of G_C for the specimens modeled with the trilinear law and the values of G_{IC} for the specimens modeled with the trapezoidal law are reported the G_C value from the modeling and the numerical simulation of the specimens that showed the trilinear and the trapezoidal behavior.

Table 2.41 Values of G_C for the specimens modeled with the trilinear law and the values of G_{IC} for the specimens modeled with the trapezoidal law

Level	V	M	A local	B local	A	B
G_C [J/mm ²]	/	/	/	1.54	3.48	2.46
G_{IC} [J/mm ²]	1.15	/	/	/	/	/

The G_{IC} value obtained by calibrating the trapezoidal model, which was used for the level V, shows agreement with the value obtained by calibrating the bilinear model and also with the value of the DBC specimen. The concordance of the value is due to the lack of both the modification of the interface morphology and the lack of fiber bridging. This demonstrate that the change of the cohesive law does not affect the G_{IC} because it is a characteristic of the cohesive material.

3 Measurement of the fiber length distribution

The use of fiber-reinforced composites is increasing in different fields, including the materials reinforced with discontinuous glass fibers. The length of the reinforcing fibers is closely linked to the increase of the mechanical properties of the material, the more the fibers long the higher the composite performance, i.e. the better are its mechanical properties, in particular the tensile strength and the elastic modulus.

It has been shown by previous studies as the transformation process by injection molding yields the breakage of glass fibers, reducing the benefit provided by the presence of the reinforcement. In order to provide these and other features of the composite materials there is a great interest in measuring and predicting the residual fibers length in the composite subsequently to the injection molding process. The proposed work has the objective of validating a new method of acquisition of images through the use of an optical scanning device and the automatic measurement of the length of the fibers through the ctFIRE software.

It was determined the uncertainty of the fibers length measurement using an adapted version of the standard used for coordinate measurement machines (UNI EN ISO 15530-3: 2011), through calibration of a sample of fibers using a CMM equipped with video sensor and using an optical acquisition device.

It was also extended the calculated measure of the uncertainty of fibers samples of larger dimensions, in which the length of each fiber was manually measured using the software ImageJ. Eventually, two cases of studies are proposed: the first evaluates the actual breakage of fibers during plasticating phase of the injection molding process, by measuring the length of fibers in samples extracted at different distances from the beginning of the plasticating screw. In the second case a number of samples were drawn from various sections of an automotive component, highlighting the variation of the average length of the fibers as a function of the flow advancement. The method developed has enabled the analysis of a large amount of fibers in a shorter amount of time than the traditional approach, allowing a fast compilation of statistics on the average residual measure of the fibers, with relative uncertainty, during and after the process.

3.1 Dependency of polymer properties on the length of the fibers

The properties of reinforced polymers depend on the type of polymeric matrix, the reinforcement material, the volume fraction, the size, the orientation, shape and distribution of the fibers. Longer fibers transmit the loads through the matrix in a better way than shorter fibers. Seminal studies by Thomason J.L. [1-8] show that increasing the length and concentration of the fibers in the polymer matrix yields an increase of the mechanical properties up to a volume fraction of 40-50%, after which the trend starts decreasing, reaching the same values of the non-reinforced matrix (Figure 3.1, Figure 3.2 and Figure 3.3).

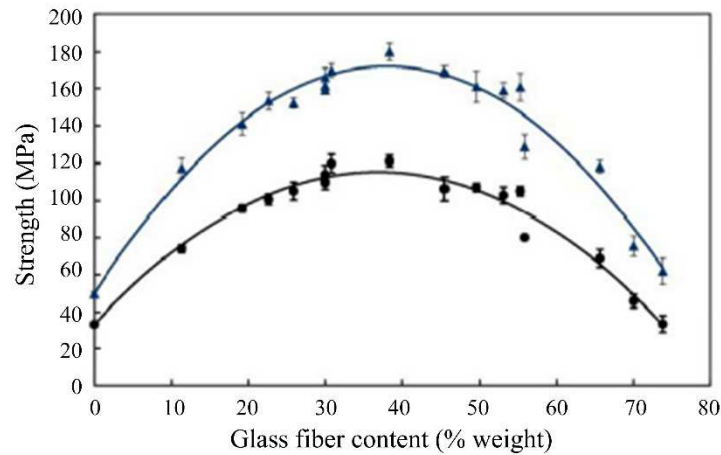


Figure 3.1 Tensile strength (in blue) and flexural strength (in black) vs. fibers content [3].

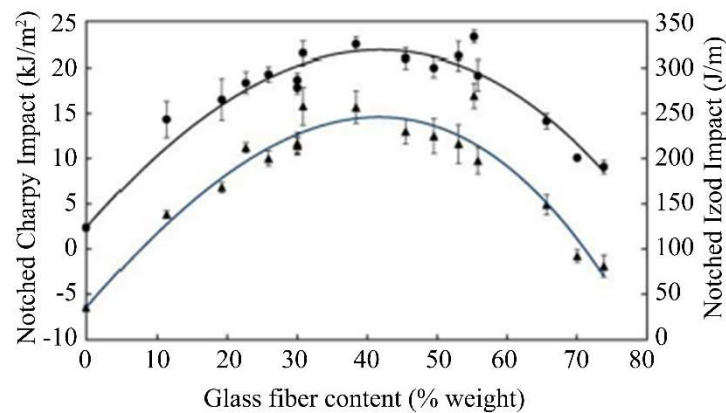


Figure 3.2 Charpy (in blue) and Izod (in black) resilience vs. fibers content [4].

The Kelly-Tyson model describes the correlation between tensile strength and the characteristics of the polymer, such as the matrix-fiber interface forces, volume fraction of the fibers and the fibers length. Thomason verified that this model is consistent with the experimental results only for a range of low volume fractions and it fails to describe the interactions between fibers in composites at higher concentrations.

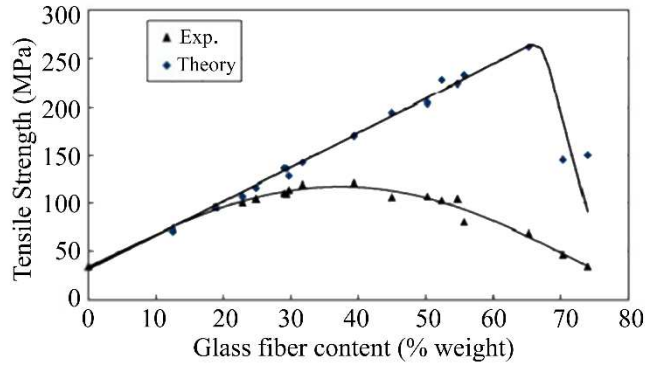


Figure 3.3 Fitting of the Kelly Tyson model [8].

The Kelly Tyson model [8] also predicts that the mechanical properties are influenced not only by the concentration of the fibers, but also by the orientation of the fibers and their length.

The increase in the length of the fibers increases the mechanical properties up to a critical level, after which the values remain constant (Figure 3.4). The critical levels differ for each mechanical property: stiffness reaches 90% of its maximum with fibers 1 mm long. The tensile stress at break reaches 90% of its maximum with fibers 7 mm long while the resilience for fibers 16 mm long. This fact shows that the critical length of the fibers in a composite must be evaluated considering its different mechanical properties.

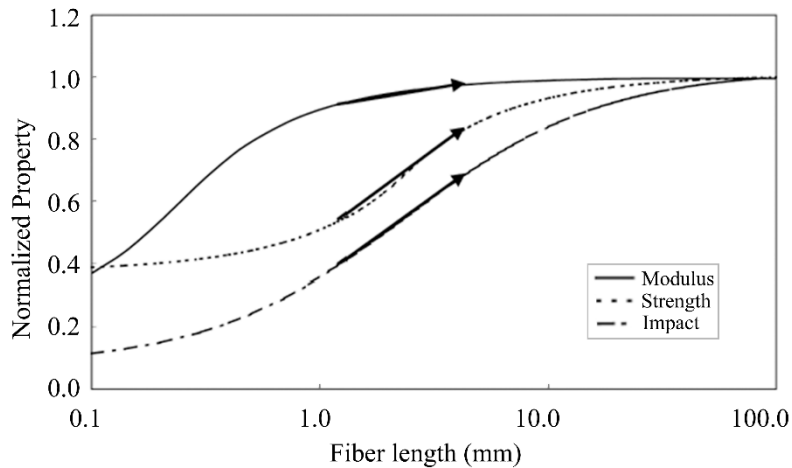


Figure 3.4 Mechanical properties vs. normalized fiber length [8].

One of the important parameters that affect the mechanical properties and the value of the critical fiber length is the adhesion strength at the interface. Adding additives, such as a compatibilizer, during the impregnation of the fibers increase the tensile strength from 6 to 10% can be obtained as shown in Figure 3.5.

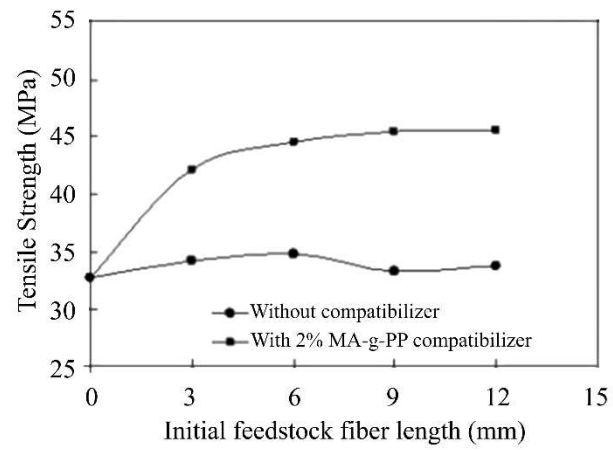


Figure 3.5 Effect of fiber length on tensile strength with and without compatibilizer [9].

3.2 Traditional experimental procedure for fiber length distribution measurement

To study the effect of the process on degradation of the fibers length in polymer composites, it is necessary to define a robust procedure to get the fibers length distribution in the sample after processing.

The traditional methodology is expensive and very time consuming, but it is the most used in this kind of experiments because it is still the only robust procedure for direct measurement of fibers length distribution. Indirect methods (e.g. based on impact resistance) are more convenient but normally they need to be calibrated, and they have low accuracy. Furthermore, they can be used to determine a single characteristic, for example an average value for the length, but not a complete distribution. The variation of the average length is often very small, so in order to determine the effect of process parameters on fibers length variation, the measurements must be highly accurate. Therefore indirect methods are not suitable, and the direct method, which will be described in next paragraphs, is the most used in experimental campaigns.

3.2.1 Pyrolysis

A small piece of material is taken from each sample. During this operation a portion of the central part of the sample is normally removed, avoiding both the initial and the final areas as possibly affected by transient phenomena (e.g. the opening and closing of the valve nozzle). To make a direct measurement of the fibers length it is necessary, as a first step, to eliminate the polymer matrix from the sample. Since the fibers constituting the reinforcement are resistant to high temperatures, unlike the polymer matrix, the separation is performed by heating the sample in an oven. The oven temperature is set up at about 700 °C and the sample, which was previously cut out, is put on a metal plate, which is positioned on a refractory stone inside the oven. The complete pyrolysis of the matrix requires less than four hours. At this point the plate with the fibers is picked up from the oven, it is placed gently on a second metal plate and allowed to cool for a few minutes before being able to put the portion of the fibers in a plastic container.

3.2.2 Ultrasound bath

When the residual fibers are removed from the oven, they are highly entangled, as they were in the initial composite sample. In these conditions it is not possible to measure their lengths because the entangled fibers form a three-dimensional structure that does not allow to discriminate each single fiber from the others. A small amount of fibers is taken from the sample using a pair of tweezers, trying to avoid the zone adjacent to the cut, since the fibers in this zone can be further damaged. In order to separate the fibers as much as possible, so that they will be easily recognizable and measurable, this small sample is put inside a glass slide for optical microscopy and some water is added. The slide is then immersed in an ultrasonic bath: the high frequency energy produced by an ultrasonic generator is converted into mechanical energy by special piezoelectric vibration systems and then transferred to the liquid bath. In this way millions of air micro bubbles are produced and they instantly collapse as a result of compression waves produced by ultrasonic vibration. In the bath high-energy pressure waves are generated, which can dissolve the entanglement of fibers inside the specimen without causing the breakage of the fibers themselves. Before inserting the slide into the bath, the former should be sealed with tape because the ultrasonic energy tends to open it, causing the dispersion of the fibers inside the water. The ultrasonic bath is equipped with an adjustable timer: treating each sample for 15 minutes allows the dispersion of the entanglement.

3.2.3 Image acquisition

The slide containing the fibers is taken from the ultrasonic bath and, once dried, it is posed in the center of the working area of an optical coordinate measurement machine (CMM). The image is focused on the fibers through the complex system of lights provided: three circular crowns of red LEDs that illuminate from above, a white light LED in the center of the crown and a white diascope light from below very useful to emphasize the contours of the objects to be measured. After focusing the image, a fiber is chosen and the measurement is taken by selecting the two edges of the fiber itself. In this way the software provided with the CMM takes the position (XYZ) of the two extreme points and then calculates the distance projected in three directions XYZ and the total one. This value is then used to make the calibration in the image analysis software. Since the measure of the length of the fiber is made from a two-dimensional image, the operator should check that the distance in Z direction between two extreme points of the fiber sample is null, otherwise a systematic error is induced in the measurement. To obtain a good calibration, the used fiber sample must be completely contained in the XY plane of the CMM.

Furthermore, to make a good calibration it is desirable that the sampled fibers are isolated from the others (or at least that their contact details are sufficiently clear to be selected without error). It is also preferable that the sampled fibers are long, so any error committed in the selection of its ends is spread over a larger length and thus the percentage error is smaller.

3.2.4 Image analysis

After calibration, from the fibers sample a set of images are acquired using the optical CMM. These images are successively imported in an image processing software. The image is initially modified using a series of filters, to highlight the exposure of the fibers against the background of the photo (Figure 3.6).

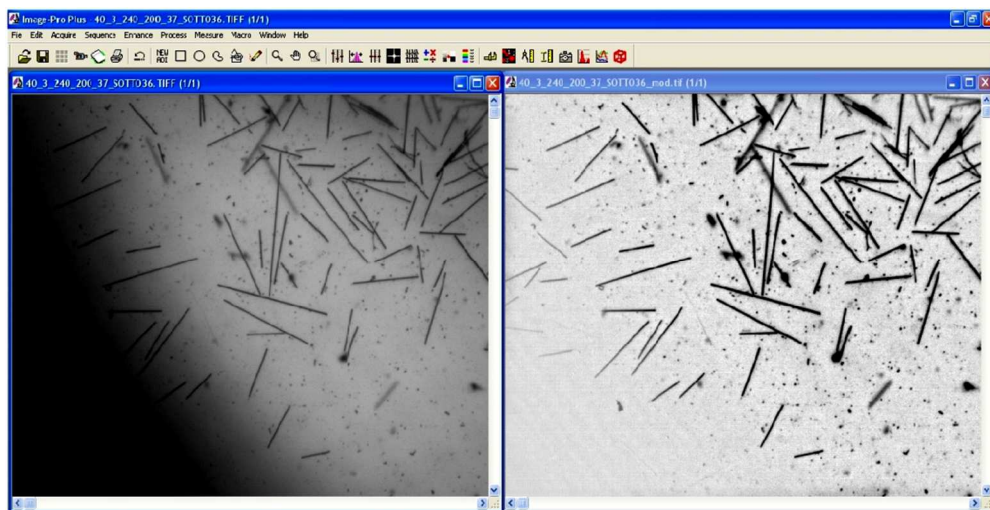


Figure 3.6 Example of image before and after digital filtering [10]

This can be done for every image acquired, and after that it is possible to proceed to the calibration of the measurement system. Figure 3.7 shows the reference fiber, which is highlighted to be recognizable, and the measure realized with the optical CMM. The fiber is measured using a line as comparator. It is possible to associate a measure in millimeters, performed with the CMM machine, to a measure in pixel, performed with the image analysis software. The scale factor so calculated can be used to scale all the other images of the same sample.

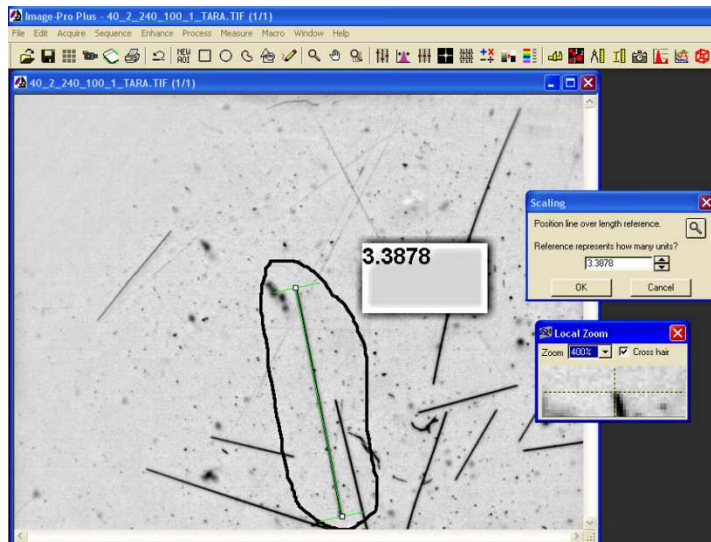


Figure 3.7 Scale factor determination with reference fiber [10]

It is then possible to measure all the fibers in all the images, tracing line or arc over the fibers. Figure 3.8 shows an example of fibers measurement on an image.

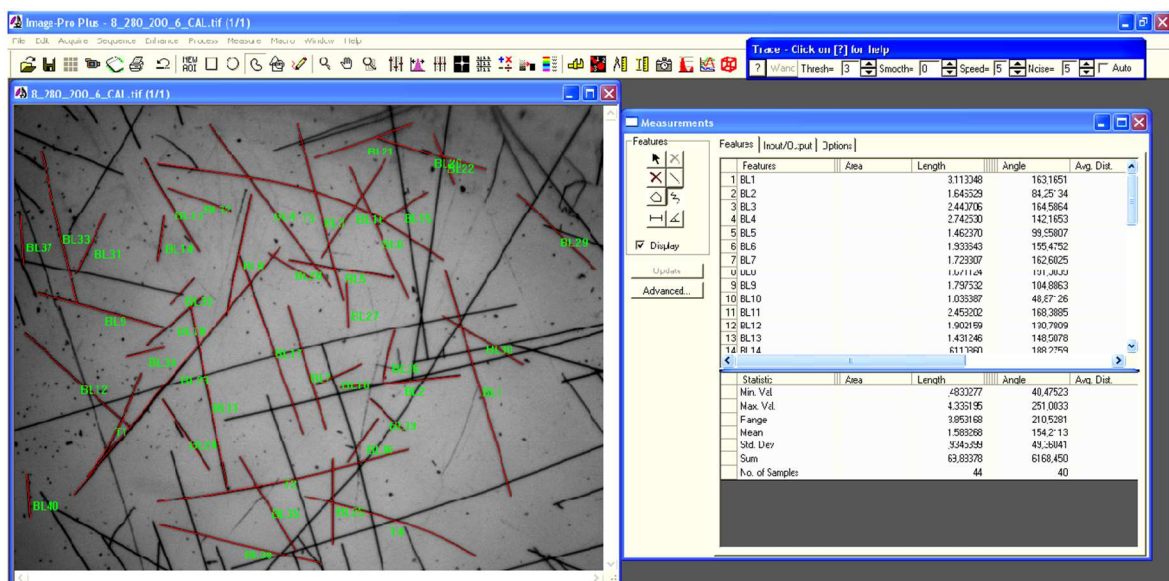


Figure 3.8 Example of fibers measurement [10]

3.2.5 Critical aspect of measurement procedures

As already mentioned, the purpose of the measuring procedure is to extract, from a sample obtained in specific process conditions, some information about the length of fibers contained within it. Processing this information, it is possible to report the breakage suffered by the fibers with the considered process parameters.

In order to obtain accurate results, all the above steps have to be carefully conducted, especially those considered more critical. The first critical aspect is the selection of fibers from the processed samples. It was already mentioned that when the portion of material is removed from the initial sample, the area at the edge of the sample must be avoided, to neglect transient phenomena. The initial part, for example, could be weakened by the process

conditions used in the molding of the previous sample. Furthermore, both the initial and the final area are subjected to further damage caused by the opening/closing nozzle.

Another step of particular importance is the picking of the fibers from the samples after burning the matrix. During this operation, the fibers must not be taken from the area near the cut made during the extracting of the sample, because the cutting could damage the fibers.

Another important aspect to consider in this step is the morphology of the fibers leaving the furnace. As already mentioned, at this stage the specimen presents a three-dimensional structure of strongly entangled fibers. In these conditions the extraction of the fibers without damaging them requires to operate as carefully as possible. Furthermore, inside the three-dimensional structure there are fibers whose length is extremely variable, from some micrometers to about one centimeter for the longer ones. Sampling with tweezers inevitably operates as filter for two main reasons. First, depending on the geometry of the part location the sample is taken (curve, straight, etc.) it is possible to get different length distributions. Second, the tweezers tips easily hold long fibers, but it is more difficult to get the shorter ones.

Since it is almost impossible to avoid such errors, it is necessary to try to reduce them as much as possible. To prevent that the area selected for the extraction of the fibers affect the final result, it is possible to get the fibers in different locations of the part, being careful not to stir too much the tweezers so limiting the loss of shorter fibers.

Another important step to analyze is the capturing of the images. Often this is done by searching for specific areas within the specimen, in which it is possible to capture a good number of fibers contained entirely in the size of the picture, and possibly not too tangled to facilitate the future operations of measurement. In particular, to get a good length distribution, 1000 fibers for each sample must be measured.

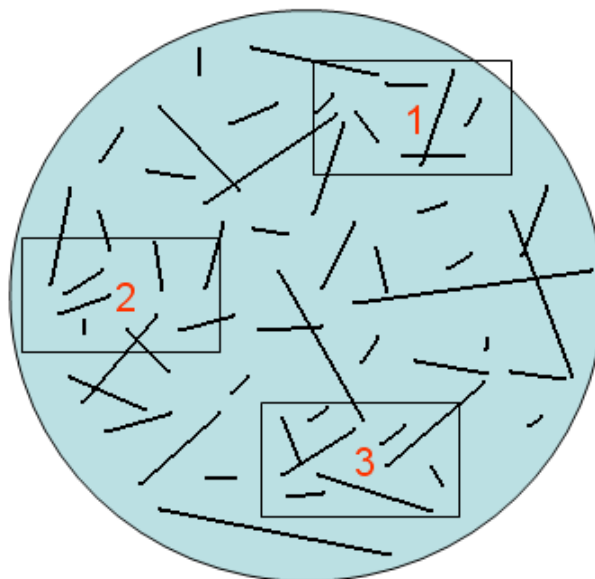


Figure 3.9 Scheme of fiber disposition on the slide and example of captured areas

In this way, however, a further filtering is inevitably performed on the fibers length distribution, because choosing one particular area rather than others can exclude from counting the fibers of the remaining zones, where the distributions of length can be very different from those of the chosen areas (Figure 3.9). In addition to this, the images captured

with the CCD of the CMM do not have dimensions comparable to those of the slide. Only the fibers wholly contained within the CCD area can be measured, but the length of fibers intersecting the edges of the image cannot be evaluated. This problem is obviously much more serious when the fibers to be measured are long and it affects the results even if the maximum length of the fibers in the slide is shorter than the field of view of the vision system. Since the probability of intersecting the edges of the image is larger for longer fibers than for shorter ones, the measurement returns an underestimation of average length value. This happens especially when there are several fibers in the slide, because increasing the density of the fibers facilitates the entanglements among the longer fibers. Usually these areas are so dense that it is very difficult to distinguish one fiber from another, as can be seen in Figure 3.10.

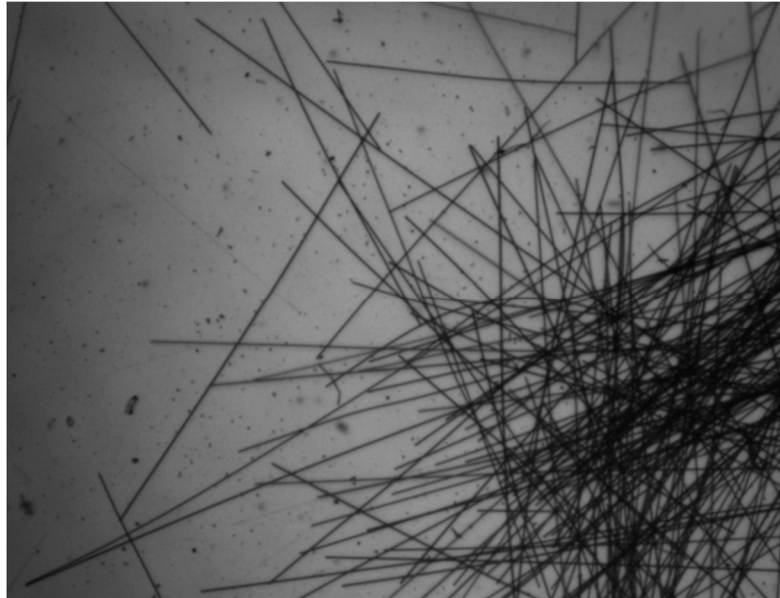


Figure 3.10 Example of fiber entanglement on the slide

3.3 Other technique for measuring of fiber length

Image mosaic technique

An additional method [11] has been developed for the accurate determination of the length of the fibers, through the analysis of an image obtained with the "image-mosaic" technique, which consists in automatically creating a large image from a series of smaller images (Figure 3.11). This method allows the analysis and the measurement of fibers of any length, eliminating the edge effect, namely that effect that occurs when too long fibers are out of the visual field of the acquisition system, in this case a CMM. Moreover, it can both determine the distribution of the lengths and the average length.

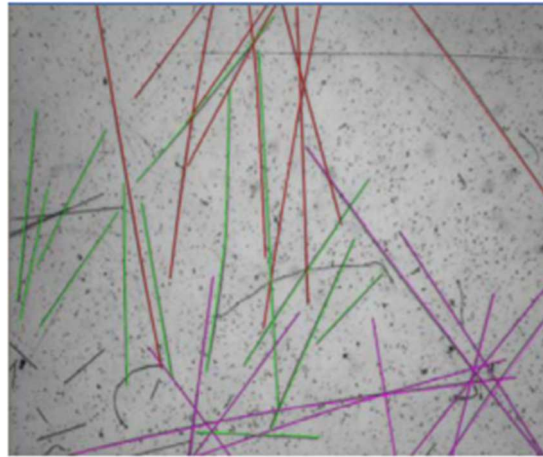


Figure 3.11 Example of not processable image because the fibers are not completely contained in the field of view of the instrument [11].

The "image-mosaic" technique can transform a sequence of images, which partially overlap, in a larger composition with a resolution that remains unchanged compared to the original images. The process that allows it to operate the optimal transformation is called image registration and, if the acquisition system allows precise shift, it turns into a redefinition of pixels coordinates with reference to a fixed coordinate system.



Figure 3.12 Example of "image-mosaic" technique [11].

In the example in Figure 3.12 you can see the fibers shown in the red selection longer on average than those in the blue selection. This technique therefore allows not to underestimate the average fiber length by measuring the entire length. In fact, following the traditional technique, in which images have a limited field of vision, the operator tends to measure only the fibers that fall completely in the image encountering an inevitable loss of information.

Use of a desktop scanner for image acquisition

An automatic technique for counting and the measuring fibers, which is very similar to the one proposed in this work, has also been used by Peter Hine and Bushra Parveen [12] in their experiments. Polypropylene samples reinforced with glass fibers were subjected to pyrolysis. The fibers were then dispersed on a transparent glass and scanned using a flatbed scanner. Counting fibers images were processed using ImageJ software, which allows to automatically recognize the straight fibers. Fibers that crosses each other and curved fibers were not automatically acquired but they were measured manually and then added to the statistics.

Experimental campaign of Pacific Northwest National Laboratory

An important experimental investigation aimed at accurately predict the orientation and distribution of the length of long carbon fibers in injection molded thermoplastic composites was initiated in 2012 by the Pacific Northwest National Laboratory (PNNL) and it is still ongoing [13]. The project aims to integrate, optimize and validate the models for fibers orientation and length distribution previously developed and implemented in the application Autodesk Simulation Moldflow Insight (ASMI) for long carbon fibers in injection molded thermoplastic composite. The Pacific Northwest National Laboratory, along with the University of Illinois and Autodesk Inc., has developed a unique system of algorithms that represents the state of the art for processes and constitutive models, in order to increase the capacity of commercial software applications to predict the orientation of the fibers and their length distribution, as well as the subsequent mechanical properties of the parts manufactured by injection molding. These predictive capabilities were validated on two-dimensional structures (plates) injection-molded starting from pellets with long glass fibers and polypropylene or polyamide matrix, with accuracy of results of 15%. The experimental investigation by the PNNL aims to make the already developed models more robust and efficient, to improve and integrate their implementation in Autodesk and also to validate the method for three-dimensional artifacts made of thermoplastic matrix reinforced with long carbon fibers and used by the automotive industry, specifically by Toyota Motor Engineering and Manufacturing North America. The measuring system of the fibers is managed by Purdue University, and it uses an optical microscope with motorized stage, able to obtain an image with high contrast and focus even with varying heights. The image is then processed using software application written in Matlab language, for measuring the length of the fibers. The system is able to recognize the fibers and to assign a number to each of them (Figure 3.13), and to create a representative graph of the fiber length distribution (Figure 3.14)

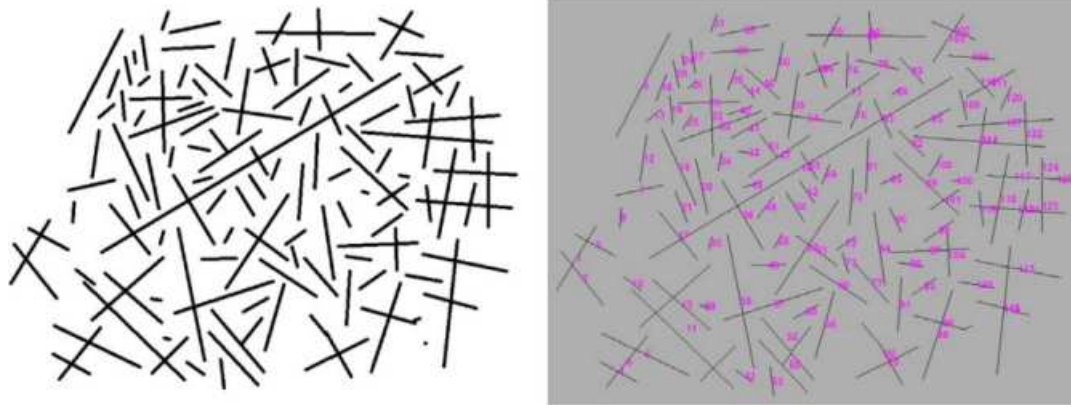


Figure 3.13 Automatic identification and labeling of a sample image with numerous cross fibers, using the software application used by Purdue University for PNNL [14].

The accuracy in the length of the fibers was determined using a precision requirement of 15%. The criterion was assessed by comparing the predicted and measured values of tensile and flexural moduli.

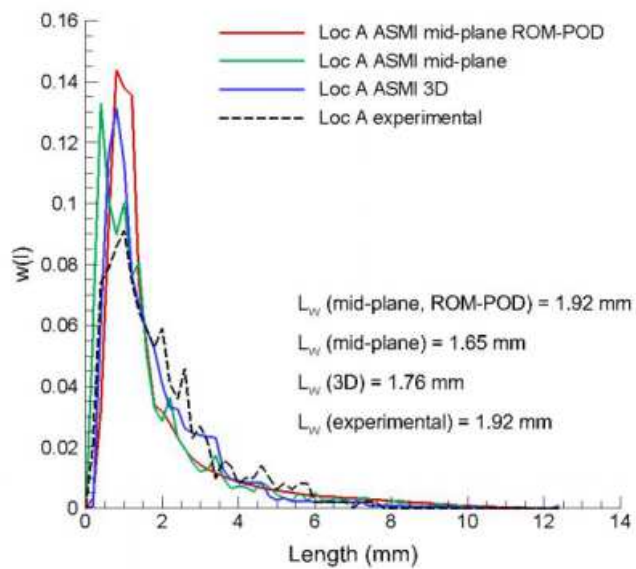


Figure 3.14 Distribution of the length of the fibers expected from simulations and experimentally measured [13].

3.4 Materials and methods

For the validation of the system, glass fibers coming from the pyrolysis of a specimen obtained by injection molding of Celstran GF30 have been used. The system has been applied to the study of the effects of the plasticating phase on the reinforcing fibers. In particular, the samples originate from specific zones, defined along the profile of the plasticizing screw at different distances from the hopper. The system has been successively optimized in order to reduce the background noise and to be able to determine the uncertainty to be assigned to the measure. The procedure, optimized and validated, has been applied to the measurement of fibers deriving from one of the previously analyzed plasticizing cycles and to a second industrial case, with the objective of evaluating the degradation of the fibers due to the different nozzle opening of a hot runner system.

3.4.1 Material

For the experimental campaign two materials were used, reinforced with glass fibers and having a thermoplastic matrix of polypropylene:

- *CELSTRAN PP GF30 02 (10 mm long fiber) used in the validation of the measuring system and the evaluation of the effects of plasticizing*
- *STAMAX 30YM240 (16 mm long fiber) used for the injection molding of a car spoiler.*

3.4.2 Experimental apparatus for the image acquisition

The method developed for the automatic measurement involves the use of an office scanner EPSON AcuLaser CX11 connected to a PC. The scanner is equipped with a CCD optical sensor (Charge-Coupled Device) and it has a maximum resolution of 600 dpi. The scanned image is then processed by the ctFIRE software, which allows automatic identification of the fiber length. Various trials have been made to reach a compromise between the following parameters:

- *Accuracy in the recognition of the fibers.*
- *Image processing time related to the resolution and size.*
- *Number of images to be processed.*

Too large images, which contain a high number of fibers, require long processing times, tending in some cases to yield available memory errors, making the analysis impossible using standard PC. Very small images, instead, allow quick processing but, due to resolution issues, they allow the analysis of only a few fibers, therefore increasing the operator's job to submit more samples to scan. A compromise was reached by scanning an A4-size glass, which the fibers were laid on, with a resolution of 600 dpi and a size of 5100 x 7019 pixels, obtaining color images having a size of 102 MB each. This large image is then appropriately cut into smaller of 971 x 971 pixels at 72 dpi, having a size of about 2.4 MB.

To overcome the limit of the length of the fibers, which does not always fall within the visual field of the microscope or any other image acquisition tool, a rubber grid (or template) was used, having dimensions of 220 mm x 310 mm with square holes of 20 mm side and 20 mm pitch (Figure 3.15).

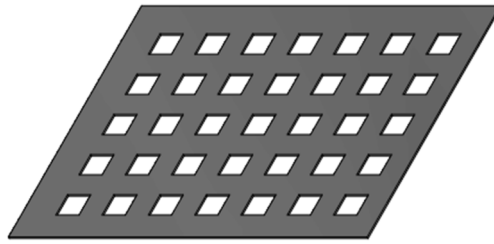


Figure 3.15 Rubber grid

Figure 3.16 shows the black box used for the scans. It is completely black painted and equipped with a bottom glass. The glass is integral with a black sheet. In the various calibration tests, this is the configuration that allowed the best image sharpness and the least amount of shadow. It can be noted the neoprene on the edge, having the function of completely isolating the glass with the fibers from external light during the scan.

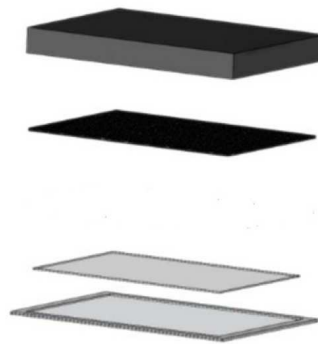


Figure 3.16 Black box

Procedures for spreading of the fibers

The rubber grid is located with respect to a reference system and positioned on the glass that will support the fibers in such a way that it is always aligned. This arrangement is important because the image processing procedure requires a precise image positioning, with a maximum error of a few millimeters. Once prepared the so composed tray, the fibers are manually scattered. This operation is the only one that requires an operator sensitivity and a certain initial training. The deposition of the fibers on the grid takes place dispersing them homogeneously on the entire surface. Some fibers will fall into the empty spaces, some others on the grid.

The choice of the fibers to be placed is arbitrary but must follow some precautions:

- *It should be a small amount of fibers withdrawn from the inside of a larger group.*
- *All collected fibers are deposited on the glass.*
- *The fibers are to be dispersed gently with the aid of small tools.*
- *The laboratory must not have air motions that lead the lightest fibers off the grid.*

Once deposited the fibers, a quick visual check is conducted by means of a lens in order to verify that all the empty spaces of the grid have been filled and they are not overly busy, otherwise the recognition by the software will fail. After performing these steps, the rubber grid and the paper are removed with slow movements, in order not to cause air movements that could affect the correct position on the glass fibers. Some of the fibers, located on the edge of the grid, will fall on the glass, occupying the surrounding space, which remains inside squares of 35 mm side. The glass with the fibers can then be placed on the scanner

and the image can be acquired. The result obtained, after thresholding, is similar to the one reported in Figure 3.17. The figure shows a portion of the glass with only 4 of the 35 filled openings. The effect is to obtain groups of fibers confined in a well-defined space to be able to then apply the automatic cutout software that, by nature of the method used, cannot recognize and measure fibers located close to the edge.

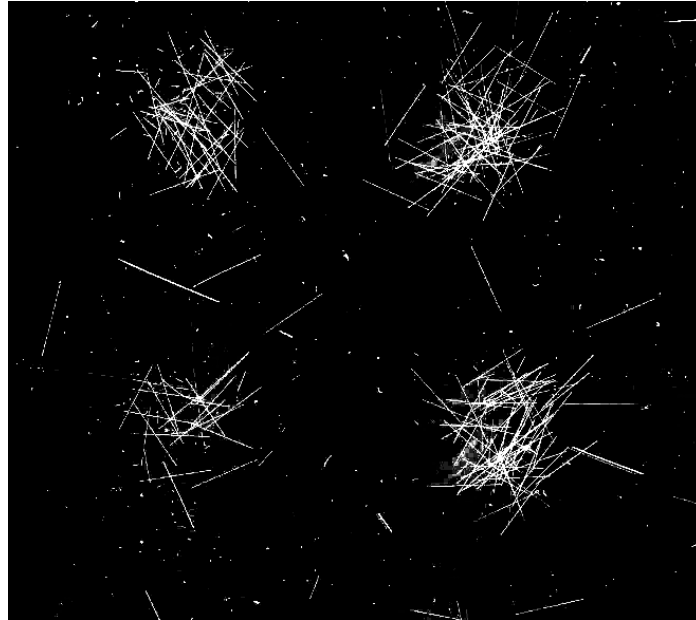


Figure 3.17 Sample acquisition. For illustrative purpose this is only a selected portion containing 4 of 35 images. It can be noted as the rubber grid allows space for cropping the images leaving a significant margin, in order not to cut any fiber.

Measurement of the rate pixel/millimeter

The calibration procedure consists in the acquisition of an image with a scanner. The procedure for using the scanner for the acquisition of the images was developed by trials and in the final form includes the following steps:

- *Cleaning of all surfaces by means of transparent paper, which does not release impurities that can be confused with the fibers or that increase the noise in the images.*
- *Preparation of a transparent glass, which the fibers to be measured are positioned on. The glass has the size of an A4 sheet and its edges were covered with black insulation tape, which protrudes of 8 mm within the area of the glass*
- *Placement of the fibers on the spotless glass.*
- *Arrangement of the glass above the scanner surface*
- *The scanner and the glass are now covered by a wooden black box, black painted to minimize reflection and thus minimize the fiber shadows.*
- *Acquisition of the fibers and storage on hard drives.*

The fiber measurement is performed using the software application ImageJ. Using pointers and placing them on the ends of the fibers it is possible to obtain the measurement of the distance in pixels. Through this program and it is possible to manually measure the fibers length on the screen of the scanned image and compare this measurement with that provided by ctFIRE. It is important to highlight that the measure obtained by ImageJ is also affected

by error. However, being a manual measurement, it is much more accurate than that performed by the ctFIRE software, because there are no skipped or broken fibers and, using a high magnification, the pixels at the ends are not omitted.

The fibers are then measured with the coordinate-measuring machine Werth Video-Check IP 400 (Figure 3.18). This system allows to measure the distance between two points in 3D as it is equipped with encoders on translation axes x, y, z.



Figure 3.18 Werth Video-Check IP 40.

The field of view is very limited and for measuring the length of a few millimeters of the fiber it is necessary to move the focal. After measuring some fibers the measurements in millimeters and pixels are then compared, obtaining the conversion factor for the resolution set in the scanner.

Image acquisition and processing

Preprocessing

Once the large images (7100 x 5019 pixels) are acquired, they are processed by two Matlab scripts, written specifically for this application:

- *Script for the calibration of the cropping script*
- *Cropping script that automatically divides the input image in 35 small images, which will be analyzed by the ctFIRE recognition software*

The first script allows extrapolating the coordinates to be used by the latter, to center a virtual grid on the initial image, in order to obtain, by means of the second script, images whose edges completely contain the small pane with the fibers.

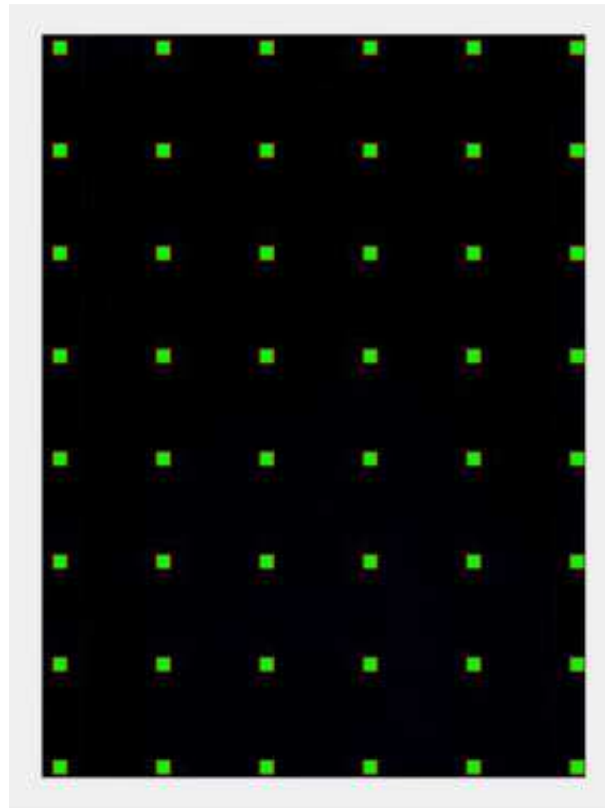


Figure 3.19 The script in Matlab code provides this output screen to refine the subsequent cropping coordinates.

At this point by changing two values within the script, the division illustrated in Figure 3.19 can be obtained. By linking the green squares with vertical and horizontal lines, 35 images are obtained. From this description it is evident how important is the correct alignment between the scanner surface, the glass and the grid. This matching procedure has to be performed again only when changing the acquisition tool or if the glass references to the scanner are lost.

The second script processes the image according to the parameters found in the first and its output consists in 35 consecutively numbered images, which allow the operator to trace back to their positions in the grid (Figure 3.20).

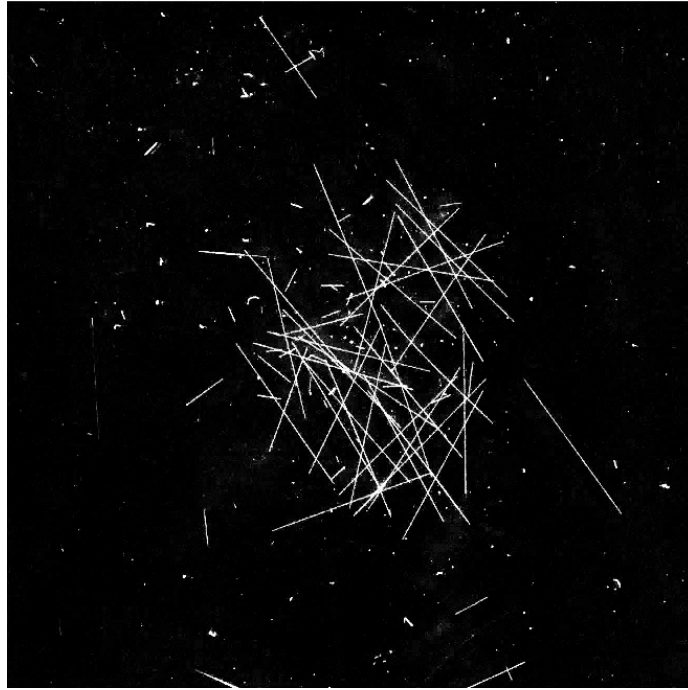


Figure 3.20 Cropped image. It is possible to notice the overlapping rectilinear fibers. The software has no problem in solving the crossings. A particular care is only required in not overlapping the images, which comes easier after a short training phase in acquisition operations.

Image analysis

The software application used for fibers identification, automatic measuring and counting is called ctFIRE (from curvelet transform and Fiber Extraction) and it is a stand-alone package of Matlab. The version used is 1.3 Beta2. The software is based on the Java language and it was developed in the medical field. It was created with the purpose of allowing users to automatic extrapolate fibers of collagen obtained from an image of cancerous tissue under a microscope and to measure fibers for calculating statistics, such as the width and length of the fibers and their angle of curvature [15]. The algorithm requires a considerable number of parameters to be adjusted; some are directly accessible by the user, via the stand-alone interface; others are adjustable by means of Matlab scripts, which are provided by the authors. The images are processed through the ctFIRE program in batch mode. The operator only needs to set the input and output folders and algorithm parameters. The ctFIRE software analyzes an image and delivers the output as an Excel file, which is formatted as a single column of detected length values. The output consists of an Excel file for each image, for a total of 35 files for each acquisition. The considered parameters that mostly affect the correct recognition of the fibers are shown in Table 3.1.

Table 3.1 Comparison of the parameters modified in ctFIRE software

number	parameter	long fiber	default
7	s_xlinkbox	2	8
10	thresh_ext	70	70
17	s_fiberdir	20	4
18	thresh_linkd	15	15

Post-processing

All the .csv files containing the measures of the fibers in pixels are opened sequentially by a Matlab script, which is used to reformat all the data into a matrix of 35 rows and 1000 columns. Subsequently, all the data filtering operations are performed on the elements of the array to remove any noise, for the calculation of averages and for a random count of about 1000 fibers for each acquisition. The script provides the output value of the average fibers length. The average proposed by Huq and Hazaiez (Equation 3.1) was used because it gives greater weight to the longer fragments, which have more influence on the mechanical properties [11,16].

$$L_{Huq} = \sqrt{\frac{\sum L_i^3 N_i}{\sum L_i N_i}} \quad \text{Equation 3.1}$$

3.5 Industrial case study

The screws used in this experimental campaign are the following (Figure 3.21):

- The first one is a three-zone screw, having a square pitch and a 40 mm diameter.
- The second screw was designed by Maxi Melt. It has a conical core, a dynamic mixer in the metering section and a variable pitch, which increases towards the tip.

Both screws are equipped with ring-type no-return valve, anti-friction and anti-corrosion surface coating.

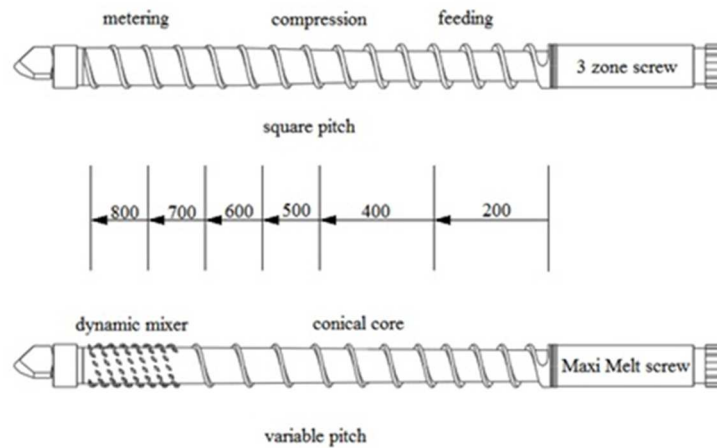


Figure 3.21 Three-zone (above) and Maxi Melt (below) screws employed in the case study

The dimensions of the three-zone screw are the following:

- Diameter of 40 mm
- Square pitch of 40 mm
- Ridge height of 6.1 mm at 390 mm from the channel start
- The second conical zone is located between 390 mm and 626 mm from the channel start
- Ridge height of 2.1 mm from 626 mm up to the end of the screw.
- The conical section is 236 mm long and it has an angle of 1.94°

We can also define the aspect ratio as a parameter of comparison between the two screws, i.e. the ratio between the channel width and the height of the ridge in the reference positions where the material was sampled: 200, 400, 500, 600, 700, 800 mm from the channel start respectively (Table 3.2).

Table 3.2 Aspect ratio of the three-zone screw

Sampling distance (mm)	200	400	500	600	700
H ridge (mm)	6.1	6.1	4.1	2.1	2.1
L channel (mm)	35	35	35	35	35
L channel/ H ridge	5.74	5.74	8.54	16.67	16.67

For the Maxi Melt screw (Table 3.3):

- Diameter of 40 mm
- Variable pitch
- Ridge height of 7.5 mm at the channel start

- Ridge height of 2.5 mm at a length of 710 mm from the channel start
- Pitch length of 38 mm at the channel start
- Pitch length of 37 mm at 710 mm
- Taper of 0.81°

Table 3.3 Aspect ratio of the Maxi Melt screw

Sampling distance (mm)	200	400	500	600	700
H ridge (mm)	6.09	4.68	3.98	3.27	2.57
L channel (mm)	34.13	35.25	35.82	36.38	36.94
L channel/ H ridge	5.60	7.53	9.00	11.11	14.37

3.5.1 Plasticating settings

The experimental campaign consists of extracting samples of solidified material from the screw at specific locations along its length. The defined methodology for these tests consists in setting the injection molding machine with a clean screw (each of the considered screws), a clean and empty cylinder and a hopper, which does not present residues of other polymers. The material is then loaded in the hopper and the plasticating parameters are set according to the values reported in Table 3.4.

Table 3.4 Comparison between optimal and sub-optimal parameters

	Optimal conditions (A)	Sub-optimal conditions (B)
Rotational speed (rpm)	75	150
Backpressure [bar]	0	100
Shot size [mm]	65	130
Cycle time [s]	35	35

The profile of the plasticating temperature was set according to Table 3.5 and Table 3.6 on advice of the customer.

Table 3.5 Set temperatures for optimal parameters

Optimal conditions (A)	Nozzle	Center	Hopper
T three-zone (°C)	240	220	200
T Maxi Melt (°C)	240	230	220

Table 3.6 Set temperatures for sub-optimal parameters

Sub-optimal conditions (B)	Nozzle	Center	Hopper
T three-zone (°C)	240	220	200
T Maxi Melt (°C)	240	240	220

Four tests were carried out with the two screws used at the two plasticating condition. For each run of the experimental plan, before performing the procedure of the screw sampling, 10 plasticating cycles were carried out to reach regime conditions. The purge temperature was monitored using an immersion probe, type-K thermocouple, controlled by a Hasco thermometer.

A scan of the glass for each screw sample taken at 200, 400, 500, 600, 700 and 800 mm respectively was performed. The plasticating effects on the residual fibers length were analyzed for different process conditions and different types of screws. There were 4 cases to analyze for each of the screw section for a total of 24 scans to be conducted, which led to the storage of 48 images divided into 35 smaller images each for a total of 840 photos to be submitted to ctFIRE, and a total output of 840 Excel files stored with the lengths of the fibers.

3.6 Preliminary results

The experimental data showed that the reduction of the fiber length takes place significantly near the hopper. The length was reduced by 40% at 200 mm from the hopper, between the 5th and the 6th flight. The measurements of the sample taken from the first section, shown in Figure 3.22, highlighted the presence of numerous fragments of fiber less than 1 mm long. Moving to the last section, shown in Figure 3.23, an increase of the shorter fragments can be observed.

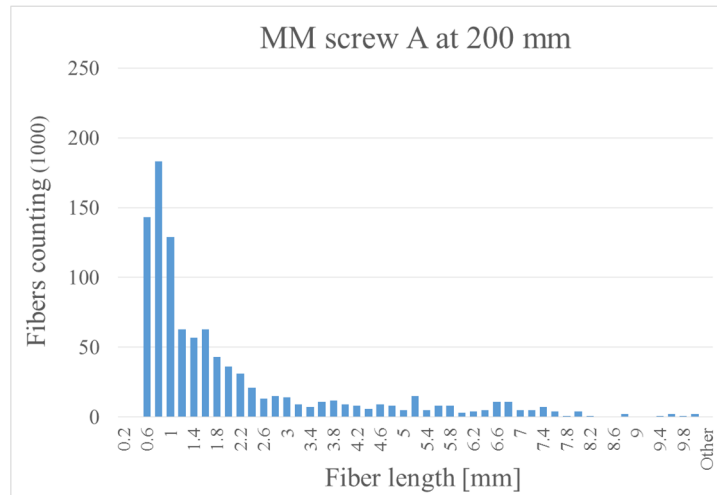


Figure 3.22 Fibers length distribution at 200mm from the hopper.

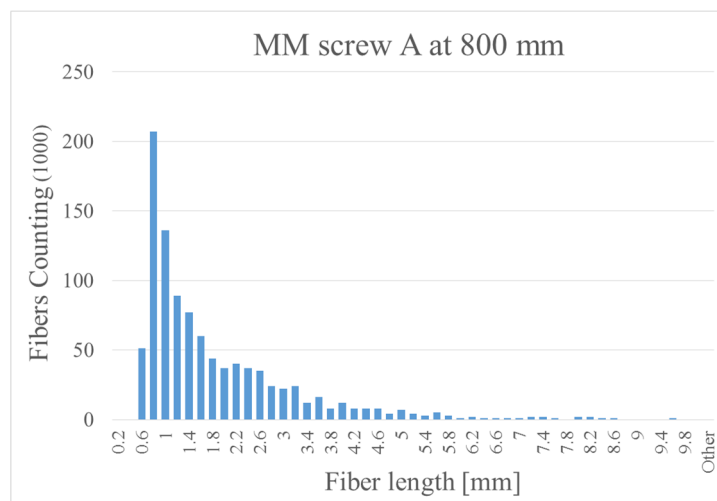


Figure 3.23 Fiber length distribution at 800mm from the hopper.

The average fibers length along the screw was calculate applying the model proposed by Huq and Azaiez [11, 16]. A comparison of the measured values in the 4 tests that were carried out did not show particular discrepancies (Figure 3.24). It was assumed that the residual length of the fibers was leveled out at 4 mm, passing through the metering zone independently of the screw geometry. The total fibers length reduction, from the hopper to the non-return valve, amounts to 60%.

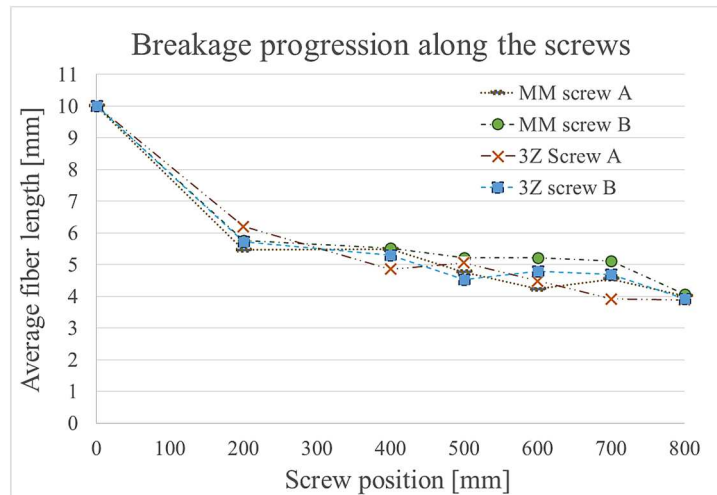


Figure 3.24 Breakage progression along the screws.

The measurement of the fiber length in the molten material indicated that a reduction of 40% is achieved in the zone at 200 mm from the hopper.

Table 3.7 Percentage reduction at section 200 mm.

	Average fiber length at section 200 [mm]	Reduction %
Three-zone, optimal conditions	6.03	39.7
Three-zone, sub-optimal conditions	5.93	40.7
Maxi Melt, optimal conditions	5.25	47.5
Maxi Melt, sub-optimal conditions	5.31	46.9

In order to better discuss the breakage evolution, a zoom of the graph is reported in Figure 3.25.

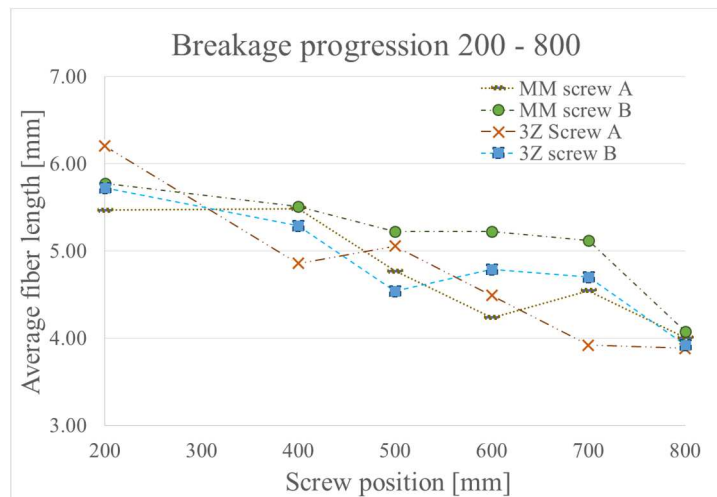


Figure 3.25 Experimental average length of the reinforcement along each screw in conditions A and B

The values of the average length in the final zone highlight that the presence of the dynamic mixer did not adversely affect the breakage (Table 3.8). It was supposed that the results is due to the geometric factors of height and width of the channel that, in relation to the residual length of the fibers at 700 mm, had an aspect-ratio high enough to avoid a further

reduction of the fibers length, which is the case with the standard screw. The governing feature of the breakage phenomenon is therefore the height of the channel.

Table 3.8 Comparison of the maximum and minimum value at section 800 mm

	Average fiber length at section 800 [mm]
Three-zone, optimal conditions	4.17
Maxi Melt, optimal conditions	3.95

On the other hand, it was possible to evaluate how the different process conditions, which differ mainly in the value of back pressure, affected the fibers breakage. Weighting the amount of material leaving the nozzle allowed the calculation on the residence time of the material inside the plasticizing unit. As shown in Table 3.9, the residence time of the polymer in condition A is 4 times compared to that obtained in condition B.

Table 3.9 Comparison of weight in conditions A and B

Screw	Weight [g]		Ratio (B/2)/A
	A	B	
3Z	18.2	161.0	4.4
MM	15.8	149.8	4.7

This involves a greater stress on the material with consequent reduction of the remaining length of the fibers. In Figure 3.25 it is possible to see how the curve, corresponding to condition A, is slightly steeper.

3.7 Uncertainty calculation

UNIEN ISO 15530-3:2011 standard defines a procedure for the evaluation of the uncertainty for measurements obtained by CMM and by means of parts or calibrated measurement standards [17]. The standard provides an experimental technique for simplifying the uncertainty evaluation according to an approach (measurements by replacement) that is based on measurements conducted in the same way as the actual measurements, using calibrated parts of similar size and geometry [18].

In the replacement method reported in the standard both a sample piece and a control standard are measured using a CMM, to fix additional CMM systematic errors. The conditions of use of the standard are based on the similarity of:

- *size and geometry of the standard piece used in the actual and the calibrated piece used in the evaluation of uncertainty;*
- *measurement procedure in the evaluation of measurement uncertainty and the procedure of actual measurement;*
- *environmental conditions during the evaluation of uncertainty of measurement and actual measurement.*

The evaluation of the uncertainty of measurement consists of a sequence of measurements, carried out in the same way and under the same conditions as the actual ones. The only difference is that, instead of the pieces to be measured, one or more calibrated parts are measured. The differences between the results obtained from the measurement and the known calibration values of these parts are used to estimate the uncertainty of the measurements. The standard proposes the following method to assess the uncertainty of measurement: the calibrated parts are measured instead of the standard ones; standard parts and calibrated ones must satisfy the above-mentioned similarity conditions. To obtain a sufficient amount of data for uncertainty evaluation, at least 10 cycles and a total of at least 20 measurements were carried out on calibrated parts. During the evaluation of uncertainty, the position and orientation of the calibrated parts are varied systematically within the limits imposed by the procedure of actual measurements. A measuring cycle must contain all the actions involved in a real measure to ensure the similarity of environmental conditions. The measurement result y , and its expanded uncertainty U , are expressed in the form $y \pm U$, where U is determined with a recommended coverage factor $k = 2$ for an approximate coverage factor of 95%. As regards the expanded uncertainty calculation, the standard provides the four fundamental uncertainty contributions:

- *u_{cal} : standard uncertainty associated with the calibration of the part shown in the calibration certificate;*
- *u_p : standard uncertainty associated with the standard deviation of the measures;*
- *u_b : standard uncertainty associated with the bias of the evaluated measurement process using the calibrated part;*
- *u_w : standard uncertainty associated with the material and manufacturing variations (due to the variation of the coefficient of expansion, shape errors, roughness, elasticity and plasticity).*

The expanded measurement uncertainty U is calculated from these standard uncertainties such as:

$$U = k \sqrt{u_{cal}^2 + u_p^2 + u_b^2 + u_w^2} \quad \text{Equation 3.2}$$

The standard refers to measurement procedures using CMM, but it has been adapted to other measuring instruments. For example Müller et al. [19] presented the application of the replacement method for the estimation of measurement uncertainty using calibrated parts in X-ray computed tomography (CT).

In this thesis an adapted version of the replacement method has been used, which is described in ISO 15530-3 [17], applying it to the 2D scanner. A sample of 25 fibers has been calibrated using a CMM. The sample meets the requirements of similarity with those parts that are normally measured with this method. Consequently, the uncertainty that has been determined from this sample is applicable to all measures that are performed by following this procedure. It is emphasized that the uncertainty was measured for fibers analyzed with the specific optical acquisition system used in this work. The procedure is however suitable for other systems.

The uncertainty of measurement concerns the entire measurement procedure, and consists of different contributions:

- *Due to the experimental measurement procedure, in this case by means of the 2D scanner.*
- *Due to the CMM during the calibration procedure. It is important to point out that the full effect of the changes of the environment should be included to perform a full evaluation of measurement uncertainty.*

The replacement method reported in the standard [18], recommends that the same calibrated part be subjected to the specific measurement technique for which the uncertainty has to be determined. The approach requires the execution of a series of repeated measurements; at least 20 measurements are recommended by the standard. In this work 50 measurements have been conducted, under the same similarity conditions. To satisfy the similarity requirement, the calibrated samples were identical to the samples that are normally measured with the proposed procedure. Therefore the contribution of u_w uncertainty was neglected. The proposed formula for the calculation is resumed in Equation 3.3 where the symbols used are described in Table 3.10. The uncertainty was calculated for each of the five areas of the scanner.

$$U = k \sqrt{u_{cal}^2 + u_w^2 + (u_p \cdot t)^2 + b_1^2 + b_2^2} \quad \text{Equation 3.3}$$

where $u_{cal} = 0.002$ mm. In this case u_w is zero, because there is no uncertainty contribution related to the difference between nominal calibrated parts and parts calibrated to evaluate the uncertainty. The systematic error b for each fiber in each zone was calculated as:

$$b = \bar{L} - L_{calibrated} \quad \text{Equation 3.4}$$

where L is the average length of each fiber, different from area to area. The systematic error is sometimes smaller and sometimes greater than zero. If in one or more images a fiber is not detected, its relative systematic error in these images is 100%. The average of systematic errors, b_l , was then calculated.

The second error contribution, which is also treated as a systematic error, is related to broken fibers. These are less than 1% of all fibers used in the uncertainty calculation. It is estimated that they would break in half with a rectangular error distribution.

$$b_2 = \frac{1\% \cdot 50\% \cdot L}{\sqrt{3}} \quad \text{Equation 3.5}$$

The maximum length of 10 mm was chosen as L , not to underestimate the error.

Table 3.10 Variables used in the uncertainty calculation

Symbol	Description
U	expanded uncertainty
k	coverage factor, $k=2$ for a level of confidence of approximately 95 %
u_{cal}	uncertainty of calibration
u_w	contribute that take in to account the differences between the measure of the workpiece and the calibrated workpiece. Set equal to 0
u_p	mean of the standard deviation of each measured fiber
t	safety factor related to the repeatability of the measurement
b_1	mean of the systematic error
b_2	contribute due to the fragmented fibers

3.7.1 Experimental procedure with the reference sample

The reference sample is constituted by a sample of 25 fibers arranged on a square slide of side 40 mm and thickness of 3 mm. The dimensions were limited in order to easily place the same sample in 5 different areas of the scanning area. The arrangement of the fibers was manually performed by means of tweezers, and the final configuration presented some typical problems of random arrangements:

- *Crossed fiber*
- *Aligned fibers*
- *Long fragments*
- *Short excerpts*

Also in this case, for the measurement of the length of the fiber fragments a Werth Video-Check IP 400 multisensor CMM was used. Its maximum permissible error (MPE) for 10x magnification at which fibers were measured is calculated as:

$$MPE = 1.8 + \frac{L[mm]}{250} [\mu m] \quad \text{Equation 3.6}$$

The length L has been chosen as the largest, which is approximately 10 mm. For rectilinear fibers a segment was used, for the curved ones a broken line was used following as much as possible the curve of the fiber. Subsequently, the same sample of calibrated fibers was subjected to the measurement procedure using a high resolution desktop scanner, as described in the next section. The same sample was subsequently acquired in 5 zones of the scanner as shown in Figure 3.26.

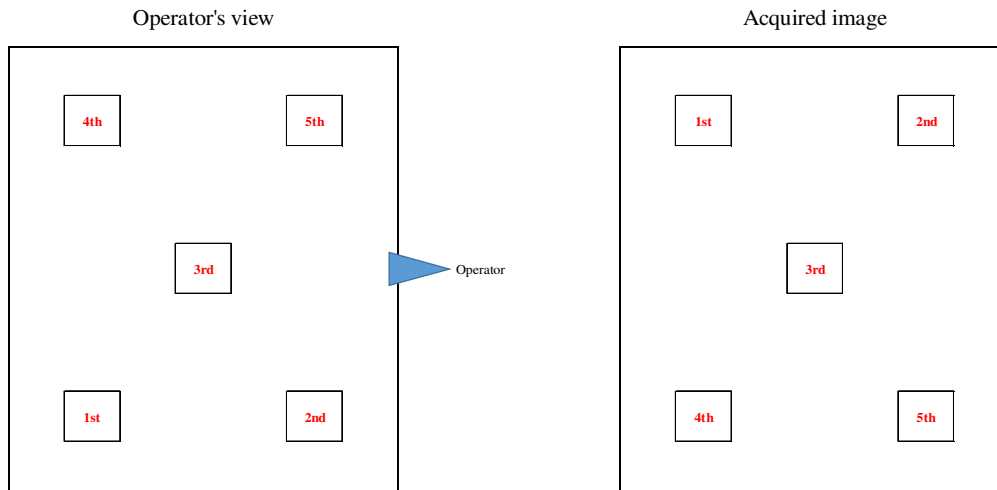


Figure 3.26 Schematic view of the five zones: from the operator point of view and how the pictures are acquired

After several tests, 24-bit color images were acquired, with a resolution of 600 dpi. The size is equal to the largest glass and it is the closest possible to an A4 sheet 210 x 297 mm. It was necessary to add a fabric mask between the slide and the scanner glass, because it appeared an unwanted glare on the acquisition, as can be seen in Figure 3.27.

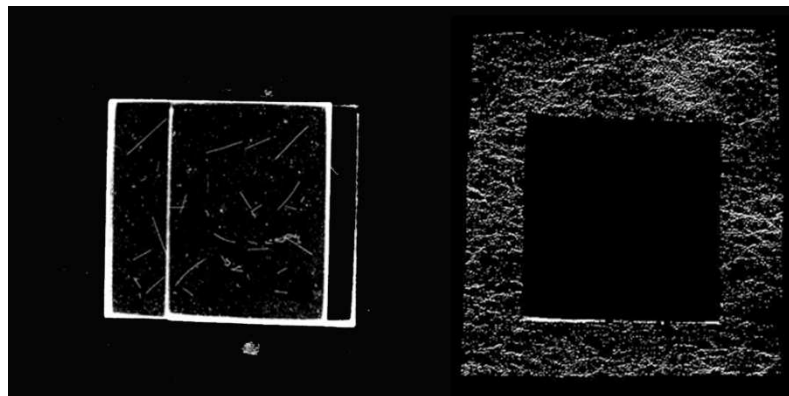


Figure 3.27 Defect created by the edges of the slide in the acquisition (left). The image is subjected to a high brightness threshold to make it evident. Mask fabric (right) on which, at the center, the slide is placed.

For the same reason, while acquiring the image with the largest glass, two fabric strips were posed on the edge of the long sides, without entering the acquisition area. To calculate the uncertainty the slide with the calibrated fibers was repeatedly scanned in five areas of interest, the four corners and the center area, in order to better test the entire scanner surface. For each zone 10 acquisitions were made, for a total of 50 scans. For each acquisition, the slide was removed and repositioned.

The images were cropped using a Matlab script. The same script also allows the conversion of on images in 8-bit gray, required for the post processing using ctFIRE. Processing the 50 images that contain the calibrated fiber it was evident the importance of identifying which fiber each length value supplied in output by the software refers to, in order to calculate the mean of the standard deviation and the systematic error between the average length of each fiber and the length calibrated using the CMM for that fiber. The ctFIRE software allows, through the post processing and advanced output function, to label each fiber, even if limited to a single image at a time. The procedure used to process images is as follows:

- Optimization of the software parameters for five images, one for each zone.
- Extension of the parameters to all 50 images
- At this point missing and broken fibers appeared in the central area of a number of acquisitions. The parameters were optimized separately for this area and a tradeoff was then looked for.
- Reprocessing of an image at a time by selecting all the possible output and immediate post processing by automatically labeling the fibers, according to the order in which the length is provided in the .csv file in output.

Selecting *Select File* you can reopen the input image, the scanned one, which must necessarily be in 8-bit and the software will also open its output with the fibers overlapping the starting image by labeling each fiber with numbers in ascending order. The numbering is done by software before filtering the output image, having a default definition of 30 pixels, therefore a few numbers are missing. Bringing the threshold to zero the numbering is complete. However, some dust particles are included, as you can see in Figure 3.28.

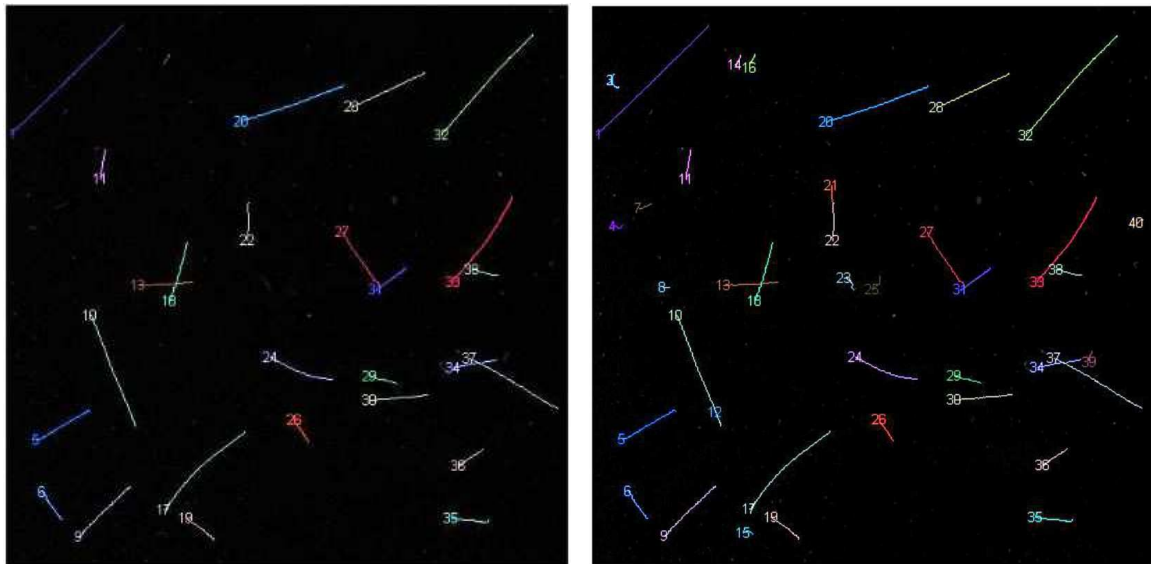


Figure 3.28 (1) counting of the fiber in *ctFIRE*; (2) counting of the fiber in *ctFIRE* without the threshold on the number of pixels

It can be noted that the software looks for the fibers top-down, from left to right. It is important to highlight that not all of the 50 acquired images share the same numbering order, because moving the slide by just a few degrees affects the numbering order. To determine the standard deviation, the average of each fiber and the systematic error of this with respect to the calibrated measure, therefore, it was necessary to carry out the post processing for each image, identifying the fibers and then reordering them manually.

3.7.2 Extension of the uncertainty to a 50-fibers sample

In order to verify that the calculated uncertainty was valid also for larger sample sizes, about fifty fibers were distributed on the same slide used for the uncertainty calculation; they were processed with *ctFIRE* and measured manually with *ImageJ*. To proceed with manual measurements of the fibers through *ImageJ*, it is essential to set a scale as a first step. For 600 dpi images a conversion from pixels to millimeters is provided by the software, as shown in Figure 2.24. For a resolution of 600 pixels per inch, the conversion factor in millimeters is obtained by multiplying by the conversion factor from inches to millimeters (1 inch = 25.4

mm) and dividing by 600. The manual measurement of the fibers was carried out with the aid of two screens, the first one was used to embrace the entire image, applied with a slight brightness threshold, as a map for orientation. On the second screen the fibers have been measured on an enlarged image, being careful not leaving out any fiber and not to measure twice the same fiber. Instead of matching each fiber measurement obtained in output from ctFIRE with the corresponding length measured with ImageJ, it was given greater importance to the averages obtained with each method, because of interest both in the practical case and in order to later process samples with a large number of fibers. Three statistics have been used: the arithmetic mean, the weighted mean, as recommended by ISO 22314: 2006 [20], and the average according to Huq and Azaiez model [16], which takes better account of the long fibers.

$$L_{arithmetic} = \frac{\sum_{i=1}^n L_i}{n} \quad \text{Equation 3.7}$$

$$L_{weighted} = \frac{\sum_{i=1}^n L_i^2 n_i}{\sum_{i=1}^n L_i n_i} \quad \text{Equation 3.8}$$

$$L_{Huq-Azaiez} = \sqrt[2]{\frac{\sum_{i=1}^n L_i^3 n_i}{\sum_{i=1}^n L_i n_i}} \quad \text{Equation 3.9}$$

The means calculated with the output data from ctFIRE, with the relative uncertainty, were compared with those calculated from the lengths manually measured with ImageJ.

3.7.3 Extension of the uncertainty to the full sample made of 35 images.

The next step was to extend the uncertainty to an acquisition sample of about 1000 fibers, distributed on a glass having the size of an A4 sheet and divided into 35 sub-images, each having side of 970 pixels. All fibers were manually measured using ImageJ. This operation took a long time to be carried out carefully. For each of the sub-images the differences between the various types of average obtained from ctFIRE with the corresponding averages measured with ImageJ were calculated, evaluating if they were within the calculated uncertainty. Eventually, for the full sample consisting of 35 sub-images, the overall averages were calculated. At this point it was necessary to perform additional filtering on the ctFIRE output lengths, because some scratches and imperfections on the scanner glass were recognized by software as very long fibers, skewing the average length. It was therefore decided to proceed in parallel, analyzing the same sub-images:

- using the default threshold of 30 pixels
- setting to zero pixels the minimum length that a fiber must have to be considered by the software

In this second case the filtering was done later, using a Matlab script. Both larger and smaller lengths were filtered. The calculation of averages has been implemented in the same script. It is important to note that the ctFIRE parameters that were used to process the complete sample of 35 sub-images are slightly different from those used for the slide, in particular it was necessary to lower the main threshold in the complete sample. Particular attention was paid to avoiding the separation by gravity of the smaller fragments during sampling, because very different amounts of fibers on the scanner glass cause more reflections and unwanted interactions. It was therefore accepted that some small impurities and dust were sometime recognized as fibers, in order not to break the longer fibers.

3.8 Industrial case studies for validation

3.8.1 Reprocessing of the fibers of the plasticating experiment

The samples from plasticating trial with the MaxiMelt screw operating in sub-optimal conditions were reprocessed. The results after the optimization of the measurement procedure were compared with the previous ones.

3.8.2 Evaluation of the damage induced by the opening level of the hot-chamber nozzles

The samples were prepared by cutting them from the molded part, an automotive spoiler (Figure 3.29). The letter and the initial number, which were used to code the samples (M1, M3, M4), correspond to the different valve gates. It was required that each sample was large at least three times the original fiber length, in order to avoid considering fibers that had been damaged and broken in cutting the spoiler into pieces. The fibers were sampled from the central zone after removing a frame 14 mm thick. The fibers to be analyzed were carefully chosen within the sample, avoiding those compromised by the cutout. Unfortunately, some samples contained a lot of ash from the pyrolysis of the matrix. Particular attention was paid to avoid the separation by gravity of the smaller fragments during sampling.

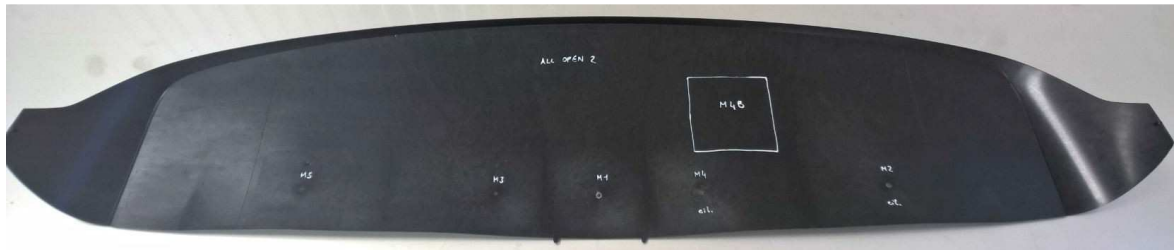


Figure 3.29 Automotive spoiler where the analyzed sample were cut.

3.9 Results

In this section all the results from the optimization of the measuring system are presented.

3.9.1 Evaluation of the uncertainty with the 25 fibers sample

After a series of preliminary tests, the ideal parameters for processing the fibers of the sample and for calculating the uncertainty of measurement were found (Table 3.11). The default filter of 30 pixels has been kept active, in order to filter the background noise. The main threshold after which the pixels are bright was raised by one unit, to make sure that small impurities or dust (even under the scanner glass) were not identified as possible fibers. The second parameter, the radius of the distance function for the search of local maxima, was lowered after the nucleation points were found. It was noted that this selection ensures a better fibers identification. The third parameter indicates the maximum angle by which a fiber can divert along its extension. Even though there are no fibers deviating from 90°, it has been noticed that by increasing this parameter the curved fibers were more recognizable. It was then slightly raised the minimum threshold for both free fibers and crossed ones. The next parameter was raised from 4 to 15 to increase the measurement accuracy at the expense of the processing time. The maximum distance between two fibers, below which two fibers can be connected, has been increased. Finally the eighth parameter was changed from -150 to -130, raising the minimum angle below which two fibers can be connected.

Table 3.11 Setting of the parameter of ctFIRE used for the calculation of the uncertainty

Parameter	Value
thresh im2	6
s xlinkbox	4
thresh ext	90
thresh dang L	20
thresh short L	20
s fiberdir	15
thresh linkd	7
thresh linka	-130
thresh flen	15

In the following series of graphs, the length of the fibers measured with the CMM is reported on the x-axis. The first and the second area of the scanner, corresponding to the first two areas subjected to the CCD sensor passage, are those that present the lowest average of the standard deviation, see Figure 3.30 and Figure 3.31, and the lowest systematic errors, see Figure 3.35 and Figure 3.36. While the last two areas to be scanned, the fourth and the fifth one, have the higher average of the standard deviation, Figure 3.33 and Figure 3.34, and the highest systematic error, see Figure 3.38 and Figure 3.39. The average of the systematic errors, shown in Figure 3.41, is particularly high in the fourth zone, since all errors are negative, i.e. the average length output from ctFIRE is lower for each of the fiber length measured by the CMM. The standard deviation and the systematic error for the twenty-fifth fiber, which is the last one on the right side, is particularly high in the first three zones because in some areas of the 10 images the software does not identify the fiber and its length is set equal to zero, with a 100% error. The fiber was missed two times in the first and the second area and three times in third area.

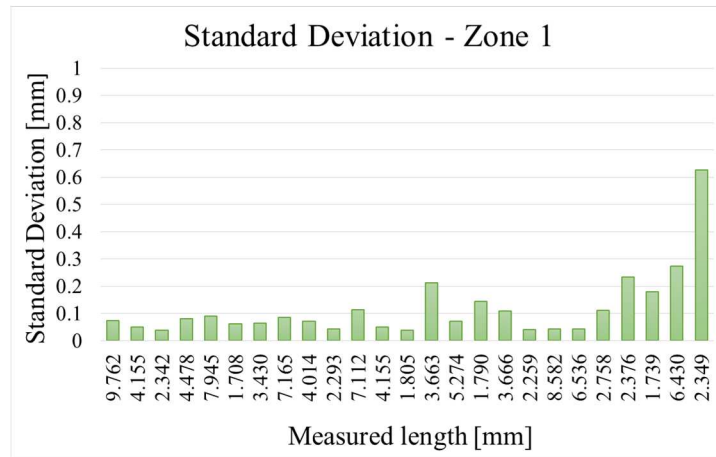


Figure 3.30 Standard deviation of the measurement of each fiber (25 bars) repeated 10 times in the first zone

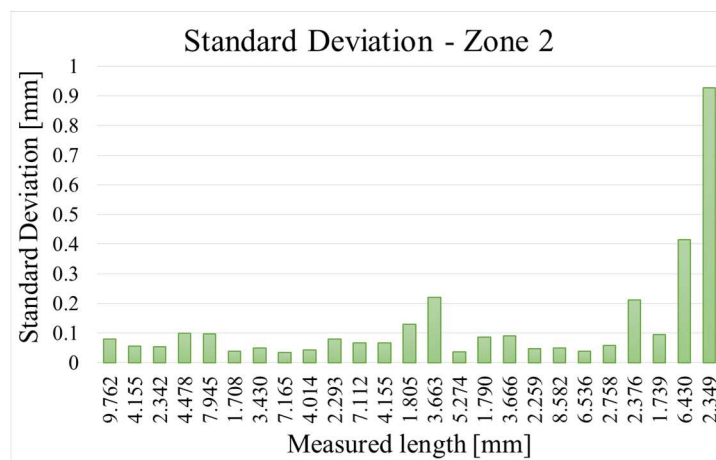


Figure 3.31 Standard deviation of the measurement of each fiber (25 bars) repeated 10 times in the second zone

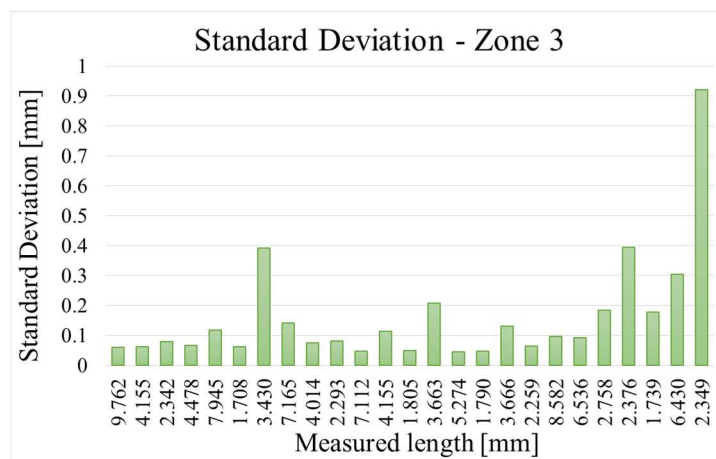


Figure 3.32 Standard deviation of the measurement of each fiber (25 bars) repeated 10 times in the third zone

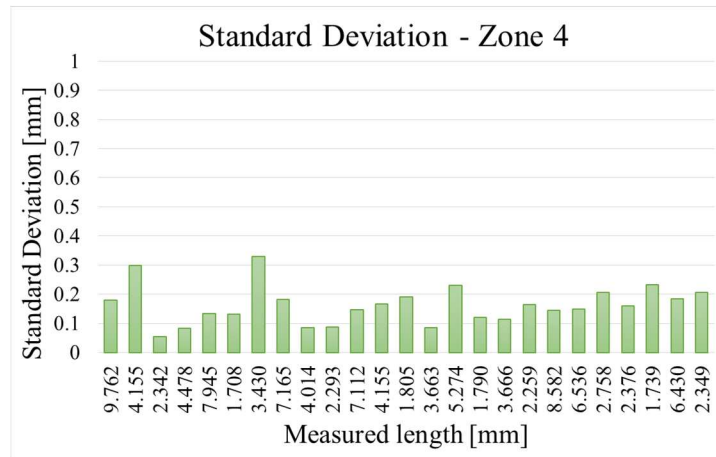


Figure 3.33 Standard deviation of the measurement of each fiber (25 bars) repeated 10 times in the fourth zone

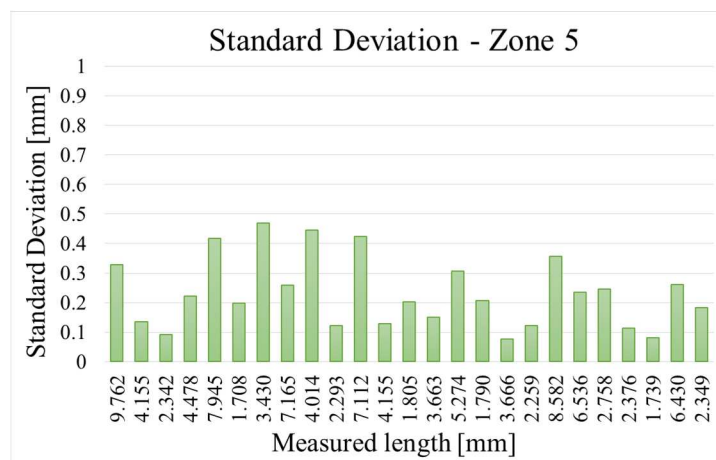


Figure 3.34 Standard deviation of the measurement of each fiber (25 bars) repeated 10 times in the fifth zone

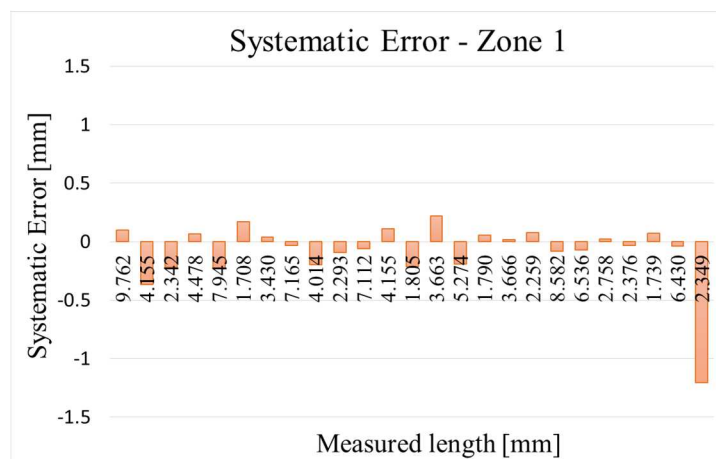


Figure 3.35 Systematic error of the measurement of each fiber (25 bars) repeated 10 times in the first zone

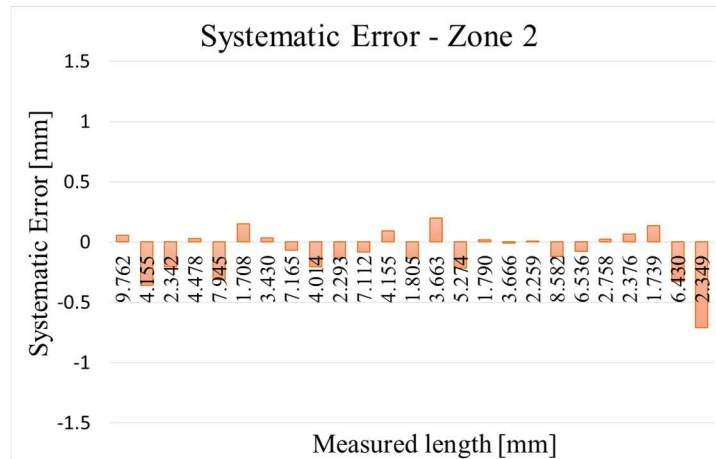


Figure 3.36 Systematic error of the measurement of each fiber (25 bars) repeated 10 times in the second zone

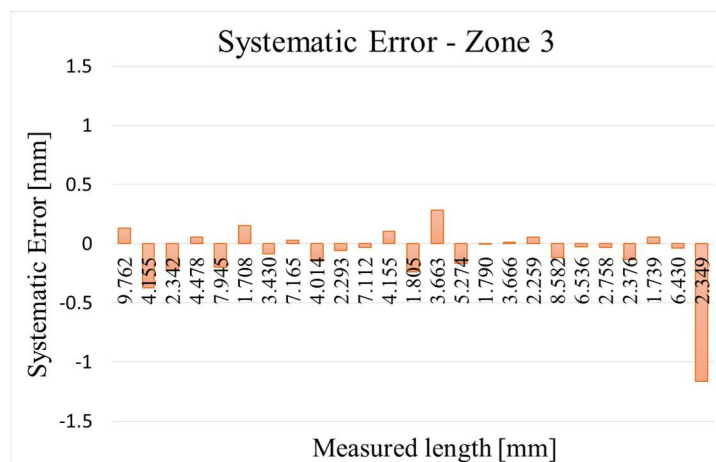


Figure 3.37 Systematic error of the measurement of each fiber (25 bars) repeated 10 times in the third zone

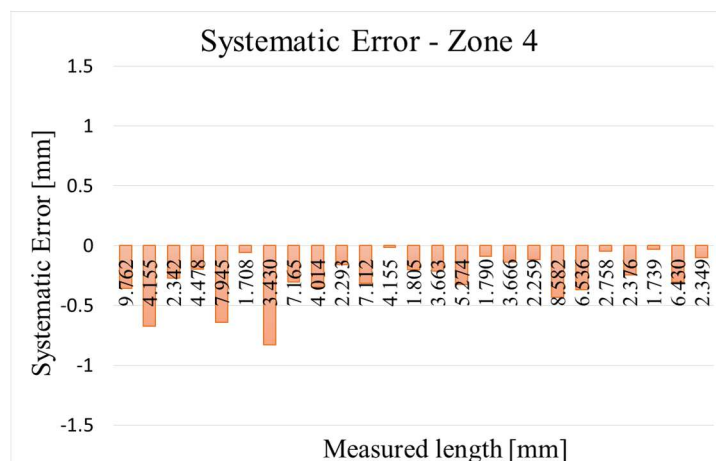


Figure 3.38 Systematic error of the measurement of each fiber (25 bars) repeated 10 times in the fourth zone

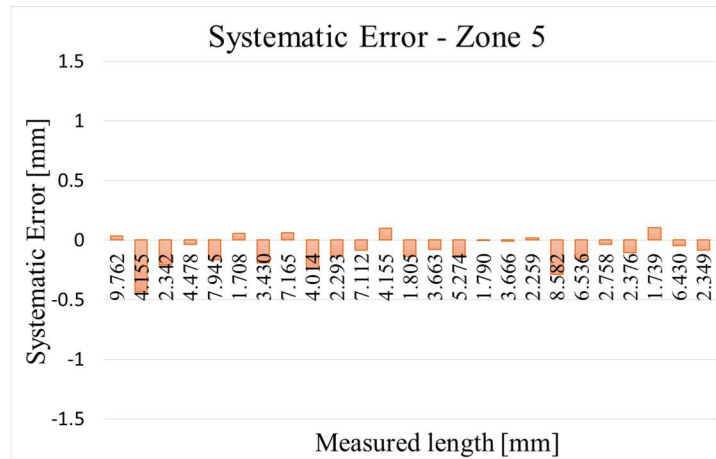


Figure 3.39 Systematic error of the measurement of each fiber (25 bars) repeated 10 times in the fifth zone

In the fourth and fifth zone the systematic errors and the standard deviations are higher and there are some broken fibers. It is not clear why this happens, it can be assumed that the scanner performance is not uniform, and the last area to be scanned has some light reflections within the system. The average of the standard deviation for each area is shown in Figure 3.40. It can be noted that this is higher in the fifth zone. While in Figure 3.41 it is clear that the systematic error in the fourth zone is significantly higher. Also the arithmetic mean in the fourth zone (Figure 3.43) deviates the most from the value obtained by the length measured during the calibration. It is important to highlight that in all areas the average obtained by ctFIRE is lower than the average calculated with the calibrated lengths. This is likely due to having raised the threshold of bright pixels, which makes the fibers less recognizable at their ends, where fibers are not cut sharply but they thin or are broken irregularly. Figure 3.42 shows the uncertainty calculated using the Equation 3.2. The greater value of the uncertainty, calculated in the fourth zone, is equal to 0.651 mm, and it is the value adopted in the subsequent uncertainty extensions. The lengths relative to the few fibers that were broken, were added up, taking into account their relative error through the term b_2 .

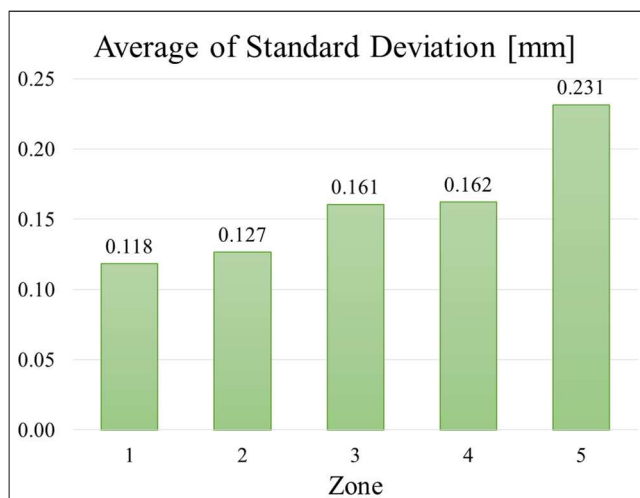


Figure 3.40 Average of the Standard Deviation of the length of the fibers in each zone (1-5)

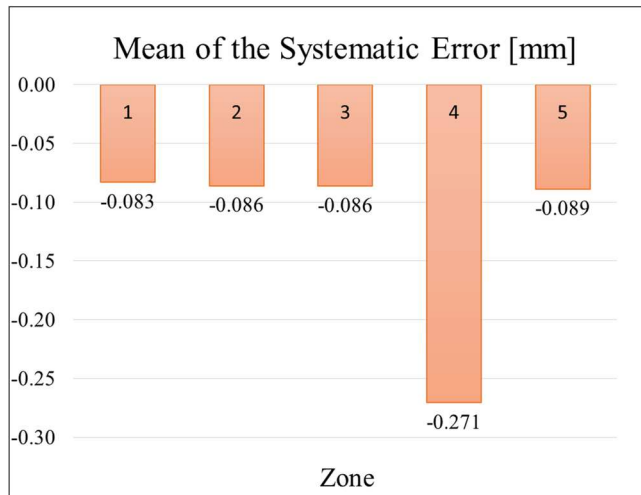


Figure 3.41 Mean of the systematic error in each zone (1-5)

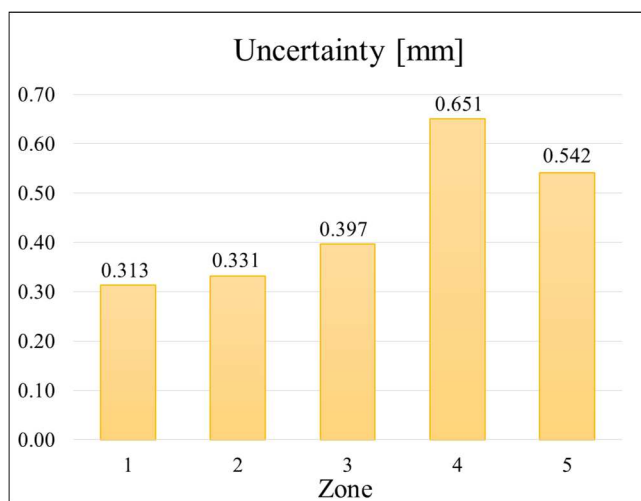


Figure 3.42 Calculated uncertainty of each zone (1-5)

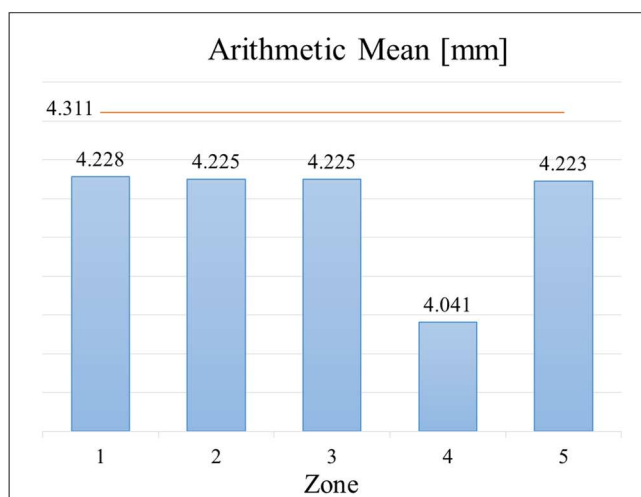


Figure 3.43 Arithmetic mean of the length of the fibers in each zone (1-5)

3.9.2 Extension of the uncertainty to a 50-fibers sample

Before analyzing a complete sample containing about 1000 fibers, a gradual transition was carried out, placing a more manageable number of fibers on the same slide used for the calculation. The sample was purposely selected with many crossed and curved fibers in order

to test the capabilities and limitations of the software. At this stage it was noted that in order to optimize the result, a change of the ctFIRE main parameters was necessary. In particular, the main threshold of the bright pixels was lowered. This was possible because the measurement of the fibers took place immediately after cleaning the slide, which then showed very little dust and impurities. Moreover, an increased amount of fiber affects the light reflection and the brightness of the image. For this reason the parameters slightly differ from those used for calibration and they are summarized in Table 3.12. Many were reset to the default value. The threshold of the minimum size that a fiber must have to be counted and measured was set to the default value of 30 pixels, or about 1.27 mm.

Table 3.12 Setting of the parameters of ctFIRE that are used for the acquisition of the larger sample with 50 fibers

Parameter	Uncertainty calculation 25 fibers	Sample with 50 fibers
thresh im2	6	5.5
s xlinkbox	4	4
thresh ext	90	90
thresh dang L	20	15
thresh short L	20	15
s fiberdir	15	10
thresh linkd	7	10
thresh linka	-130	-150
thresh flen	15	15

It can be noted that for this first sample of 50 fibers the average obtained from the manually measured lengths is always greater than the one calculated with the data in output from ctFIRE. This is due to the fact that the software has troubles in tracing the fiber ends, especially with a high threshold for pixel brightness. There are also a couple of broken fibers, which were taken into account in the uncertainty calculation, in particular in the term b_2 , estimating that the break occurs at 50% of the fiber length and with a rectangular distribution of the error. The measures are in fact contained in the calculated margin of uncertainty.

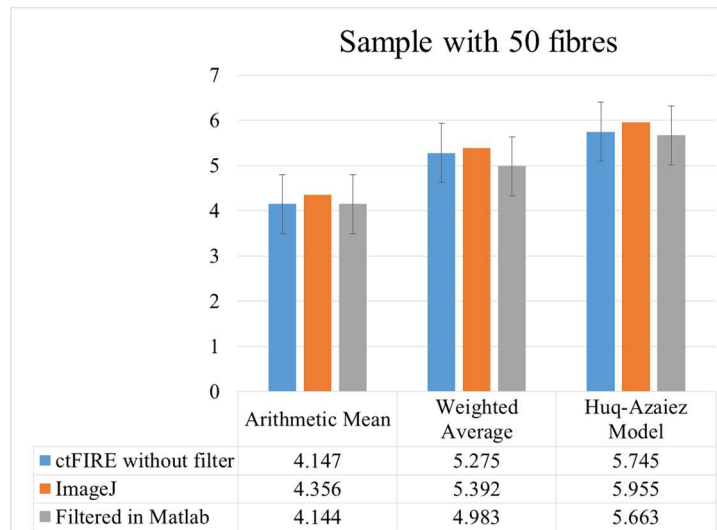


Figure 3.44 Comparison of the three average models that are applied without filtering the data from ctFIRE, on the data measured in ImageJ and by filtering the data from ctFIRE in Matlab

3.9.3 Extension of the uncertainty to the full sample made of 35 images

The complete sample of the size of an A4 sheet was acquired using the rubber grid. After the acquisition, the image was cropped with a Matlab script in 35 sub-images that were suitable to be processed with ctFIRE. All the fibers on the screen, about a thousand, were manually measured with ImageJ. The arithmetic mean, the weighted mean and the Huq-Azaiez mean were calculated for each of the 35 sub-images, using both the manually measured data and those provided by ctFIRE. The selected parameters were the same used for the slide containing 50 fibers and the threshold of the minimum size that a fiber must have to be counted and measured was set to the default value of 30 pixels, or about 1.27 mm. The following figures (Figure 3.45, Figure 3.46, Figure 3.47) show the differences between the means calculated from the measured data and from the software output. The horizontal lines represent the uncertainty value calculated in the previous chapter.

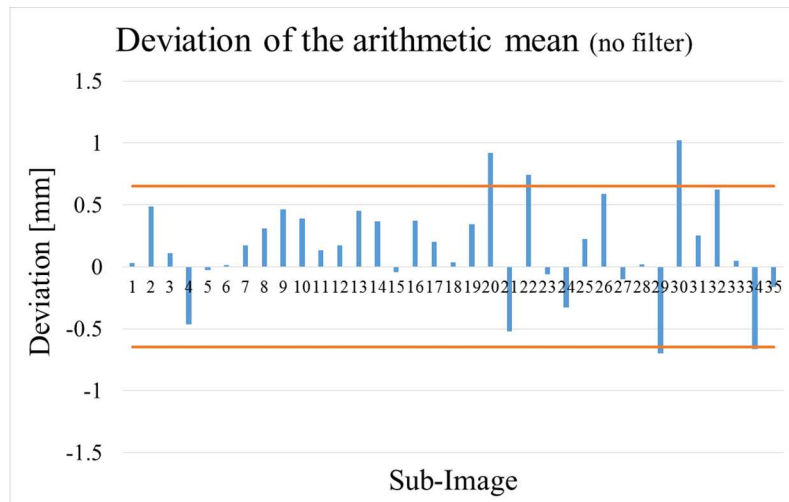


Figure 3.45 Deviation of the arithmetic mean calculated on the ctFIRE output from the arithmetic mean calculated with the measurement made in ImageJ (no filter)

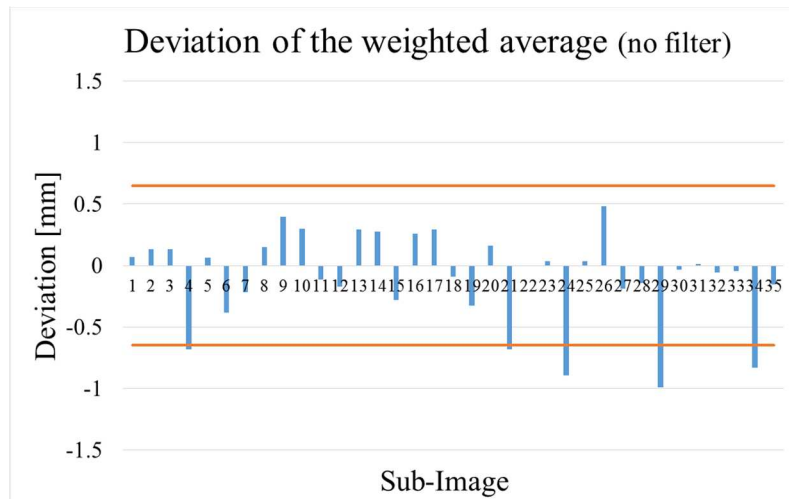


Figure 3.46 Deviation of the weighted average calculated on the ctFIRE output from the weighted average calculated with the measurement made in ImageJ (no filter)

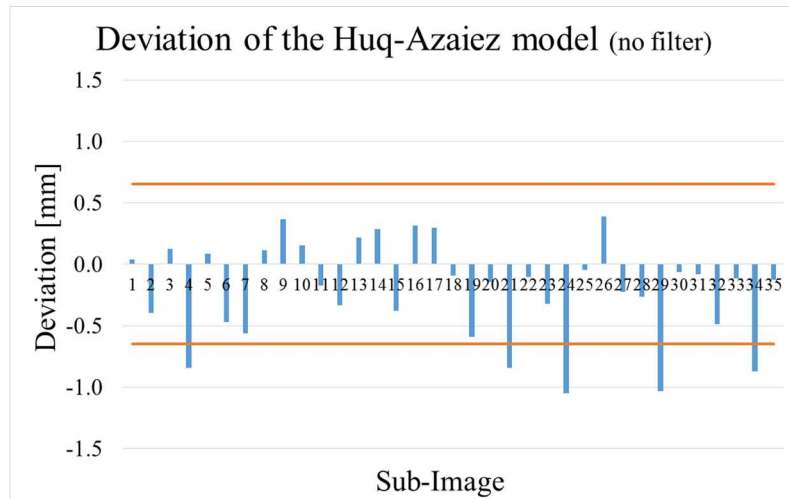


Figure 3.47 Deviation of the Huq-Azaiez model calculated on the ctFIRE output from the Huq-Azaiez model calculated with the measurement made in ImageJ (no filter)

It was noted that in some images the deviation is larger than the uncertainty. Analyzing the data in details, it has been noticed that this is due to some scratches on the scanner screen, which are identified as very long fibers by the software (Figure 3.48). These scratches were not considered by the operator because they were not visually confused with the fibers.

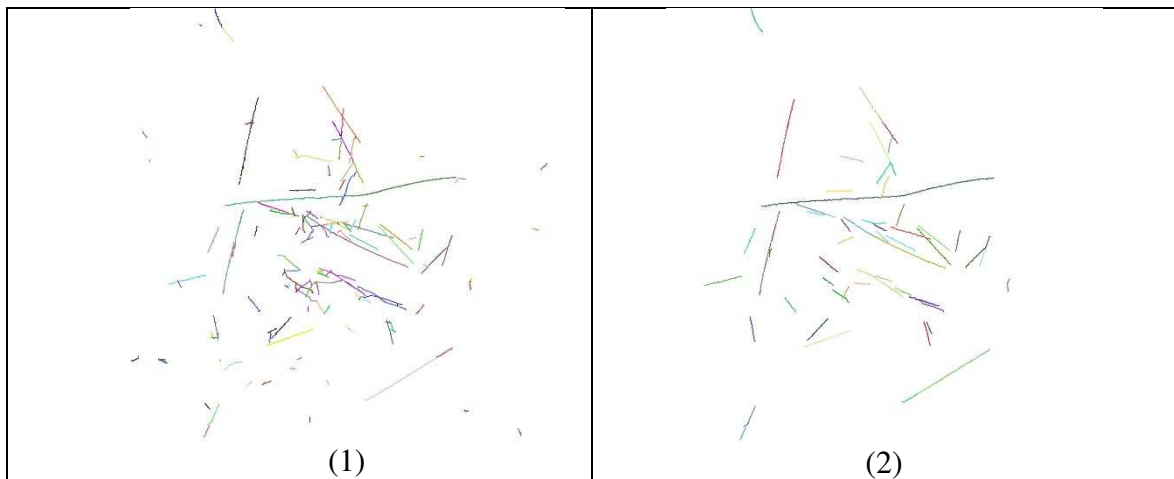


Figure 3.48 The same image is presented as ctFIRE output without any filter on the minimum length. The longer line is an example of the scratches on the scanner screen that are recognized as a fiber (1). In this case the lower filter is set equal to 30 pixel (2)

The measures in output from ctFIRE corresponding to these defects were manually removed from the statistics of this first full acquisition, thus obtaining new deviation values reported in Figure 3.50, Figure 3.51 and Figure 3.51. In subsequent acquisitions, an automatic filter for longer fibers was applied to the ctFIRE output. The filter script was written in Matlab language and it includes the calculation of averages. In this way, the deviations of both the weighted and the Huq-Azaiez mean are lower than the calculated uncertainty.

The filter was first tested on the sample with 50 fibers (Figure 3.44), and then on the sample with 35 sub-images. In order to investigate the effect of the filter on the minimum length, the images have been reprocessed with ctFIRE, setting first to 0 and then to 30 pixels the minimum length that a fiber must have to be considered. The sample image comparing the two settings is presented in Figure 3.48, which includes some noise. The fibers counted without filter were 153 (1) and 56 with the filter (2). To decide the lower filter value several

tests were carried out, for example setting the ctFIRE threshold at 24 pixels (approximately 1 mm), to get an idea of how much dust, noise and dirt affected the measurement and, at the same time, how many of the smaller fibers were identified. Eventually, the best compromise was obtained with the threshold of 30 pixels (1.27 mm), as the software default.

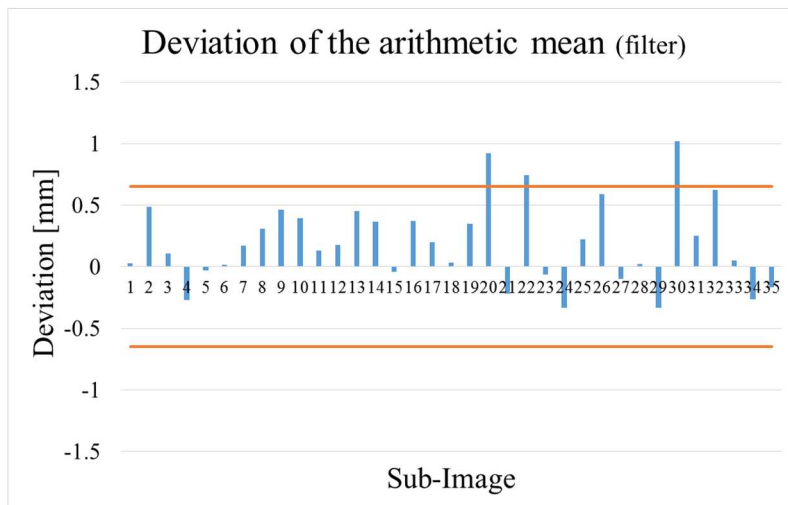


Figure 3.49 Deviation of the arithmetic mean calculated with the ctFIRE output from the arithmetic mean calculated with the measurement made in ImageJ (filter)

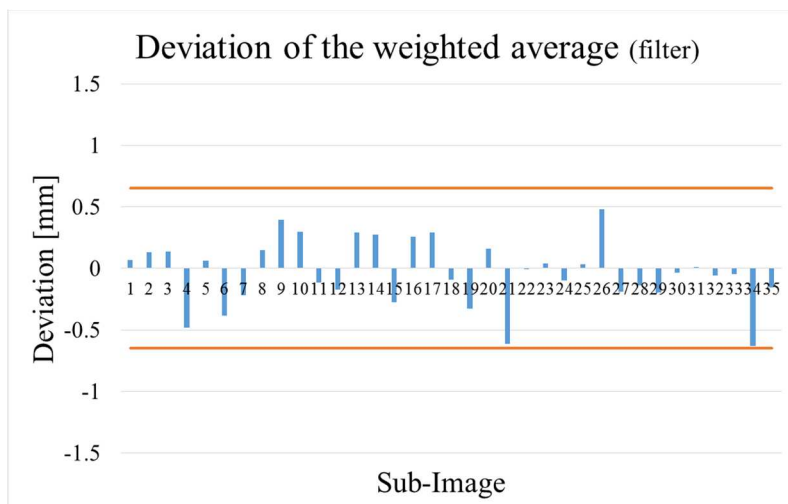


Figure 3.50 Deviation of the weighted average calculated with the ctFIRE output from the weighted average calculated with the measurement made in ImageJ (filter)

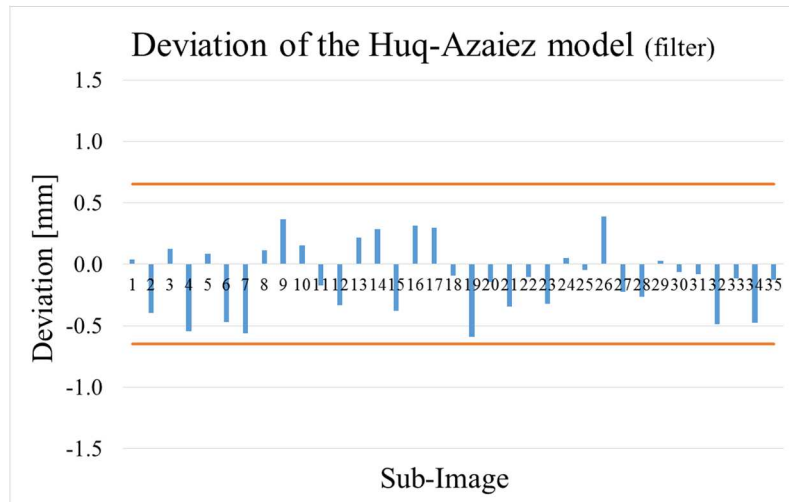


Figure 3.51 Deviation of the Huq-Azaiez model calculated with the ctFIRE output from the Huq-Azaiez model calculated with the measurement made in ImageJ (filter)

It should be stressed that in the manual measurement with ImageJ smaller fibers have also been detected (less than 1 mm in length), but a compromise was looked for between the detection of the short fibers and the presence of defects in the image. The noise was evaluated through a blank image of the scanner glass that was acquired and analyzed by ctFIRE with zero pixel threshold. It was noted that the software detects some small fibers even on an empty glass. In order not to detect these defects, the threshold to be set is approximately the software default, i.e. 30 pixels (1.27 mm). As regards the upper filter the highest value measured with ImageJ was chosen, which is approximately 10 mm. The obtained result, compared to the previous one (i.e. with no filter and without manually removing the screen scratches that the software identified as fibers), is shown in Figure 3.52. It can be noted that the arithmetic mean on the total of 1000 fibers does not vary significantly. As regards the other two means, the values obtained using the filter are closer to the ones calculated from ImageJ measurements. All the values are within the uncertainty limits.

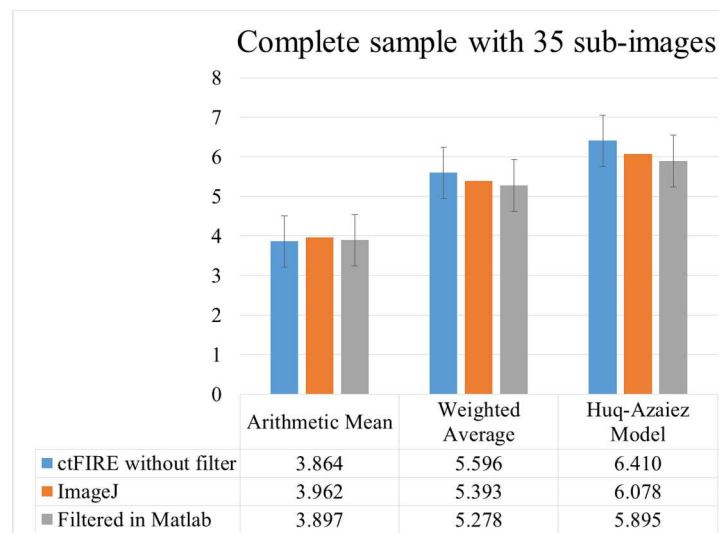


Figure 3.52 Comparison of the three average models that are applied without filtering the data from ctFIRE, on the data measured in ImageJ and by filtering the data from ctFIRE in Matlab

3.9.4 Reprocessing of the fibers of the plasticating experiment

The samples were re-acquired using the scanner and analyzed by means of ctFIRE, applying different parameters values with respect to the ones previously used. Specifically, the main threshold was lowered, to make the pixels brighter, reducing the risk of the fibers being broken by the software. This causes a greater presence of dust and noise but it allows the operator to use the filter for smaller lengths. To improve the software accuracy, the second parameter was also lowered to a minimum, making radius of the search for local maxima as small as possible. The parameters are summarized in Table 3.13. The number of the analyzed fibers is not always the same for all zones, because even trying to keep constant the number of fibers deposited in each sample, with the manual method used the fibers are more numerous in the samples containing the smaller fibers. The number of fibers counted in the statistics is between 1250 and 1450.

Table 3.13 Setting of the parameters of ctFIRE that are used for the acquisition of the fiber from the plasticating trials

Parameter	Uncertainty calculation - 25 fibers	Complete sample 35 images	Reprocessing of the fiber (screw)
thresh im2	6	5.5	4.7
s xlinkbox	4	4	1
thresh ext	90	90	90
thresh dang L	20	15	15
thresh short L	20	15	15
s fiberdir	15	10	10
thresh linkd	7	10	10
thresh linka	-130	-150	-150
thresh flen	15	15	15

After the thorough cleaning of all surfaces and the arrangement of the fibers on the glass, with the aid of the rubber grid, the images were captured and cropped using the Matlab script. To test the validity of the chosen parameters, the sub-images were first processed with the default filter of 30 pixels (1.27 mm). This allows to get images as the central one in Figure 3.53, which also shows the other two versions of the same image. The left image was processed without any filtering threshold: the noise that the software identifies as small fibers can be clearly noticed. The right image was processed with a 1.5 mm filter, erasing some smaller fibers.

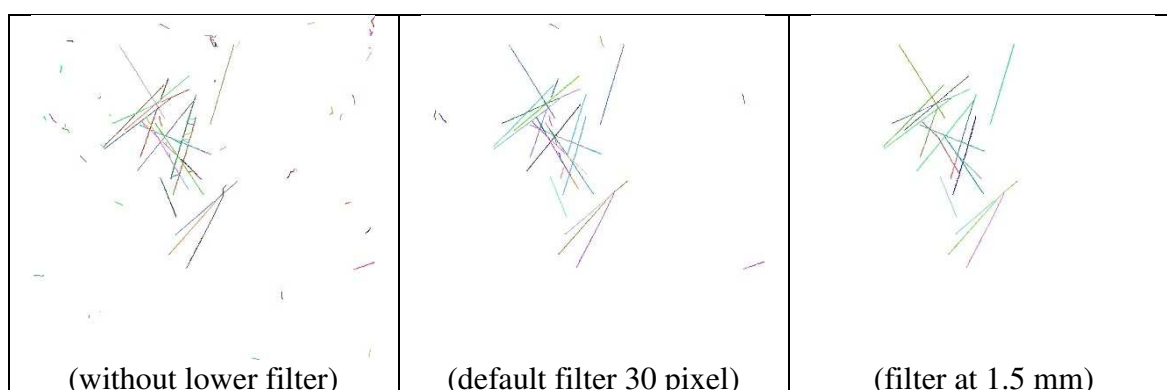


Figure 3.53 Example of the effect of the lower filter in recognizing the fibers

In order to efficiently study the effect of filtering on the lengths obtained from the processed images, the ctFIRE threshold value was set to zero and the filtering was performed using the

Matlab script, changing the lower and upper values. The upper filter was initially set to 10 mm, the starting length of the fibers, to be able to directly compare the results before and after the optimization. Before optimizing the filter on smaller lengths had been set to 1.50 mm. The results comparison (Figure 3.54) shows that the average length trend, which had been uneven, is consistently decreasing after the optimization, with the improvements made to the acquisition system and software.

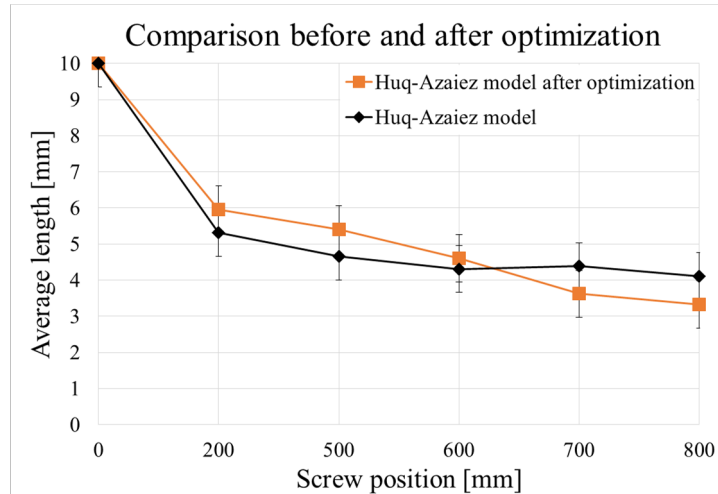


Figure 3.54 Comparison between the average values calculated with Huq-Azaiez model before and after the optimization

Table 3.14 Comparison between the averages calculated with the Huq-Azaiez model before and after the optimization of the method

Section of the screw	Previous approach		After optimization	
	Measure	Reduction	Measure	Reduction
200	5.31	46.90 %	6.66±0.65	33.40 %
500	4.66	53.40 %	5.54±0.65	44.60 %
600	4.31	56.90 %	4.79±0.65	52.10 %
700	4.39	56.10 %	3.65±0.65	63.50 %
800	4.11	58.90 %	3.33±0.65	66.70 %

Table 3.14 shows the values of the average length obtained before and after the optimization, in the same filtering conditions. Percentage reductions are compared to the initial length of the fibers. It is evident that the initial reduction, up to 200 mm from the hopper, is quite significant in both cases but after the optimization the final average percentage reduction is greater.

The average length obtained without filtering is not a reliable measurement but it was kept as a reference in the following comparisons. After manually measuring some of the long fibers identified by ctFIRE, it was found that very few of them sometimes exceeded the maximum length of 10 mm. Having set a rather low bright threshold, the software tends to merge some noise pixels with the ends of the fibers. Obviously, the fibers cannot be longer than 10 mm, but removing all those ones that exceed the maximum length of 10 mm significantly bias the statistics. After measuring the scratches on the screen and considering that they far exceeded the 10.5 mm length, the upper threshold of the filter was set to this value. The new results are shown in Figure 3.55, Figure 3.56 and Figure 3.57. It is evident that both the weighted and the Huq-Azaiez means are higher in the first zone and that the decreasing trend along the plasticizing screw is less marked for these statistics.

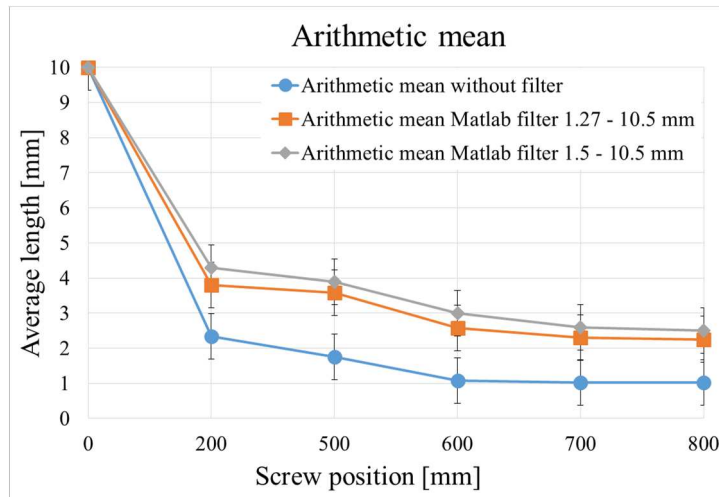


Figure 3.55 Comparison of the arithmetic mean calculated without any filter, with lower filter of 30 pixels (1.27 mm) and the upper of 10.5 mm, and with lower filter of 1.5 mm and the upper of 10.5 mm

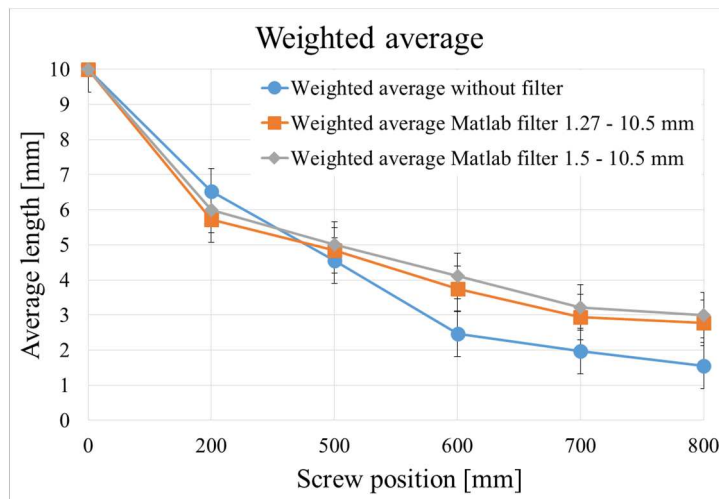


Figure 3.56 Comparison of the weighted average calculated without any filter, with lower filter of 30 pixels (1.27 mm) and the upper of 10.5 mm, and with lower filter of 1.5 mm and the upper of 10.5 mm

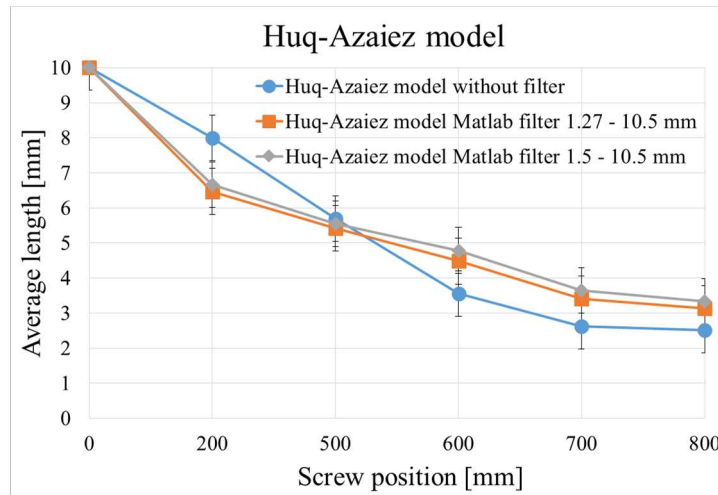


Figure 3.57 Comparison of the mean calculated with the Huq-Azaiez model without any filter, with lower filter of 30 pixels (1.27 mm) and the upper of 10.5 mm, and with lower filter of 1.5 mm and the upper of 10.5 mm

The filter selected as the best compromise for the mean calculation is the one that considers lengths from 1.27 mm to 10.5 mm. The results are shown in Figure 3.58 and in Table 3.15.

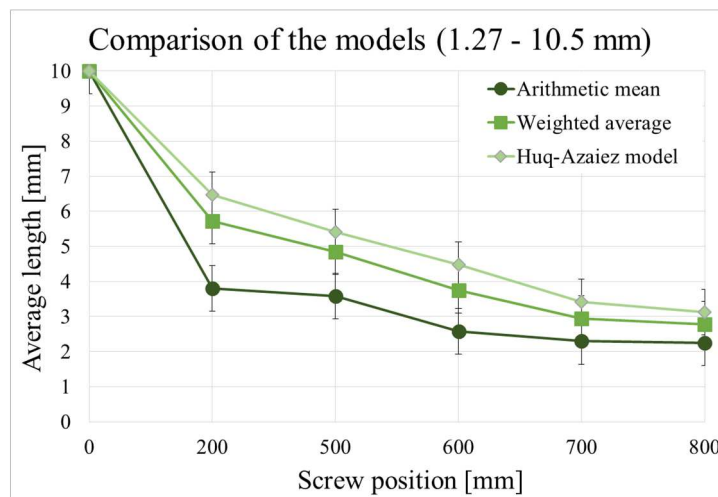


Figure 3.58 Comparison of the mean calculated with the three model by applying a lower filter of 30 pixels (1.27 mm) and the upper one of 10.5 mm.

Table 3.15 Average length of the fiber with lower filter at 1.27 mm and upper filer at 10.5 mm

Section of the screw	Arithmetic mean [mm]	Weighted average [mm]	Huq-Azaiez model [mm]
200	3.799±0.651	5.716±0.651	6.470±0.651
500	3.586±0.651	4.840±0.651	5.416±0.651
600	2.575±0.651	3.741±0.651	4.478±0.651
700	2.295±0.651	2.941±0.651	3.411±0.651
800	2.256±0.651	2.772±0.651	3.133±0.651

Eventually, the ratio between weighted and arithmetic means was reported in Table 3.16, as suggested by the standard for fibers measurement [20]. The higher the ratio the more significant the contribution of the longer fibers. In the first zones of the screw, the ratio is higher due to the greater presence of long fibers.

Table 3.16 Rate between weighted average and arithmetic mean for each section of the screw

Section of the screw	Rate between averages
200	1.505
500	1.450
600	1.453
700	1.281
800	1.229

Eventually, an extension of the uncertainty was performed on a random sub-image for each area of the screw with the optimal filtering. The results are summarized in Figure 3.59. The manual measurement is always contained within the uncertainty interval centered on the value obtained from the software.

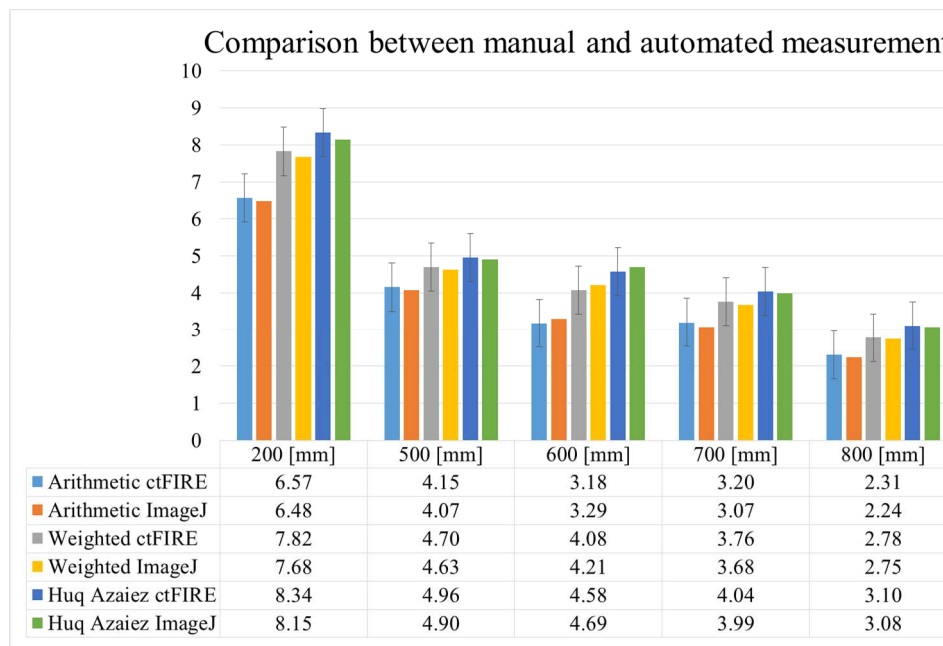


Figure 3.59 Comparison between the average values calculated on a random sub-image for each zone. The uncertainty was directly applied.

3.9.5 Evaluation of the damage induced by the opening level of the hot-chamber nozzles

Within the ten samples of side 50 mm and thickness 3 mm, supplied by INglass, the central fibers were selected, to exclude those compromised by cutting operations. The initial length of the fibers was measured with ImageJ, choosing longer fibers in the acquisition of M1A, SS and SP samples, which visually contained longer fibers. The greatest length manually measured is equal to 14.2 mm. Therefore, applying the same reasoning as in the previous Maxi Melt case, the upper fiber length filter was set to 14.5 mm. The uncertainty in the INglass case is slightly higher, having considered 14 mm as the maximum length in the calculation formula. All the fibers in the selected samples were analyzed. Three complete acquisitions were carried out for each zone, for a total of 105 sub-images per sample. In all the samples some ash is present, particularly in the M3 series. The arrangement of the fibers in this case required time and attention for not neglecting the small fibers without polluting the samples with ash. In all analyzed samples, the smallest fibers are the most numerous. Therefore it was necessary to lower the first ctFIRE parameter, i.e. the threshold above which the pixels are bright, thus trying not to neglect or break any fiber. The parameters used in the preparation of the fibers are shown in Table 3.17.

Table 3.17 Setting of the parameters of *ctFIRE* that are used for the acquisition of the fiber from INglass samples

Parameter	Uncertainty calculation	Complete sample	Reprocessing of the fiber	INglass samples
thresh im2	6	5.5	4.7	2.5
s xlinkbox	4	4	1	1
thresh ext	90	90	90	90
thresh dang L	20	15	15	15
thresh short L	20	15	15	15
s fiberdir	15	10	10	10
thresh linkd	7	10	10	10
thresh linka	-130	-150	-150	-150
thresh flen	15	15	15	15

An example of processed images is shown in Figure 3.60, where two of the sub-images are proposed, one from the sample M1A (left) and one from the sample M3D (right), both filtered at 30 pixels and 2 mm, respectively. The filtering in this case was performed in *ctFIRE*. Instead, the stage of the upper filtering process, the counting and the calculation of averages were performed using the Matlab script. Figure 3.61, Figure 3.62, Figure 3.63 and Figure 3.64 show the trend of the average fibers length in the M1 and M3 areas by varying the opening of the nozzle. The values of the average fibers length are reported for both filter thresholds: 1.27 mm (30 pixels) and 2 mm. The count of measured fibers varies depending on the threshold used: less than 3000 for the 2 mm threshold and less than 4000 for the 1.27 mm threshold.

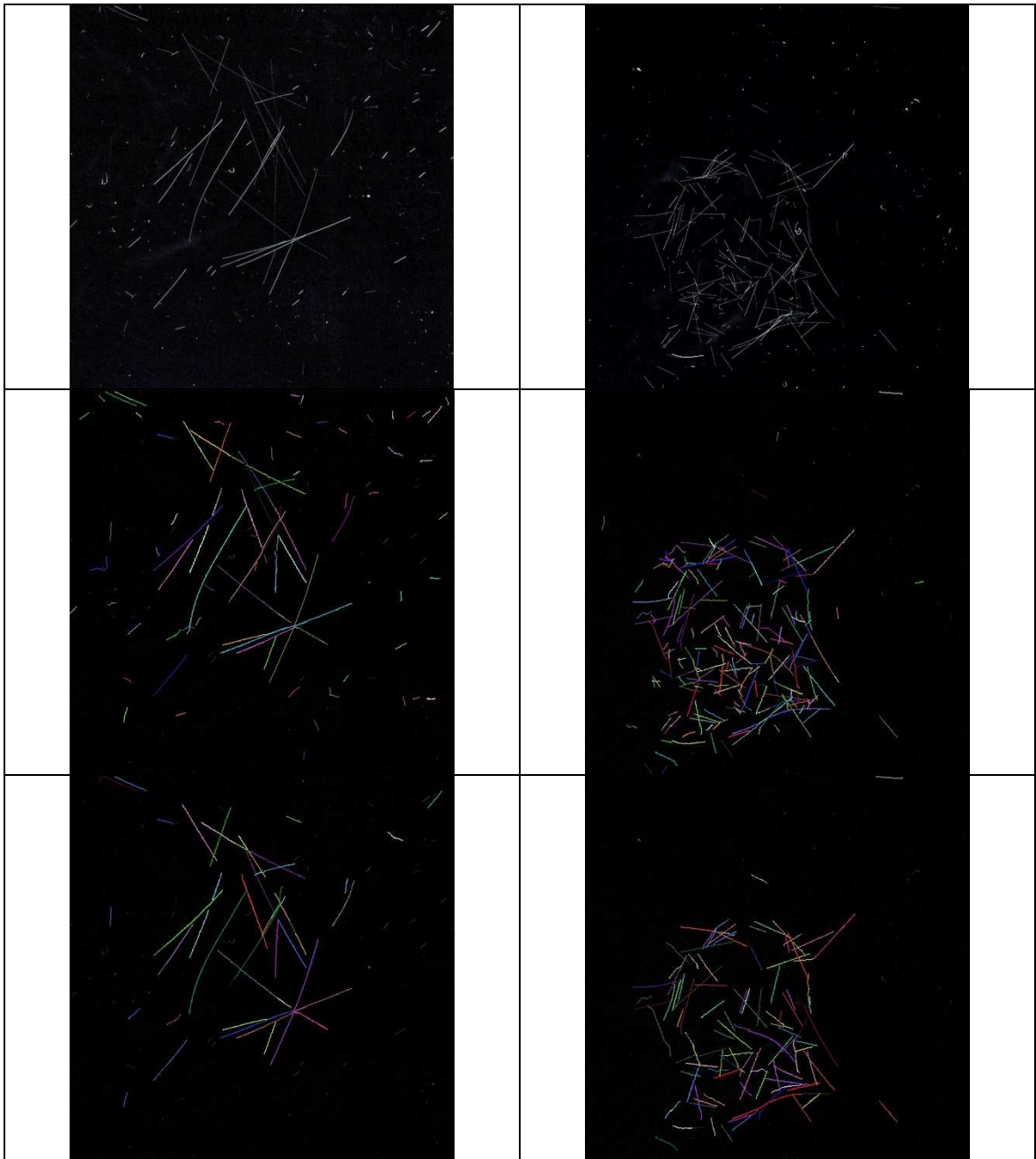


Figure 3.60 Example of the image processing with long fragments (M1A) on the left and short fragments (M3D) on the right. In the first row the images are presented with a light threshold. In the second and third

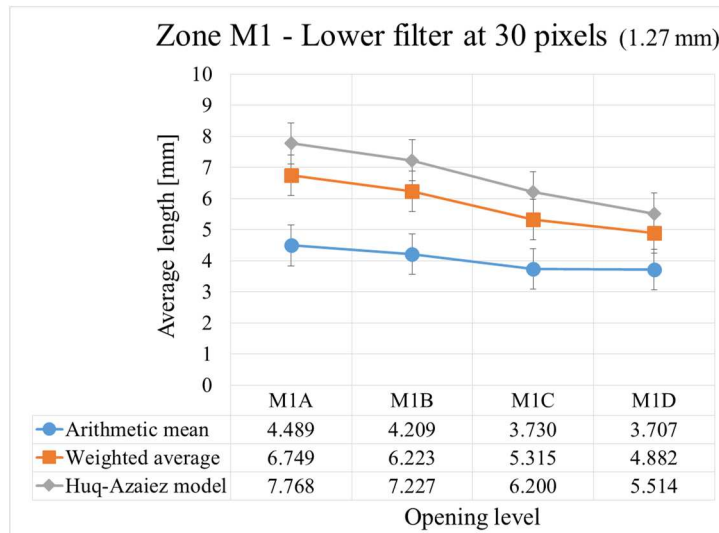


Figure 3.61 Average length in the zone M1 by reducing the overture of the hot nozzle. The lower filter at 30 pixels (1.27 mm) was applied

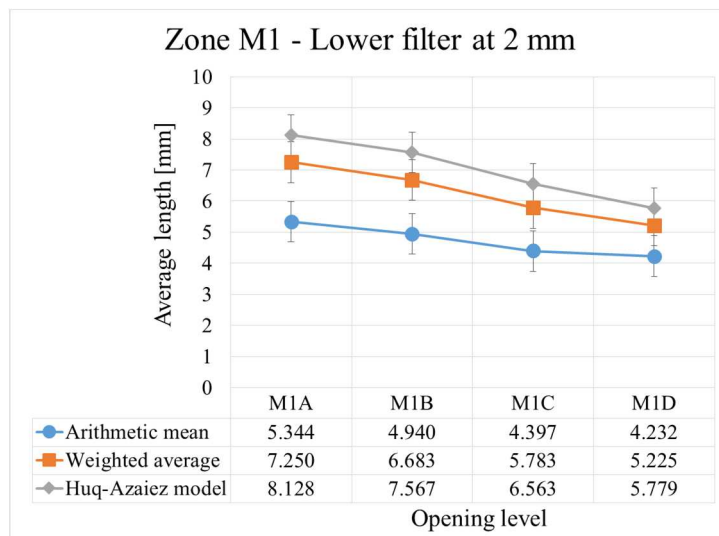


Figure 3.62 Average length in the zone M1 by reducing the overture of the hot nozzle. The lower filter at 2 mm was applied

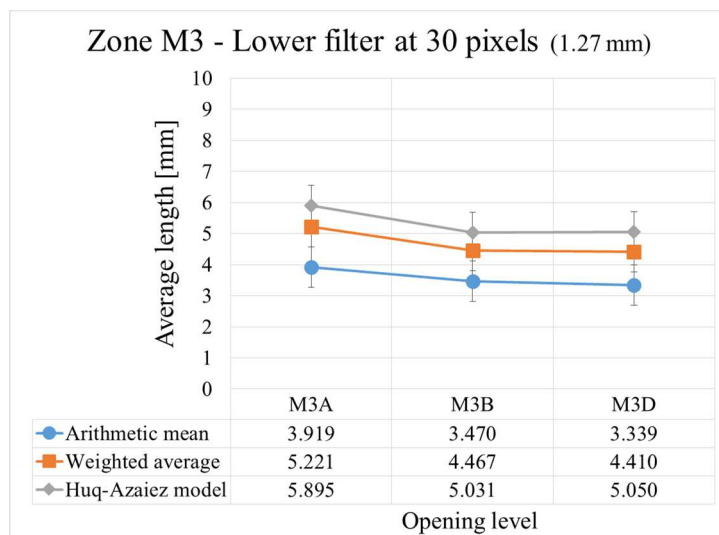


Figure 3.63 Average length in the zone M3 by reducing the overture of the hot nozzle. The lower filter at 30 pixels (1.27 mm) was applied

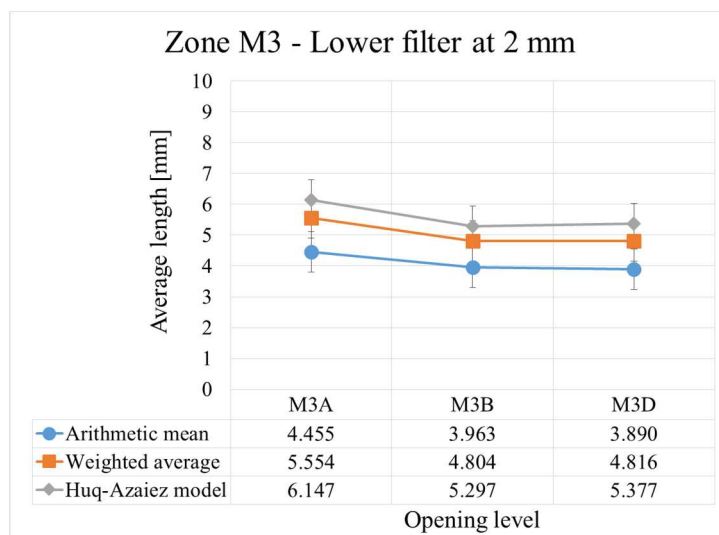


Figure 3.64 Average length in the zone M3 by reducing the overture of the hot nozzle. The lower filter at 2 mm was applied

The results obtained at the end of the study based on the samples provided by INglass are first summarized in Figure 3.65 and Figure 3.66.

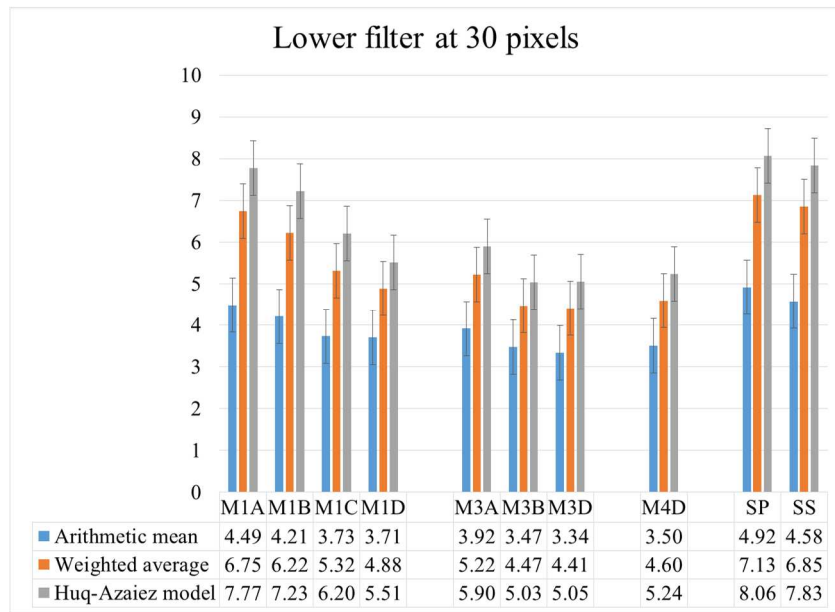


Figure 3.65 Average length of the fibers in the 10 samples by applying the lower filter at 30 pixels (1.27 mm)

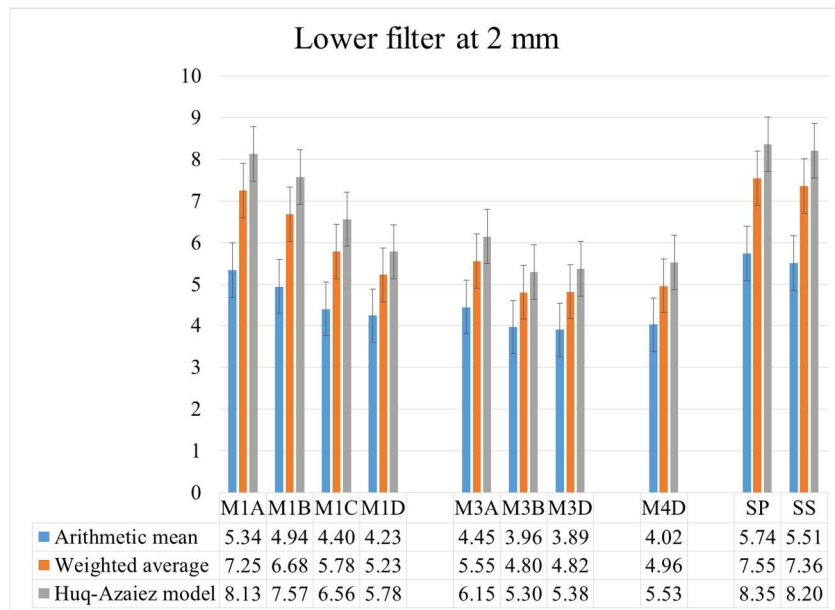


Figure 3.66 Average length of the fibers in the 10 samples by applying the lower filter at 2 mm

In Table 3.18 the averages, with relative uncertainty are summarized, for each sub-sample analyzed, taking the filter on the lengths below the default value of 30 pixels (1.27 mm). Table 3.19 shows the ratio between weighted average and arithmetic mean, as required by the standard.

Table 3.18 Average values of the fiber length that was measured with a lower filter at 30 pixels

Lower filter at 30 pixels (1.27 mm)			
	Arithmetic mean [mm]	Weighted average [mm]	Huq-Azaiez model [mm]
M1A	4.489±0.653	6.749±0.653	7.768±0.653
M1B	4.209±0.653	6.223±0.653	7.227±0.653
M1C	3.730±0.653	5.315±0.653	6.200±0.653
M1D	3.707±0.653	4.882±0.653	5.514±0.653
M3A	3.919±0.653	5.221±0.653	5.895±0.653
M3B	3.470±0.653	4.467±0.653	5.031±0.653
M3D	3.339±0.653	4.410±0.653	5.050±0.653
M4D	3.499±0.653	4.597±0.653	5.242±0.653
SP	4.920±0.653	7.133±0.653	8.061±0.653
SS	4.581±0.653	6.846±0.653	7.831±0.653

Table 3.19 Rate between weighted average and arithmetic mean of the fiber length that was measured with a lower filter at 30 pixels

Zone of the spoiler and opening level of the nozzle	Rate between weighted average and arithmetic mean
M1A	1.503
M1B	1.478
M1C	1.425
M1D	1.317
M3A	1.332
M3B	1.280
M3C	1.321
M4D	1.314
SP	1.450
SS	1.491

The fiber length distributions for the M1A and the M1D samples are reported in Figure 3.67 and Figure 3.68. It is particularly evident the large number of very small fibers, especially in the M1A sample, which is exclusively due to the effect of the lower filter. The fiber breakage is higher for the lower level of the nozzle opening and the filter cuts out the shorter fragments. Factors that contribute to the fiber breakage are responsible of the histogram shift to the left and the filter hides the shorter fragment from the graphical representation. A similar effect is noticed by increasing the filtering value from 1.27 mm to 2 mm, as it is reported for the sample M1A and M1D, in Figure 3.69 and Figure 3.70 respectively.

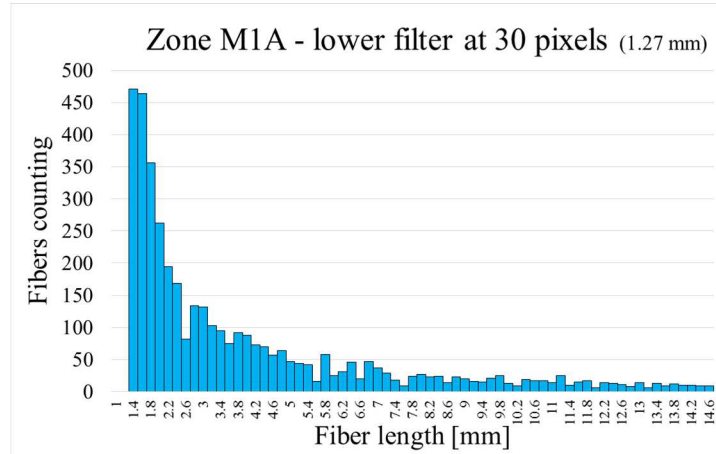


Figure 3.67 Fibers counting in each class of the sample M1A with the values that are lower filtered at 30 pixels. The graph is representative of the frequency in a sample on 4000 fibers

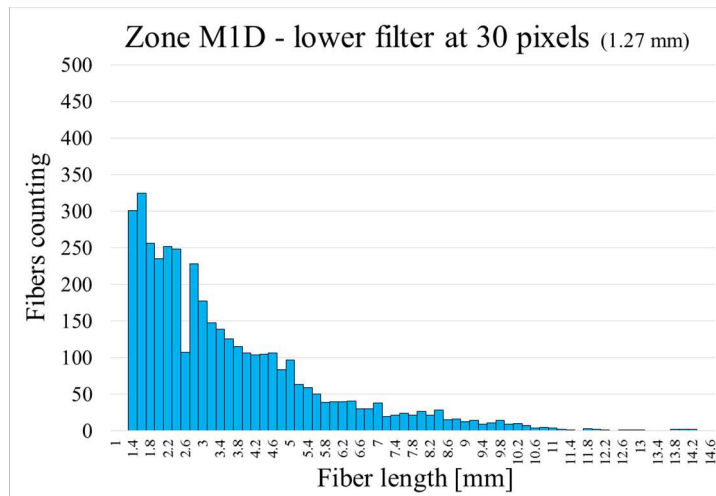


Figure 3.68 Fibers counting in each class of the sample M1D with the values that are lower filtered at 30 pixels. The graph is representative of the frequency in a sample on 4000 fibers

However this expedient was necessary because during the spreading of the samples, the presence of impurities due to the matrix pyrolysis or to additional unknown filler was detected. The presence of dust limits the software capability in recognizing and measuring the fibers. In general ctFIRE tends to recognize and add the dust, creating small fibers that bias the statistics. In order to minimize this problem, the lower filter was increased to 2 mm.

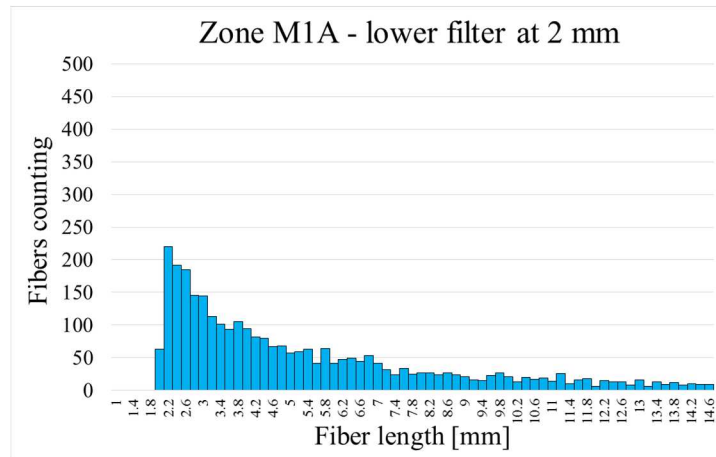


Figure 3.69 Fibers counting in each class of the sample M1A with the values that are lower filtered at 2 mm. The graph is representative of the frequency in a sample on 3000 fibers

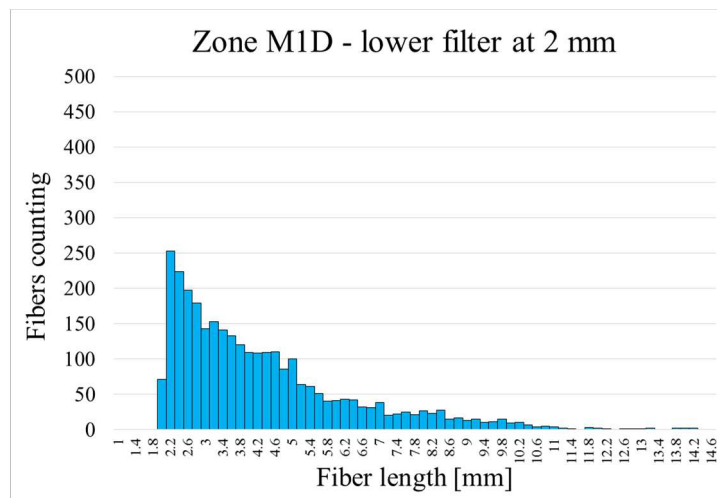


Figure 3.70 Fibers counting in each class of the sample M1D with the values that are lower filtered at 2 mm. The graph is representative of the frequency in a sample on 3000 fibers

The averages were recalculated after having applied the filter at 2 mm and the values are summarized in Table 3.20. The ratio between weighted average and arithmetic mean is reported in Table 3.21.

Table 3.20 Average values of the fiber length that was measured with a lower filter at 2 mm

Lower filter at 2 mm			
	Arithmetic mean [mm]	Weighted average [mm]	Huq-Azaiez model [mm]
M1A	5.344±0.653	7.250±0.653	8.128±0.653
M1B	4.940±0.653	6.683±0.653	7.567±0.653
M1C	4.397±0.653	5.783±0.653	6.563±0.653
M1D	4.232±0.653	5.225±0.653	5.779±0.653
M3A	4.455±0.653	5.554±0.653	6.147±0.653
M3B	3.963±0.653	4.804±0.653	5.297±0.653
M3D	3.890±0.653	4.816±0.653	5.377±0.653
M4D	4.016±0.653	4.958±0.653	5.530±0.653
SP	5.742±0.653	7.546±0.653	8.350±0.653
SS	5.507±0.653	7.360±0.653	8.197±0.653

Table 3.21 Rate between weighted average and arithmetic mean of the fiber length that was measured with a lower filter at 2 mm

Zone of the spoiler and opening level of the nozzle	Rate between weighted average and arithmetic mean
M1A	1.356
M1B	1.353
M1C	1.316
M1D	1.235
M3A	1.247
M3B	1.212
M3C	1.238
M4D	1.235
SP	1.314
SS	1.336

3.10 Conclusions

This work has allowed to develop a method for automatically measuring and counting samples of thousands glass fibers and to calculate its relative uncertainty of measurement. The method makes use of an optical acquisition system and a software application for fibers recognition. An adapted version of the ISO standard 15530-3, which describes the so-called replacement method, was applied. A sample of fibers was calibrated using an optical CMM. The same sample was scanned with the acquisition system and analyzed using the software ctFIRE, identifying each time which measurement corresponds to each fiber, for a total of 50 fibers. The uncertainty of measurement was calculated using the systematic errors and standard deviations of the fibers identified and measured by the software. This uncertainty, as measured from the sample, is applicable to all measurements that are performed by following this procedure. The cleaning operations and the arrangement of fibers on the scanner screen were improved, trying to minimize the presence of impurities and dust that ctFIRE can detect as small fibers. In parallel, the understanding of how ctFIRE works was improved, in particular of how noise affects the results, making it necessary a filtering of shorter fibers. The study also made it possible to find the best user-adjustable parameters for the various cases examined. It was noticed as the parameters to be adjusted could not be the same for both a small slide that for the complete acquisition of large samples, due to the different amount of fibers. The uncertainty of measurement was extended by manually measuring first a sample of 50 fibers and then a sample of 35 sub-images, using the ImageJ software, both for the single sub-image and for the full sample. However, long scratches were identified on the scanner screen that alter in particular the value of the weighted and Huq-Azaiez means, which take greater account of the longer fibers.

It was necessary to implement a filter on the maximum fiber length considered by the software. In this way, for each sub-image, the weighted average and the Huq-Azaiez mean values, obtained using the ImageJ software, were always within the ctFIRE measures, considering their uncertainty. This does not always apply to the arithmetical average of the single image because the default lower filter (30 pixels) cuts out the shortest fibers, which were manually measured instead. However, by lowering this filter threshold, ctFIRE measurements were affected by a lot of noise that affects even more the average statistics. This effect is, however, reduced if the statistic is extended to the full sample of 35 sub-images, where the average is also within the uncertainty limits.

In the Maxi Melt screw case study, some fibers samples collected from an injection molding plasticizing screw were analyzed. The samples were taken at various distances from the hopper of the screw, after the pyrolysis of the matrix. The arithmetic, weighted and Huq-Azaiez averages were calculated for all zones. It was noted that each average, as expected, shows a decreasing trend along the screw. The Huq-Azaiez average values, obtained from the analysis respectively before and after the optimization, were compared, with the same lower (1.5 mm) and upper (10 mm) filtering thresholds. The percentage reductions of fiber length were also compared. The percentage reduction in the first section examined (200 mm from the hopper) is equal to 33% and it is lower than value calculated before di optimization (45%). The percentage reduction of the fibers calculated for the last section (800 mm from the hopper) is higher after optimization (67%) than before (59%).

The understanding of how filtering affects the measurements was improved, and it was decided to set the lower threshold to 1.27 mm (30 pixels) and the higher threshold to 10.5 mm. In this way, long scratches on the scanner screen, noise and dust were excluded but many fibers, which had been previously neglected, were included in statistics, such as those

one that ctFIRE considers little longer than 10 mm because it merges some noise pixels to the ends of long fibers.

As a final case study, ten samples of fibers supplied by INglass were analyzed. They were collected from various locations of a car spoiler and, after trimming, the matrix was pyrolysed. Given the presence of a lot of ash and dust in the samples (they likely contained a contaminating filler), the low filtering threshold was set to 2 mm, and in parallel the analysis was performed setting the same threshold to 1.27 mm (30 pixels). About 3000 fibers were analyzed in the first case and 4000 in the latter. The arithmetic, weighted and Huq Azaiez averages were calculated for each zone, with both filtrations. Furthermore the trend of the average length of the fibers in the zones M1 and M3 was analyzed at different opening levels of the valve gate, with both filtrations.

Bibliography

Part 1

- [1] Regulation (EC) No 661/2009 on the general safety of motor vehicles of the European Parliament and of the Council
- [2] Regulation (EC) No 78/2009 on the protection of pedestrians and other vulnerable road users of the European Parliament and of the Council
- [3] Regulation (EC) No. 44 on the Child Restraint Systems of the European Parliament and of the Council
- [4] Regulation (EC) No. 129 on the Child Restraint Systems used on board of motor vehicles (ECRS) of the European Parliament and of the Council
- [5] http://europa.eu/legislation_summaries/internal_market/single_market_for_goods/motor_vehicles/interactions_industry_policies/mi0046_it.htm
- [6] Regulation (EC) No 443/2009 of the European Parliament and of the Council
- [7] http://www.area.trieste.it/opencms/export/area/en/informa_en/allegati_pubblicazioni_en/pubblicazioni_en/pubblicazioni_tt_en/autodemolizione.pdf
- [8] Directive 2000/53/EC on End-of-Life Vehicles of the European Parliament and of the Council
- [9] Lyu M. Y. and Choi T. G., Research Trends in Polymer Materials for Use in Lightweight Vehicles, *International Journal of Precision Engineering and Manufacturing*, Vol. 16, No. 1, pp. 213-220, 2015
- [10] Stacy C. D., Susan W. D. and Robert G. B., *Transportation Energy Data Book: Edition 33*, http://cta.ornl.gov/data/tedb33/Edition33_Full_Doc.pdf (Accessed 3 DEC 2014)
- [11] Zhang Y., Zhu, P., and Chen G., Lightweight Design of Automotive Front Side Rail based on Robust Optimisation, *Thin-Walled Structures*, Vol. 45, No. 7, pp. 670-676, 2007.
- [12]. Kastensson A., Developing Lightweight Concepts in the Automotive Industry: Taking on the Environmental Challenge with the Sånätt Project, *Journal of Cleaner Production*, Vol. 66, pp. 337-346, 2014.
- [13] Mahajan G. V. and Aher V. S., Composite Material: A Review over Current Development and Automotive Application, *International Journal of Scientific and Research Publications*, Vol. 2, No. 11, pp.1-5, 2012.
- [14] Park C. K., Kan C. D. S., Hollowell W. T., and Hill S. I., Investigation of Opportunities for Lightweight Vehicles using Advanced Plastics and Composites, *National Highway Traffic Safety Administration*, Document ID: DOT HS 811 692, 2012.
- [15] Stewart R., Automotive Composites Offer Lighter Solutions, *Reinforced Plastics*, Vol. 54, No. 2, pp. 22-28, 2010.
- [16] Park H. S., Dang X. P., Roderburg A. and Nau B., Development of Plastic Front Side Panels for Green Cars, *CIRP Journal of Manufacturing Science and Technology*, Vol. 6, No. 1, pp. 44-52, 2013.

- [17] Sancaktar E. and Gratton M., Design, Analysis, and Optimization of Composite Leaf Springs for Light Vehicle Applications, *Composite Structures*, Vol. 44, No. 2, pp. 195-204, 1999.
- [18] Gaikwad D., Sonkusare R., and Wagh S., Composite Leaf Spring for Light Weight Vehicle-Materials, Manufacturing Process, Advantages & Limitations, *International Journal of Engineering and Technoscience*, Vol. 3, No. 2, pp. 410-413, 2012.
- [19] Leibfried R., PEEK Parts-Reduce Weight without Sacrificing Performance, *Advanced Materials & Processes*, Vol. 171, No. 5, pp. 35-37, 2013.
- [20] Cantor B., Grant P. and Johnston C., *Automotive Engineering: Lightweight, Functional, and Novel Materials*, CRC Press, pp. 29-35, 2008.
- [21] Hergenrother P. M., The Use, Design, Synthesis, and Properties of High Performance/High Temperature Polymers: An Overview, *High Performance Polymers*, Vol. 15, No. 1, pp. 3-45, 2003.
- [22] Al-Hussaini A. S., Synthesis and Characterization of New Thermally Stable Polymers as New High-Performance Engineering Plastics, *High Performance Polymers*, Vol. 26, No. 2, pp. 166-174, 2014.
- [23] Sandor R. B., PBI (Polybenzimidazole): Synthesis, Properties and Application, *High Performance Polymers*, Vol. 2, No. 1, pp. 25-37, 1990.
- [24] Lee L. J., Zeng C., Cao X., Han X., Shen J. and Xu G., Polymer Nanocomposite Foams, *Composites Science and Technology*, Vol. 65, No. 15-16, pp. 2344-2363, 2005.
- [25] Deligio T., Injection Molding with Mucell: Mucell Microcellular Foam Bubbling up in a Variety of Automotive Applications, *Modern Plastics Worldwide*, Vol. 87, No. 7, pp. 12-15, 2010.
- [26] Park C. B., Behravesh A. H. and Venter R. D., Low Density Microcellular Foam Processing in Extrusion Using CO₂, *Polymer Engineering and Science*, Vol. 38, No. 11, pp. 1812- 1823, 1998.
- [27] Reglero Ruiz, J. A., Vincent, M. and Agassant, J. F., Numerical modeling of bubble growth in microcellular polypropylene produced in a core-back injection process using chemical blowing agents *International Polymer Processing*, 31 (1), pp. 26-36 (2016)
- [28] Mallick P. K., *Materials, Design and Manufacturing for Lightweight Vehicles*, Elsevier, pp. 208-230, 2010.
- [29] Orgeas L. and Dumont P. J. J., *Wiley Encyclopedia of Composite*, John Wiley & Sons, pp. 2683-2718, 2011.
- [30] Friedrich K. and Almajid A. A., Manufacturing Aspects of Advanced Polymer Composites for Automotive Applications, *Applied Composite Materials*, Vol. 20, No. 2, pp. 107-128, 2013.
- [31] Elmarakbi A., *Advanced Composite Materials for Automotive Applications: Structural Integrity and Crashworthiness*, John Wiley & Sons, pp. 3-28, 2014.
- [32] Kim D. H., Choi D. H. and Kim H. S., Design Optimization of a Carbon Fiber Reinforced Composite Automotive Lower Arm, *Composites Part B: Engineering*, Vol. 58, pp. 400-407, 2014.

- [33] Ryu J. B. and Lyu M. Y., A Study on the Mechanical Property and 3D Fiber Distribution in Injection Molded Glass Fiber Reinforced PA66, *International Polymer Processing*, Vol. 29, No. 3, pp. 389-401, 2014.
- [34] Hufenbach W., Böhm R., Thieme M., Winkler, A., Mäder, E. et al., Polypropylene/Glass Fibre 3D-Textile Reinforced Composites for Automotive Applications, *Materials & Design*, Vol. 32, No. 3, pp. 1468-1476, 2011.
- [35] Kim K. S., Bae K. M., Oh S. Y., Seo M. K., Kang C. G. and Park S. J., Trend of Carbon Fiber-Reinforced Composites for Lightweight Vehicles, *Elastomers and Composites*, Vol. 47, No. 1, pp. 65-74, 2012.
- [36] Ernst H., Henning F. and Robbins J. R., Long Fiber Reinforced Thermoplastic LFT-D and Thermosetting D-SMC Processes for Lightweight Parts Production - Trends and Recent Applications, *Proceeding of the 9th Automotive Composites Conference and Exhibition*, 2009.
- [37] Beardmore P. and Johnson C. F., The Potential for Composites in Structural Automotive Applications, *Composites Science and Technology*, Vol. 26, No. 4, pp. 251-281, 1986.
- [38] Fais C., Lightweight Automotive Design with HP-RTM, *Reinforced Plastics*, Vol. 55, No. 5, pp. 29-31, 2011.
- [39] Hillermeier R. W., Hasson T., Friedrich L. and Ball C., Advanced Thermosetting Resin Matrix Technology for Next Generation High Volume Manufacture of Automotive Composite Structures, *Proceeding of the SAE 2013 World Congress and Exhibition*, pp. 1176-1185, 2013.
- [40] Verrey J., Wakeman M. D., Michaud V. and Månson J. A., Manufacturing Cost Comparison of Thermoplastic and Thermoset RTM for an Automotive Floor Pan, *Composites Part A: Applied Science and Manufacturing*, Vol. 37, No. 1, pp. 9-22, 2006.
- [41] Abounaim M., Hoffmann G., Diestel O., and Cherif C., Thermoplastic Composite from Innovative Flat Knitted 3D Multi-Layer Spacer Fabric using Hybrid Yarn and the Study of 2D Mechanical Properties, *Composites Science and Technology*, Vol. 70, No. 2, pp. 363-370, 2010.
- [42] Herranen H., Pabut O., Eerme M., Majak J., Pohlak, M., et al., Design and Testing of Sandwich Structures with Different Core Materials, *Materials Science*, Vol. 18, No. 1, pp. 45-50, 2012.
- [43] Bannister D., An Introduction to Core Materials, *Reinforced Plastics*, Vol. 58, No. 2, pp. 32-37, 2014.
- [44] Jacob A., Sandwich Solutions, *Reinforced Plastics*, Vol. 48, No.5, pp. 30-33, 2004.
- [45] Stewart R., At the Core of Lightweight Composites, *Reinforced Plastics*, Vol. 53, No. 3, pp. 30-35, 2009.
- [46] George T., Deshpande V. S. and Wadley H. N., Mechanical Response of Carbon Fiber Composite Sandwich Panels with Pyramidal Truss Cores, *Composites Part A: Applied Science and Manufacturing*, Vol. 47, pp. 31-40, 2013.
- [47] George T., Deshpande V. S., Sharp K., and Wadley H. N., Hybrid Core Carbon Fiber Composite Sandwich Panels: Fabrication and Mechanical Response, *Composite Structures*, Vol. 108, pp. 696-710, 2014.

- [48] Evans A. G., *Lightweight Materials and Structures*, MRS Bulletin, Vol. 26, No. 10, pp. 790-797, 2001.
- [49] Hyun S. and Torquato S., *Optimal and Manufacturable Two-Dimensional, Kagome-Like Cellular Solids*, *Journal of Materials Research*, Vol. 17, No. 1, pp. 137-144, 2002.
- [50] Hutchinson R. G., Wicks N., Evans A. G., Fleck N. A. and Hutchinson J. W., *Kagome Plate Structures for Actuation*, *International Journal of Solids and Structures*, Vol. 40, No. 25, pp.6969-6980, 2003.
- [51] Grujicic M., Sellappan V., Omar M., Seyr N., Obieglo A., et al., *An Overview of the Polymer-to-Metal Direct-Adhesion Hybrid Technologies for Load-Bearing Automotive Components*, *Journal of Materials Processing Technology*, Vol. 197, No. 1, pp. 363-373, 2008.
- [52] Honkanen M., Hoikkanen M., Vippola M., Vuorinen J. and Lepistö T., *Metal-Plastic Adhesion in Injection-Molded Hybrids*, *Journal of Adhesion Science and Technology*, Vol. 23, No. 13-14, pp. 1747-1761, 2009.
- [53] Amancio Filho S. and Dos Santos J., *Joining of Polymers and Polymer-Metal Hybrid Structures: Recent Developments and Trends*, *Polymer Engineering & Science*, Vol. 49, No. 8, pp. 1461-1476, 2009.
- [54] Lucchetta G., Marinello F., and Bariani P., *Aluminum Sheet Surface Roughness Correlation with Adhesion in Polymer Metal Hybrid Overmolding*, *CIRP Annals-Manufacturing Technology*, Vol. 60, No. 1, pp. 559-562, 2011.
- [55] Ferret B., Anduze M. and Nardari C., *Metal Inserts in Structural Composite Materials Manufactured by RTM*, *Composites Part A: Applied Science and Manufacturing*, Vol. 29, No. 5, pp. 693-700, 1998.
- [56] https://techcenter.lanxess.com/scp/emea/en/docguard/TI_2009003_EN_Nylon_Composite_Sheets.pdf?docId=12406805 visited on 13/11/2016
- [57] Müller T., Kuehnert I. and Osswald T. A., *Injection Molding of High-Performance Hybrid Composites in Series-Production*, *Proceeding of the 67th Annual Technical Conference of the Society of Plastics Engineers*, pp. 1233-1237, 2009.
- [58] Fiorotto M. and Lucchetta G., *Experimental Investigation of a New Hybrid Molding Process to Manufacture High-performance Composites*, *International Journal of Material Forming*; Vol. 1, No. 6, pp. 179-185, 2013
- [59] <https://techcenter.lanxess.com/scp/americas/en/innoscp/tech/78310/article.jsp?docId=78310> visited on 13/11/2016
- [60] <http://techcenter.lanxess.com/scp/emea/en/innoscp/tech/79047/article.jsp?docId=16923133> visited on 13/11/2016
- [61] <http://www.compositesworld.com/articles/what39s-new-in-automotive-front-end-modules> visited on 13/11/2016
- [62] http://lanxess.com/en/media-download/hightech-plastics-for-lightweight-solutions_de/ visited on 13/11/2016
- [63] <http://www.borealisgroup.com/Global/Polyolefins/Engineering%20Applications/Automotive/Fibermod/fibermod-fiber-reinforced-polypropylene-for-light-integrated-high-performing-solutions.pdf> visited on 13/11/2016

- [64] <http://www.ptonline.com/articles/the-new-lightweights-injection-molded-hybrid-composites-spur-automotive-innovation> visited on 13/11/2016
- [65] Holzinger G.P., Wurtele M., Schierl S. and Kruppa S., Efficient Injection Molding Processes for the Serial Production of Continuous Fiber Reinforced Parts, Proceedings of the Second International MERGE Technologies Conference, pp. 119-126, 2015.
- [66] http://www.kraussmaffei.com/media/files/kmdownloadlocal/immen/IMM_BR_FiberForm_en.pdf visited on 13/11/2016
- [67] http://worldaccount.basf.com/wa/plasticsAP~en_GB/portal/show/common/plasticsportal_news/2012/12_187 visited on 13/11/2016
- [68] <http://bond-laminates.com/en/technology/processing-options/hybrid-molding/> visited on 13/11/2016
- [69] <http://bond-laminates.com/en/technology/processing-options/insert-molding/> visited on 13/11/2016
- [70] http://lanxess.com/uploads/tx_lxsmatrix/Tepex_Folder_9.5..pdf visited on 13/11/2016
- [71] <http://www.ipt.fraunhofer.de/en/Press/Pressreleases/20160308lightflexjec.html> visited on 13/11/2016
- [72] Hopmann Ch., Hildebrandt M., Janssen H., Beste C. and Werne D., Individualized Production of Thermoplastic Composites Parts – Combining Additive Manufacturing and Thermoforming, Proceeding of the 3rd International Conference & Exhibitions on Thermoplastic Composites, Vol. 1 pp 82-84, 2016.
- [73] Kaiser R., Technology Assessment of Automotive Applications of Metal-plastic Laminates, Argos Associates, Inc. Final report for the U.S. Department of Transportation, Vol. 2, pp. 3-4, 1980
- [74] Altair Engineering Inc., Hypermesh Desktop Introduction Pre-Processing for Finite Element Analysis. HyperWorks 13.0 , 2014
- [75] Ansys Inc., Introduction to Contact: Ansys Mechanical Structural Nonlinearities, Ansys Customer Training Material, 2013.
- [76] Giusti R. and Lucchetta G., Modeling the Adhesion Bonding Mechanism in Overmolding Hybrid Structural Parts for Lightweight Applications, Key Engineering Materials, Vols. 611-612, pp. 915-921, 2014 DOI: 10.4028/www.scientific.net/KEM.611-612.915
- [77] Moritzer E., Budde C., Tröster T. and Pöhler S., Study of the Bond Strength of a Combination Consisting of Composite Sheet and Short-fiber Thermoplastic, Proceedings of the Euro Hybrid Materials and Structures 2014, Vol. 1, pp. 188-192, 2014.

Part 2

- [1] Amancio-Filho S. T., dos Santos J. F., Joining of Polymers and Polymer-Metal Hybrid Structures: Recent Developments and Trends. *Polymer Engineering and Science*, Vol. 49, No. 8, pp. 1461-1476, 2009. DOI 10.1002/pen.21424
- [2] Grewell D. Benator A. Welding of Plastics: Fundamentals and New Developments. *International Polymer Processing Journal of the Polymer Processing Society (2007)* Vol. 22, No. 2, pp. 43-60, 2007. DOI: 10.3139/217.0051
- [3] Stevens S. M., The evaluation of Molecular Orientation and Structural Changes in Polypropylene Welds, *Proceedings of the Annual Technical Conference of the Society of Plastic Engineering*, pp. 378-380, 1993.
- [4] Yan B., Wu H., Jiang G., Guo S. and Huang J., Interfacial Crystalline Structures in Injection Over-molded Polypropylene and Bond Strength, *ACS Applied Materials and Interfaces*, Vol. 2, No. 11, pp. 3023-3036, 2010. DOI: 10.1021/am1003574
- [5] Park J.B. and Benatar A., Moire Interferometry Measurement of Residual Strains in Implant Resistance Welding of Polycarbonate, *Proceedings of the Annual Technical Conference of the Society of Plastic Engineers*, Vol. 1, pp 353-358, 1992.
- [6] Park J.B. and Benatar A., Thermal and Residual Stress Formation during Plastic Welding, *Annual Technical Conference for the Society of Plastic Engineers Proceedings Society of Plastic Engineers*, 1991.
- [7] Anantharaman S., Benatar A., Measurement of Residual Stresses in Clearwelds using Photoelasticity, *Proceedings of the Annual Technical Conference of the Society of Plastic Engineers Proceedings*, Vol. 1, pp. 1051-1055, 2003.
- [8] Anantharaman S. and Benatar A., Measurement of Residual Stresses in Laser welded Polycarbonate using Photoelasticity, *Proceedings of the Annual Technical Conference of the Society of Plastic Engineers*, pp. 1061-1065, 2003.
- [9] Park J. B., Theoretical and Experimental Analysis of Residual Stress Formation after Implant Resistance Welding of Polycarbonate, Ph.D. Thesis, 1992.
- [10] Grujicic M, Sellappan V., Omar M. A., Seyr N., Obieglo A., Erdmann M. and Holzleitner J., An Overview of the Polymer-to-metal Direct-Adhesion Hybrid Technologies for Load-bearing Automotive Components. *Journal of Materials Processing Technology*, Vol. 197, No. 1, pp. 363–373, 2008.
- [11] Grujicic M, Sellappan V., Arakere G., Seyr N. and Erdmann M., Computational Feasibility Analysis of Direct-adhesion Polymer-to-metal Hybrid Technology for Load-bearing Body-in-white Structural Components. *Journal of Materials Processing Technology*, Vol. 195, No. 1, pp. 282–298, 2008.
- [12] Ramani K. and Moriarty B., Thermoplastic Bonding to Metals via Injection Molding for Macro-composite Manufacture. *Polymer Engineering and Science*, Vol. 38, No. 5, pp. 870–877, 1998.
- [13] Fabrin P. A., Hoikkanen M. E. and Vuorinen J. E., Adhesion of Thermoplastic Elastomer on Surface Treated Aluminum by Injection Molding. *Polymer Engineering and Science*, Vol. 47, No. 8, pp. 1187–1191, 2007.

- [14] Dayss E., Leps G. and Meinhardt J., Surface Modification for Improved Adhesion of a Polymer-metal Compound, *Surface and Coatings Technology*, Vol. 116, pp. 986-990, 1999. DOI: [http://dx.doi.org/10.1016/S0257-8972\(99\)00184-X](http://dx.doi.org/10.1016/S0257-8972(99)00184-X)
- [15] Hopmann Ch., Boettcher A. and Fischer K., Investigation of Bonding Approaches and Initial Bond Strength for the Intrinsic Manufacturing of Laminary Bonded Hybrids Made of Thermoplastic Composite and Metal, *Journal of Plastic Technology*, Vol. 9, No. 6, pp 254-274, 2013.
- [16] Lucchetta G., Marinello F. and Bariani P. F., Aluminum Sheet Surface Roughness Correlation with Adhesion in Polymer Metal Hybrid Overmolding. *CIRP Annals – Manufacturing Technology*, Vol. 60, pp. 559-562, 2011.
- [17] Aurrekoetxea J., Castillo G., Cortes F., Sarrionandia M. A. and Urrutibeascoa I., Failure of Multimaterial Fusion Bonding Interface Generated during Over-Injection Molding/Thermoforming Hybrid Process, *Journal of Applied Polymer Science*, Vol. 102, No. 1, pp. 261-265, 2006. DOI 10.1002/app.23696
- [18] Moritzer E., Budde C., Tröster T. and Pöhler S., Study of the Bond Strength of a Combination Consisting of Composite Sheet and Short-fiber Thermoplastic, *Proceedings of the Euro Hybrid Materials and Structures 2014*, Vol. 1, pp. 188-192, 2014.
- [19] Giusti R. and Lucchetta G., Modeling the Adhesion Bonding Mechanism in Overmolding Hybrid Structural Parts for Lightweight Applications, *Key Engineering Materials*, Vols. 611-612, pp. 915-921, 2014 DOI: 10.4028/www.scientific.net/KEM.611-612.915
- [20] Fiorotto M. and Lucchetta G., Experimental Investigation of a new Hybrid Molding Process to Manufacture High-Performance Composite, *International Journal of Material Forming*, Vol. 6, No. 1, pp. 179-185, 2013. DOI:10.1007/s12289-011-1066-3
- [21] <http://www.ipt.fraunhofer.de/en/Press/Pressreleases/20160308lightflexjec.html> visited on 13/11/2106
- [22] Hopmann Ch., Hildebrandt M., Janssen H., Beste C. and Werne D., Individualized Production of Thermoplastic Composites Parts – Combining Additive Manufacturing and Thermoforming, *Proceeding of the 3rd International Conference & Exhibitions on Thermoplastic Composites*, Vol. 1 pp 82-84, 2016.
- [23] De Gennes P. J., Reptation of a Polymer Chain in The Presence of Fixed Obstacles, *Journal of chemical physics*, Vol. 55, pp. 572-579, 1971.
- [24] Edwards S. F., The Statistical Mechanics of Polymerized Material, *Proceedings of the Physical Society*, Vol 92, No. 1, pp. 9, 1964.
- [25] Doi M. and Edwards S. F., Dynamics of Concentrated Polymer Systems. Part 1- Brownian Motion in the Equilibrium State. *Journal of the Chemical Society, Faraday Transactions 2: Molecular and Chemical Physics*, Vol. 74, pp. 1789-1801, 1978.
- [26] Kim Y. H., and Wool R. P., A theory of healing at a polymer-polymer interface. *Macromolecules*, Vol.16, No. 7, pp. 1115-1120, 1983.
- [27] Graessley W. W., Some Phenomenological Consequences of the Doi-Edwards Theory of Viscoelasticity, *Journal of Polymer Science: Polymer Physics Edition*, Vol. 18, No. 1, pp. 27-34, 1980.

- [28] Liu C., He J., van Ruymbeke E., Keunings R., Baily C., Evaluation of Different Methods for the Determination of the Plateau Modulus and the Entanglement Molecular Weight, *Polymer*, Vol. 47, pp. 4461-4479, 2006. DOI:10.1016/j.polymer.2006.04.054
- [29] Buesche F., *Physical Properties of Polymers*. Interscience, New York, 1962.
- [30] Ferry J. D., *Viscoelasticity of Polymers*. John Wiley & Sons, Inc., New York, 1980.
- [31] Debondue E., Fournier J. E., Lacrampe M. F. and Krawczak P., Weld-line Sensitivity of Injected Amorphous Polymers, *Journal of Applied Polymer Science*, Vol. 93, pp. 644-650, 2004.
- [32] Lafranche E., Renault T., Krawczak P., Effect of the Interdiffusion at the Polymer-Polymer Interface on the Flexural Properties of Overmolded Short Glass Fiber-Glass Fabric Reinforced PA6 Composites, *Key Engineering Materials*, Vol. 611-612, pp. 821-828, 2014.
- [33] Bastien L. J. and Gillespie J. W., A Non-Isothermal Healing Model for Strength and Toughness of Fusion Bonded Joints of Amorphous Thermoplastics, *Polymer Engineering and Science*, Vol 31, pp. 1720-1730, 1991.
- [34] Yang F. and Pitchumani R., Nonisothermal Healing and Interlaminar Bond Strength Evolution During Thermoplastic Matrix Composites Processing, *Polymer Composites*, Vol. 24, pp. 263-279, 2003.
- [35] Sonmez F. O., Hahn H. T., Modeling of Heat Transfer and Crystallization in Thermoplastic Composite Tape Placement Process, *Journal of thermoplastic Composite Material*, Vol. 10, pp. 198-240, 1997
- [36] Teraoka I., *Polymer Solution: An introduction to Physical Properties*, John Wiley & Sons Inc. pp. 18, 2002
- [37] Dugdale D. S., Yielding of Steel Sheets Containing Slits, *Journal of the Mechanics and Physics of Solids*. Vol. 8, No. 2, pp. 100–104, 1960. DOI:10.1016/0022-5096(60)90013-2.
- [38] Barenblatt G. I., The Mathematical Theory of Equilibrium Cracks in Brittle Fracture, *Advances in Applied Mechanics*, Vol. 7, pp. 55–129, 1962. DOI:10.1016/S0065-2156(08)70121-2.
- [39] Chandra N., Li H., Shet C. and Ghonem H., Some Issues in the Application of Cohesive Zone Model for Metal-Ceramic Interfaces, *International Journal of Solids and Structures*, Vol. 39, No. 10 , pp. 2827-2855, 2002.
- [40] Geubelle P. H. and Baylor J. S., Impact-Induced Delamination of Composites: a 2D Simulation, *Composites Part B: Engineering*, Vol. 29, No. 5, pp. 589-602, 1998.
- [41] Giuliese G., Palazetti R., Moroni F., Zucchelli A. and Pirondi A., Cohesive Zone Modeling of Delamination Response of a Composite Laminate with Interleaved Nylon 6,6 Nanofibers, *Composites Part B*, Vol. 78, pp. 384-392, 2015.
- [42] Xie D. and Waas A., Discrete Cohesive Zone Model for Mixed Mode Fracture Using Finite Element Analysis, *Engineering Fracture Mechanics*; Vol. 73, No. 13, pp. 1783-96, 2006.
- [43] Vandellos T., Martin E. and Leguillon D., Comparison Between Cohesive Zone Models and a Coupled Criterion for Prediction of Edge Debonding, *16th European Conference on Composite Materials*, 2014.
- [44] Neira-Velázquez M. G., Rodríguez-Hernández M. T., Hernández-Hernández E. and Ruiz-Martínez A. R., Polymer Molecular Weight Measurement, *Handbook of Polymer*

Synthesis, Characterization and Processing edited by Saldiva-Guerra E. and Vivaldo-Lima E., pp. 355-366, 2013. DOI: 10.1002/9781118480793.ch17

[45] Dutta A., On viscosity-Melt Flow Index Relationship, *Rheologica Acta*, Vol. 23, No. 5, pp 565-569, 1984. DOI: DOI:10.1007/BF01329290

[46] <http://www.ampolymer.com/Mark-HouwinkParameters.html> visited on 13/11/2016

[47] Shenoy A. and Saini D. R., *Thermoplastic Melt Rheology and Processing*, Edited by Taylor and Francis, 1996

[48] Standard, ASTM D3039/D3039M-08, Standard Test Method for Tensile Properties of Polymer Matrix Composite Materials.

[49] Standard, ASTM D3518/D3518M-94, Standard Test Method for In-Plane Shear Response of Polymer Matrix Composite Materials by Tensile Test of a \pm 45° Laminate.

[50] Genta G., *Progettazione e Calcolo Strutturale con i Materiali Compositi*, Edited by Tecniche Nuove, 1982.

[51] Standard, ASTM D5528-13, Standard Test Method for Mode I Interlaminar Fracture Toughness of Unidirectional Fiber Reinforced Polymer Matrix Composites.

[52] Kim S. J., Kim S. H., Pak S. Y. and Youn J. R., Formation of Thermally Induced Craze and Prevention by Using Infrared Radiation Annealing Method, *Journal of Applied Polymer Science*, Vol. 125, pp. 3029-3037, 2012. DOI: 10.1002/app.36351

[53] Wang W., Zhao G., Wu X. and Zhai Z., The Effect of High Temperature Annealing Process on Crystallization Process of Polypropylene, Mechanical Properties, and Surface Quality of Plastic Parts, *Journal of Applied Polymer Science*, Vol. 132, No. 46, pp. 42773, 2015 DOI: 10.1002/app.42773

[54] Calhoun A. *Polypropylene, Multilayer Flexible Packaging: Technology and Applications for the Food*, Elsevier 2nd Edition, Edited by John R. and Wagner Jr., 2010.

[55] Mark E. J. *The Polymer Data Handbook*, Edited by Oxford University Press, 2009.

[56] Ding J., Ding X., Xu R. and Yu D., Viscoelastic Properties and Determination of Plateau Modulus for Ziegler-Natta Catalyzed Ethylene-Propylene Random Copolymer, *Journal of Macromolecular Science, Part B Physics*, Vol. 44, No. 3, pp. 303-315, 2004.

[57] Fetters L. J., Lohse D. J. and Colby R. H., Chain Dimensions and Entanglement Spacing, *Physical Properties of Polymer Handbook 2nd Edition*, Edited by Mark E. J., Springer New York, pp. 447-454, 2007.

[58] Eckstein A., Suhm J., Friedrich C., Maier R. D., Sassmannshausen J., Bochmann M. and Mulhaupt R., Determination of Plateau Moduli and Entanglement Molecular Weights of Isotactic, Syndiotactic, and Atactic Polypropylenes Synthesized with Metallocene Catalyst, *Macromolecules*, Vol. 31, No. 4, pp. 1335-1340, 2008.

[59] Villa R., Modeling of the Interfacial Cohesion between a Thermoplastic Matrix Laminate and an Overinjected Part, Master Thesis carried out at University of Padova under the supervision of G. Lucchetta and R. Giusti, 2015.

[60] Chadegani A., Strain Energy Release Rate Analysis of Adhesive-Bonded Composite Joints with a Prescribed Interlaminar Crack, *Journal of Aircraft*, Vol. 46, No. 1, pp. 203-215, 2009. DOI: 10.2514/1.37513

[61] Shimamoto K., Sekiguchi Y. and Sato C., The Critical Energy Release Rate of Welded Joints Between Fiber-Reinforced Thermoplastics and Metals When Thermal Residual Stress is Considered, *The Journal of Adhesion*, Vol. 92 , No. 4, pp. 306-318, 2016. DOI: <http://dx.doi.org/10.1080/00218464.2015.1031339>

[62] Mahaphasukwat S., Shimamoto K., Hayashida S., Sekiguchi Y. and Sato C., Mode I critical fracture energy of adhesively bonded joints between glass fiber reinforced thermoplastics, *Applied Adhesion Science*, Vol. 3, No. 4, pp. 1-13, 2016. DOI 10.1186/s40563-015-0036-2

Part 3

- [1] Thomason J. L. and Vlug M. A., Influence of fiber length and concentration on the properties of glass fiber-reinforced polypropylene: 1. Tensile and flexural modulus, *Composites Part A: Applied Science and Manufacturing*, Vol. 27, No. 6, pp. 477-484, 1996.
- [2] Thomason J. L. and Groenewoud W. M., The influence of fiber length and concentration on the properties of glass fiber reinforced polypropylene: 2. Thermal properties, *Composites Part A: Applied Science and Manufacturing*, Vol. 27, No. 7, pp. 555-565, 1996.
- [3] Thomason J. L., Vlug M. A., Schipper G. and Krikor H., Influence of fiber length and concentration on the properties of glass fiber-reinforced polypropylene: Part 3. Strength and strain at failure, *Composites Part A: Applied Science and Manufacturing*, Vol. 27, No. 11, pp. 1075-1084, 1996.
- [4] Thomason J. L. and Vlug M. A., The influence of fiber length and concentration on the properties of glass fiber reinforced polypropylene: 4. Impact properties, *Composites*, Vol 28A, pp. 277–288, 1997.
- [5] Thomason J. L., The influence of fiber length and concentration on the properties of glass fiber reinforced polypropylene: 5. Injection molded long and short fiber PP, *Composites: Part A*, Vol.33, pp. 1641–1652, 2002.
- [6] Thomason J. L., The influence of fiber length and concentration on the properties of glass fiber reinforced polypropylene. 6. The properties of injection molded long fiber PP at high fiber content, *Composites: Part A*, Vol. 36, pp. 995–1003, 2005.
- [7] Thomason J. L., The influence of fiber length and concentration on the properties of glass fiber reinforced polypropylene: 7. Interface strength and fiber strain in injection molded long fiber PP at high fiber content, *Composites Part A: Applied Science and Manufacturing*, Vol.38, Issue 1, pp. 210-216, 2007.
- [8] Thomason J. L. and Schoolenberg G. E., An investigation of glass fiber/polypropylene interface strength and its effect on composite properties, *Composites*, Vol. 25, pp. 197–203, 1994.
- [9] Senthil Kumar K., Ghosh A. K. and Bhatnagar N., Mechanical Properties of Injection Molded Long Fiber Polypropylene Composites, Part 1: Tensile and Flexural Properties, *Polymer Composites*, Vol.28, No. 2, pp. 259–266, 2007.
- [10] Cellere A., Injection molding of LGF-reinforced thermoplastics: numerical and experimental investigations of fibers breakage, Ph.D. thesis, 2010.
- [11] Berton M., Cellere A. and Lucchetta G., A new procedure for the analysis of fibre breakage after processing of fibre-reinforced thermoplastics, *International Journal of Material Forming*, Vol. 3, No. 1, pp. 671-674, 2010.
- [12] Hine P., Parveen B., Brands D. and Caton-Rose F., Validation of the modified rule of mixtures using a combination of fibre orientation and fibre length measurements, *Composites Part A: Applied Science and Manufacturing*, Vol. 64, pp. 70-78, 2014.

- [13] Nguyen B. N., Fifield L. S., Mori S., Gandhi U. N., Wang J., Franco C., Wollan E. J. and Tucker III C. L., Predictive Engineering Tools for Injection-Molded Long-Carbon-Fiber Thermoplastic Composites, FY 2015 Third Quarterly Report; PNNL-24472, Pacific Northwest National Laboratory, Richland, WA, 2015.
- [14] Nguyen B. N. and Simmons K. L., Predictive Engineering Tools for Injection-Molded Long-Carbon-Fiber Thermoplastic Composites, Project LM083, Pacific Northwest National Laboratory, Richland, WA, 2014.
- [15] Stein A. M., Vader D. A., Jawerth L. M., Weitz D. A. and Sander L. M., An algorithm for extracting the network geometry of three-dimensional collagen gels. *Journal of microscopy*, Vol. 232, No. 3, pp. 463-475, 2008.
- [16] Huq A. M. A. and Azaiez J., Effects of length distribution on the steady shear viscosity of semiconcentrated polymer-fiber suspensions. *Polymer Engineering & Science*, Vol. 45, No. 10, pp. 1357-1368, 2005.
- [17] Standard, ISO 15530-3:2011, Geometrical product specifications (GPS). Coordinate measuring machines (CMM): Technique for determining the uncertainty of measurement. Part 3: Use of calibrated workpieces or measurement standards.
- [18] Standard, UNI EN ISO 14253-3:2011, Geometrical product specifications (GPS). Inspection by measurement of workpieces and measuring equipment. Part 3: Guidelines for achieving agreements on measurement uncertainty statements.
- [19] Müller P., Hiller J., Dai Y., Andreasen J. L., Hansen H. N. and De Chiffre L., Estimation of measurement uncertainties in X-ray computed tomography metrology using the substitution method. *CIRP Journal of Manufacturing Science and Technology*, Vol. 7, No. 3, pp. 222-232, 2014.
- [20] Standard, ISO 22314:2006, Plastics. Glass-fibre-reinforced products. Determination of fibre length.